Conjugated molecules for the elaboration of optical sensors for water monitoring

Christian Murga Cotrina

INSTITUT POLYTECHNIQUE DE PARIS

ÉCOLE POLYTECHNIQUE

IP PARIS

Conjugated molecules for the elaboration of optical sensors for water monitoring

Thèse de doctorat de l'Institut Polytechnique de Paris
préparée à l'École Polytechnique

École doctorale n°626 École doctorale de l'Institut Polytechnique de Paris (ED IP Paris)
Spécialité de doctorat: chimie

Thèse présentée et soutenue à Palaiseau, le 16/11/2023, par

Christian Murga

Composition du Jury :

Dr. Isabelle Leray Directrice de Recherche CNRS, Laboratoire de Photophysique et Photochimie Supramoléculaires et Macromoléculaires, ENS Paris-Saclay	Présidente
Pr. Rachel Méallet-Renault Professeure, Institut des Sciences Moléculaires d'Orsay, Université Paris-Saclay	Rapporteuse
Dr. Mourad Elhabiri Directeur de Recherche CNRS, Laboratoire de Chimie Bioorganique et Médicinale, Université Strasbourg	Rapporteur
Dr. Damien Aureau Chargé de Recherche CNRS, Laboratoire Institut Lavoisier de Versailles, Université Versailles-Saint Quentin	Examinateur
Dr. Grégory Danoun Chargé de Recherche CNRS, Laboratoire de Chimie Moléculaire, Institut Polytechnique de Paris	Examinateur
Dr. Sophie Bourcier Ingénieure de Recherche, Laboratoire de Chimie Moléculaire, École Polytechnique	Invitée
Dr. Gaël Zucchi Chargé de Recherche CNRS, Laboratoire de Physique des Interfaces et des Couches Minces, École Polytechnique	Directeur de thèse

NNT : 2023IPPAX133

Thèse de doctorat

I. Résumé

L'activité anthropique a eu la conséquence de modifier profondément les conditions environnementales sur Terre. L'une des principales causes de cet effet est le rejet inconsidéré de produits chimiques dans l'air, le sol et l'eau, qui perturbe les écosystèmes et pose également un problème de santé publique important. En particulier, la mesure de la qualité de l'eau du robinet reçue par le grand public est un problème qui doit être traité de manière efficace.

Les métaux lourds et les pesticides sont deux familles de produits chimiques qui ont des effets toxiques sur l'homme. Si la plupart des métaux lourds sont essentiels à la vie en très petites quantités parce qu'ils régulent des processus enzymatiques dans le corps, ils deviennent extrêmement dangereux lorsque leur concentration dépasse certains seuils. De plus, ils forment dans l'eau des aqua-ions stables, ce qui favorise une biodisponibilité accrue et leur absorption par les plantes ou les animaux en est grandement facilitée. Par ailleurs, s'il n'est pas possible de négliger les énormes avantages sociétaux et économiques des pesticides, c'est leur dissémination non méthodique dans le sol et l'eau qui a favorisé leur présence, voire leur accumulation, à des concentrations représentant un danger pour la santé humaine. En particulier, l'herbicide glyphosate, répandu principalement en Amérique du Nord et en Europe, a été l'objet d'études particulières au cours de la dernière décennie.

Outre ces familles de produits chimiques nocifs, il en existe d'autres dont la présence est généralement le signe d'un environnement sain. L'anion hypochlorite, par exemple, est utilisé comme désinfectant des canalisations, ce qui signifie que sa présence est considérée comme une garantie à l'absence de bactéries dans les systèmes d'eau domestique. Néanmoins, sa concentration doit être contrôlée car il peut produire des composés toxiques en réagissant avec la matière organique. La quantité d'oxygène dissout est un autre paramètre important à contrôler/surveiller car il témoigne de la capacité du milieu à soutenir correctement la vie aquatique.

Il existe plusieurs techniques analytiques pour détecter et surveiller les espèces susmentionnées et elles sont principalement basées sur des mesures spectroscopiques telles que la GC-MS ou la HPLC. Ces techniques offrent une grande sensibilité, leurs limites de détection pouvant atteindre le niveau du ppb, mais elles nécessitent des instruments lourds et coûteux, ainsi que du personnel hautement qualifié pour les utiliser.

Il est donc nécessaire de développer des techniques simples et rapides qui permettent d'atteindre les mêmes objectifs, et l'une des plus puissantes est la spectroscopie de luminescence. Cette technique présente plusieurs avantages par rapport aux techniques classiques : elle n'est pas invasive, elle ne consomme pas le fluorophore ou l'analyte si l'interaction est réversible, elle ne nécessite pas de références, elle est portable (ce qui permet des réponses rapides et un suivi in situ en temps réel), elle est facile à utiliser, elle est très sensible et, surtout, elle peut être sélectif en fonction des groupes chimiques présentes dans les molécules.

L'objectif principal de ce travail est de concevoir et de synthétiser de nouvelles molécules conjuguées ayant des propriétés optiques adéquates à la reconnaissance sélective d'entités parmi celles énumérées ci-dessus. Ces molécules sont telles que, en interagissant avec un analyte cible, elles peuvent modifier leur fluorescence ou leur phosphorescence de manière à permettre l'identification et/ou la quantification de ces espèces.

Dans le cadre de ce travail de thèse, 11 nouveaux composés dotés de capacités de détection ont été développés à partir des familles chimiques pyrène (composés **M1**, **M2** et **M3**), benzazole (composés **M4**, **M5** et **M6**), coumarine (composé **M7**) et porphyrine (composés **M8-Pd**, **M8-Pt**, **M9-Pd** et **M9-Pt**). Les études de luminescence ont montré qu'ils peuvent détecter efficacement les ions Al^{3+}, Fe^{2+}, Fe^{3+}, Cu^{2+}, Zn^{2+}, OCl^{-}, le glyphosate et O_2 dissous dans des environnements aqueux, ce qui en fait des candidats intéressants pour l'évaluation de la qualité de l'eau dans la vie réelle.

II. Abstract

Anthropogenic activity has had the consequence of deeply modifying the environmental conditions on Earth. One of the main causes of this effect has been the indiscriminate release of chemicals into the air, soil and water that disturbs ecosystems and also poses a significant public health concern. In particular, measuring the quality of tap water that is received by individuals is a problem that needs to be tackled effectively and efficiently.

A first family of chemicals that has toxic effects on humans are heavy metals. While most of them are essential to life in very small quantities because they regulate enzymatic processes in the body, they become extremely dangerous when their concentration exceeds certain thresholds. Moreover, they form stable aquo-ions which promotes an increased bioavailability and their intake by plants or animals is greatly facilitated.

A second family of contaminants are pesticides. It is not possible to neglect the enormous societal and economic benefits of using these chemicals; however, it is their unmethodical release in soil and water that has promoted them to be found at concentrations that represent a danger to human health. In particular, the herbicide glyphosate, widely widespread in North America and Europe, has been subject to scrutiny in the last decade.

Besides these families of harmful chemicals, there are compounds which presence is generally indicative of a healthy environment. The hypochlorite anion, for example, is used as a pipeline disinfectant, meaning that its presence is taken as a guarantee of bacterial absence in household water systems. Nonetheless, its concentration must be controlled as it can produce toxic compounds when reacting with organic matter. Finally, dissolved oxygen is another parameter of importance to be controlled as it is a testament of a healthy aquatic life.

Evidently, several analytical techniques exist to detect and monitor the aforementioned species and they are mostly based on spectroscopic measurements like GC-MS or HPLC. These techniques provide great sensitivity as their detection limits can reach the ppb level, but they require heavy and expensive instrumentation, and highly skilled people to operate them.

Hence, there is a need for developing simple and fast techniques that accomplish the same goals, and one of the most powerful ones is luminescence spectroscopy. this technique provides several advantages over the classic techniques such as being not invasive, it either does not consume the fluorophore or the analyte if the interaction is

reversible, nor requires any references, it allows real-time in-situ measurements thanks to the portability of the devices, it can be sensitive enough, and, very importantly, luminescent molecules can be designed to specifically interact with the targeted species.

The main goal of this project is thus to design and synthesize novel conjugated molecules with adequate optical properties. These molecules are such that, upon interacting with a target analyte, a change in their emission is observed in a way that identification and/or quantification of such species can be made.

Within the scope of this thesis work, 11 new compounds with sensing capabilities have been developed using molecules belonging to the pyrene (compounds **M1**, **M2** and **M3**), benzazole (compounds **M4**, **M5** and **M6**), coumarin (compound **M7**) and porphyrin (compounds **M8-Pd**, **M8-Pt**, **M9-Pd** and **M9-Pt**) chemical families. Sensing studies with these compounds have shown that they can effectively detect Al^{3+}, Fe^{2+}, Fe^{3+}, Cu^{2+}, Zn^{2+}, OCl^{-}, glyphosate and dissolved O_2 in aqueous environments, making them interesting candidates for real-life water quality assessment.

III. Acknowledgments

In the first place, I would like to express my most sincere gratitude to my supervisor Dr. Gaël Zucchi for mentoring me during the course of my PhD. All the great advice and motivation, the intense and rewarding scientific discussions, and how he pushed me to become a better researcher corroborate that I could not have worked with a better advisor and person. Thank you immensely.

Secondly, I would like to thank Prof. Rachel Méallet-Renault and Dr. Mourad Elhabiri for accepting the roles of *rapporteurs* of my thesis, and Dr. Isabelle Leray, Dr. Grégory Danoun, Dr. Sophie Bourcier and Dr. Damien Aureau for accepting the roles of *examinateurs*.

I would also like to particularly thank Dr. Sophie Bourcier for her help performing the mass spectra measurements and the subsequent analysis, Dr. Alain-Louis Joseph for his help in the use of the NMR spectrometer, Dr. Nicolas Casaretto for his help in performing the X-ray crystallography measurements and resolving the structures, Dr. Holger Vach for performing theoretical simulations and calculations, and Dr. Isabelle Leray and Dr. Baptiste Amouroux for allowing me to perform photophysical measurements at ENS Paris-Saclay.

I would also like to show my deep appreciation to all my present and past colleagues of LPICM. Your advice, friendship and kindness were paramount for reaching this point in my career. Thank you as well to my colleagues from LSO, PMC, LCM and ENS Paris-Saclay for their support and fruitful scientific discussions. Especially, I would like to thank former and present members of the Zucchi Group: Qiqiao, Aram, Katya, Arghyadeep, Shenming, Manel, Camilla and Issoufou; and former and present colleagues of the wing 5 laboratories: Shiwei, Amir, Pingping, Inass, Qiao, Marta, Guili, Xinlei and Martina. Your friendship became invaluable over the curse of my PhD.

Finally, I would like to thank my family and friends back home. It was your support that allowed me to focus on my research all these years.

IV. Table of abbreviations

AcOH	acetic acid
AIE	aggregation-induced emission
AMPA	aminomethylphosphonic acid
BH	Benesi-Hildebrand
CHEF	chelation-enhanced fluorescence
DCM	dichloromethane
DDQ	2,3-dichloro-5,6-dicyano-1,4-benzoquinone
DMF	N,N-dimethylformamide
DMSO	dimethyl sulfoxide
DO	dissolved oxygen
EA	ethyl acetate
ESI-MS	electrospray ionization mass spectroscopy
ESIPT	excited-state intramolecular proton transfer
EtOH	ethanol
HEPES	4-(2-hydroxyethyl)-1-piperazineethanesulfonic acid
HMTA	hexamethylenetetramine
HOMO	highest occupied molecular orbital
ICT	intramolecular charge transfer
ISC	intersystem crossing
LoD	limit of detection
LUMO	lowest unoccupied molecular orbital
MeCN	acetonitrile
MeOH	methanol
NMR	nuclear magnetic resonance
PET	photoinduced electron transfer
PhCN	benzonitrile
ppb	parts per billion
ppm	parts per million
R. T.	room temperature
THF	tetrahydrofuran
TsOH	*p*-toluenesulfonic acid
UV-vis	ultraviolet-visible

V. Table of contents

1 General context – Sensors for the environment

The rapid increase in human population and the concomitant development of industrialization on the planet has brought along the uncontrolled release of toxic chemicals into the environment. They vary from ionic species like metallic cations that can be dissolved in aqueous medium and enter the human body to organic compounds like the so-called POPs (Persistent Organic Pollutants) that can exist for timeframes larger than the human lifespan and can be easily transported around the globe, among other species [1] [2]. In a similar note, some chemicals present in the environment (introduced by either natural or anthropological means) have the role of serving as indicators of its quality, meaning that their excess or lack could indicate an imbalance of the system and eventually generate problems to living species, including human beings. Thus, it has become an absolute necessity to be able to determine in-situ the nature and quantity of these chemical species, so that solutions for treatment, removal and remediation can be fast applied.

In this Chapter, the theoretical framework of the present thesis work will be displayed. In Section 1.1, a brief review of two families of toxic chemicals, namely heavy metals and pesticides, will be provided. Also, the hypochlorite anion and molecular oxygen, which are two important substances that serve as indicators of good water quality will be described.

Afterwards, in Section 1.2, classic methods to detect these species present in the environment will be outlined. The focus will then be directed into the use of chemical compounds for fluorescent detection, with particular emphasis in the discussion of the advantages of this technique, the description of their sensing mechanisms and their general chemical design for targeting analytes.

1.1 Analytes in the environment

1.1.1 Heavy metals

1.1.1.1 Introduction

Heavy metals are defined as the kind of metallic species whose density is higher than 4.5 g/cm^3, are ubiquitous and non-degradable. This category comprises quite toxic substances such as cadmium (Cd), chromium (Cr), mercury (Hg), lead (Pb) or arsenic

(As), as well as others which are essential for life, albeit in very small quantities, such as iron (Fe), copper (Cu), nickel (Ni) and zinc (Zn) [3] [4].

Heavy metals in their cationic forms can be found widespread throughout the Earth's crust as they are naturally occurring elements. However, due to the fast and continuous industrialization processes the Planet is immersed in, which requires the mining and processing of metallic ores and the subsequent use of the refined metals in everyday life, ranging from industrial to domestic and agricultural applications, exposure towards them has risen dramatically in the last decades [3] [4]. Thus, as a consequence of anthropogenic activities, heavy metals can be found in increasing concentrations in the atmosphere, water and soil, where they accumulate and aggregate, and find their way into the food chain posing a significant threat to public health. The main general issues that arise due to heavy metal poisoning being carcinogenesis, deformity, mutation, all mainly due to oxidation stress in the human body [3] [4] [5].

Evidently, exposure to heavy metals is heavily regulated by local and international law, as well as by international organizations. As an example, the maximum allowed concentrations of heavy metals in drinking water according to the European Union Council Directive 98/83/EC are shown in Table 1.

Table 1. Maximum allowed concentration of heavy metals in water for human consumption according to the European Union Council Directive 98/83/EC[1]

Heavy metal	Maximum concentration allowed (mg/mL)
Antimony (Sb)	0.005
Arsenic (As)	0.01
Cadmium (Cd)	0.005
Chromium (Cr)	0.05
Copper (Cu)	2.0
Lead (Pb)	0.01
Mercury (Hg)	0.001
Nickel (Ni)	0.02
Selenium (Se)	0.01
Aluminum (Al)	0.2
Iron (Fe)	0.2
Manganese (Mn)	0.05

[1] https://www.lenntech.com/applications/drinking/standards/eu-s-drinking-water-standards.htm

1.1.1.2 Impact of heavy metals on the environment

Generally, heavy metals generate negative impacts on biotic and abiotic systems when their concentration surpasses a specific threshold. As mentioned before, they can be nowadays found in the air, soil and water, always exceeding their natural pre-industrial era concentrations. For instance, heavy metals are anthropogenically introduced into the atmosphere through industrial emissions, mining, as part of combustion systems in vehicles, among other ways [3]. Once in this medium, they can easily form or get adsorbed into the surface of atmospheric particulate matter, where they can even help to catalyze undesired reactions that contribute to air pollution [6].

In soils, heavy metal contamination comes principally from the uncontrolled use of fertilizers, pesticides, biosolid deposition, waste and e-waste deposition, and metal mining and its processing industry. While normally metals found in soils are inert and their concentration is fairly low, the disturbance of the native geochemical cycles promoted by human activity has turned them to be more mobile, meaning they have become more bioavailable [7]. This has the obvious consequence of facilitating their uptake by plants and animals, where they bioaccumulate and eventually enter the food chain with even higher concentrations than the ones present in contaminates soils [8]. Also, this has the side effect of facilitating their leaching and lixiviation, which allows them to enter both the underground and superficial water media [9].

Thus, in water, besides these two processes, heavy metal contamination mainly arises from industrial wastewater release – including coal-fired power plants and mining –, solid waste disposal and recycling, and polluted urban stormwater and agricultural runoff [10]. In a similar fashion as described in the above paragraph, heavy metals present in water, which are already oxidized and are forming stable aquaions, have an increased bioavailability and their intake by plants or animals is greatly facilitated.

Then, if entering into biological systems, according to Tchounwou [4], heavy metals affect cellular organelles such as the cell membrane, mitochondria, lysosome, etc., and select enzymes involved in the metabolism, detoxification and damage repair cellular processes. Moreover, metallic ions can interact with the whole family of DNA components, damaging it and causing conformational changes than can lead to carcinogenesis or apoptosis by the production of radical oxygen species.

Particularly in plants, heavy metals in general can disturb their germination, metabolism, growth and resistance mechanisms. They can also alter their chlorophyll concentration,

decreasing the rates of photosynthesis, hence reducing the plant's growth and rendering it sick [8]. Other toxic effects include free-radical production (by cadmium and arsenic), disruption of the Fe uptake and promotion of oxidative stress (by nickel), and damage of the photosynthetic apparatus (by mercury) [11].

The effect of heavy metals in animals is extensive and has been widely described and reviewed [12] [13] [14] [15] thus, the focus of this paragraph will be just on the repercussions of some of them on human beings' health. For example, in our species, it has been documented that mercury can solubilize and bioaccumulate in the liver, plasma and blood, and cause significant damage to the brain, nerves and vision, and can even be transferred by breast milk into babies. Moreover, cadmium promotes high blood pressure, cardio and cerebrovascular diseases, and damage to bones, liver and kidneys. For its part, lead tears down the fetus' nervous system causing congenital mental retardation. Also, arsenic in its V valence can replace phosphate in cells impairing their respiration and it can also generate skin damage and apoptosis. Finally, copper can cause Wilson disease and also promote the formation of superoxide and hydroxyl radicals that promote oxidative stress in the cells [3] [4] [11].

1.1.2 Pesticides

1.1.2.1 Introduction

Pesticides are chemical compounds designed to kill, repel or control certain lifeforms that are considered to be pests. Among them, there are herbicides, which kill herbs and other unwanted vegetation; fungicides, which kill and prevent the growth of molds and mildew; disinfectants, which kill bacteria; and others. As can be implied, they are potentially toxic to organisms not considered pests, as human beings or domestic animals, and to the environment, so they need to be manufactured, used and disposed safely and properly [16] [17].

Particularly in agriculture, where the use of pesticides offers significant economic benefits by enhancing the production and yield of crops, they have unfortunately induced several environmental and human health problems. In fact, for example, pesticides have been shown to decrease the number of honey bees' and bumblebees' colonies, affecting their queen's production and decreasing their pollination capabilities. Also, pesticides, when applied directly or when leached into the soil, can undermine soil quality and soil invertebrate population. Furthermore, as they appear in residues of drinking water and food either because accidental exposure or by lack of appropriate water treatment, they

can be a threat to human health. For instance, it has been conservatively estimated that approximately 300 000 people, most of them farmers, die from fortuitous pesticide self-poisoning every year [18] [19]. As a result, the maximum allowed total concentration of pesticides in drinking water is heavily regulated and, for instance, is set at 0.0005 mg/mL by the European Union Council Directive 98/83/EC[2].

1.1.2.2 Impact of pesticides on the environment

There are several chemical families of pesticides. It is not within the scope of this manuscript to cover them all in detail, but to briefly review the most important ones: organophosphates, carbamates, organochlorines, quaternary ammonium salts and glyphosate. While the latter is not a chemical family on its own, its use is so widespread in the Earth that it is worth to be given a special consideration. In Figure 1, examples of chemical structures of representative compounds of each of the aforementioned families can be observed, along with their common and chemical names.

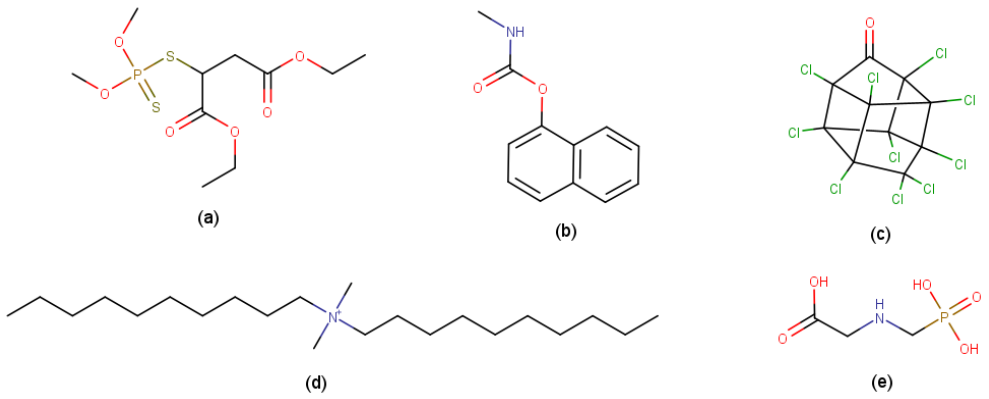

Figure 1. Chemical structures of representative compounds of each of the most important pesticide families. (a) Malathion, diethyl 2-[(dimethoxyphosphorothioyl)sulfanyl]butaniedioate; (b) Carbaryl, 1-naphthylmethycarbamate; (c) Chlordecone, 1,2,3,4,6,7,8,9,10,10-decachloropentacyclo[5.3.0.02,6.03,9.04,8]decan-5-one; (d) Didecyl-dimethylammonium chloride; and (e) Glyphosate, N-(phosphonomethyl]glycine.

Both organophosphates and carbamates are potent insecticides that share the same purpose: they inhibit the neural enzyme acetylcholinesterase (AChE). As its name indicates, AChE is the enzyme that catabolizes acetylcholine (ACh), which is a neurotransmitter that is released by motor neurons to activate muscles both in the neuromuscular junction and in the autonomic nervous system, and also functions as a

[2] https://www.lenntech.com/applications/drinking/standards/eu-s-drinking-water-standards.htm

neuromodulator in the brain. Thus, AChE is critical to normal control of nerve impulse transmission from nerve fibers to smooth and skeletal muscle cells, secretory cells, autonomic ganglia, and to the central nervous system itself. Organophosphates inhibit AChE by phosphorylating a hydroxyl group of a serine residue located in its esteratic site, mimicking what ACh does. On its part, carbamates inhibit AChE by carbamylation of the same serine residue, the difference being that this inhibition is reversible while the one caused by organophosphates is not. This generates a decrease in the availability of AChE needed to catabolize ACh, which in turn generates an overstimulation of the effector organ due to cholinergic poisoning. In a nutshell, these families of pesticides kill or disable insects by disrupting their nervous system. However, as AChE is also present in mammals, organophosphates and carbamates can be toxic to species of that animal realm as well [20] [21] [22].

Organochlorines, by their side, are broad range insecticides that can have different modes of action depending on their structure. Briefly, for the poli-chlorinated diphenyl-methanes, family in which DDT is the most known example, the mechanism seems to involve an interference in the sodium and potassium ions balance across the nerve membrane. For the hexachlorocyclopentadiene family, in which chlordecone and Aldrin are the most recognizable compounds, the mechanism also involves changing the flow of sodium and potassium ions through the cellular membrane, but also includes disturbing the Ca^{2+}-ATPase and phosphokinase activities. Moreover, they block the action of the neurotransmitter *γ*-aminobutyric acid, resulting in uncontrolled excitation of neurons with the consequence of firing incorrect signals in very short amounts of time and thus stressing and inactivating proteins in muscle cells [23].

Finally, glyphosate is a non-selective, systemic, post emergence herbicide that controls more weed species than any other commercial compound known. It acts by inhibiting the synthesis of essential amino acids as a result of its binding to and posterior inactivation of the enzyme 5-enolypyruvylshikimate-3-phosphate synthase, which is critical in the Shikimate pathway[3] that, among other functions, controls the metabolism of a variety of phenolic compounds that are very important for the plant's immunity. Thus, by preventing the biosynthesis of this compounds, glyphosate allows soil-borne pathogens to attack the plants and kill them [24] [25] [26].

The widespread and, most of the time, uncontrolled use of glyphosate for weed management, however, has led to an increase in glyphosate-resistant weeds and plants

[3] The Shikimate pathway is a biological pathway used by most non-animal living species for the synthesis of aromatic compounds [288].

worldwide, which currently represents the biggest threat to sustained weed control in major agricultural crops [25]. Moreover, glyphosate, while being developed to act over an enzyme that is not possessed by species outside the plant realm, can have harmful effect on insects and mammals. For example, it exterminates the beneficial bacteria living in honey bees' stomachs, indirectly affecting these insects, and affects the reproduction and development of water snails. Also, high glyphosate concentrations have been deemed toxic to some small fish species and it causes damages in cells of other small vertebrates. As for its effects on humans, Roundup, which is a commercial formulation containing glyphosate, has been shown to damage the epithelial cell membrane of human buccal epithelial cell lines. Additionally, as it also kills human gut bacteria, it is linked with gastrointestinal disorders, obesity, heart disease, among other illnesses. To conclude, this organophosphonate compound has been shown to damage human DNA in *in vitro* essays with Hep-2 cells [27].

1.1.3 Hypochlorite

1.1.3.1 Introduction

The hypochlorite is the conjugated base of hypochlorous acid according to the following reaction:

$$\mathrm{HOCl} \rightleftharpoons \mathrm{H^+} + \mathrm{OCl^-}$$

Generally, hypochlorites are inherently unstable, even starting to break down during preparation until completely decomposing, hence they are rarely present as solids and are much more easily available as solutions. While the stability of hypochlorite-containing solutions is not great, controlling production and storage factors such as concentration, pH and temperature of the solution, and exposure to light prevent the anions decomposition in the mid to long term [28].

The most important hypochlorite-containing species is sodium hypochlorite, which is commonly known as bleach in household solutions that contain between 3 and 6 % of this chemical. NaOCl is a powerful oxidizing agent that is used worldwide as a disinfectant and bleaching agent in both the domestical and food industry, in public health care to treat potable water, and as the main disinfectant in endodontics [29] [30]. It is produced in large scale by the Hooker's method, in which both sodium hypochlorite and sodium chloride (NaCl) are formed when treating cold sodium hydroxide solutions with

chlorine gas [28]. The global sodium hypochlorite market is expected to grow 5 % yearly to reach an approximate total of $ 422 million by 2030[4].

1.1.3.2 Chemistry of hypochlorite

Despite being a reactive organic species, the direct impact of hypochlorite in the environment is limited because of its high reactivity: it degrades before its intake into living species. Moreover, it is in fact produced by the enzyme myeloperoxidase in neutrophils, a type of white blood cell, to kill bacteria during microbial infection, although in very small concentrations [31] [32]. Also, it is well established that the reaction between hypochlorite and hydrogen peroxide produces singlet oxygen, which is a highly reactive species that is very important for photodynamic cancer therapy because it locally kills cancerous cells [33]. However, if overproduced in the body, it can cause some diseases like arthritis, nephropathy, atherosclerosis [34], which are the consequence of the hypochlorite being a strong oxidant that can rapidly react with thiols and amines, modifying proteins and enzymes, and with lipids [35].

As for its water chemistry, the hypochlorite anion exists in equilibrium with hypochlorous acid:

$$HOCl \rightleftharpoons H^+ + OCl^- \ldots\ldots\ldots\ldots \quad pK_a = 7.57 \text{ [36]}$$

This pK_a value means that around pH = 9.5, all species present in solution correspond to hypochlorite while at around pH = 5, all species are present as HOCl. Moreover, for very acidic pH values, HOCl decomposes into the toxic gas Cl_2 with a pK_a value of 3.39 [36].

1.1.4 Molecular oxygen

1.1.4.1 Introduction

Dioxygen is perhaps the most important molecule for life: it is essential for aerobic breathing and for decomposition of organic waste. Also, it plays critical roles in medicine, several industries, agriculture, and other human and non-human processes.

Among others, a key reason that Earth is a place where biological activity thrives is the presence of molecular oxygen. Its concentration and variation in distribution in the environment depend on the biological, chemical and physical processes that occur on

[4] https://www.alliedmarketresearch.com/sodium-hypochlorite-market-A14440

and beneath Earth's surface. While its concentration in the atmosphere has remained nearly constant over the last 600 million years, there are several ways in which large fluxes of O_2 are released to (photosynthesis) and consumed from (aerobic respiration, sulfide mineral oxidation, oxidation of reduced volcanic gases, oxidation of fossil fuels) it [37].

Presently, the concentration of O_2 in Earth's atmosphere at sea-level is approximately 0.21 bar, which represents around 21 % of the total gas moles in it. Its concentration varies depending on altitude, season and latitude. In air-saturated water, on the other hand, oxygen concentration depends on temperature, Henry's Law constant and ionic strength. Biological processes as photosynthesis and aerobic respiration may, however, supersaturate or deplete the local concentration of O_2, making these systems rarely being at their perfect oxygen saturation point [37]. Anthropogenic activities can also disturb, directly or indirectly, dissolved oxygen concentration. For example, the excess in nutrient availability in freshwater and coastal marine resources, which is caused by disposal of agricultural fertilizers, gives rise to eutrophication. This phenomenon consists of the body of water becoming overly enriched with minerals and nutrients and, thus, inducing an excessive grow of algae which, in turn, depletes dissolved oxygen concentration, among other damages to aquatic ecosystems. Other human-induced important cause of the decrease of dissolved oxygen concentration is global climate change, which is causing the rise in mean Earth's temperature. This phenomenon depletes dissolved oxygen by stimulating microbial respiration, mineralizing organic matter and decreasing oxygen solubility [38] [39].

1.1.4.2 Chemistry of dioxygen

The two atoms in the dioxygen molecule are chemically held together by, in the simplest explanation, a double covalent bond. In its electron configuration, as can be seen in Figure 2, there are two unpaired electrons, which cause the O_2 molecule to be paramagnetic and to be in a spin triplet state: that is why the ground state of this molecule is referred to as triplet oxygen, ${}^3\Sigma_g^+$. The bond order of the molecule is two as a result of the bonding contribution from the electrons occupying the bonding σ_g, π_x and π_y molecular orbitals, and the corresponding cancellation from the electrons occupying the antibonding π^*_x and π^*_y orbitals [40].

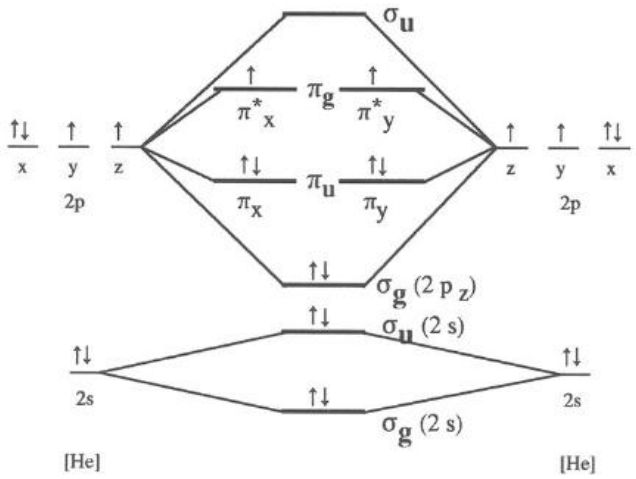

Figure 2. Electronic configuration of dioxygen. The image shown is taken from [40].

The fact that the ground state of dioxygen is triplet makes it thermodynamically very stable: its direct reaction with many closed-shell organic compounds is forbidden unless a route via a diradical intermediate is available [41]. Upon excitation, molecular oxygen converts to two possible singlet states, $^1\Delta_g$ and $^1\Sigma_g^-$. This involves a change in the multiplicity of the excited electron and a small change in the O – O bonding distance. In these excited states, dioxygen can emit energy and relax back to its ground triplet state. It should be noted that the lifetime of the $^1\Delta_g$ species is long because its relaxation to the ground state is spin-forbidden, making this species much more reactive than when it is in its triplet state [42].

1.2 Sensors for the detection of analytes

As should be evident, continuous detection and monitoring of heavy metals, pesticides, hypochlorite and dioxygen is of critical importance, not only because they possess a threat to public health, but also because they are indicators of a healthy and robust environment medium, particularly the aquatic one. To achieve this objective, the development of sensing technologies is a scientific area of research that has attracted considerable and increasing attention over the last few decades.

1.2.1 Spectroscopic sensors

The determination of heavy metals in water samples can be readily achieved by several well-established and instrumental-heavy methods such as Inductively Coupled Plasma - Atomic Emission Spectroscopy (ICP-AES), Atomic Absorption Spectroscopy (AAS),

Electron Microprobe Analysis (EMP), Neutron Activation Analysis (NAA), among others [3] [43]. For their part, pesticides are mostly determined by means of Gas or Liquid Chromatography for separating the analytes routinely coupled with Mass Spectrometry for their identification (GC-MS or LC-MS), although the detection techniques may sometimes be rather unique like Electron Capture Detector (EPD) or Nitrogen Phosphorous Detector (NPD) [44] [45] [46].

While all the outlined methods enable the detection of the analytes with high sensitivity and resolution, they share the same drawbacks: they are expensive, often require large sample size or long-time preparation, do not allow for continuous monitoring and need highly trained personnel to properly utilize the delicate and heavy instrumentation [43] [47].

In the case of the detection of dioxygen, the most common used method is the Clark electrode, which will be briefly described in Section 1.2.2.6.

1.2.2 Chemical sensors

1.2.2.1 Introduction

The development of rather simple devices that satisfy the same requirements and possess the same benefits as the methods described in section 1.2.1 is worth researching on, and chemical sensors are a technology that aim to fulfill this necessity. Chemical sensors are defined as “devices that transform chemical information, ranging from the concentration of a specific sample component to overall composition analysis, into an analytically useful signal” [48] or, in a simpler way, as “miniaturized devices that can deliver real-time and online information on the presence of specific compounds or ions in complex samples” [47].

In their current state, sensors can be said to be electronic devices that create a signal that carries information about an analyte, thus they are made by three main components: the sensing material, which is in charge of interacting with the analyte and experiencing a change in at least one of its properties; the transducer, which acquires the change signal and transforms it into an electric signal; and the analyzer, which converts this signal into an output that can be then interpreted [47]. In Figure 3, a schematic representation of a general chemical sensor is shown.

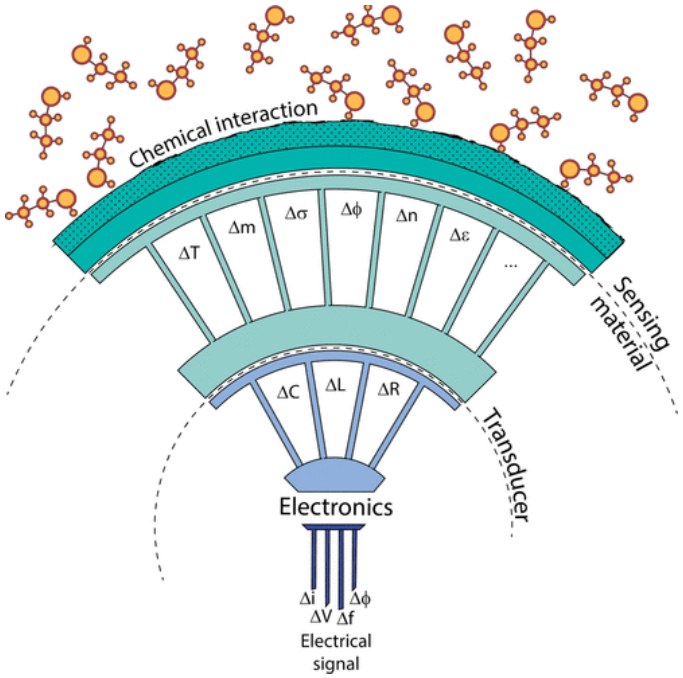

Figure 3. Logical structure of a sensor. The analyte interacts with the sensing material with a subsequent change in some of its properties: mass (Δm), temperature (ΔT), conductivity (Δσ), etc. The transducer converts the detected change into a variation of its electric parameters (electric charge, electric length, resistance), so that, finally, the electronic component outputs the sensing signal that can be analyzed. The image shown is taken from [47].

1.2.2.2 Fluorescence-based chemical sensors

As seen in Figure 3, several transduction mechanisms exist and fluorescence is one of the most powerful among them. This process involves, in short, the emission of light by a luminophore that has previously absorbed light and it is schematized in the Perri-Jablonski diagram shown in Figure 4.

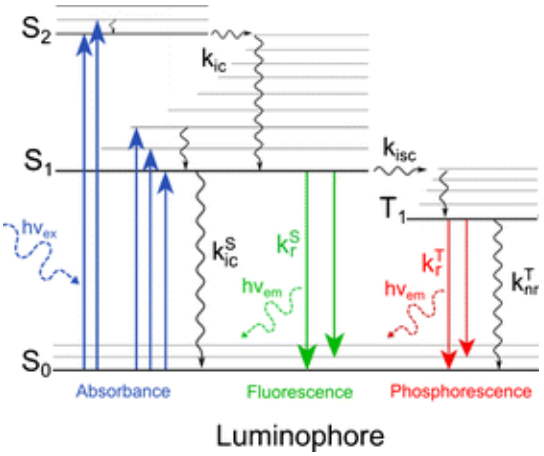

Figure 4. Perrin-Jablonski diagram for the absorption – emission process of a model luminophore. The image was taken and modified from [49].

As can be seen in the diagram, after excitation (pictured in blue straight lines), the first process that occurs is the internal conversion of excitons from the higher energy excited vibrational levels to the lowest excited level S_1. This process is non-radiative and is generally completed before emission. Afterwards, from S_1, two important radiative processes are possible: (1) a fluorescence emission (pictured in green straight lines) which is a spin-allowed transition and (2) a phosphorescence emission (pictured in red straight lines) from the lowest excited triplet state of the luminophore which needs nonradiative intersystem crossing (ISC) between two isoenergetic vibrational levels that are not in the same multiplicity (S_1 to T_1). After either of these two processes, the excited molecule returns to the ground state upon emission of light of a lower wavelength compared to the one that was used to excite it. This difference between the excitation and emission wavelengths is called the Stokes' shift [49].

There are several advantages for the use of fluorescence as a transduction mechanism, such as the technique being not invasive, not consuming the fluorophore or the analyte if the interaction is reversible, not needing references and also having the enormous advantage that different experiments can be designed based on distinct aspects of the fluorescence output, such as intensity, lifetime, anisotropy, etc. [50]. Moreover, other characteristics of fluorescence based chemical sensors include their portability, thus allowing for real-time in-situ responses and monitoring, their ease of operation, their sensitivity – as detection limits can reach the ppb levels –, and, very importantly, their design-dependent selectivity [43] [49] [51].

Thus, the chemical sensors that use fluorescence as transduction mechanism came to be known as chemosensors[5], which were precisely defined by Basabe-Desmonts as all compounds that "complex to an analyte reversibly with a concomitant fluorescent signal transduction and it constitutes only the active transduction unit of a sensor" [50]. It can be then said that, generally, chemosensors rely on the integration of three systems: the sensors chemistry, the optical system and the electronic system. The sensors chemistry system involves the composition of the sensing material: whether a polymer or a molecule is used, and the addition of additives such as plasticizers or binders. The optical system consists of a light source or a microscope and photodetectors. Finally, the electronic system relates to the digitalization, handling, processing and displaying of the fluorescence data [47] [51] [52].

As schematized in Figure 5, the sensor chemistry system consists basically of an emissive unit, which is known as the fluorophore, and a detection unit, which is known as the probe, that is meant to interact with the target analyte in such a way that the luminescent properties of the molecule change [50] [52].

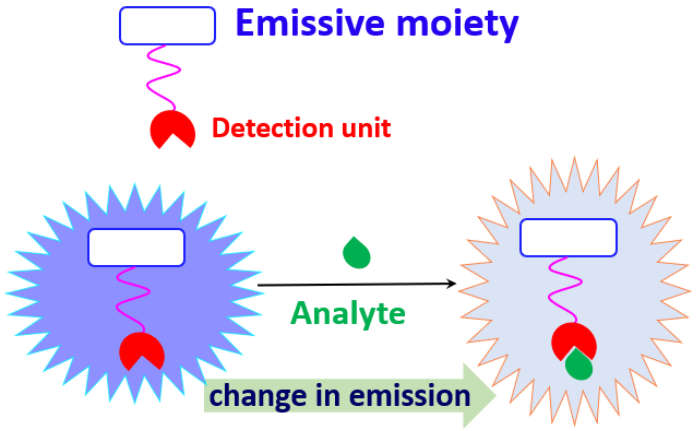

Figure 5. Basic scheme of the fluorescence recognition process of a target analyte by an emissive molecule: the interaction with a specific species generates a change in the emission, which is measured and quantified.

The photochemical nature of this change is determined by the sensing mechanism of the chemosensor towards the analyte. Classically, chemosensors can be classified as 1) intramolecular charge-transfer (ICT), 2) dual-wavelength process, 3) Förster resonance

[5] To avoid confusions and remain consistent, chemical sensors in which the transduction mechanism is fluorescence will be referred to as chemosensors for the rest of the manuscript.

energy transfer (FRET) based, 4) photoinduced electron-transfer (PET), and 5) aggregation-induced emission (AIE) based [52] [53].

1.2.2.2.1 Intramolecular charge transfer chemosensors (ICT)

ICT chemosensors are those in which the fluorophore and the detection unit are directly connected with each other forming a single scaffold in which one of them acts as a donor and the other as an acceptor. In these systems, the HOMO of the chemosensor has an electron density close to the acceptor group while the LUMO level is close to the donor group in such a way that a dipole moment is generated upon excitation [53].

Upon interacting of the analyte, however, the dipole strength is altered, which leads to a conversion of the photophysical behavior, including the emission wavelength, lifetime and quantum yield. For instance, if the detection unit is electron-acceptor, its interaction with the analyte generates an increase in its electron-withdrawing properties, enhancing the total conjugation of the molecule and red-shifting the emission. On the other hand, if the detection unit is electron-donating, its interaction with the analyte decreases its electron-giving character, thus diminishing the conjugation in the whole molecule and blue-shifting the emission [53] [54]. A schematic representation of this mechanism can be seen in Figure 6.

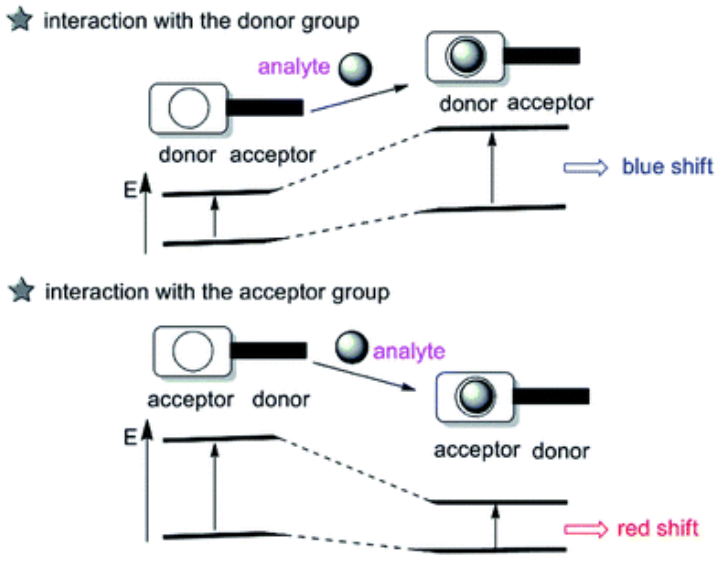

Figure 6. Schematic representation of the ICT process. The image shown is taken from [54].

1.2.2.2.2 Dual-wavelength process chemosensors

Dual-wavelength process chemosensors are those in which the species in the ground state is different from the one in the excited state, thus giving rise to a second emission band at higher wavelengths [52]. A schematic representation of this process is shown in Figure 7.

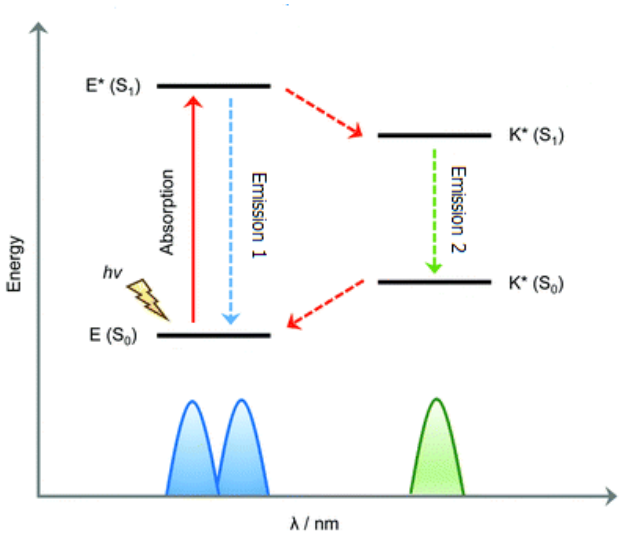

Figure 7. Schematic representation of the dual-wavelength mechanism. The image shown is taken from [55] and modified accordingly.

The most common and studied example of dual-wavelength process is the Excited-State Intramolecular Proton Transfer (ESIPT) mechanism, which will be described with great detail in section 2.1.2.1.

1.2.2.2.3 Förster resonance energy transfer chemosensors (FRET)

The FRET mechanism is a process that depends on the spacial distance between a pair of fluorophores that act as energy donor and acceptor, respectively, with their excited states interacting between each other. This process involves the non-radiative transfer of excitation energy from the donor to the acceptor units through a non-radiative dipole-dipole coupling. It is then the acceptor that provides the emission of the chemosensor with a fairly high Stoke's shift [53] [54] as can be seen in Figure 8.

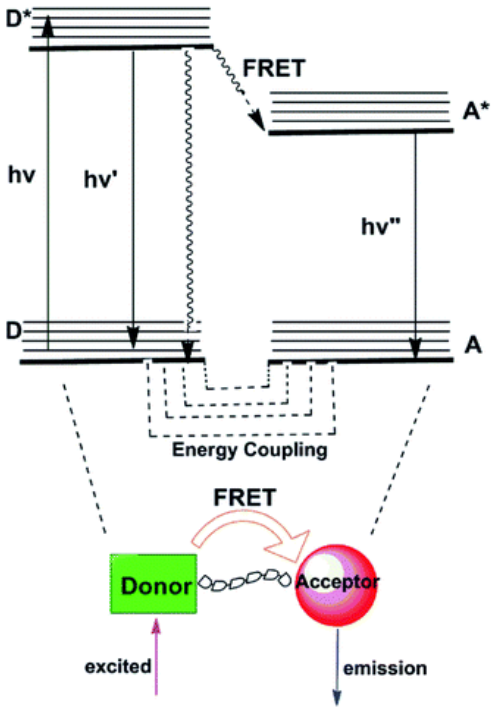

Figure 8. Schematic representation of the FRET mechanism. The image shown is taken from [54].

1.2.2.2.4 Photoinduced electron-transfer chemosensors (PET)

PET chemosensors generally consist of a fluorophore and a receptor linked by an aliphatic spacer that separates their π-conjugated systems. In the reductive PET process, which is the most common among typical chemosensor designs, the fluorophore is reduced while the probe, which bears free pairs of electrons, is oxidized. In other words, the latter acts as an electron-donating unit, and the fluorophore as electron-acceptor. Upon excitation of a PET molecule, an electron from the fluorophore's HOMO gets promoted to its LUMO. This creates a partially unoccupied HOMO in the [fluorophore]* that is readily occupied by the transfer of one electron coming from the free pair of the receptor, which is the PET process itself. Upon relaxation, the once-excited electron that was in the LUMO of the fluorophore is transferred to the vacant site in the HOMO of the receptor. Since this deactivation pathway is non radiative, the luminescence of the molecule is quenched (or turned OFF), meaning that the chemosensor is in a PET-On state [43] [52] [54].

However, when the analyte binds to the receptor *via* its free electron pairs, its HOMO is subsequently stabilized and resides now at lower energy than the one of the fluorophore, blocking the PET mechanism as these electrons cannot be transferred anymore. The consequence is that now the decaying pathway of the excited electron of the fluorophore

is radiative, which gives rise to a strong fluorescence and chemosensor in a PET-Off state, or turned ON [52]. In the oxidative PET process, the mechanism is basically inversed [56]. In Figure 9, a schematic representation of the reductive PET mechanism is shown.

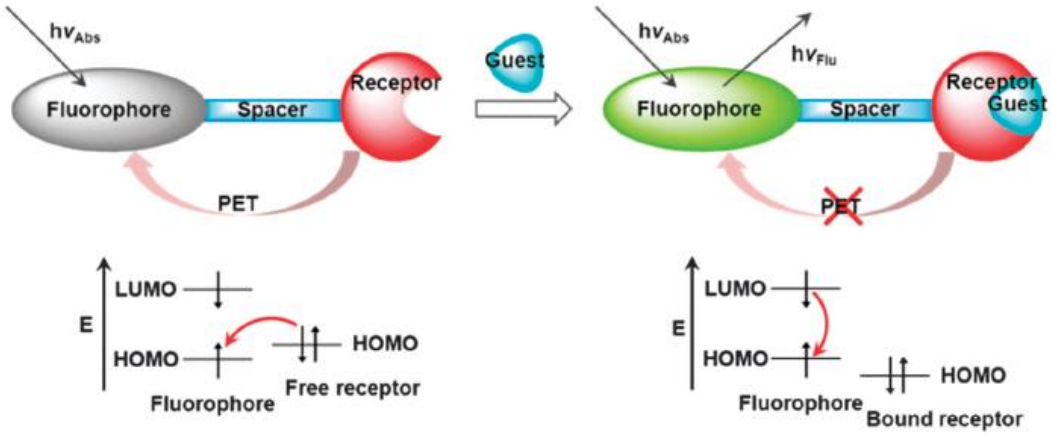

Figure 9. Schematic representation of the PET mechanism. The image shown is taken from [57].

1.2.2.2.5 Aggregation-induced emission chemosensors (AIE)

AIE chemosensors comprises molecules that do not show emission in solution because the energy is effectively released in non-radiative ways. However, upon aggregating in a suitable solvent environment in which they are not completely soluble, their intramolecular rotation is hindered obstructing the non-radiative relaxation channels, and thus greatly enhancing their emission intensity [53] [58] [59]. A visual representation of this phenomenon can be appreciated in Figure 10.

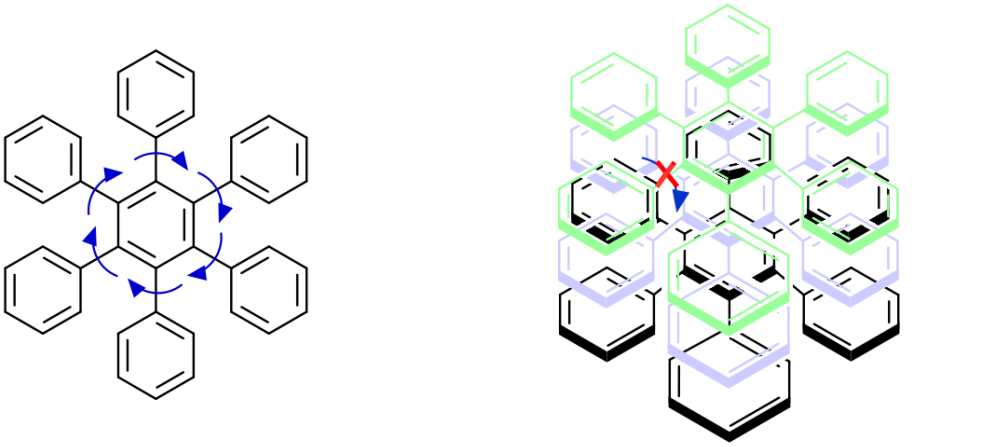

Figure 10. Representation of the AIE mechanism of a model molecule. By limiting its intramolecular rotation due to the formation of aggregates, the species becomes highly emissive.

1.2.2.3 Chemosensors for heavy metals

It is clear that heavy metals present a severe threat to the Earth's environment and that their presence has become so widespread that they are also a matter of serious public health concern. Particularly, the detection of metal ions, which are dissolved in aqueous systems that facilitate their intake by plants, animals and humans, has gained tremendous attention from the scientific community.

As described in Section 1.2.2.1, a general chemosensor is typically comprised by a fluorophore and a detection unit, the latter being responsible for the recognition of the analyte. Particularly for the detection of heavy metal ions, the sensitivity and selectivity of this recognition event depends basically on 3 aspects: 1) the topology of the ligand, 2) the physical and chemical properties of the heavy metal ion (ionic radius, charge, coordination number, hardness, etc.), and 3) the nature of the solvent [43].

The ligands that are used for the detection of metal ions can be classified (1) according to their sensing mechanism (outlined in section 1.2.2.2), but also depending on (2) the chemical family of their fluorophore or (3) the chemical architecture by which they interact with the target analyte. Classic fluorophore families include pyrene, 4,4-difluoro-4-bora-3a,4a-diaza-s-indacene (BODIPY), quinone, coumarin, rhodamine, fluorescein, benzazoles, naphthalimide, porphyrin, etc [60] [61] [62]. Basic chemical structures of these families can be appreciated in Figure 11.

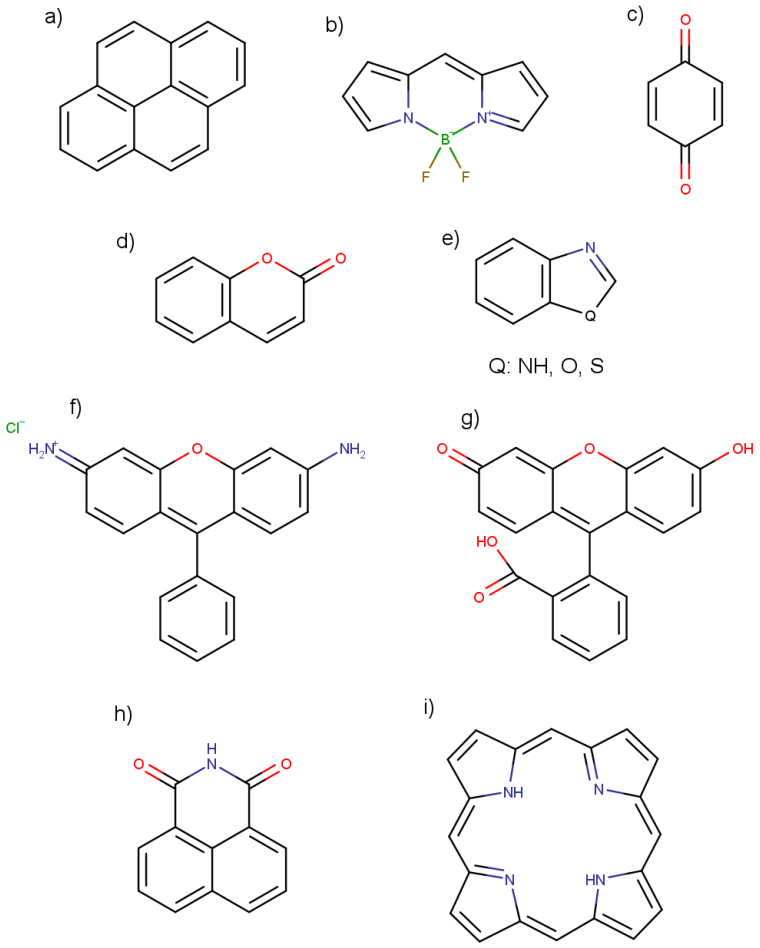

Figure 11. Chemical structures of common fluorophores: a) pyrene, b) BODIPY, c) quinone, d) coumarin, e) Q: NH benzimidazole, Q: O benzoxazole, Q: S benzothiazole, f) rhodamine, g) fluorescein, h) naphthalimide and i) porphyrin.

As for the way they interact with target analytes, ligands may be of at least three types: chelating ligands, macrocyclic ligands or chemodosimeters [60] [63]. Chelating ligands are those in which a complex, called the chelate, is formed between a metallic ion and a ligand *via* at least 2 bonds, rendering them thermodynamically more stable than a monodentate ligand and meaning that the ligand must include in its design at least two atoms that can interact with the target analyte [60]. An example of a chelating ligand used for the detection of Zn^{2+} is 9-(4-(bis(pyridine-2-ylmethyl)amino)phenyl)-3,3,6,6-tetramethyl-3,4,6,7,9,10-hexahydro-1,8(2H,5H)acridinedione, which chemical structure can be seen in Figure 12 [64]. In this molecule, the acridinedione moiety acts as the fluorophore and the pyridylmethyl amine, as a tridentate detection unit towards the aforementioned analyte.

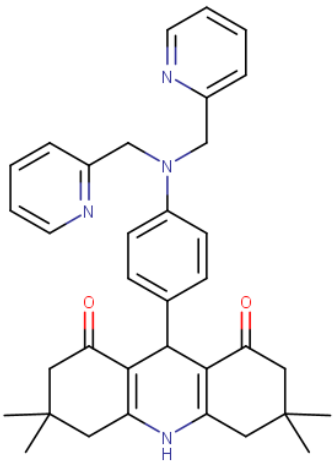

Figure 12. Example of the chemical structure of a chelating ligand [64].

For their part, macrocyclic ligands are those in which the complexing site is rigid and already formed by the structure itself of the molecule in a so-called preformed cavity of the adequate size to bind a target species [60]. For instance, for the ligand shown in Figure 12 to effectively chelate zinc, the pyridylmethyl moieties must rotate and reorientate themselves to form a pseudo cage. The increased thermodynamical stability of macrocyclic complexes with respect to chelate ones has been described to be the consequence of three factors: preorganization, solvation and dipole-dipole repulsion in the central cavity. These three effects contribute to a higher energy state for the macrocyclic ligand, which is relieved in complex formation making it substantially more stable [65].

Chemical families of this ligands include porphyrins, crown ethers and cryptands, among others [60]. An example of a macrocyclic ligand is 7-hydroxyl-4-methyl-8-(4'-phenylaza-15-crown-5-acryloyl)-coumarin, that can detect Al^{3+}, Cu^{2+} and Mg^{2+} and its chemical structure is shown in Figure 13 [66]. In this molecule, the crown-ether entity is the detection unit while the coumarin acts as the fluorophore.

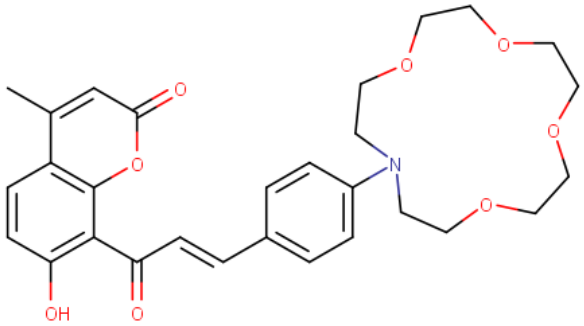

Figure 13. Example of the chemical structure of a macrocyclic ligand [66].

Finally, chemodosimeters are species that experience an irreversible chemical reaction when interacting with the analyte, completely changing their chemical nature and their fluorescence properties [63]. An example of a chemodosimeter is 2-amino-2'-(diethylamino)-2,3-dihydro-12'-oxa-8'-azaspiro[isoindole-1,5'-tetraphen]-3-one that can detect Hg^{2+} [67]. In this ligand, which chemical structure can be seen in Figure 14, the rhodamine moiety is the fluorophore while the reactive site towards the mercury cation is located in the isoindole ring.

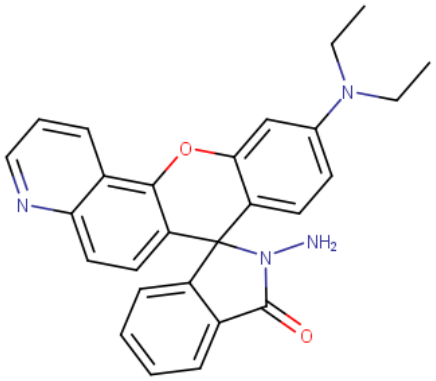

Figure 14. Example of the chemical structure of a chemodosimeter ligand [67]

1.2.2.4 Chemosensors for pesticides: glyphosate and AMPA

Based on what has been described in Section 1.1.1.2, it is evident that several efforts have been and are being made to develop technologies that can detect and measure pesticide presence in the environment, either in air, soil or water, and the literature that covers this particular topic is extensive and well-documented [44] [46] [45] [68] [69] [70] [71]. For the scope of this manuscript, however, due to their economic and environmental importance and their widespread distribution in the world, the focus will rely solely on the

optical detection of the herbicide glyphosate and its main decomposition metabolite, aminomethyl phosphonic acid (AMPA) [25] [26], whose structures are presented in Figure 15.

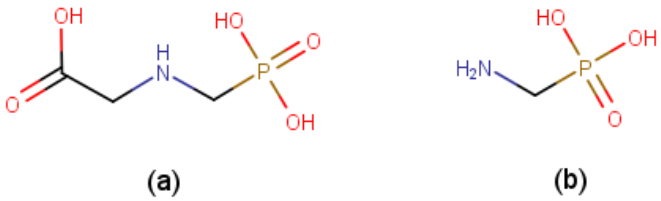

Figure 15. Chemical structures of (a) glyphosate and (b) AMPA.

It is worth describing that, in solution, glyphosate forms a complex equilibrium system with several species owing to several labile hydrogens present on its chemical structure (Figure 15a) [72] [73]. In Figure 16, some of the different glyphosate species in equilibrium and their correspondent pK_a values are shown.

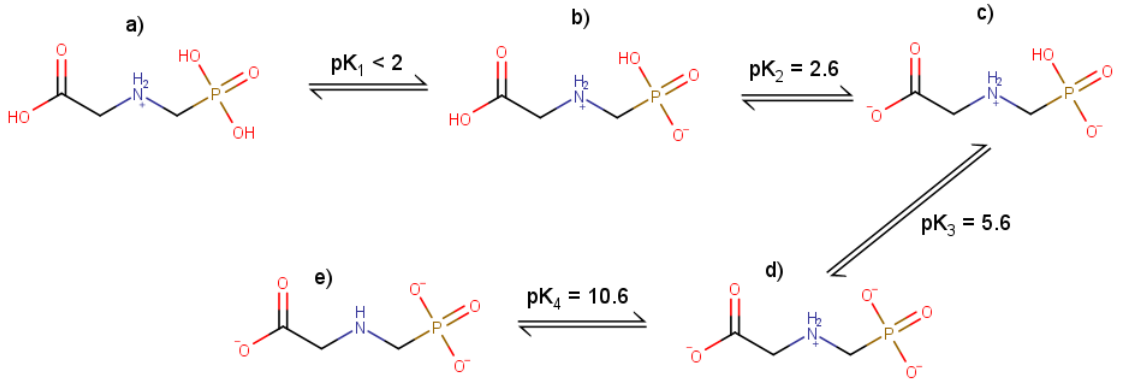

Figure 16. Different species of glyphosate equilibrium in aqueous solution [72].

Ligands for glyphosate and AMPA should follow the same basic principle as the ones described in Section 1.2.2.3: they carry a fluorophore which provides the luminescent properties and the detection unit that interacts with the analyte. However, up to date, it has not been possible to find in published literature a ligand that directly interacts and detects either of these molecules using fluorescence as transduction mechanism. The strategy used, on the contrary, is an indirect detection: on a first step, researchers design molecules that can chelate metallic cations, typically Zn^{2+} or Cu^{2+}, with a concomitant change in their fluorescence properties; subsequently, taking advantage of the powerful binding capabilities of the phosphate or the carboxylate entities of the glyphosate

molecule, which at pH ~7 – 8 in aqueous solutions are mostly deprotonated (Figure 16d), they use the herbicide to decomplex the cations, thus recovering the initial emission of the ligand [74] [75].

1.2.2.5 Chemosensors for hypochlorite

While hypochlorite is not an anion that could be considered directly harmful to the environment, there are two main reasons that make its constant monitoring important. On the first place, as it is widespread used as a household disinfectant agent, its presence in discharged water is generally taken as a warranty of microbial absence and hence, good water quality [76]. Secondly, being a highly active oxidizer, hypochlorite (and the chlorinated products in which it degrades depending on the pH of the medium) can readily interact with organic matter present in water systems and produce extremely dangerous organochlorine products such as trihalomethanes, haloacetic acids, haloketones, among others, that are linked to various forms of cancer [77] [78]. Thus, monitoring this species, especially in water media where there is a constant influx of organic matter, like swimming pools, is necessary.

The detection of this analyte in the environment can be done by amperometric or other electrochemical methods, but the most common method involves spectrophotometric analysis [76]. Molecules that target hypochlorite follow the same principles as the ones for heavy metal ions or pesticides (Sections 1.2.2.3 and 1.2.2.4). Moreover, after looking into the available literature, it was found that all of them act as chemodosimeters: they react irreversibly with OCl^- to form a new oxidated species [79] [80] [81].

Thus, typical units that are incorporated into the ligands that can react with hypochlorite include oxime [82], sulfur containing groups (thioethers, thioamides and thioesters) [83], diaminomaleonitrile [84], among others. Moreso, in some cases, like in arylamides or hydrazones, hypochlorite completely cleaves the ligand [85] [86]. Some examples of the reactions that these groups experience upon treated with OCl^- are shown in Figure 17.

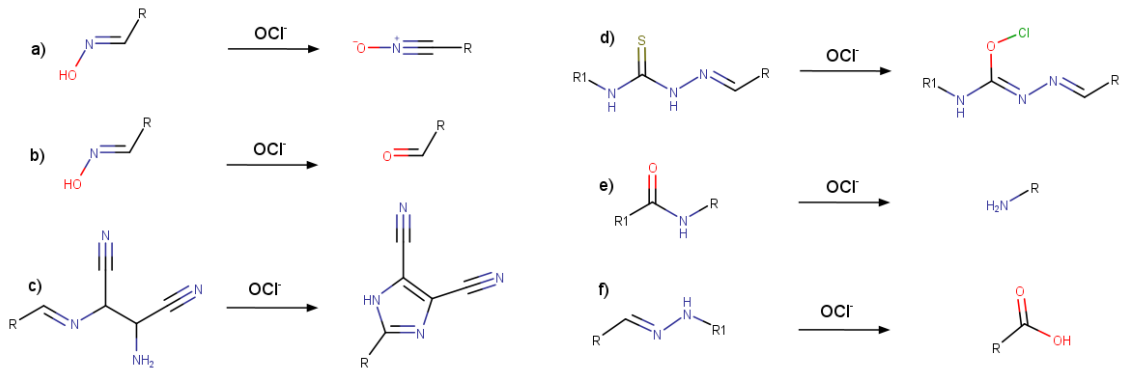

Figure 17. Different chemical units that react with hypochlorite in ligands and the product. a) an oxime turns into an nitrile oxide [82]; b) an oxime turns into an aldehyde [87]; c) a diaminomaleonitrile turns into an imidazole [84]; d) a thiourea hydrazone turns into a methylhypochlorite [83]; e) an arylester is cleaved into an amine [86]; and f) a hydrazone is cleaved into a carboxylic acid [85].

1.2.2.6 Chemosensors for molecular oxygen

Dissolved oxygen (DO) concentration is a very important water quality parameter, along with temperature, pH, total suspended solids, oil and grease, biological oxygen demand (BOD) and chemical oxygen demand (COD) [88]. Continuous detection and measurement of the dioxygen molecule is extremely important in various areas, such as medicine, chemistry, environmental and marine analysis, molecular biotechnology, bioprocess control, food packaging and industrial production. This is why several technologies that can monitor DO concentration quickly, precisely and effectively have been and are being developed. They can be broadly classified as electrochemical (amperometric, potentiometric and conductometric), optical (absorption changes or photoluminescence) or chemical (Winkler titration, radioisotope techniques, magnetic resonance and electron resonance) [49] [51].

Among all the methods that exist, the most common one, because of its robusticity and reliability, is the Clark electrode, based on amperometry, which consists of a Pt electrode covered with an O_2 permeable membrane made of an organic fluoropolymer that reduces the oxygen molecule upon the application of a voltage. In the last three decades, however, optical sensing technology of oxygen has received increasing attention because these sensors can be pretty inexpensive, are not invasive, do not consume oxygen and do not suffer from electrical interference, as opposed the methods mentioned in the above paragraph [47] [49] [51].

The type of optical oxygen sensor depends on the spectroscopical method used: absorption spectroscopy, reflectometry, luminescence, infrared and Raman spectroscopy, interferometry and surface plasmon resonance, etc. However, the vast majority of the sensors for the detection of O_2 rely on the luminescence quenching that the oxygen molecule achieves on an indicator dye, meaning that they utilize the fluorescence properties of the luminophore to detect this analyte [49].

As described in section 1.2.2.1, in general terms, when the indicator dye, or luminescent molecule, absorbs a photon, it is excited from its ground state S_0 to a higher vibrational level that corresponds to either the first or second electronic state S_1 or S_2. The ensuing possible de-excitation pathway and the effect of O_2 on it can be appreciated in Figure 18, which shows a Perrin-Jablonski diagram for this particular mechanism [49].

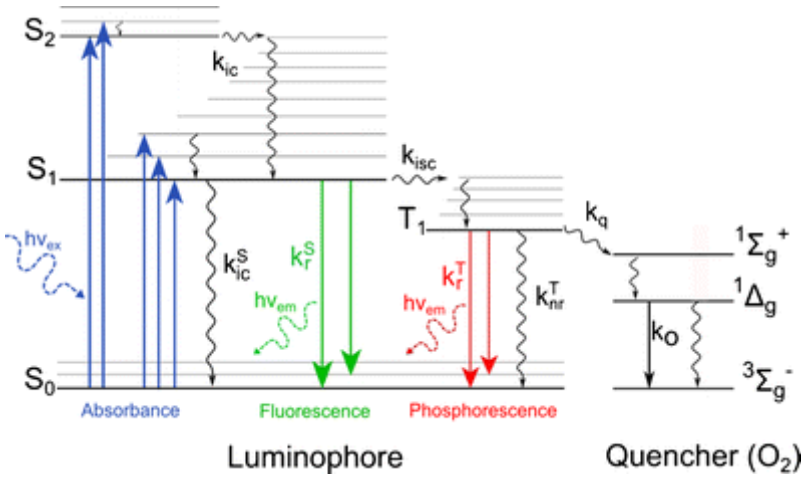

Figure 18. Perrin-Jablonski diagram for the possible de-excitation pathway of a luminescent molecule quenched by O_2. The image is taken from [49].

While the mechanism is still not fully understood yet, it is known that O_2 causes a radiationless deactivation process called collisional quenching. One first theory is that this occurs via an energy transfer mechanism, in which the O_2 molecule promotes or enhances the luminophore to undergo intersystem crossing to the triplet state while promoting itself to either of its excited states $^1\Delta_g$ or $^1\Sigma_g^-$ and, afterwards, returning to its triplet ground state $^3\Sigma_g^+$ (seen in the black straight line). This possible mechanism is supported by the fact that singlet oxygen is formed when O_2 interacts with the luminescent molecule [47] [49].

Another possible quenching mechanism is electron transfer, especially when the chemosensor is a transition metal complex. In this case, the luminescent molecule and

the quencher require a spatial overlap of the wavefunctions of their molecular orbitals. As in the energy transfer mechanism, the luminophore needs to be in the triplet excited state for the electron transfer process to occur [49] [52].

Despite having several advantages over other methods used to measure dioxygen, optical O_2 chemosensors need to consider a few important factors that may distort the results they provide. The first and most important one, when measuring low concentrations of O_2, is the possibility of O_2 photoconsumption. While it is usually stated that optical chemosensors do not consume the analyte, singlet oxygen, which is very reactive, is formed as part of the collisional quenching mechanism as explained before. Thus, it is possible that this activated species reacts with the luminescent probe or with impurities that may be present in the medium. The best way to eliminate oxygen photoconsumption is to utilize a chemosensor that resists oxidation. Other potential sources of error are the depletion of the ground state of the chemosensor (which is the consequence of the dye being in finite supply and can result problematic if a significant amount of it is excited), triplet-triplet annihilation (which can be prevented by decreasing the probe concentration or lowering the photon flux) and singlet oxygen accumulation (which is only important when measuring ultratrace concentrations of O_2) [89].

This being said, there are several families of compounds that have been reported as fluorescence oxygen chemosensors: polycyclic aromatic hydrocarbons (PAHs), transition metal polypyridyl complexes, metalloporphyrins, cyclometallated complexes, fullerenes, metal-organic frameworks and quantum dots [49] [90] [91] [92]. In the present thesis work, inspired by the fact that oxygen in the human body is supplied and stored by hemes, a family of Fe(II)-containing porphyrins (Figure 19) [93], it was decided to focus on this specific type of organic compound in a way of mimicking what nature has developed over millions of years of evolution.

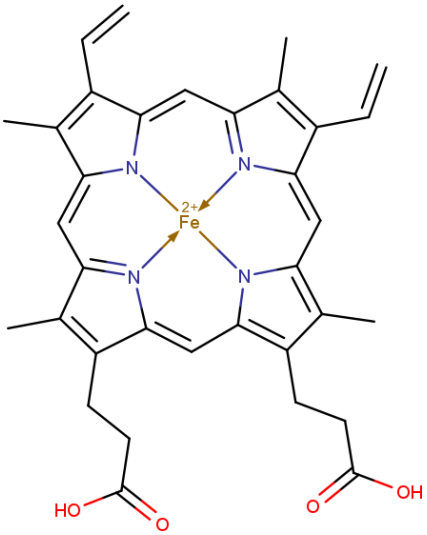

Figure 19. Chemical structure of heme B, one of the metalloporphyrins that binds oxygen in the bloodstream.

The interaction between the iron ion at the central core of heme B – and of all other porphyrins that transport this gas – has been subject of active debate for longtime. Nowadays, the consensus supports the Weiss model, in which the Fe-O_2 species can be described as a ferric-superoxide complex with the low spin metal cation Fe^{3+} coupled to a doublet superoxide anion O_2^{-}. Considering that O_2 is linked to the metal ion in a bent, end-on mode, it has been shown that the bond involves a dative σ contribution from the π^* of oxygen to the vacant $3d_{z^2}$ orbital of iron and a weak π retrodonation from the filled d_{xy} orbital of iron into the $\pi_{\perp}^{*}$ orbital of oxygen [41] [94]. A schematic representation of the Weiss model for the Fe-O_2 interaction can be seen in Figure 20.

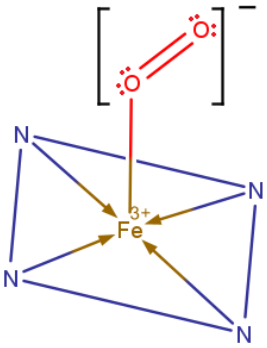

Figure 20. Schematic representation of the Fe-O_2 bond in a metalloporphyrin (the macrocycle is represented by the 4 nitrogen atoms of its central core linked together).

1.3 Small conjugated molecules as chemosensors

Based on what has been described in the previous sections, our research group focused firstly on the development of conjugated polymer fluorescence chemosensors for the detection of heavy metals present in water medium. Thanks to their backbone chain which alternates double or triple bonds with single bonds, there is an overlapping of π-orbitals that generates a delocalized system of π electrons in the macromolecule, which gives rise to exploitable optical properties such as the amplification of emission of light [95]. Thus, in the work carried out by a former member of our research group, X. Wang synthesized a series of polyfluorene and polycarbazole co-polymers that were shown to be able to detect Cu^{2+}, Ni^{2+} and Zn^{2+} [96].

In the present work, it was decided to develop conjugated molecules as fluorescence chemosensors. The driving reasons were that i) the characterization of small molecules and the corresponding species that they form with the detected analytes can be done in a much more precise way than that of the polymers, using techniques such as ^{1}H-NMR or mass spectrometry, ii) the solubility of these molecules in systems containing water could be achieved in a much facile way, and iii) molecular families such as pyrenes or benzazoles with high emission intensities and quantum yields, comparable to those of conjugated polymers, have been recently developed for fluorescence sensing [97] [98].

With this in mind, within the scope of this thesis work, 11 new ligands with potential sensing capabilities have been produced: three pyrene derivatives, three benzazole derivatives, one coumarin derivative and four porphyrin-complex derivatives. These four molecular families were chosen owing to their favorable photophysical properties, like high absorption coefficients and emission in the UV-vis section of the spectrum, which will be further explored and discussed in the following chapters of this manuscript.

It is important to mention that during the first months of the present thesis work, other members of our research group had begun investigating the possibility of functionalizing single and multi-walled carbon nanotubes with pyrene-based compounds by taking advantage of their π-π interaction potential [99] [100] [101] in order to elaborate electrical sensors. Thus, to fulfill the need of potential chemosensors bearing this moiety, it was decided that the first compounds to be synthesized were three derivatives of this chemical family.

Then, three benzazole compounds were prepared in the search for ligands that could exhibit ratiometricity, which is a better and unique response towards target analytes and

will be thoroughly discussed in Section 2.1.2.1. The coumarin derivative was afterwards synthesized in order to take advantage of its particular structure that was thought to allow an indirect sensing of the pesticide glyphosate.

Finally, four porphyrin complexes were developed specifically for the detection of dissolved oxygen. Besides what was described in Section 1.2.2.6, a second motive to utilize this chemical family was that, in the same manner as with the pyrene derivatives, members of our research group had interest in researching the functionalization of carbon nanotubes with this macrocycle [102] [103] to finally obtain electrical devices.

These 11 potential sensing compounds will be presented in the following chapters of the manuscript. For instance, in Chapter 2, the rationale behind their design in terms of fluorophore and detection unit chosen, and potential sensing mechanism will be debated, as well as the synthetic pathway used to obtain them, with a particular emphasis being put in the chemistry involved. Afterwards, in Chapter 3, their photophysical properties in terms of their emission and absorption spectra will be shown and analyzed. Finally, in Chapter 4, their sensing performance will be evaluated and discussed, emphasizing the nature of the recognition event.

2 Experimental part

In this Chapter, the choice of each of the fluorophore families that were studied within the scope of the present thesis work will be justified. Then, for each of the 11 potential chemosensors, it will be shown how their specific design was rationalized so that they could be able to interact with their target analytes. Special emphasis will be placed in the description of the chemistry that led to the obtention of these molecules. Finally, methodological procedures, both synthetic and for performing fluorescence measurements, will be presented.

2.1 Design and synthesis of sensing molecules

2.1.1 Pyrene-based chemosensors: M1, M2 and M3

2.1.1.1 General design

Pyrenes (Figure 21) are a family of fluorophores that possess interesting luminescent properties. For instance, their expanded *π*-electron delocalization and planarity confers them intense and anisotropic fluorescence, elevated fluorescence quantum yield, that can reach a value of 0.81, and relatively long excited-state lifetimes [97] [104] [105] [106]. Particularly, pyrenes are a typical example of a molecule that can provide excimer emission [107].

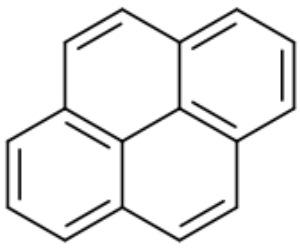

Figure 21. Chemical structure of the pyrene unit.

An excimer is the dimeric molecular photoassociation that results from the collision of a molecule in its lowest singlet excited state (M^*) with another that is in its ground state (M), as shown in the following chemical equation.

$$M + M^* \rightarrow (M \cdot M)^*$$

The formation of this species is favored by flat aromatic compounds with long enough excited-state lifetimes that could collide in a face-to-face manner, precisely as pyrene. Also, the fluorescence emission of the excimer is red shifted and structureless compared to that of the monomer [108].

Moreso, as mentioned in Section 1.3, at the start of the present thesis work other members of our research group had started to investigate about the possibility of functionalizing single and multi-walled carbon nanotubes with pyrene derivatives following reports like those of Petrov [100] and Georgakilas [101], creating a need to develop potential sensing compounds using this fluorophore. Motivated by this and by the favorable fluorescence properties of pyrene, it was decided to design three ligands containing it: **M1**, **M2** and **M3**. Their design and synthesis are described thereafter.

2.1.1.2 Design of M1

M1 (Figure 22) was designed as a pyrene-thiourea-bromophenyl ligand with the pyrene group (in violet) acting as a fluorophore and the thiourea (in green) as a possible detection unit.

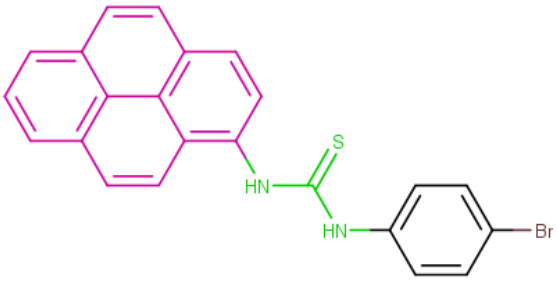

Figure 22. Chemical structure of **M1**.

The thiourea group was chosen as the detection unit based upon its reported capability for detecting anions such as F^- and carboxylate species mainly through hydrogen bonding interactions [109] [110] [111], and OCl^- although acting as a chemodosimeter in this particular case [83] [112] [113] [114] [115] [116]. Moreover, this moiety also has the potential of interacting with metal cations such as Cu^{2+}, Zn^{2+} and Hg^{2+} *via* a specific soft-soft interaction with the sulfur atom [117] [118] [119] [120] [121]. In particular, it is expected that **M1** could detect Cu^{2+} or Hg^{2+} based on the results that Lin obtained with a fairly similar molecule [117].

2.1.1.3 Synthetic approach for M1

The synthesis of asymmetric aryl thioureas can be achieved from several ways: from the 2-step condensation of amines with carbon disulfide in solvent [122] or in solventless microwave-assisted medium [123] to the three-component reaction between isocyanides with sulfur and amines [124]. However, the easiest, catalyst free and time-efficient method, albeit used only for obtaining simple thioureas, is the classic equimolar mixture of an amine and an isothiocyanate in a "bad"-thiourea solvent so that the product precipitates instantly after being formed. Thus, to go along with a rather simple design, this method to obtain the desired product was chosen: the direct reaction between 1-aminopyrene and the corresponding phenylisothiocyanato. The synthetic scheme for attaining **M1** can be seen in Figure 23 and the detailed procedure is described in Section 2.1.1.3.1.

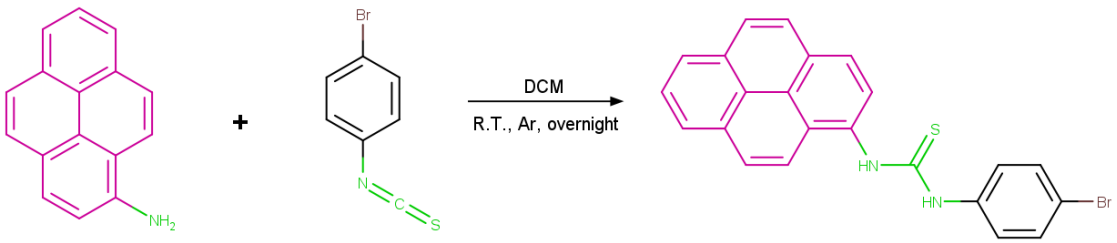

Figure 23. Synthetic scheme for the obtention of **M1**.

2.1.1.3.1 Synthesis of M1

In a 25 mL round-bottom flask, 108.7 mg (0.5 mmol) of 1-aminopyrene and 107.1 mg (0.5 mmol) of 4-bromophenylisothiocyanato are dissolved in 8 mL of dichloromethane under an argon atmosphere. A pale-yellow precipitate appears after 30 minutes and the reaction is left stirring overnight at room temperature. Afterwards, the solid is collected, washed with DCM and hexane, and dried under reduced pressure. ^{1}H-NMR (DMSO-d_6, 300 MHz, Figure 65): δ (ppm) 10.33 (s, Ha,b), 9.88 (s, Ha,b), 8.32 – 8.05 (m, 9Hpyr), 7.54 – 7.48 (m, 4Hbz). ^{13}C-NMR (DMSO-d_6, 75 MHz): δ (ppm) 182.56, 140.35, 134.04, 132.35, 131.88, 131.68, 130.64, 128.75, 128.71, 128.41, 127.89, 127.61, 127.44, 127.28, 126.66, 126.44, 126.23, 125.75, 125.05, 123.85, 117.79. ESI-MS: **M1** + H^+ (m/z), calculated: 431.0218; found: 431.0202. Yield: 71.2 mg (33 %).

2.1.1.4 Design of M2

The new molecule **M2** (Figure 24) was planned as a pyrene-imine-dihydroxyphenyl ligand. Evidently, the pyrene unit (in purple) serves as the fluorophore while the imine-dihydroxyphenyl ensemble (in green) serves as the detection unit.

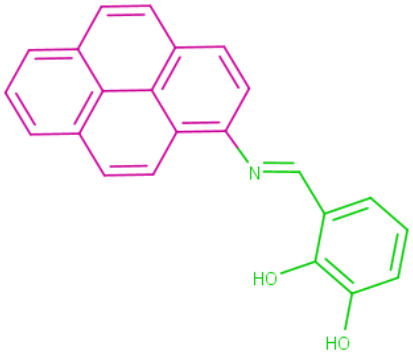

Figure 24. Chemical structure of **M2**.

The choice of the imine-hydroxy ensemble as the recognition unit for **M2** was made based on the desire to study, with a quite simple molecule, a different sensing mechanism than those that were thoroughly explained in Section 1.2.2.2: the inhibition of the free C=N isomerization. Ligands that operate through this mechanism possess in their molecular architecture a Schiff base, which is a chemical group that contains a C=N unit) and a second coordinating unit in close proximity (normally in *ortho* position to the Schiff base). These ligands are very lowly emissive due to the free intramolecular rotation – or isomerization – of the Schiff base in solution that promotes a nonradiative relaxation of the excited state of the molecule. However, the binding of the ligand with the analyte greatly enhances its emission intensity by forming a 5- or 6-membered ring that rigidifies it and restricts the C=N free rotation [58] [125] [126]. The first report of the use of this mechanism for the optical detection of an analyte is shown in Figure 25, where Wu proposed that the complexation of Zn^{2+} inhibited the free C=N isomerization of their ligand with a concomitant 200-fold increase of the emission intensity [127].

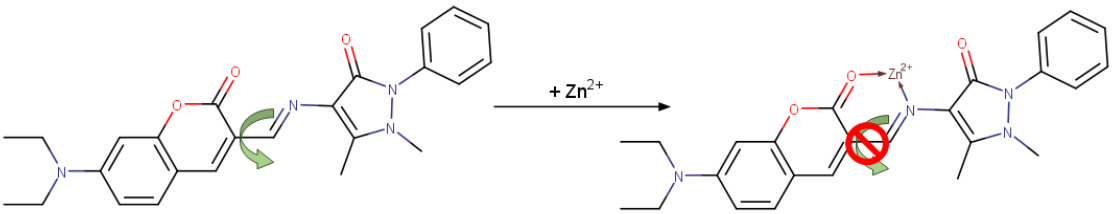

Figure 25. Mechanism of the inhibition of C=N isomerization as proposed by Wu [127].

Then, it has also been reported and extensively reviewed by Roy [128] that the precise arrangement of the -OH group at the ortho position of a Schiff base generates a pocket whose size is well-suited to fit the Al^{3+} cation. However, several other reports have shown that such arrangement could yield efficient ligands sensitive to other species such as Zn^{2+} and Cd^{2+} [129], Fe^{2+} or Fe^{3+} [130] [131], Zn^{2+}, Al^{3+}, Fe^{2+} and Fe^{3+} [132], Zn^{2+}, Cu^{2+} and Fe^{2+} [133], Zn^{2+} [134], vanadate [135], and Cu^{2+} [136]. In consequence and unfortunately, *a prori* this kind of chemosensor does not seem to exhibit any selectivity as it can exhibit sensitivity towards several analytes at the same time. Moreover, in the few cases where selectivity has been reported, it can easily be noticed that the authors have conveniently not tested their ligands against some of the most probable interaction-causing cations, such as Al^{3+}. Despite this, it is believed that the -OH + Schiff base arrangement that **M2** carries is worth of investigating. Particularly, the focus of the present design will rely on two factors: simplifying it, as it seems from the literature review that the addition of more binding groups has the effect of decreasing the selectivity; and adding a second -OH group in *meta* position to the Schiff base that is not expected to participate in the recognition event, but can help with the compatibility of the molecule with water, which is the medium in which the sensed analytes are dissolved.

2.1.1.5 Synthetic approach for M2

The synthesis of imines consists, in a nutshell, of reacting an aldehyde or ketone with an amine, forming a Schiff base and water, as can be seen in Figure 26 [137]. This reaction can be either acid catalyzed to activate the carbon of the carbonyl group and make it more prone to a nucleophilic attack [138], or base catalyzed to deprotonate the amine and make it a better nucleophile [139]. Also, as the newly formed C=N bond is prone to hydrolysis, water needs to be removed from the system as it is being formed. For this, several strategies exist: using Dean-Stark systems, molecular sieves, or protic solvents that capture the produced H_2O [139] [140].

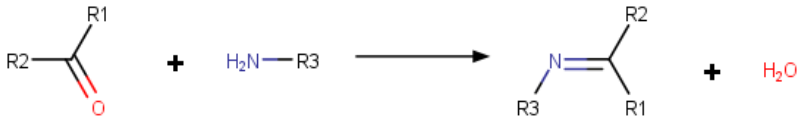

Figure 26. Basic synthetic scheme for imine formation from a carbonyl and an amine.

This being said, the simplest system to obtain imines consists in dissolving both the amine and the carbonyl in hot ethanol or methanol and mixing them together under reflux conditions, allowing the imine to precipitate upon cooling. Using either of these solvents confers the synthesis one important practical advantage: diaryl imines are fairly insoluble in alcohols and tend to precipitate instantly, rendering the product collection easy and efficient. It was thus this approach that was used to synthesize **M2**. The synthetic scheme for this ligand can be seen in Figure 27 and the synthetic procedure is detailed in Section 2.1.1.5.1.

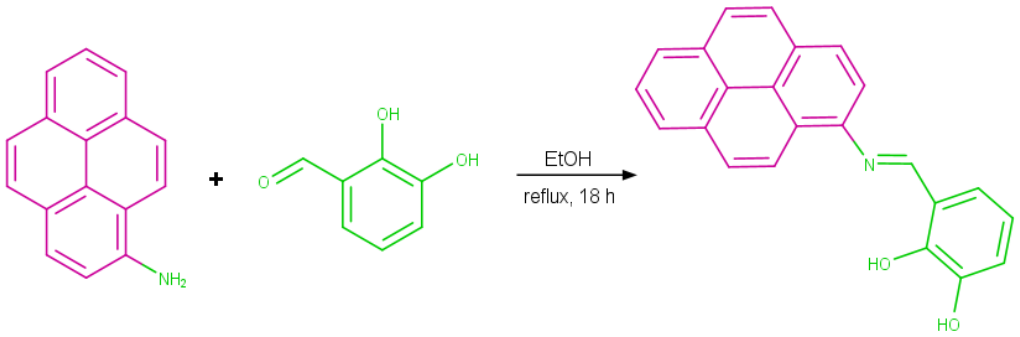

Figure 27. Synthetic scheme for obtaining **M2**.

2.1.1.5.1 Synthesis of M2

In a 25 mL round bottom flask, 108.7 mg (0.5 mmol) of 1-aminopyrene are dissolved in 5 mL of absolute EtOH at 50 °C. In another flask, 69 mg (0.5 mmol) of 2,2-dihydroxybenzaldehyde are dissolved in 8 mL of absolute EtOH at 50 °C. The latter solution is added dropwise to the former one and the reaction mixture is left stirring for 16 h in reflux conditions. The deep red precipitate formed is then collected, washed with EtOH and hexane, and dried under reduced pressure. ^{1}H-NMR (DMSO-d_6, 300 MHz, Figure 66): δ (ppm) 13.54 (s, Ha), 9.38 (s, Hb), 9.19 (s, H1), 8.44 – 8.04 (m, 9Hpyr), 7.24 (d, H2), 7.02 (d, H4), 6.86 (t, H3). ^{13}C-NMR (DMSO-d_6, 75 MHz): δ (ppm) 165.98, 165.84, 150.61, 146.98, 142.89, 132.20, 131.86, 130.82, 129.25, 128.50, 128.29, 127.85, 127.23, 126.82, 126.53, 125.59, 125.47, 125.12, 124.09, 122.82, 121.29, 120.50,

120.30, 117.53. ESI-MS: **M2** + H^+ (m/z), calculated: 338.1181; found: 338.1166. Yield: 108.0 mg (64 %).

2.1.1.6 Design of M3

The design of **M3** (Figure 28) is based on a pyrene coupled with a 4-hydroxyphenyl group connected *via* a Schiff base in *ortho* position with another hydroxyphenyl entity. Once again, the pyrene group (in violet) is the fluorophore while the ensemble hydroxyphenyl-imine-hydroxyphenyl (in green) is the recognition unit.

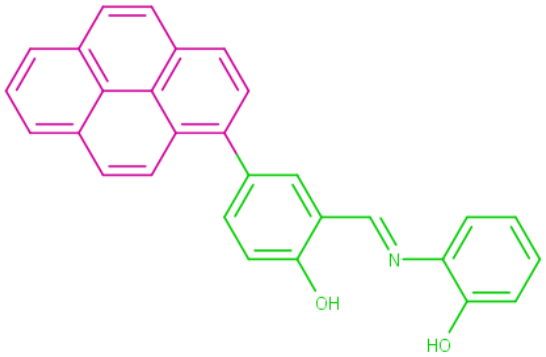

Figure 28. Chemical structure of **M3**.

The rationale behind this design was to obtain a ligand with several hydrogen bonding positions in order to attain an efficient interaction with two target analytes: glyphosate and its main metabolite AMPA (which chemical structures are shown in Figure 15). It was thought that, in order to achieve a direct detection of this pesticide, one strategy could be to take advantage of its own structure, which at pH ~7 is predominantly found in one of its anionic forms (shown in Figure 29) as discussed in Section 1.2.2.4. As can be seen, at neutral pH, the structure of glyphosate can be dissected in three parts: a negatively charged entity (the carboxylate, in violet), followed by a positively charged one (the ammonium, in blue), followed by another negatively charged one (the phosphonate, in green). Thereafter, the molecular design should contain in its architecture acidic entities that could interact with the carboxylate or the phosphonate units, or basic units that could be capable of interacting with the ammonium unit. This strategy mimics what has been reported in literature for the detection of phosphate, pyrophosphate and ATP [141] [142] [143] [144] [145].

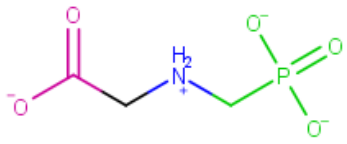

Figure 29. Chemical structure of the most common glyphosate species at pH ~7.

Thus, **M3** was designed to comply with the chemical structure of the predominant glyphosate species at this pH: its recognition unit includes firstly a phenol – an acidic group that could interact with a negatively charged species –, then an imine – a basic group which could interact with a positively charged species –, and finally another acidic group in the second phenol.

Moreover, due to the presence of the ensemble hydroxyphenyl – Schiff base in *ortho* position in its structure, it could also be expected that **M3** detects some metal cations, particularly Al^{3+} or Zn^{2+}, in a similar way as what was described for **M2** in Section 2.1.1.4, meaning that probably this ligand will operate via the inhibition of C=N isomerization mechanism.

2.1.1.7 Synthetic approach for M3

The synthesis of **M3** should basically consist of two steps, independently of the order: the imine formation (reaction which has already been described in Section 2.1.1.5) and the C-C coupling between the pyrene unit and the hydroxyphenyl group. Carbon – carbon coupling is a type of coupling reaction in which two carbon atoms from different molecules are linked together, commonly requiring the aid of a metallic catalyst. These reactions can be either homo-coupling, when the two joined molecules are identical, or cross-coupling, when they are different. The most common homo-coupling reaction is the Ullman coupling [146], while typical cross-coupling reaction methods include the Suzuki reaction [147], which creator was awarded with the Nobel Prize of Chemistry in 2010, the Stille coupling [148], the Sonogashira coupling [149], among others.

The Suzuki reaction was chosen to synthesize **M3** as it had already been used for years in our research group. Moreover, it presents several advantages in comparison with other cross-coupling methods, such as its environmentally friendly nature owing to the presence of boronic compounds, the possibility to carry it out using milder aqueous or heterogenous conditions, its high tolerance for a broad range of functional groups, its regio- and stereoselectivity, etc [150] [151].

In essence, the Suzuki reaction consists in the carbon-carbon coupling between a halide – including aryls, alkyls, alkenyls and alkynyls –, and an organoboron compound in the form of boronic acid, boronate esters or trifluoroborates in presence of a palladium catalyst and a base, as seen in the schematic representation shown in Figure 30. The reaction involves three steps: an oxidative addition of the halide species into the palladium catalyst that oxidizes it, followed by the transmetallation of the second coupling species from the boron to the palladium, and finally a reductive elimination where the coupled product is obtained and the catalyst is regenerated [150].

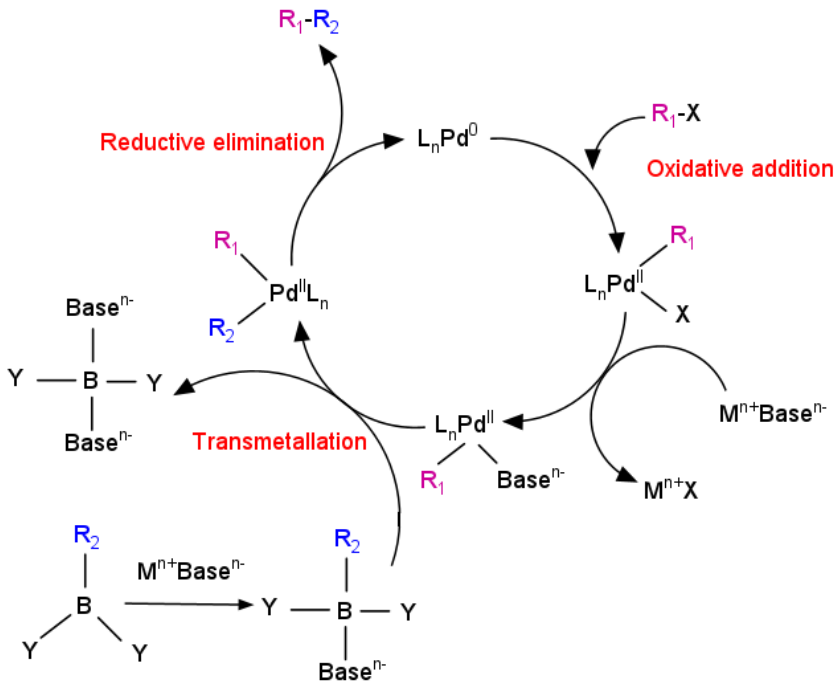

Figure 30. Schematic representation of the Suzuki reaction [150].

For the synthesis of **M7**, two pathways were envisioned. In the first one, the initial step involved the imine synthesis between 5-bromosalicylaldehyde and 2-aminophenol, followed by the Suzuki coupling of the formed product with pyrene-1-boronic acid. This pathway did not yield the product, probably because the palladium catalyst lost its activity due to being complexed by the imine group. Thus, in the second pathway, the Suzuki coupling between the mentioned boronic acid and bromide was carried out first, with the final step being the imine formation.

At first, standard conditions used in our research group for performing the Suzuki coupling were applied: 1 mol% of tetrakis(triphenylphosphine)palladium(0) catalyst with 1eq of K_2CO_3 in a toluene/ethanol/water solvent mixture at 90 °C. However, initial yields

were quite low, which is abnormal for this type of cross-coupling reaction. A first attempt to increase the yield was made by changing the solvent mixture into DMF/H_2O, as it was thought that it could possibly better solubilize the materials used in the synthesis and promote the reaction. However, the result was a dark complicated mixture that proved impossible to separate via column chromatography. Then, after looking more carefully into the isolated products from the low-yield reaction, it was noticed that the main one was indeed pure pyrene, probably obtained due to a competitive protodeboronation reaction [152]. It is reported in literature that one of the best approaches to tackle and minimize this side-reaction is to use catalysts with higher activity, such as Pd(dppf)Cl_2 or Pd(*t*-Bu)$_3$ [151][6], so the former was finally utilized and it was proved effective in increasing the yield of the reaction by 25 %. Moreover, an increase in the temperature from 90 °C to 105 °C also demonstrated it efficacy in increasing the final yield by an additional 10 %.

Finally, to obtain **M3**, the imine synthesis was carried out using the same approach as described in Section 2.1.1.5 for the synthesis of **M2**. The full synthetic scheme can thus be seen in Figure 31 and the detailed synthetic steps, in Sections 2.1.1.7.1 to 2.1.1.7.2.

It is worth to mention that efforts were made to obtain the analog of **M3** in which the last synthetic step was made using 2-thiophenol instead of 2-aminophenol, in order to compare the difference in sensing performance just by changing one atom in the entire molecule. However, the product obtained was the corresponding benzothiazole instead of the expected Schiff base, accounting for the ease of the ***S*** atom to oxidize in the synthetic conditions that were used [153]. Unfortunately, this benzothiazole derivative is of little interest within the scope of this thesis work as it has already been reported in the literature, albeit with a completely different obtention method and for a totally different application [154].

[6] As seen in Figure 30, the active catalyst species in the Suzuki cross-coupling reaction is Pd(0). When a Pd(II) catalyst is used, such as Pd(dppf)Cl_2, it should be activated *via* a reductive elimination reaction [146]. In the setup used, the base has this additional role.

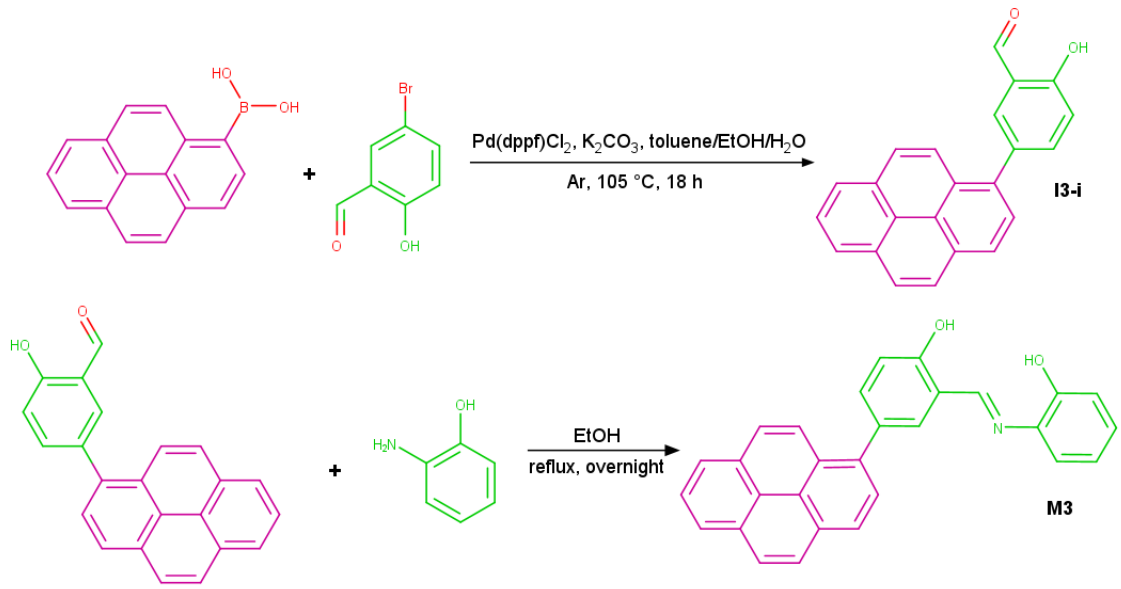

Figure 31. Synthetic scheme for the obtention of **M3**.

2.1.1.7.1 Synthesis of I3-i

In a 50 mL round-bottom flask, 246.1 mg (1 mmol) of pyrene-1-boronic acid, 201 mg (1 mmol) of 5-bromosalycilaldehyde and 276.5 mg (2 mmol) of potassium carbonate are dissolved with a 24 mL of a 2 : 3 : 1 mixture of toluene : ethanol : water under argon atmosphere. Afterwards, 7.3 mg (0.01 mmol) of [1,1'-bis(diphenylphosphino)ferrocene]dichloropalladium(II) are added to the mixture. The temperature is raised until 90 °C and the reaction is left stirring with constant monitor by TLC. After 18 h, the solvents are removed by vacuum distillation and the crude solid residue is column chromatographed using hexane : chloroform in a gradient from 13 : 1 to 6 : 1 to obtain **I3-i** as a yellow solid. ^{1}H-NMR ($CDCl_3$, 300 MHz): δ (ppm) 11.16 (s, Ha), 10.01 (s, H1), 8.25 – 7.80 (m, 9Hpyr, H3 and H4), 7.21 (d, H2). Yield: 189.4 mg (57 %). The chemical structure of **I3-i** with its assigned protons can be seen in Figure 32.

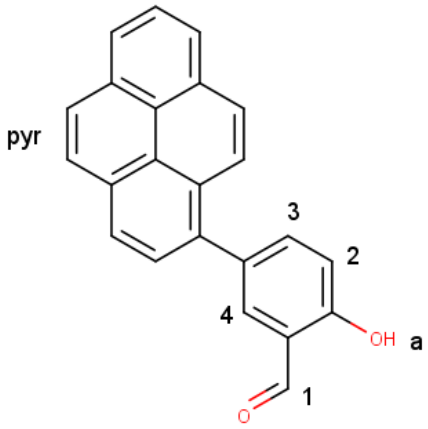

Figure 32. Chemical structure of **I3-i**.

2.1.1.7.2 Synthesis of M3

In two separate 25 mL round-bottom flasks, 128.8 mg (0.4 mmol) of **I3-i** and 43.6 mg (0.4 mmol) of 2-aminophenol are dissolved in 10 and 3 mL of hot absolute ethanol, respectively. The former solution is added dropwise to that of the amine and the reaction is left stirring under reflux conditions overnight. Then, the formed precipitate is collected, washed with ethanol and hexane, and dried under reduced pressure to obtain **M3** as a bright orange solid. ^{1}H-NMR (DMSO-d_6, 300 MHz, Figure 67): δ (ppm) 14.03 (s, Hb), 9.80 (s, Ha), 9.11 (s, H5), 8.37 – 8.03 (m, 9Hpyr), 7.90 (d, H4), 7.65 (d of d, H3), 7.39 (d, H6), 7.16 (d, H2), 7.13 (t, H7 or H8), 6.97 (d, H9), 6.87 (t, H7 or H8). ^{13}C-NMR (DMSO-d_6, 100 MHz): δ (ppm) 161.49, 160.39, 151.21, 136.38, 134.78, 134.71, 133.75, 130.97, 130.65, 130.42, 129.94, 128.18, 127.73, 127.71, 127.67, 126.39, 125.28, 124.95, 124.91, 124.65, 124.20, 124.05, 119.59, 119.56, 119.45, 117.08, 116.53. Yield: 125.7 mg (76 %).

2.1.2 Benzazole-based chemosensors: M4, M5 and M6

2.1.2.1 General design

Azoles are 5-membered aromatic heterocycles in which at least one of the atoms forming the ring is a nitrogen. They are widely found in nature and, in general terms, they constitute the backbone of several commercially important drugs and fungicide agents [155].

On their side, benzazoles are a family of heterocyclic aromatic compounds in which a benzene ring is fused with an azole ring (In Figure 33, chemical structures of selected

members of this family can be seen). Due to their biologically-active capabilities, they are among the most used heterocycles in pharmacological studies [156] [98]. Besides, owing to their interesting properties like high quantum yields, and very good chemical, photochemical and thermal stabilities, they have become a commonly used fluorophore moiety in the design of fluorescence chemosensors. Particularly, for benzimidazoles, benzoxazoles and benzothiazoles, their photophysics are governed by their rigidity and planarity that yields a highly conjugated aromatic system. The electron-withdrawing capabilities of these three sub-families of molecules can be furthermore exploited when they are derivatized at their 2-position (marked with a red dot in Figure 33) with another π-conjugated unit, leading to compounds that exhibit even superior luminescent properties [98].

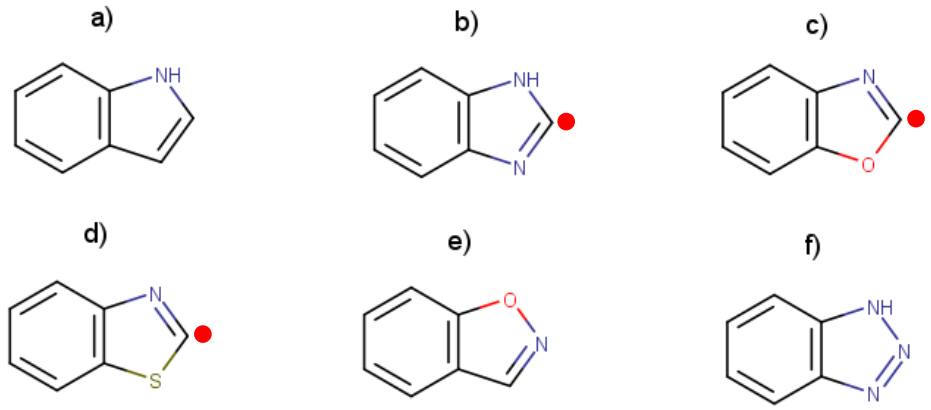

Figure 33. Chemical structures of some members of the benzazole family: a) benzopyrrole (commonly known as indole); b) benzimidazole; c) benzoxazole; d) benzothiazole; e) benzoisoxazole; and f) benzotriazole.

It is in fact the substitution at the 2-position of benzimidazoles, benzoxazoles and benzothiazoles with a 2-hydroxyphenyl unit that gives rise to a whole new family of compounds (Figure 34) because of the notable mechanism that governs their photophysics: they undergo the so-called Excited-State Intramolecular Proton Transfer (ESIPT).

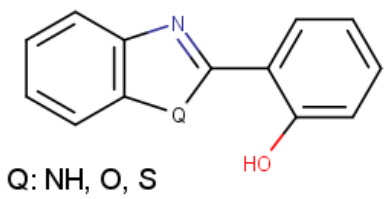

Figure 34. Chemical structure of a 2-(2-hydroxyphenyl)benz(oxa,imida,othia)zole.

ESIPT is a photochemical process than generates a keto-enol (or an imine-enamine) excited-state tautomer thanks to a hydrogen atom transfer from a donor group (N-***H*** or O-***H***) to an acceptor group (C=***N*** or C=***O***) exclusively in the first excited state [157] [158] owing to the excited state-induced increased acidity of the hydrogen bond donor and basicity of the hydrogen bond acceptor [55]. This process takes places *via* preformed intramolecular hydrogen bonds or, more rarely and only if the geometry does not allow it, *via* tunneling with the solvent serving the role of a proton-relay [159]. In essence, the result of the ESIPT mechanism is an ultrafast phototautomerization ($k_{ESIPT} > 10^{12}$ s^{-1}) in which the excited-state enol form of the molecule (E*) converts into its correspondent excited-state keto form (K*), each of these tautomeric forms having different emissions because of their different electronic structures. After the subsequent radiative relaxation, a reverse proton transfer takes place to restore the molecule back to its original enol form (E) [55] [160]. This kind of molecules have remarkable properties, such as large Stokes shifts, dual emission, and spectral sensitivity to the solvent medium [55] [160]. Because of these distinct properties, ESIPT-type molecules have been used in a wide range of fields such as biotechnology, molecular logic gates, UV-absorber, fluorescence sensing and imaging, among others [160]. It should be noted that, while there are several molecular families in which the ESIPT process takes place, the most common one is precisely the 2-(2-hydroxyphenyl)benzazole family, as it is for them that the higher Stokes shifts have been reported [55] [161]. In Figure 35, a schematic representation of the ESIPT mechanism in a model molecule, namely 2-(2-hydroxyphenyl)benzoxazole, is shown.

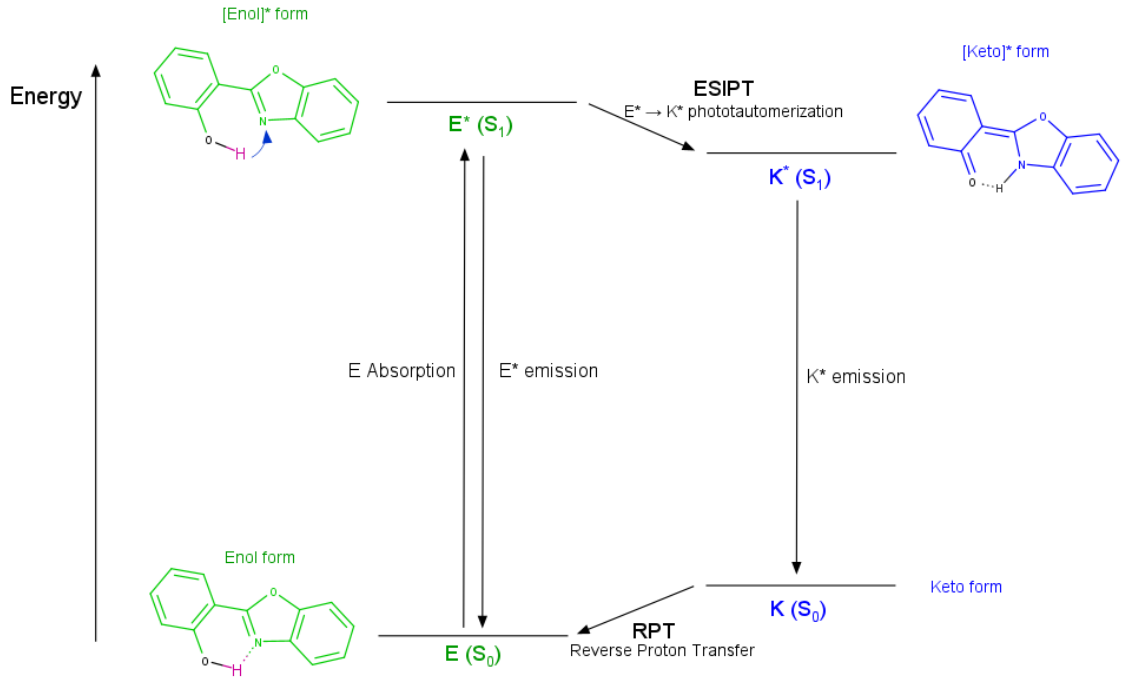

Figure 35. Schematic representation of the ESIPT mechanism in the model molecule 2-(2-hydroxyphenyl)benzozaxole. The blue arrow shows the direction of the proton transfer.

As for their use as chemosensors, the general design of an ESIPT-based ligand involves that the recognition event towards the target analyte blocks the proton transfer, thus inhibiting the phototautomerization and not allowing the emission of the [keto]* tautomer to be seen, usually with the concomitant promotion of a new band [55]. In turn, this allows for a ratiometric detection of the analyte instead of the classic “Turn-ON” or “Turn-OFF” detection types. This type of detection avoids typical difficulties present when using single-emission chemosensors such as interference from instrumental parameters and from the microenvironment surrounding the ligand, potential differences in local concentrations of the ligand, and photobleaching, among others. In the case of ratiometric detection, however, since the analyte generates a measurable change in the fluorescence intensity of two emission bands, it can be said that an internal referencing takes place, which greatly increases the sensitivity and provides better quantification values [162].

Taking advantage of this convenient properties and recognition capabilities, three 2-(2-hydroxyphenyl)benzazole based chemosensors with ESIPT aptitudes were designed: **M4**, **M5** and **M7**. Their design and synthesis are described next.

2.1.2.2 Design of M4

The novel molecule **M4** (Figure 36) was conceived as a 2-(2-hydroxy-3-hydroxyiminophenyl)-benzimidazole compound, with the benzimidazole moiety (in green) serving as a fluorophore and the oxime-hydroxyphenyl ensemble (in blue and violet, respectively) serving as the detection unit. The benzimidazole unit was chosen because it can serve as a multifunctional unit: it is a highly conjugated planar chromophore that has intense emission and high quantum yield (ranging from 0.5 to 0.7 [163]), possesses electron accepting and *π*-bridging properties that affect the mechanisms that govern the excited state of the molecule and could also act as a detection unit thanks to its chromogenic pH-sensitivity and metal-ion chelating capabilities [164] [165] [166]. Besides these convenient fluorogenic properties of the benzimidazole unit, as has been discussed in detail in Section 2.1.2.1, the design of **M4** with a 2-hydroxyphenyl at the 2 position of the benzimidazole ring and the oxime function in *ortho* position to the phenol group is such that it can act as an ESIPT chemosensor [160] [167]. For the particular case of **M4**, *a priori*, it is possible that the ligand undergoes two different excited-state phototautomerizations: the first, from the **H** atom of the hydroxyphenyl to the ***N*** atom of the oxime group; and the second, from the same **H** atom of the hydroxyphenyl to the ***N*** atom of the benzimidazole moiety.

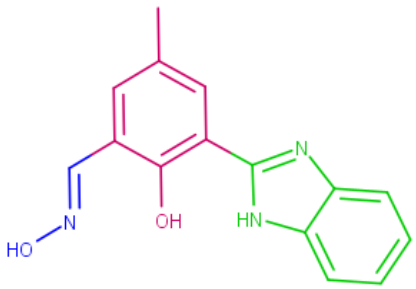

Figure 36. Chemical structure of **M4**.

As for the target analytes that **M4** is meant to detect, its design suggests that, in a similar manner as with **M3**, the presence of an -OH group at the ortho position of what could be seen as a Schiff base (both in the oxime unit and the benzimidazole moiety) will make this ligand a potential good candidate towards Al^{3+} detection, among other cations already discussed in Section 2.1.1.4. However, given the ESIPT nature of this ligand, the expectation is that a ratiometric chemosensor towards this cation can be obtained. Moreover, the inclusion of an oxime group was made to once again try to fulfill a longtime desire of our research group: the detection of hypochlorite, as it has been reported before

that this unit can react with the anion [82] [87] [168] [169] [170] [171], meaning that **M4** could act as a chemodosimeter in this particular case.

2.1.2.3 Synthetic approach for M4

The synthesis of 2-aryl-benzimidazoles is well known and can be carried out in several different ways. Classic couplings involve the reaction between *ortho*-phenylenediamine with carboxylic acids using harsh reaction conditions, or a two-step reaction that first combines this same amine with aldehydes or alcohols and requires an oxidative cyclodehydrogenation in the second step. Moreover, recent advances in this synthesis show that complex additives or catalysts can be added to greatly increase the yields and reduce the formation of byproducts [172].

For the particular synthesis of **M4**, the first step should naturally involve the preparation of the 2-aryl-benzimidazole moiety. Afterwards, a classic Duff reaction can be carried out to formylate the 3 position of the hydroxyphenyl ring [173], and finally the oxime could be obtained by treatment of the newly formed aldehyde with hydroxylamine hydrochloride [174]. As the product resulting from the formylation of the 2-(2-hydroxy-5-methylphenyl)benzimidazole has already been reported by several authors, it was decided to follow a simple and effective way to obtain it instead of methods that involve the use of metallic catalysts and thus, the procedure reported by Li was chosen [84]. In his method, the first step involved the activation of the aldehyde of 2-hydroxy-5-methylbenzaldehyde with $NaHSO_3$ to form an adduct, which is then treated with ortho-phenylenediamine to form the desired 2-(2-hydroxyphenyl)-benzimidazole. In a third step, this compound was combined with hexamethylenetetramine in CF_3COOH to finally obtain the formylated product. In the particular case of **M4**, the synthesis of this precursor was carried out with two modifications: the first one, in the first step, was to change the equivalent amount of $NaHSO_3$ used in the reaction. It has been reported by Jiang [175] that sodium bisulfite does not only activate the aldehyde, but also increases the chemoselectivity of the reaction towards the desired benzimidazole product, so two equivalents of this salt were used instead of only one as originally suggested by Li. The second modification took place in the formylation step, as it was experimentally demonstrated that 72 h of reaction time instead of 8 h greatly increases the yield of the reaction up to 35 % more, obtaining a final yield closer to what has been reported in the literature.

To finalize the obtention of the new chemosensor **M4**, the step involving the reaction of 2-(2-hydroxy-3-formylphenyl)-benzimidazole to form the coveted oxime was carried out

applying the procedure reported by Zhao [174]. The complete synthetic scheme for **M4** is shown in Figure 37 and the detailed synthetic procedures are described in Sections 2.1.2.3.1 to 2.1.2.3.3.

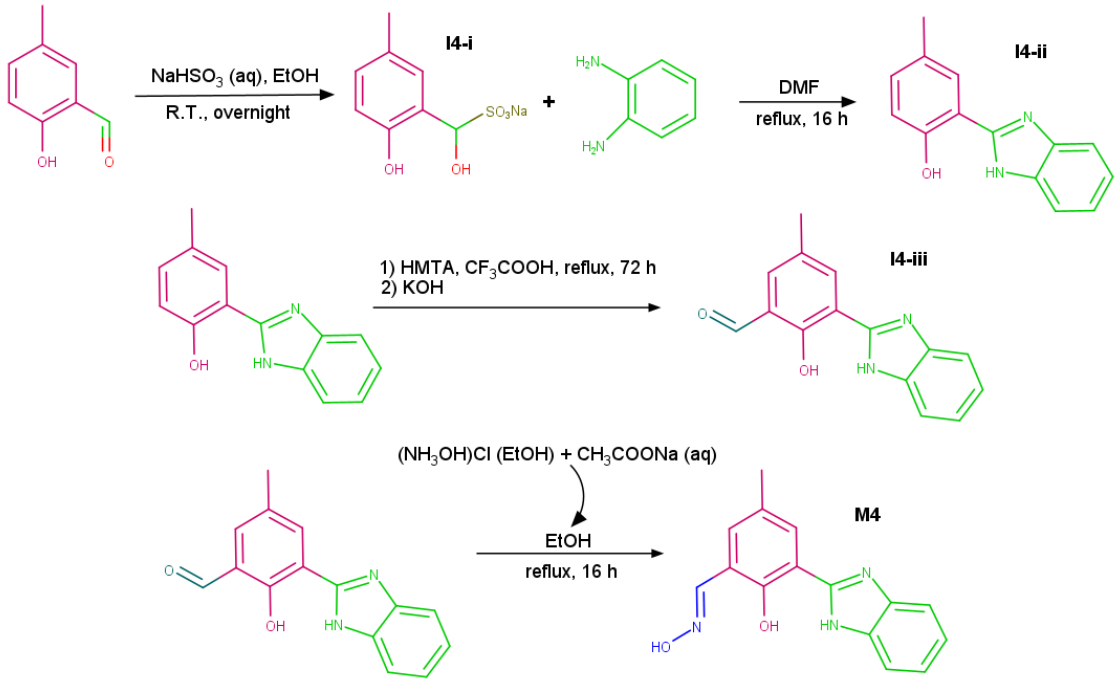

Figure 37. Synthetic scheme for the obtention of **M4**.

2.1.2.3.1 Synthesis of I4-i and I4-ii

In a 50 mL round-bottom flask, 680.8 mg (5 mmol) of 2-hydroxy-5-methylbenzaldehyde are dissolved in 20 mL of EtOH. Afterwards, 1 040.6 mg (10 mmol) of $NaHSO_3$ previously dissolved in 1 mL of H_2O are added. The mixture is stirred overnight. The white precipitate, **I4-i**, is filtered, washed with EtOH and hexane, and dried under reduced pressure. Then, this solid is suspended in 5 mL of DMF and 594.8 mg (5.5 mmol) of *ortho*-phenylenediamine are added. The mixture is refluxed and constantly monitored by TLC. After 6 h, it is cooled and poured into H_2O/ice to obtain an amber precipitate, which is subsequently dissolved in ethyl acetate, dried under Na_2SO_4 and column cromatographed using hexane : EA in a gradient from 19 : 1 to 9 : 1 to obtain **I4-ii** as a yellow greyish solid. ^{1}H-NMR (DMSO-d_6, 400 MHz): δ (ppm) 13.15 (s, Hb), 12.89 (s, Ha), 7.88 (d, H7), 7.70 – 7.61 (br m, H3 and H6), 7.28 (br m, H4 and H5), 7.20 (d of d of d, H8), 6.94 (d, H9), 2.33 (s, 3H10). Yield: 852.2 mg (76 %). The chemical structure of **I4-ii** with its assigned protons can be seen in Figure 38.

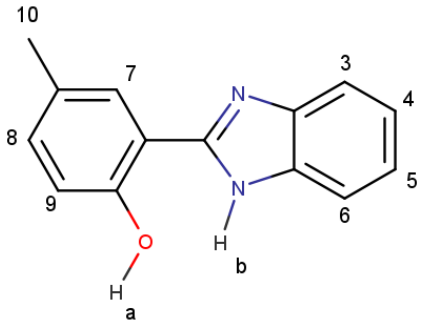

Figure 38. Chemical structure of **I4**-i.

2.1.2.3.2 Synthesis of I4-iii

In a 25 mL round-bottom flask, 1 121.5 mg (8 mmol) of hexamethylenetetramine are dissolved in 10 mL of CF_3COOH. After 30 minutes of stirring at room temperature, 897.1 mg (4 mmol) of **I4-ii** 1 are added to the solution and the reaction mixture is refluxed, and monitored by TLC each 24 h. After 72 h, the reactant medium is cooled and poured into H_2O/ice, and treated with $KOH_{(s)}$ until obtaining pH 6-7. The resulting precipitate is dissolved with ethyl acetate, dried over Na_2SO_4 and column chromatographed using hexane : EA in a gradient from 9 : 1 to 6 : 1 to obtain **I4-iii** as a yellow fluffy solid. ^{1}H-NMR (DMSO-d_6, 300 MHz): δ (ppm) 10.47 (s, H11), 8.18 (br, H8), 7.68 (br, H3 and H6), 7.59 (br, H7), 7.31 (m, H4 and H5), 2.35 (s, 3H10). Signals of protons Ha and Hb cannot be seen. Yield: 746.7 mg (74 %). The chemical structure of **I4-iii** with its assigned protons can be seen in Figure 39.

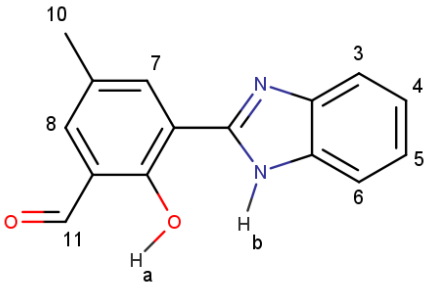

Figure 39. Chemical structure of **I4-iii**.

2.1.2.3.3 Synthesis of M4

In a 25 mL round-bottom flask, 252 mg (1 mmol) of **I4-iii** are dissolved in EtOH at 50 °C. Separately, 83.4 mg (1.2 mmol) of $(NH_3OH)Cl$ are dissolved in 4 mL of EtOH with

subsequent addition of an aqueous solution containing 123.1 mg (1.5 mmol) of CH_3COONa. The later solution is added to the former one and the reaction mixture is left stirring for 16 h at reflux conditions. The mixture is cooled until 0 °C and the resulting white greenish precipitate, **M4**, is collected, washed with cold EtOH and hexane, and dried under reduced pressure. ^{1}H-NMR (DMSO-d_6, 300 MHz, Figure 68): δ (ppm) 13.66 (s, Hb), 13.30 (s, Ha), 11.30 (s, Hc), 8.42 (s, H12), 7.93 (d of d, H8), 7.72 – 7.61 (br m, H3 and H6), 7.59 (d of d, H7), 7.30 (br m, H4 and H5), 2.35 (s, 3H10). ^{13}C-NMR (DMSO-d_6, 75 MHz): δ (ppm) 154.01, 151.38, 143.49, 140.63, 133.09, 127.82, 127.69, 127.48, 123.46, 122.53, 120.47, 117.94, 112.86, 111.60, 20.25. ESI-MS: **M4** + H^+ (m/z), calculated: 268.1086; found: 268.1093. Yield: 173.7 mg (65 %).

2.1.2.4 Design of M5

The new molecule **M5** (Figure 40) was imagined as a 2-(2-hydroxyphenyl)-benzoxazole-hydroxymethyl compound, in which the benzoxazole unit (in green) functions as a fluorophore and the 2-hydroxybenzyl alcohol (in blue and purple) helps with the recognition event. In a similar way as the benzimidazole unit described in section 2.1.2.2, the benzoxazole unit was chosen owing to its convenient fluorogenic properties. Moreover, the change from an N-H to a ***O*** atom in the structure results in a variation of the pK_a of the molecule, which can have an effect on its selectivity and photophysical properties depending on the pH of the medium [176]. Once again, in close resemblance to **M4**, the design of **M5** with a 2-hydroxyphenyl at the 2 position of the benzoxazole unit is such that the molecule can act as an ESIPT chemosensor [167] [160].

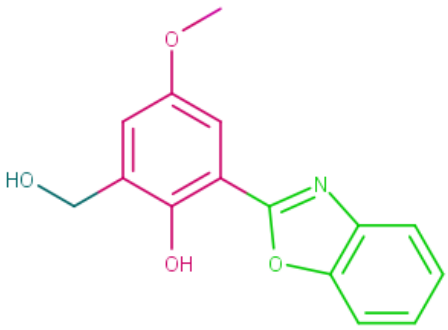

Figure 40. Chemical structure of **M5**.

Moreover, the design of **M5** is particularly based on a report by Shang [177], in which with a fairly similar molecule, the difference being that he used a 2-hydroxy-3,5-hydroxyethyl instead of 2-hydroxy-3-hydroxyethyl-5-methoxyphenyl in the present case,

he was able to detect Zn^{2+} in HEPES buffered solution. However, it is surprising that the molecule is not able to detect the Al^{3+} cation, as it carries the typical phenol in *ortho* position to an imine that has been widely reported to be able to detect this cation [53]. Besides the possible difference in sensing performance, the structural change in **M5**, switching away from a hydroxy into a methoxy group, is expected to reduce the acidity of the phenolic proton that undergoes ESIPT, lowering its transfer constant [159].

Finally, in addition to its ESIPT capabilities, it is believed that there is the possibility of an active PET mechanism in **M5** due to the fact of it having non-conjugated electrons in its hydroxymethyl group. Thus, a low emission intensity could be expected for this ligand. Compounds that exhibit a double ESIPT-PET mechanism have been reported before [178], although many authors incorrectly interpret the C=N isomerization that governs the excited state of their molecules as an active PET system [179] [180].

2.1.2.5 Synthetic approach for M5

The synthesis of 2-aryl benzoxazoles is also extensively documented in literature. The classic procedure comprises the condensation of *ortho*-aminophenols with carboxylic acids in presence of organic acids as catalysts. Evidently, several other systems that use metallic catalysts, organic ligands and salts as oxidizers have been developed [181].

Mirroring the synthetic work that was done to obtain **M4**, it was figured that the first step to obtain **M5** should involve the synthesis of the benzimidazole ring. Then, the 3 position in the phenol ring could be formylated and finally, the aldehyde could be reduced to an alcohol with sodium borohydride as a broad range reductive agent [182] to obtain the desired product. After careful consideration, it was decided to use Chang's method [183] to obtain the 2-(2-hydroxy-5-methoxyphenyl)benzoxazole intermediate. In this method, the first step involves the reaction of an aldehyde with an amine to form an imine, with subsequent oxidation of the iminic carbon atom with DDQ to obtain the desired 2-aryl-benzoxazole. The two final steps to obtain **M5**, mimic what has been reported in literature with a similar compound already described [177]. The complete synthetic scheme used for obtaining **M5** is shown in Figure 41 and the detailed procedure is described in sections 2.1.2.5.1 to 2.1.2.5.3.

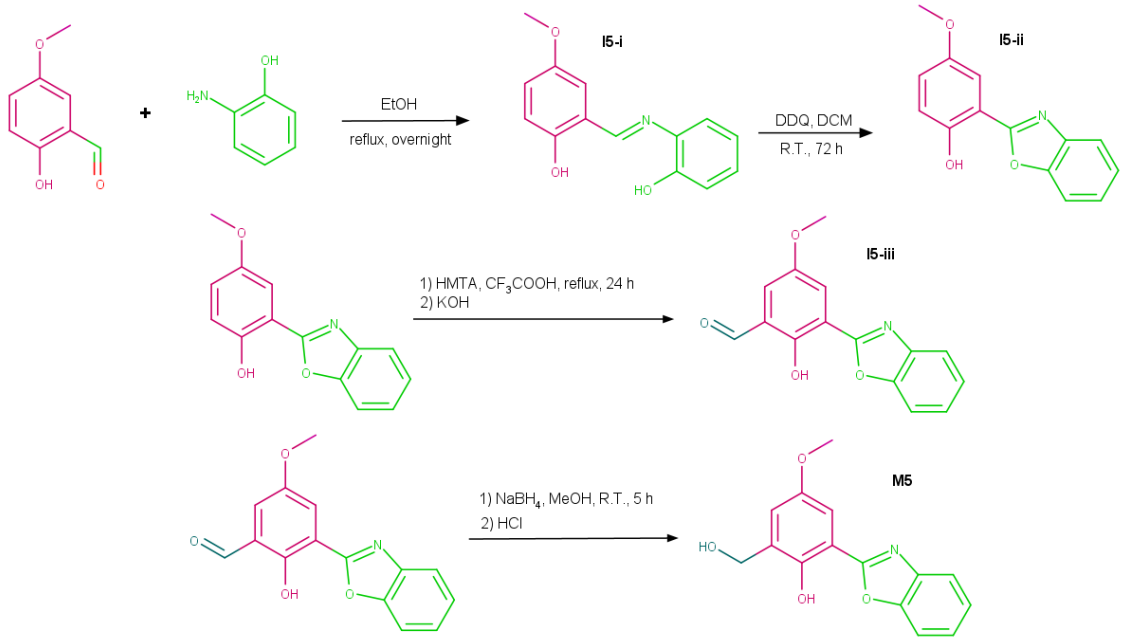

Figure 41. Synthetic scheme for the obtention of **M5**.

2.1.2.5.1 Synthesis of I5-i and I5-ii

In two separate 25 mL round-bottom flasks, 760.7 mg (5 mmol) of 2-hydroxy-5-methoxybenzaldehyde and 545.7 mg of 2-aminophenol (5 mmol) are each dissolved in 5 mL of hot absolute EtOH. The solution of the aldehyde is added dropwise to that of the amine and the mixture is left refluxing overnight under stirring. Afterwards, the solution is cooled down to let **I5-i** precipitate as a bright deep red solid, which is collected by filtration, washed with cold EtOH and hexane, and dried under reduced pressure. Immediately after, **I5-i** is dissolved in 10 mL of CH_2Cl_2 and 1 702.5 mg (7.6 mmol) of 2,3-dichloro-5,6-dicyano-1,4-benzoquinone are added. The heterogenous mixture is left stirring at room temperature for 72 h, after which the solid part is removed and washed with CH_2Cl_2. After evaporation of CH_2Cl_2, the crude product is solid packed into a chromatographic column to be finally eluted with hexane : ethyl acetate in a gradient from 99 : 1 to 9 : 1 to obtain **I5-ii** as a white solid. ^{1}H-NMR ($CDCl_3$, 300 MHz): δ (ppm) 11.09 (s, Ha), 7.72 – 7.61 (br, H3 and H6), 7.50 – 7.39 (br, H7, H4 and H5), 7.05 (s, H8 and H9), 3.87 (s, 3H10). Yield: 904.7 mg (75 %). The chemical structure of **I5-ii** with its assigned protons can be seen in Figure 42.

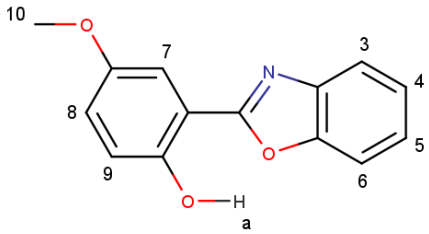

Figure 42. Chemical structure of **I5-ii**.

2.1.2.5.2 Synthesis of I5-iii

In a 25 mL round-bottom flask, 560.8 mg (4 mmol) of hexamethylenetetramine are dissolved in 10 mL of CF_3COOH. After 30 minutes of stirring at room temperature, 482 mg (2 mmol) of **I5-ii** are added and the reaction mixture is put in reflux conditions with constant monitoring by TLC. After 24 h, it is cooled and poured into H_2O/ice, and treated with $KOH_{(s)}$ until obtaining pH 6-7. The resulting precipitate is dissolved with CH_2Cl_2, dried over Na_2SO_4 and column chromatographed using hexane : EA in a gradient from 99 : 1 to 9 : 1 to obtain **I5-iii** as a white solid. ^{1}H-NMR ($CDCl_3$, 300 MHz): δ (ppm) 11.82 (s, Ha), 10.59 (s, H11), 7.81 (s, H8), 7.75 – 7.63 (b, H3 and H6), 7.52 – 7.42 (br, H7, H5 and H5), 3.88 (s, 3H10). Yield: 430.8 mg (40 %). The chemical structure of **I5-iii** with its assigned protons can be seen in Figure 43.

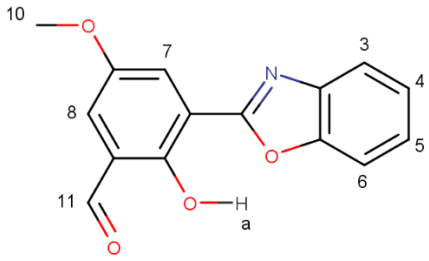

Figure 43. Chemical structure of **I5-iii**.

2.1.2.5.3 Synthesis of M5

In a 10 mL round-bottom flask, 102.4 mg (0.38 mmol) of **I5-iii** are suspended in MeOH. Then, 57.5 mg (1.52 mmol) of sodium borohydride are slowly added under mild stirring and the mixture is left reacting for 5 h, after which an addition of 1.52 mmol of $NaBH_4$ is made to ensure competition of the reaction. After 15 more minutes of stirring, the solvent is evaporated and 5 mL of H_2O are added. The pH of the medium is thereafter neutralized

with a few drops of $HCl_{(cc)}$, the crude residue is extracted with $CHCl_3$, dried over Na_2SO_4 and solid packed into a chromatographic column using hexane : EA in a gradient from 19 : 1 to 4 : 1 to obtain **M5** as a pale white solid. ^{1}H-NMR ($CDCl_3$, 400 MHz, Figure 69): *δ* (ppm) 7.75 – 7.64 (m, H3 and H6), 7.47 (d, H7), 7.42 (m, H4 and H5), 7.12 (d, H8), 4.82 (s, 2H12), 3.89 (s, 3H10). Signals of Ha and Hb protons could not be seen, but the peak of Ha has been detected in low resolution ^{1}H-NMR at *δ* 11.52 ppm. ^{13}C-NMR ($CDCl_3$, 100 MHz): *δ* (ppm) 152.36, 151.02, 149.09, 130.28, 125.52, 125.12, 120.21, 119.28, 110.70, 110.03, 108.96, 61.86, 55.99. ESI-MS: **M5** + H^+ (m/z), calculated: 272.0917; found: 272.0916. Yield: 81.4 mg (79 %).

2.1.2.6 Design of M6

M6 (Figure 44) was thought as a double benzazole-ESIP-based ligand. It carries benzothiazole (in violet) and benzoxazole (in blue) units that serve as the fluorophores, which are integrated into the same molecule *via* a hydroxyphenyl unit (in green) in their corresponding 2 positions.

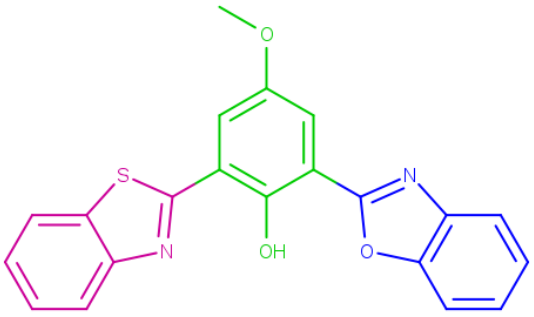

Figure 44. Chemical structure of **M6**.

Besides what has already been discussed about benzoxazoles in Section 2.1.2.4, benzothiazoles are structurally similar compounds that exhibit a wide array of pharmacological activities such as antibacterial, anticancer, anti-inflammatory, analgesic, among others. Moreover, this family of compounds possesses beneficial properties for being used as ligands for fluorescence detection, such as high quantum yields and molar extinction coefficients, large Stokes shifts, good photostability, and the capacity to help in the recognition event thanks to the binding capacity of the ***N*** atom present in its chemical structure, which shows a pK_a value of 4.51 for pure benzothiazole [184] [185].

As for its ESIPT capabilities, **M6** has, in principle and similarly to **M4**, the capacity to undergo two different phototaumerizations in its excited state: the first one, from the ***H***

atom of the hydroxyphenyl to the ***N*** atom of the benzoxazole unit; and the second one, from the same ***H*** atom of the hydroxyphenyl to the ***N*** atom of the benzothiazole moiety.

Finally, it is expected that, owing to the preformed cavity present that holds a phenol group in the *ortho* position to an imine, **M6** could detect cationic species such as Al^{3+} or Zn^{2+}. A similar benzothiazole-hydroxynaphthyl-benzoxazole ligand was reported by Li and it was shown to effectively detect Zn^{2+} although with just a fluorescence "Turn-ON" response [186], meaning that the ESIPT mechanism was probably not inhibited by the recognition event. It is possible that the low emission of that reported molecule arises from its non-planar structure due to its bulky naphthyl group that generates steric hindrance. Thus, for **M6**, a much smaller methoxy group was introduced in *para* position of the phenol with the aim of obtaining a more planar emissive molecule, which will account for a higher quantum yield and a possible ratiometric detection of the target analytes.

2.1.2.7 Synthetic approach for M6

The 2-(5-methoxy-3-carboxaldehyde-2-hydroxyphenyl)benzothiazole (**I6-i**) unit used for the obtention of **M6** was prepared by a former member of our research group following published reports [167], thus the discussion of its synthesis does not fall within the scope of the present thesis manuscript.

However, to obtain the final ligand, it was still necessary to attach the benzoxazole moiety into the available benzothiazole derivative. The first pathway investigated to achieve this was, as could be expected, to recreate the method used for **I5-ii**: a Schiff base formation between the aldehyde and 2-aminophenol, followed by oxidation of the ***O*** atom with DDQ. Unfortunately, this method proved to be ineffective, probably because the aldehyde group of the precursor of **M6** was not very chemically active. After reviewing the available literature, an interesting and simple procedure was chosen and applied: the one pot synthesis of benzoxazoles using phenyl boronic acid as a Schiff-base formation promotor and KCN as assistant of the oxazole ring-closure *via* a benzoin-type condensation [187] [188].

The schematic representation of the synthesis used to obtain **M6** can be seen in Figure 45 and the detailed procedure is described in Section 2.1.2.7.1.

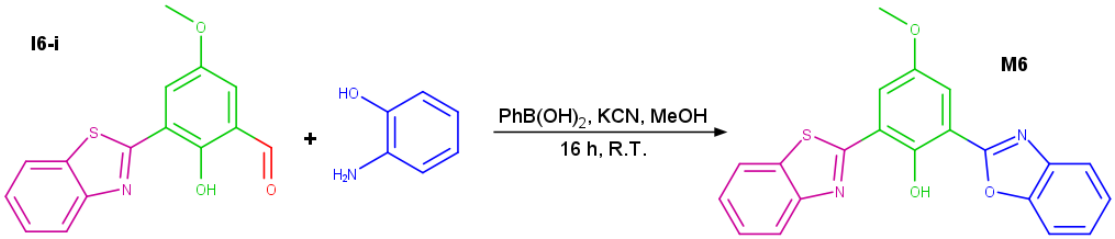

Figure 45. Synthetic scheme for the obtention of **M6**.

2.1.2.7.1 Synthesis of M6

In a 25 mL round-bottom flask, 21.8 mg (0.2 mmol) of 2-aminophenol are stirred with 10 mL of MeOH. Then, 57.1 mg (0.2 mmol) of **I6-1**, 24.4 mg (0.2 mmol) of phenyl boronic acid and 39.1 mg (0.6 mmol) of potassium cyanide are added to the mixture and the reaction is stirred at room temperature for 16 h. Afterwards, the precipitate is collected, washed with water and MeOH, and dried under reduced pressure to obtain **M6** as a pale yellowish solid. ^{1}H-NMR ($CDCl_3$, 300 MHz, Figure 70): δ (ppm) 12.69 (s, Ha), 8.18 (d, H2), 8.09 (d, 1Hbz), 7.97 (d, 1Hbz), 7.78 (m br, 1Hbz), 7.73 (d, H1), 7.64 (m br, 1Hbz), 7.51 (t, 1Hbz), 7.41 (m br, 3Hbz), 3.97 (s, 3H3). ^{13}C-NMR ($CDCl_3$, 75 MHz): δ (ppm) 163.17, 162.11, 152.29, 151.90, 151.17, 149.27, 140.00, 135.92, 126.17, 125.77, 125.19, 124.98, 122.79, 121.86, 121.46, 119.53, 117.98, 115.41, 112.35, 110.80, 56.25. Yield: 38.2 mg (51 %).

2.1.3 Coumarin-based chemosensor: M7

2.1.3.1 General design

Coumarins (Figure 46) are a family of compounds that occur naturally in the environment as they are common secondary metabolites in plants – being present in fruits, seeds, roots and leaves –, bacteria and algae. Owing to their low toxicity and high biological activity, coumarins derivatives have been extendedly used in the medicinal field mostly as anticoagulants and blood pressure regulators, but some of them can also be used as pest-control agents [189] [190].

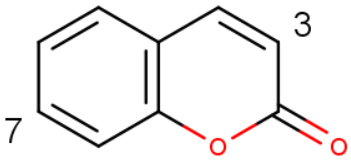

Figure 46. Basic chemical structure of a coumarin.

Coumarin derivatives also possess advantageous photophysical properties: they have high quantum yields (up until 0.8 – 0.9), especially in the visible range, possess high stability and they are biologically compatible, the latter property being particularly important for bio-sensing applications. Besides this, and due to their photophysical properties, coumarin derivatives have been used in different fields such as OLEDs, optical data storage, laser dyes, among others [190] [191].

Interestingly, coumarin in its basic structure is actually a weak fluorophore with low quantum yield. It is in fact the introduction of electron withdrawing groups at the 3 position and electron donating groups at the 7 position (marked in Figure 46), making the coumarin moiety act as a π-bridge entity, that enables all its interesting luminescent properties [192]. Moreover, the luminescence of coumarin derivatives is also influenced by the solvent medium and its pH [193].

Thus, taking advantage of the convenient properties of coumarins as fluorescence molecules, and particularly, the carbonyl group present in its chemical structure (which use will be described next), the **M7** compound bearing this unit was designed.

2.1.3.2 Design of M7

The new molecule **M7** was designed as a julolidine-fused coumarin coupled with an oxime group, as can be seen in Figure 47. Its design includes a strong electron-donating amino group linked with the coumarin fluorophore (seen in red) at the 7 position and an electron-withdrawing oxime unit at the 3 position, following what is described in Section 2.1.3.1 to enhance the photophysical properties of the ligand. In particular, the amino group introduced at the 7 position is rigidized in between two rings, which further increases its quantum yield and prevents quenching of the emission by radiationless relaxation mechanisms [192] [194]. For its part, the inclusion of the oxime group was initially inspired by our work with **M4**, which gave rise to a simple question: what would be the difference in sensitivity and stability of the ligand-metal interaction if a carbonyl

replaces the hydroxyphenyl group of **M4**, while maintaining an oxime in the *ortho* position? This will be investigated in Section 4.3.

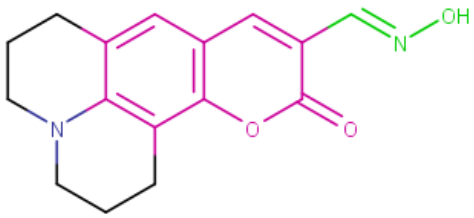

Figure 47. Chemical structure of **M7**.

Finally, as has been thoroughly discussed in section 2.1.2.2, and in particular by the results obtained by García-Beltrán [195], it can also be expected that **M7** could be sensitive towards OCl^-.

2.1.3.3 Synthetic approach for M7

The synthesis of coumarins is a very rich and extensive research topic. In general terms, their base structure can be obtained from simple commercially available starting materials (like benzaldehydes and phenols) using well-established methods with the Perkin reaction, Knoevenagel and Pechmann condensations being the most popular [196]. As with previous fluorophore families, new fancy methods that utilize metals as catalysts, and microwave or ultrasound techniques have been developed in recent years. Importantly, further derivatizations of the base coumarin structure usually occur at the 3 or 4 position, as the double bond located in between is highly reactive [194].

For the synthesis of **M7**, needless to say, the first step involves obtaining the julolidine-fused coumarin entity, followed by a formylation at the 3 position using the well-known Vilsmeier-Haack reaction to obtain an aldehyde [197]. This aldehyde compound has already been reported in the literature, so the procedure described by Jung was chosen to be used due to its simplicity [198], albeit with slight modifications that originate from empirical observations. In essence, the applied procedure included three synthetic steps: the first one was the Knoevenagel condensation of the julolidine benzaldehyde with diethyl malonate in presence of piperidine to obtain the coumarin moiety; then, the second one involved the hydrolysis and posterior decarboxylation of the coumarin with HCl and AcOH at high temperature to make its 3 position available; and finally, the last step accounted for the formylation at this same 3 position with the Vilsmeier reagent formed by the reaction of $POCl_3$ and DMF to obtain the desired product. To complete the

synthesis of **M7**, the oxime formation from the synthesized aldehyde was carried out mirroring the final step of the procedure used to synthesize **M4** [174].

The complete synthetic scheme for the obtention of **M7** can be seen in Figure 48 and the detailed synthetic steps in Sections 2.1.3.3.1 to 2.1.3.3.4.

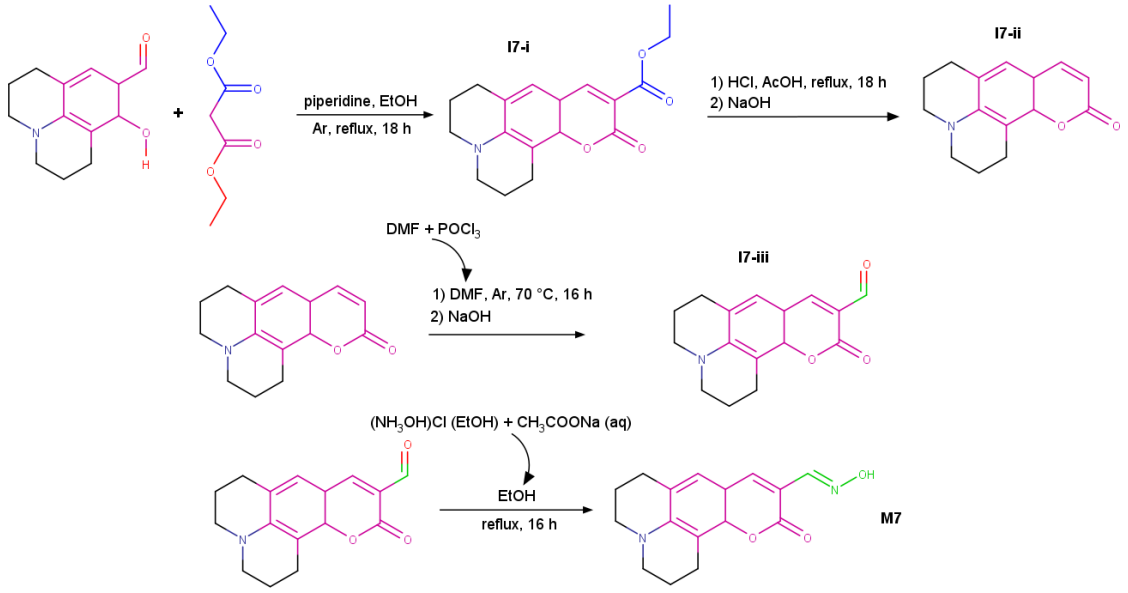

Figure 48. Synthetic scheme for obtaining **M7**.

2.1.3.3.1 Synthesis of I7-i

In a 25 mL round-bottom flask, under argon atmosphere, 217.3 (1 mmol) of 2,3,6,7-tetrahydro-8-hydroxy-1H,5H-benzo[ij]quinolizine-9-carboxaldehyde are dissolved in 10 mL of absolute ethanol. Then, 305.1 μL (2 mmol) of diethylmalonate are added to the solution along with 0.1 mL of piperidine. After 5 minutes of stirring, the temperature is raised until reflux conditions and the reaction is constantly monitored by TLC until the disappearance of the starting aldehyde spot. After 18 h, the mixture is cooled, the solvent is evaporated and the crude mixture is column chromatographed using hexane : EA 4 : 1 to obtain **I7-i** as a bright yellow powder. ^{1}H-NMR ($CDCl_3$, 300 MHz): δ (ppm) 8.32 (s, H1), 6.93 (s, H2), 4.35 (q, 2H9), 3.32 (q, 2H5 and 2H6), 2.87 – 2.75 (2t, 2H4 and 2H7), 1.96 (m, 2H 3 and 2H8), 1.38 (t, 3H10). Yield: 280.7 mg (89 %). The chemical structure of **I7-i** with its assigned protons can be seen in Figure 49.

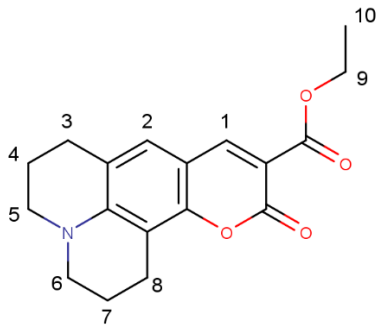

Figure 49. Chemical structure of **I7-i**.

2.1.3.3.2 Synthesis of I7-ii

In a 10 mL round-bottom flask, 315.4 mg (1 mmol) of **I7-i** is treated with 2 mL of HCl_{cc} and 2 mL of AcOH at reflux conditions for 18 h. Afterwards, the mixture is cooled down, poured into H_2O/ice and neutralized with an aqueous solution of NaOH 40 % w/w until pH 5 – 6. The formed precipitate is extracted with ethyl acetate, dried over Na_2SO_4 and column chromatographed using hexane : EA 4 : 1 to obtain **I7-ii** as a bright yellow reddish powder. ^{1}H-NMR ($CDCl_3$, 300 MHz): δ (ppm) 7.45 (d, H11), 6.84 (s, H2), 5.99 (d, H1), 3.25 (q, 2H5 and 2H6), 2.88 – 2.75 (2t, 2H4 and 2H6), 1.96 (m, 2H3 and 2H8). Yield: 133.8 mg (55 %). The chemical structure of **I7-ii** with its assigned protons can be seen in Figure 50.

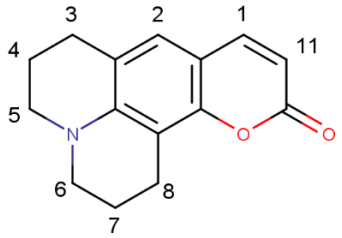

Figure 50. Chemical structure of **I7-ii**.

2.1.3.3.3 Synthesis of I7-iii

In a 10 mL round bottom flask, under an argon atmosphere, 2 mL of dry DMF are added dropwise to 2 mL of $POCl_3$. The solution is stirred at 60 °C until the color turns scarlet red and acquires a viscous consistency. At this point, 0.3 mL of this newly formed Vilsmeier reagent are transferred into a separate 5 mL round-bottom flask containing 121.5 mg (0.5 mmol) of **I7-ii** dissolved in 2 mL of dry DMF. The mixture is stirred for 16

h at 70 °C, at the end of which it is cooled down and poured into H_2O/ice. Then, the pH is adjusted to 5 using an aqueous solution of NaOH 40 % w/w, the formed solid is extracted with ethyl acetate, dried over Na_2SO_4 and column chromatographed using hexane : EA 4 : 1 to obtain **I7iii** as an orange powder. ^{1}H-NMR ($CDCl_3$, 300 MHz): *δ* (ppm) 11.11 (s, H12), 8.15 (s, H1), 6.99 (s, H2), 3.37 (q, 2H5 and 2H6), 2.89 – 2.73 (2t, 2H4 and 2H7), 1.98 (m, 2H3 and 2H8). Yield: 101.7 mg (75 %). The chemical structure of **I7-iii** with its assigned protons can be seen in Figure 51.

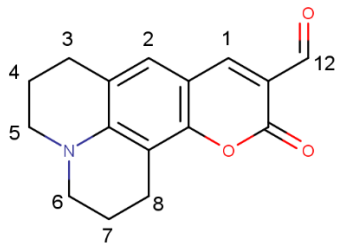

Figure 51. Chemical structure of **I7-iii**.

2.1.3.3.4 Synthesis of M7

In a 10 mL round-bottom flask, 36.5 mg (0.136 mmol) of **I7-iii** is dissolved in 3 mL of EtOH at 50 °C. Separately, 11.3 mg (0.162 mmol) of $(NH_3OH)Cl$ is dissolved in 1 mL of EtOH with subsequent addition of 1 mL of an aqueous solution containing 16.6 mg (0.203 mmol) of CH_3COONa. The later solution is added to the former one and the reaction mixture is left stirring for 16 h at reflux conditions. The deep orange precipitate, **M7**, is collected, washed with cold EtOH and hexane, and dried under reduced pressure. ^{1}H-NMR (DMSO-d_6, 300 MHz, Figure 71): *δ* (ppm) 11.21 (s, Ha), 8.01 (s, H13), 7.95 (s, H1), 7.11 (s, H2), 3.27 (m, 2H5 and 2H6), 2.70 (q, 2H4 and 2H7), 1.86 (m, 2H3 and 2H8). ^{13}C-NMR (DMSO-d_6, 75 MHz): *δ* (ppm) 161.52, 152.34, 147.62, 127.31, 119.93, 111.54, 108.79, 106.44, 28.02, 21.96, 21.05. Yield: 27.1 mg (70 %).

2.1.4 Porphyrin-based chemosensors: M8-Pd, M8-Pt, M9-Pd and M9-Pt

2.1.4.1 General design

Porphyrins and metalloporphyrins are macrocyclic compounds that have been the subject of thorough studies in the last century because they are readily available in nature, for example, as iron complexes (as the well-known heme group inside

hemoglobin), magnesium complexes (as in chlorophyll) or cobalt complexes (as in vitamin B_{12}). Thus, they play a vital role in highly important biological processes such as photosynthesis, and O_2 transport and storage.

As can be seen in Figure 52, the porphyrin molecule contains four pyrrole rings bonded together by four methylene bridges, forming a highly stable ring that exhibits aromatic character with 18 e^-. Its central core is a tetradentate ligand that can coordinate a metal ion with a maximum diameter of 3,7 Å, forming very stable complexes with high stability constants [199] [200].

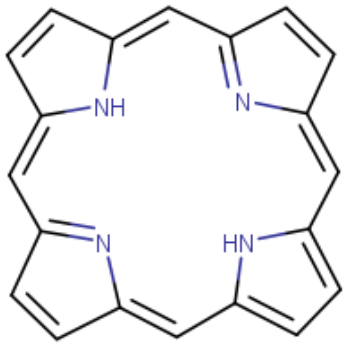

Figure 52. Basic structure of the porphyrin macrocycle.

Almost all known metalloporphyrins are 1 : 1 complexes in which the metal ion is coplanar with the macrocycle. The only exceptions with common metal cations are the Na, K and Li complexes, whose stoichiometry is 2 : 1 because the cations are incorporated in between two macrocyclic planes. Due to the versatility of the porphyrin ligand, several metals have been combined with it in order for the complex to be used in a variety of applications in science materials, biology and medicine, such as being models for biological electron transport, for oxygen transport and for metalloenzymes; in catalysis; in chemical analysis, nonlinear optics, cancer therapy, and nanomaterials [199] [200] [201].

Porphyrins and its metallocomplexes are highly sensitive chromogenic compounds, as they often show a characteristic sharp and intensive absorption band in the 400 – 500 nm range of the visible region, called the Soret band which has a molar absorptivity in the order of 10^5. Furthermore, metalloporphyrins have a rich redox chemistry as the metal ion is able to coordinate additional ligands above and below the porphyrin plane as in the case of the reduction of CO_2 seen in Figure 53 [202]. These two features, in addition to those already mentioned in the above paragraphs, allow porphyrin complexes

to be used as effective chemosensors for the detection of analytes in both gaseous and liquid phases [47] [200].

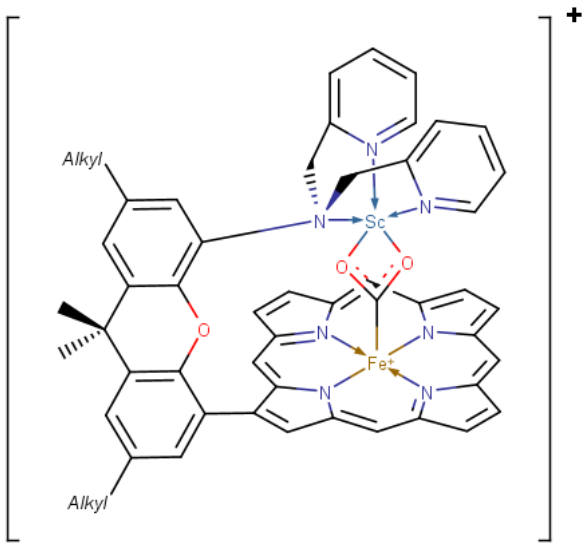

Figure 53. Example of coordination of additional ligands above the metalloporphyrin plane for the reduction of CO_2 [202].

In particular, mimicking the heme-type compounds found in nature, it was decided to use metalloporphyrins as potential oxygen sensors. Thereafter, platinum(II) and palladium(II) were chosen as the metal centers due to them providing the best luminescent properties for oxygen sensing: strong phosphorescence at room temperature, moderate to high molar absorption coefficients, large Stoke's shifts and excellent oxygen quenching constants [49] [203] [204] [205]. Needless to say, the fluorescence detection of dioxygen by platinum(II) and palladium(II) porphyrin derivatives has been achieved in the past, both in air [206] [207] [208] [209] [210] and solution [211] [212] [213] [214], the former being the most researched topic between the two. Hence, there is a desire in our research group for the development of new molecules that could achieve this detection in solution, and particularly in aqueous medium.

Moreover, as mentioned in Section 1.3 and in the same fashion as with pyrene derivatives, other members of our research group had begun studying the possibility of functionalizing porphyrin derivatives into single and multi-walled carbon nanotubes inspired by reports like those of Liu or Maligaspe [102] [103].

Thus, to comply with all these needs, two porphyrin derivatives were designed: **M8** and **M9**, which could be then metalated with platinum(II) or palladium(II) to obtain optical oxygen sensors.

2.1.4.2 Design of M8-Pd, M8-Pt, M9-Pd and M9-Pt

The design of the two porphyrin ligands comprises a porphyrin ring substituted in its *meso* position by a phenyl group, which in turn is substituted, in *para* for **M8-M** and in *meta* for **M9-M** by ether chains, as can be seen in Figure 54.

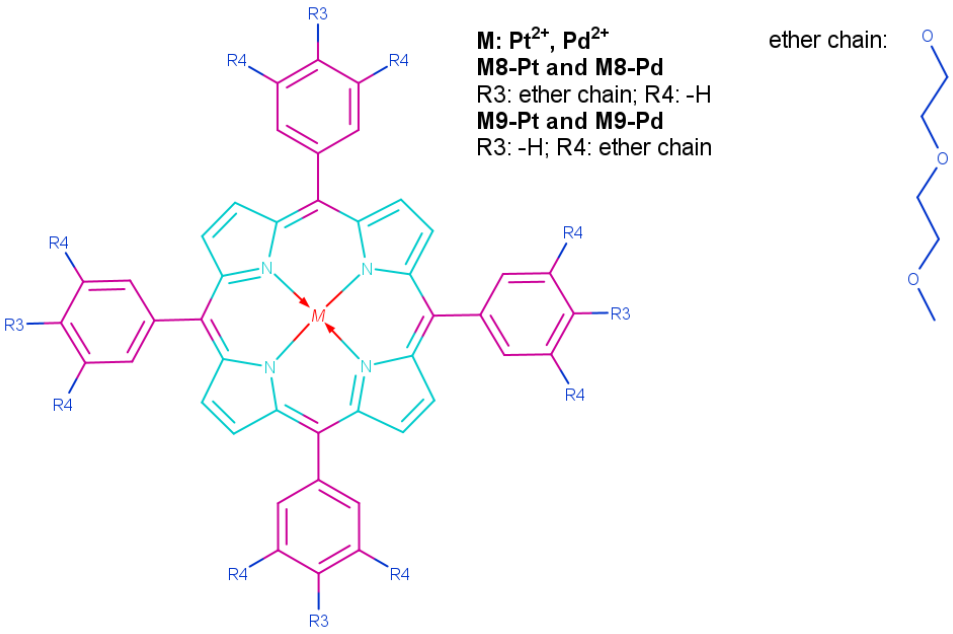

Figure 54. Chemical structures of **M8-Pd**, **M8-Pt**, **M9-Pd** and **M9-Pt**.

The introduction of ether chains into the molecular architecture of the porphyrin derivatives was made with the rationale of improving their affinity with water medium. Considering the possibility of functionalizing carbonaceous material with these molecules, it was then thought that the hydrophilic ether chains could enhance the contact of the immobilized porphyrins with the dissolved analyte in a way that better responses could be obtained.

2.1.4.3 Synthetic approach for M8 and M9

The synthesis of porphyrins is one of the richest research topics in organic synthesis, accounting for thousands of publications, books, handbooks and laboratory methods [199] [215]. The method of choice for performing this synthesis depends upon the

symmetry of the desired product, the easiest ones being applied for completely symmetric porphyrins, such as **M8** and **M9**, for which there are basically three methods: the Rothemund method, the Adler-Longo method and the Lindsey method [199].

The Rothemund method, developed in 1935 for the synthesis of 5,10,15,20-tetraphenylporphyrin, consists on a sealed tube reaction of pyrrole with benzaldehyde under acidic conditions [199]. Later, this method was improved by Adler and Longo, who switched away from high pressure chemistry and instead used refluxing propionic acid to achieve higher yields of porphyrin [216]. It was not until 1987, however, that porphyrin synthesis was completely optimized by Lindsey, whose method involved a two-step reaction in very diluted conditions. In the first step of this method, the corresponding pyrrole and aldehyde are mixed in equimolar conditions in the presence of a Lewis acid such as the boron trifluoride diethyl etherate adduct (BF_3.OEt) to obtain a mixture of porphyrinogen compounds. Then, these intermediates are oxidized by a quinone such as DDQ or p-chloranil to obtain the final porphyrin in a much cleaner way and with even higher yields than in previous methods [217]. A schematic representation of these three methods can be seen in Figure 55. In the present case, the Lindsay method was chosen to synthesize the macrocycle using pyrrole and a benzaldehyde derivative as starting materials.

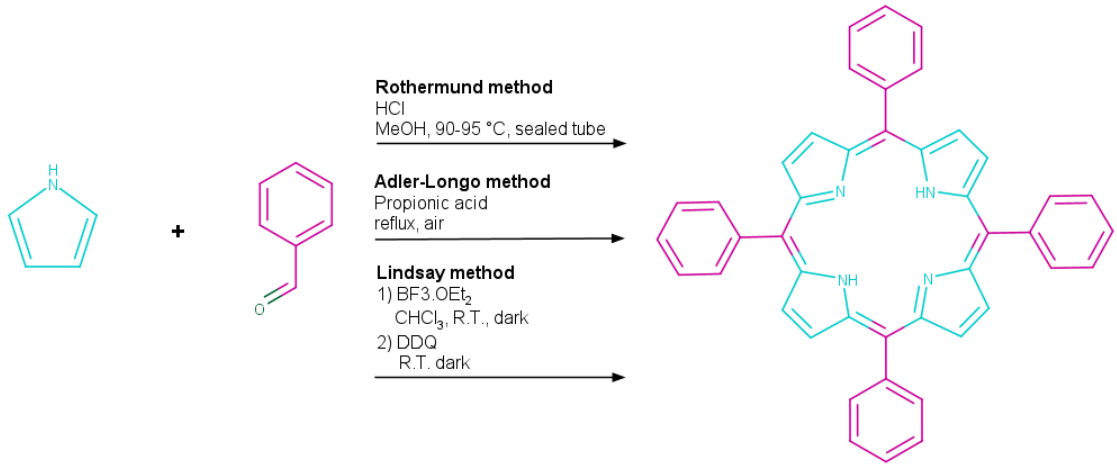

Figure 55. Basic synthetic schemes for the three classic methods for porphyrin synthesis

As for the inclusion of the ether chains, it was easily noticed that a C-O cross-coupling reaction needed to be used. In this regard, the two classic synthetic possibilities were the Ullmann ether synthesis reaction or the Buchwald-Hartwig cross-coupling reaction. These two cross-coupling reactions are similar to the already explained Suzuki cross-

coupling (Section 2.1.1.6), the difference being that they involve an heterogenous coupling in which they link together two different atoms, a carbon and an oxygen in this case, in presence of a copper(II) (for Ullmann ether synthesis) or a palladium(II) (for Buchwald-Hartwig reaction) catalyst [218].

These two reactions have their own benefits and disadvantages. In fact, due to the increased use and availability of palladium catalysts owing to developments in the Suzuki cross-coupling reaction, this family of catalysts is displacing copper in its classic role in C-O couplings [219] [220]. However, Cu(II) remains much cheaper and thus, looking for the most cost-efficient way to connect the ether chains to the phenyl entity, the Ullmann ether synthesis was chosen as the coupling reaction for the obtention of **M8** and **M9**.

In essence, the Ullmann ether synthesis occurs between an aryl halide and a nucleophile (an amine or alcohol, either alkyl or aryl). While its mechanism is not fully understood yet, it is believed that when the nucleophile is an alcohol, in a first step, it is activated with a base and is subsequently complexed into the copper cation *via* its oxygen atom. Then, there is an oxidative addition of the aryl halide into Cu, followed by a reductive elimination that yields the C-O coupled product [221]. There are several reported methods for carrying out an Ullmann ether synthesis reaction particularly for the case of an aryl halide coupled with alkyl alcohols, which vary depending on the Cu catalyst, the base, the presence of ligands, the solvent medium and the experimental conditions [222] [223] [224] [225] [226]. After some exploratory trials with simpler molecules, namely the coupling of bromobenzene with 2-(2-methoxyethoxy)ethanol, the report of Huang [225] using CuI as catalyst and lithium *tert*-butoxide as base was chosen for carrying out the C-O coupling of the ether chains with the corresponding bromobenzaldehydes.

Then, the order of the reactions needed to be sorted out, as the first step for the obtention of **M8** and **M9** could be either the porphyrin synthesis or the Ullmann ether synthesis. If the first step was the porphyrin synthesis, that meant that there should be four (for **M8**) or eight (for **M9**) C-O couplings per molecule in the second step. Thus, it was predicted that if the efficiency of the coupling did not reach 100 %, the resulting mixture was going to be extremely difficult to purify. It was then decided to carry out the cross-coupling in the first step and finish the synthesis with the porphyrin preparation.

However, it was experimentally observed that the bromobenzaldehydes did not resist the experimental conditions of an Ullmann ether synthesis, hence aldehyde protection [227] and deprotection [228] steps were introduced to mitigate this problem. A schematic pathway to obtain **M8** and **M9** can be seen in Figure 56, while the complete experimental

procedure is found in Sections 2.1.4.3.1 to 2.1.4.3.8. The synthesis of the corresponding Pt(II) and Pd(II) complexes will be discussed in Section 2.1.4.4.

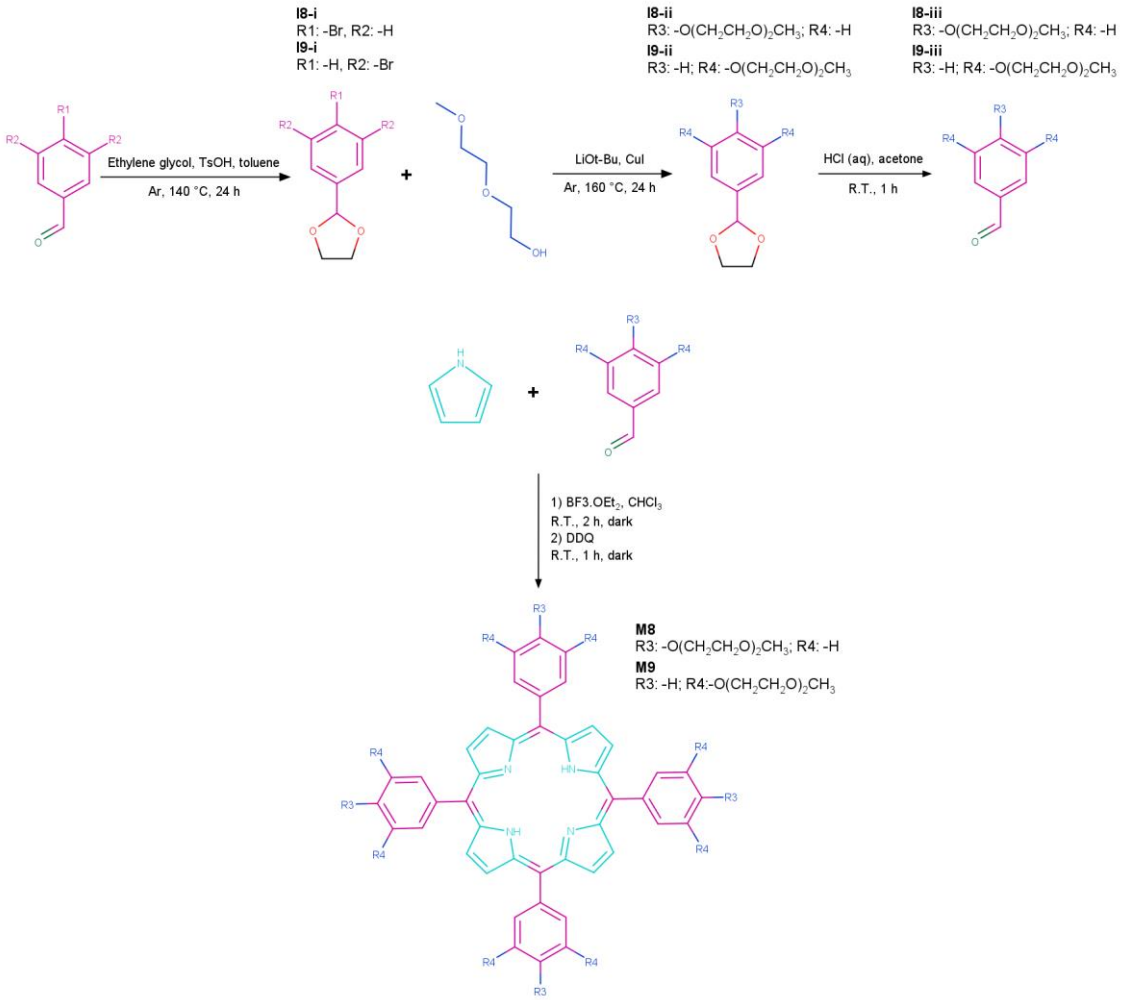

Figure 56. Synthetic scheme for **M8** and **M9**.

2.1.4.3.1 Synthesis of I8-i

In a 250 mL round-bottom flask mounted with a Dean-Stark apparatus, 4.63 g (25 mmol) of 4-bromobenzaldehyde and a catalytic amount of *p*-toluenesulfonic acid are dissolved with 100 mL of toluene under argon. Then, 2.80 mL (50 mmol) of ethylene glycol are added to the mixture and the reactant medium is refluxed. After 24 h, the mixture is cooled, toluene is evaporated and the crude residue is column chromatographed using hexane : $CHCl_3$ in a gradient from 1 : 0 to 3 : 2 to obtain a white solid of low melting point. ^{1}H-NMR ($CDCl_3$, 300 MHz): δ (ppm) 7.51 (d, 2H2), 7.35 (d, 2H1), 5.76 (s, H3), 4.06 (m, 4H4). Yield: 5.21 g (91 %). The chemical structure of **I8-i** with its assigned protons can be seen in Figure 57.

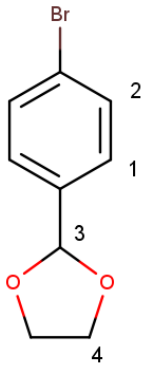

Figure 57. Chemical structure of **I8-i**.

2.1.4.3.2 Synthesis of I8-ii

In a 50 mL round-bottom flask, 3.6 g (45 mmol) of lithium tert-butoxide is treated with 15 mL of 2-(2-methoxyethoxy)ethanol under argon. After solubilization of the salt, 3.43 g (15 mmol) of **I8-i** and 285 mg (1.5 mmol) of copper iodide are added and the reaction mixture is refluxed for 24 h. The mixture is then cooled, the remaining alcohol is evaporated under vacuum distillation, the crude product is extracted with chloroform, dried under Na_2SO_4 and column chromatographed using hexane : EA in a gradient from 4 : 1 to 3 : 2 to obtain a white yellowish solid of low melting point. ^{1}H-NMR ($CDCl_3$, 300 MHz): δ (ppm) 7.38 (d, 2H1), 6.91 (d, 2H2), 5.74 (s, H3), 4.13 (m, 4H4), 4.01 (m, 2H5), 3.85 (t, 2H6), 3.71 (m, 2H7), 3.57 (m, 2H8), 3.38 (s, 3H9). Yield: 2.25 g (56 %). The chemical structure of **I8-ii** with its assigned protons can be seen in Figure 58.

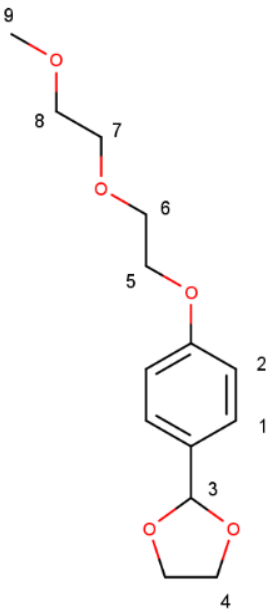

Figure 58. Chemical structure of **I8-ii**.

2.1.4.3.3 Synthesis of I8-iii

A 100 mL round-bottom flask is loaded with 3.13 g (12 mmol) of **I8-ii** and 40 mL of acetone. Then, 36 mL of a 1 mol/L aqueous solution of HCl (36 mmol) are added and the reaction mixture is stirred at room temperature. After 1 h, the product is extracted with ethyl acetate, dried over Na_2SO_4 and the solvents are removed to obtain a yellowish solid of low melting point. ^{1}H-NMR ($CDCl_3$, 300 MHz): δ (ppm) 9.88 (s, H10), 7.83 (d, 2H1), 7.01 (d, 2H2), 4.23 (t, 2H5), 3.89 (t, 2H6), 3.73 (t, 2H7), 3.58 (t, 2H8), 3.39 (s, 3H9). Yield: 2.66 g (99 %). The chemical structure of **I8-iii** with its assigned protons can be seen in Figure 59.

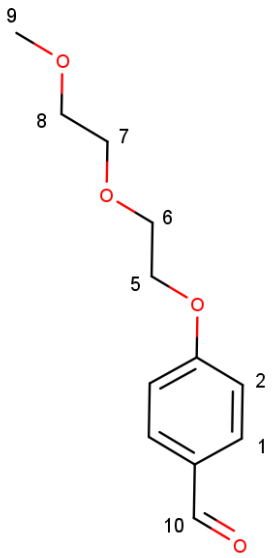

Figure 59. Chemical structure of **I8-iii**.

2.1.4.3.4 Synthesis of M8

In a 1 L round-bottom flask covered with aluminum foil, 1.12 g (5 mmol) of **I8-iii** are dissolved in 500 mL of degassed dry chloroform under argon. After 5 minutes of bubbling with argon, 0.35 mL (5 mmol) of freshly distilled 1H-pyrrole are added. The solution is bubbled with argon for 15 more minutes, and then 0.2 mL (1.5 mmol) of boron trifluoride etherate are added. After bubbling with argon for 5 more minutes, the system is closed and vigorously stirred at room temperature for 2 h. Then, and under constant argon bubbling, 0.85 g (3.75 mmol) of 2,3-dichloro-5,6-dicyano-1,4-benzoquinone are added and the reaction mixture is stirred for an additional hour. Subsequently, the solvent is evaporated and the resulting black solid is washed with methanol to yield a purple solid mixture which is finally solid packed into a chromatographic column and eluted with $CHCl_3$: MeOH in a gradient from 1 : 0 to 99 : 1 to isolate **M8** as a bright purple solid. ^{1}H-NMR ($CDCl_3$, 300 MHz, Figure 72): δ (ppm) 8.84 (s, 8H11), 8.10 (d, 8H1), 7.29 (d, 8H2), 4.45 (t, 8H5), 4.07 (t, 8H6), 3.87 (t, 8H7), 3.69 (t, 8H8), 3.47 (s, 12H9), -2.79 (s, 2Ha). ^{13}C-NMR ($CDCl_3$, 75 MHz): δ (ppm) 159.38, 136.29, 135.59, 120.46, 113.62, 72.84, 71.67, 70.73, 68.49, 59.92. Yield: 258.2 mg (19 %).

2.1.4.3.5 Synthesis of I9-i

In a 100 mL round-bottom flask mounted with a Dean-Stark apparatus, 2.64 g (10 mmol) of 3,5-dibromobenzaldehyde and a catalytic amount of *p*-toluenesulfonic acid are dissolved with 70 mL of toluene under argon. Then, 1.12 mL (20 mmol) of ethylene glycol

are added to the mixture and the reactant medium is refluxed. After 24 h, the mixture is cooled, toluene is evaporated and the crude residue is column chromatographed using hexane : $CHCl_3$ in a gradient from 1 : 0 to 2 : 3 to obtain a white solid of low melting point. ^{1}H-NMR ($CDCl_3$, 300 MHz): δ (ppm) 7.65 (s, H1), 7.55 (s, 2H2), 5.75 (s, H3), 4.05 (m, 4H4). Yield: 2.86 g (93 %). The chemical structure of **I9-i** with its assigned protons can be seen in Figure 60.

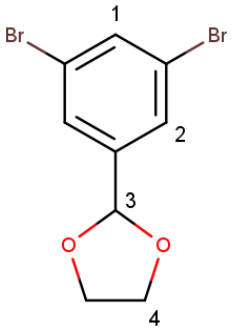

Figure 60. Chemical structure of **I9-i**.

2.1.4.3.6 Synthesis of I9-ii

In a 50 mL round-bottom flask, 4.80 g (60 mmol) of lithium tert-butoxide is treated with 20 mL of 2-(2-methoxyethoxy)ethanol under argon. After solubilization of the salt, 3.08 g (10 mmol) of **I9-i** and 380.9 mg (2 mmol) of copper iodide are added and the reaction mixture is refluxed for 24 h. After this time, the mixture is cooled, the remaining alcohol is evaporated under vacuum distillation, the crude product is extracted with chloroform, dried under Na_2SO_4 and column chromatographed using hexane : EA in a gradient from 4 : 1 to 3 : 2 to obtain a yellowish dense liquid. ^{1}H-NMR ($CDCl_3$, 300 MHz): δ (ppm) 6.63 (t, 2H2), 6.47 (d, H1), 5.73 (s, H3), 4.11 (t, 2H5), 4.03 (m, 4H3), 3.83 (t, 2H6), 3.70 (t, 2H7), 3.56 (t, 2H8), 3.38 (s, 3H9). Yield: 1.31 g (34 %). The chemical structure of **I9-ii** with its assigned protons can be seen in Figure 61.

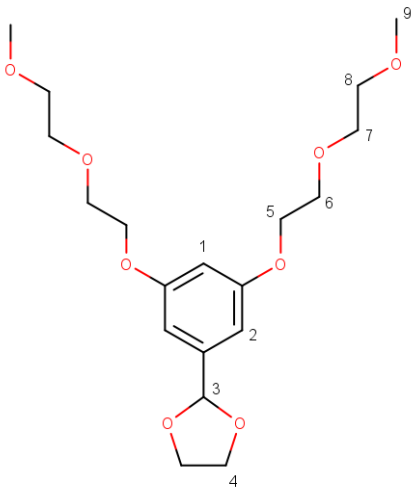

Figure 61. Chemical structure of **I9-ii**.

2.1.4.3.7 Synthesis of I9-iii

A 25 mL round-bottom flask is loaded with 1.55 g (4 mmol) of **I9-ii** and 25 mL of acetone. Then, 12 mL of a 1 mol/L aqueous solution of HCl (12 mmol) are added and the reaction mixture is stirred at room temperature. After 1 h, the product is extracted with ethyl acetate, dried over Na_2SO_4 and the solvents are removed to obtain a yellowish dense liquid. ^{1}H-NMR ($CDCl_3$, 300 MHz): δ (ppm) 9.87 (s, H10), 7.01 (t, 2H2), 6.75 (d, H1), 4.16 (t, 2H5), 3.86 (t, 2H6), 3.71 (t, 2H7), 3.57 (t, 2H8), 3.38 (s, 3H9). Yield: 1.36 g (99 %). The chemical structure of **I9-iii** with its assigned protons can be seen in Figure 62.

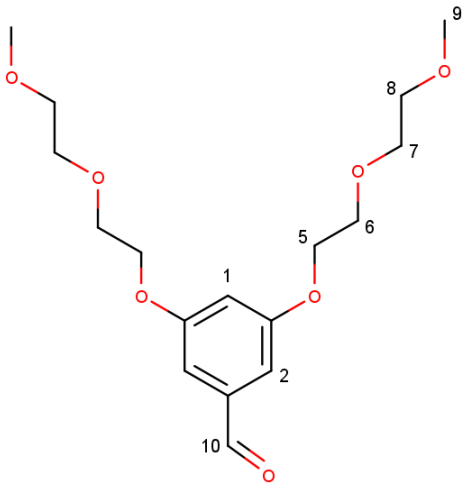

Figure 62. Chemical structure of **I9-iii**.

2.1.4.3.8 Synthesis of M9

In a 500 mL round-bottom flask covered with aluminum, 649 mg (2 mmol) of **I9-iii** are dissolved in 200 mL of degassed dry chloroform under argon. After 5 minutes of bubbling with argon, 0.14 mL (2 mmol) of freshly distilled 1H-pyrrole are added. The solution is bubbled with argon for 15 more minutes, and then 0.08 mL (0.6 mmol) of boron trifluoride etherate are added. After bubbling with argon for 5 more minutes, the system is closed and vigorously stirred at room temperature for 3 h. Then, and under constant argon bubbling, 0.34 g (1.5 mmol) of 2,3-dichloro-5,6-dicyano-1,4-benzoquinone are added and the reaction mixture is stirred for an additional hour. Subsequently, the solvent is evaporated and the resulting black solid is solid packed and column chromatographed with $CHCl_3$: MeOH 19 : 1. The thick purple band is collected and is again solid packed into a chromatographic column and eluted with a very slow gradient of $CHCl_3$: MeOH from 1 : 0 to 197 : 3 to isolate **M9** as a bright purple jelly-like liquid. ^{1}H-NMR ($CDCl_3$, 400 MHz, Figure 73): δ (ppm) 8.91 (s, 8H11), 7.41 (d, 8H1), 6.96 (t, 4H2), 4.33 (t, 16H5), 3.96 (t, 16H6), 3.77 (m, 16H7), 3.61 (m, 16H8), 3.39 (s, 24H9), -2.88 (s, 2Ha). ^{13}C-NMR ($CDCl_3$, 100 MHz): δ (ppm) 157.94, 143.87, 114.67, 71.96, 70.82, 69.84, 67.75, 59.11. Yield: 101.4 mg (13%).

2.1.4.4 Synthetic approach for M8-Pd, Pt and M9-Pd, Pt

Synthesis of metalloporphyrins can be generally achieved by mixing equimolar amounts of the free base with the corresponding metal acetate or chloride salt in refluxing dry DMF, although in some particular cases a small excess of the metal should be used to completely push the reaction to completion [229]. This direct method was chosen for the synthesis of the **M8-Pd** and **M9-Pd** complexes.

There are few exceptions to the described general synthesis of metalloporphyrins and one of them is for the obtention of platinum(II) porphyrins. Due to the bigger size of the platinum(II) cation, there is the need for more energy in the form of temperature so that it can enter the porphyrin central cavity. Thus, a solvent with higher boiling point than DMF should be used and the typical choice is benzonitrile. The synthesis then proceeds in a similar way: an excess of platinum(II) chloride or acetate mixed with the porphyrin in refluxing dry PhCN yields the corresponding complex [230] [231]. This is the method that was chosen for obtaining **M8-Pt** and **M9-Pt**.

The schemes for the synthesis of the palladium(II) and platinum(II) porphyrin complexes can be seen in Figure 63, and in Figure 64, respectively. The complete procedures for these syntheses are described in Sections 2.1.4.4.1 to 2.1.4.4.4.

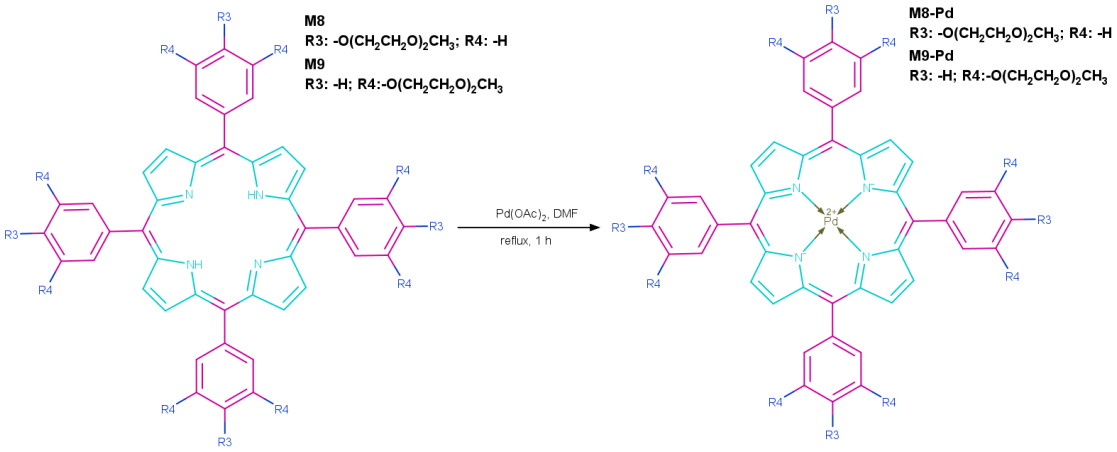

Figure 63. Synthetic scheme for the obtention of **M8-Pd** and **M9-Pd**.

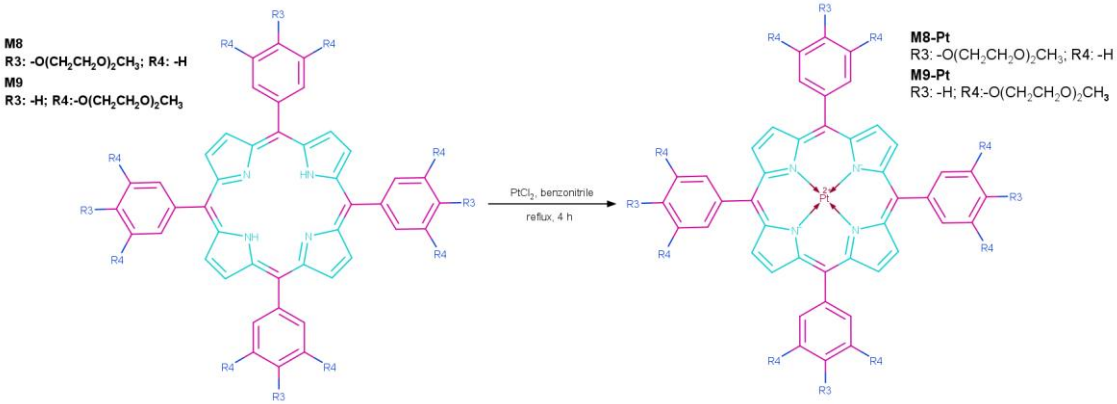

Figure 64. Synthetic scheme for the obtention of **M8-Pt** and **M9-Pt**.

2.1.4.4.1 Synthesis of M8-Pd

In a 10 mL round-bottom flask, 50 mg (0.046 mmol) of **M8** are dissolved in 3 mL of dry DMF under argon at 80 °C. In a separate 10 mL round-bottom flask, 20.7 mg (0.09 mmol) of palladium(II) acetate are dissolved in 2 mL of dry DMF under argon at 80 °C. The latter solution is then added dropwise to the former and the temperature is increased to 140 °C. The mixture is vigorously stirred and constantly monitored using UV-vis spectrophotometry until the original Soret band of the porphyrin has completely disappeared. After 15 additional minutes of stirring, the reaction mixture is cooled down,

the solvent is evaporated under vacuum distillation and the crude residue is solid packed and column chromatographed using $CHCl_3$: MeOH in a gradient from 1 : 0 to 99 : 1 to obtain **M8-Pd** as a bright scarlet solid. ^{1}H-NMR ($CDCl_3$, 300 MHz, Figure 74): δ (ppm) 8.82 (s, 8H11), 8.05 (d, 8H1), 7.28 (d, 8H2), 4.44 (t, 8H5), 4.06 (t, 8H6), 3.86 (t, 8H7), 3.69 (t, 8H8), 3.47 (s, 8H9). ^{13}C-NMR ($CDCl_3$, 100 MHz): δ (ppm) 141.85, 135.07, 134.38, 130.89, 121.35, 112.85, 72.08, 70.92, 69.97, 67.69, 59.20. ESI-MS: **M8-Pd** + H^+ (m/z), calculated: 1 191.3941; found: 1 191.3927. Yield: 35.1 mg (64 %).

2.1.4.4.2 Synthesis of M9-Pd

In a 10 mL round-bottom flask, 64 mg (0.04 mmol) of **M9** are dissolved in 3 mL of dry DMF under argon at 80 °C. In a separate 10 mL round-bottom flask, 18.5 mg (0.08 mmol) of palladium(II) acetate are dissolved in 2 mL of dry DMF under argon at 80 °C. The latter solution is then added dropwise to the former and the temperature is increased to 140 °C. The mixture is vigorously stirred and constantly monitored using UV-vis spectrophotometry until the original Soret band of the porphyrin has completely disappeared. After 15 additional minutes of stirring, the reaction mixture is cooled down, the solvent is evaporated under vacuum distillation and the crude residue is solid packed and column chromatographed using $CHCl_3$: MeOH in a gradient from 1 : 0 to 197 : 3 to obtain **M9-Pd** as a bright scarlet jelly-like liquid. ^{1}H-NMR ($CDCl_3$, 400 MHz, Figure 75): δ (ppm) 8.85 (s, 8H11), 7.34 (d, 8H1), 6.93 (t, 4H2), 4.29 (m, 16H5), 3.93 (m, 16H6), 3.75 (m 16H7), 3.59 (m, 16H8), 3.37 (s, 24H9). ^{13}C-NMR ($CDCl_3$, 100 MHz): δ (ppm) 158.00, 141.28, 130.94, 114.16, 71.96, 70.81, 69.84, 67.76, 59.10. ESI-MS: **M9-Pd** + H^+ (m/z), calculated: 1 662.6383; found: 1 662.6341. Yield: 43.3 mg (65 %).

2.1.4.4.3 Synthesis of M8-Pt

In a 10 mL round-bottom flask, 50 mg (0.046 mmol) of **M8** are dissolved in 3 mL of dry benzonitrile under argon at 100 °C. In a separate 10 mL round-bottom flask, 48.9 mg (0.184 mmol) of platinum(II) chloride are dissolved in 2 mL of dry benzonitrile under argon atmosphere at 100 °C. The latter solution is added dropwise to the former and the temperature is increased to 180 °C. The mixture is vigorously stirred and constantly monitored with UV-vis spectrophotometry until the original Soret band of the porphyrin has completely disappeared. After 15 additional minutes of stirring, the reaction mixture is cooled down, the solvent is evaporated under vacuum distillation and the crude residue is solid packed and column chromatographed using $CHCl_3$: MeOH in a gradient from 1 : 0 to 99 : 1 to obtain **M8-Pt** as a bright red solid. ^{1}H-NMR ($CDCl_3$, 400 MHz, Figure 76): δ (ppm) 8.78 (s, 8H11), 8.05 (d, 8H1), 7.28 (d, 8H2), 4.42 (t, 8H5), 4.06 (t, 8H6), 3.88 (m,

8H7), 3.71 (m, 8H8), 3.49 (s, 12H9). ^{13}C-NMR ($CDCl_3$, 100 MHz): δ (ppm) 158.60, 141.12, 134.84, 133.95, 130.62, 121.93, 112.91, 72.07, 70.91, 69.96, 67.66, 59.22. ESI-MS: [**M8-Pt**]$^+$ (m/z), calculated: 1 279.4476; found: 1 279.4487. Yield: 41.8 mg (71 %).

2.1.4.4.4 Synthesis of M9-Pt

In a 10 mL round-bottom flask, 35.4 mg (0.02 mmol) of **M9** are dissolved in 3 mL of dry benzonitrile under argon at 100 °C. In a separate 10 mL round-bottom flask, 24.1 mg (0.09 mmol) of platinum(II) chloride are dissolved in 2 mL of dry benzonitrile under argon at 100 °C. The latter solution is added dropwise to the former and the temperature is increased to 180 °C. The mixture is vigorously stirred and constantly monitored with UV-vis spectrophotometry until the original Soret band of the porphyrin has completely disappeared. After 15 additional minutes of stirring, the reaction mixture is cooled down, the solvent is evaporated under vacuum distillation and the crude residue is solid packed and column chromatographed using $CHCl_3$: MeOH in a gradient from 1 : 0 to 197 : 3 to obtain **M9-Pt** as a bright dark red jelly-like liquid. ^{1}H-NMR ($CDCl_3$, 400 MHz, Figure 77): δ (ppm) 8.82 (s, 8H11), 7.34 (d, 8H1), 6.94 (t, 4H2), 4.31 (m, 16H5), 3.95 (m, 16H6), 3.77 (m, 16H7), 3.61 (m, 16H8), 3.39 (s, 24H9). ^{13}C-NMR ($CDCl_3$, 300 MHz): δ (ppm) 158.09, 143.05, 140.56, 130.66, 121.89, 113.90, 101.50, 71.96, 70.81, 69.83, 67.76, 59.11. ESI-MS: **M9-Pt** + H^+ (m/z), calculated: 1 752.7074; found: 1 752.7084. Yield: 23.1 mg (66 %).

2.2 Chemical characterization of molecules

2.2.1 Characterization of M1

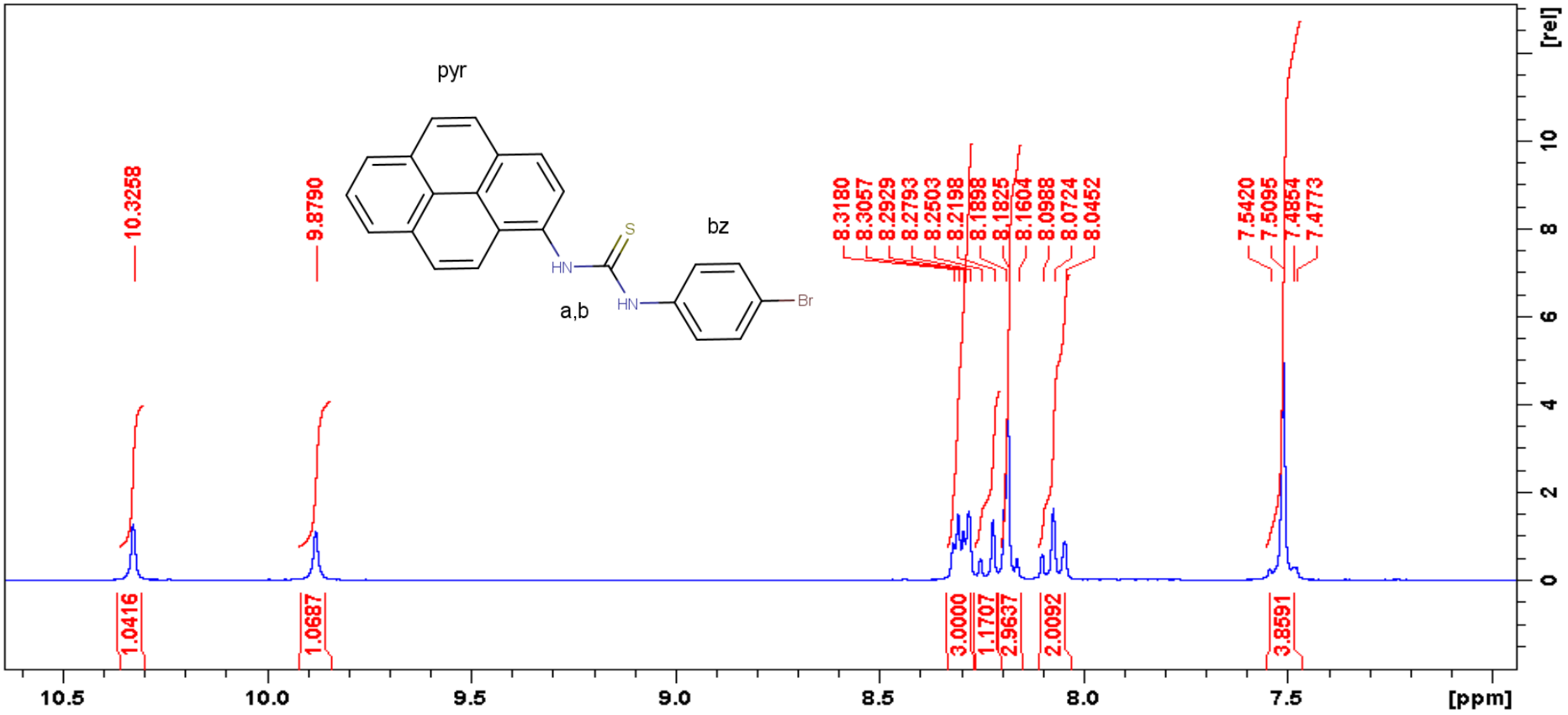

Figure 65. ^{1}H-NMR spectrum (DMSO-d_6, 300 MHz) of **M1**.

2.2.2 Characterization of M2

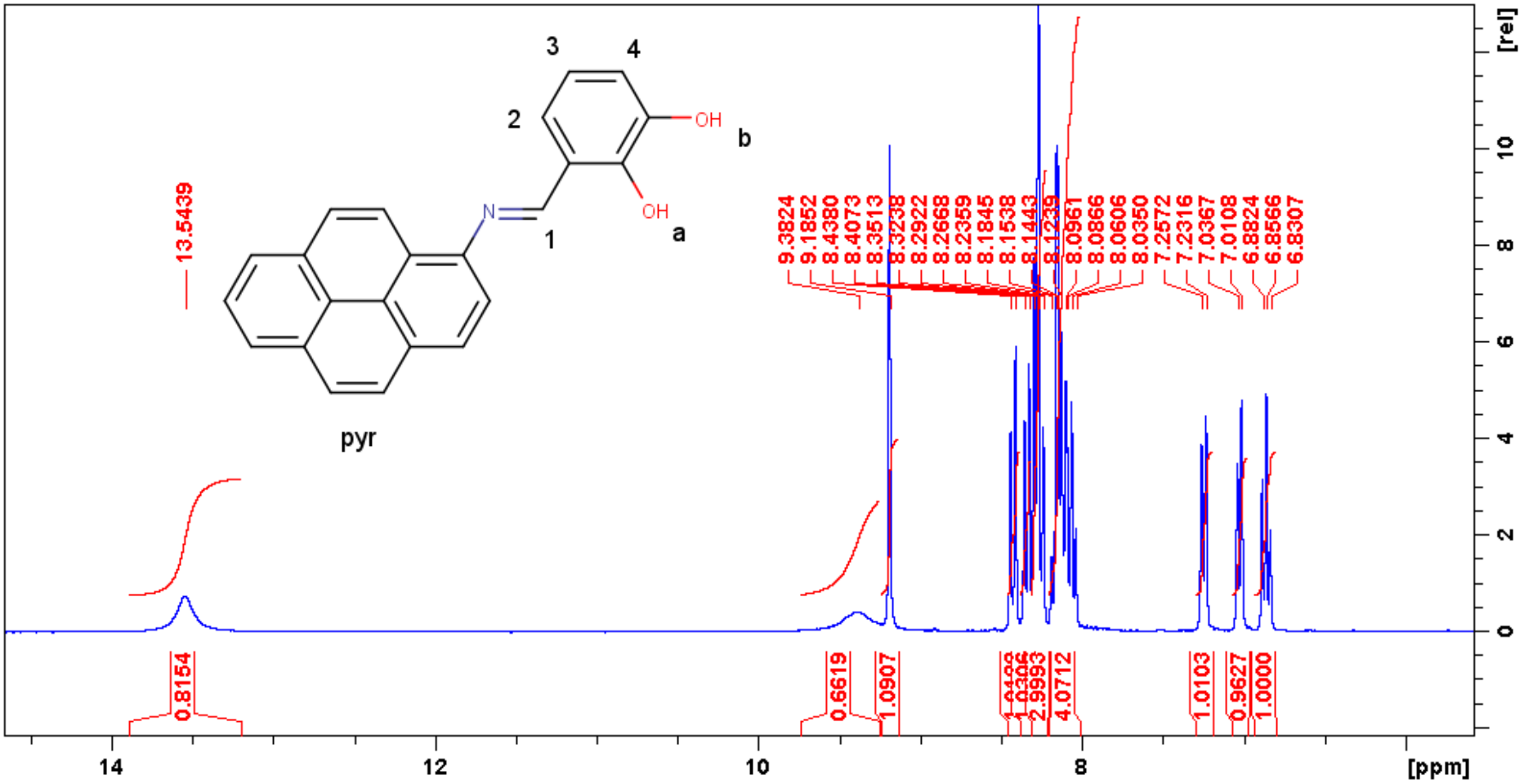

Figure 66. ^{1}H-NMR spectrum (DMSO-d_6, 300 MHz) of **M2**.

2.2.3 Characterization of M3

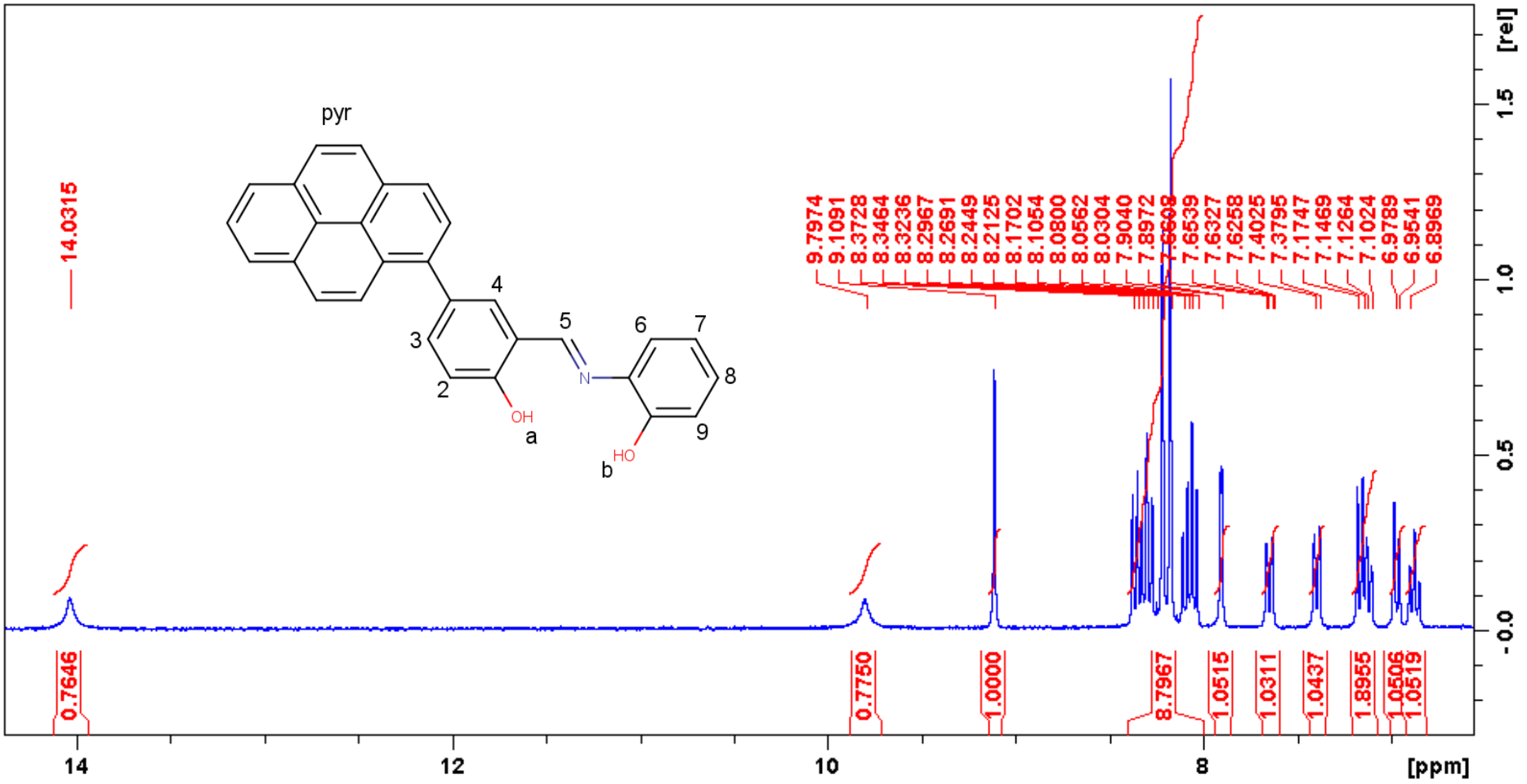

Figure 67. ^{1}H-NMR spectrum (DMSO-d_6, 300 MHz) of **M3**.

2.2.4 Characterization of M4

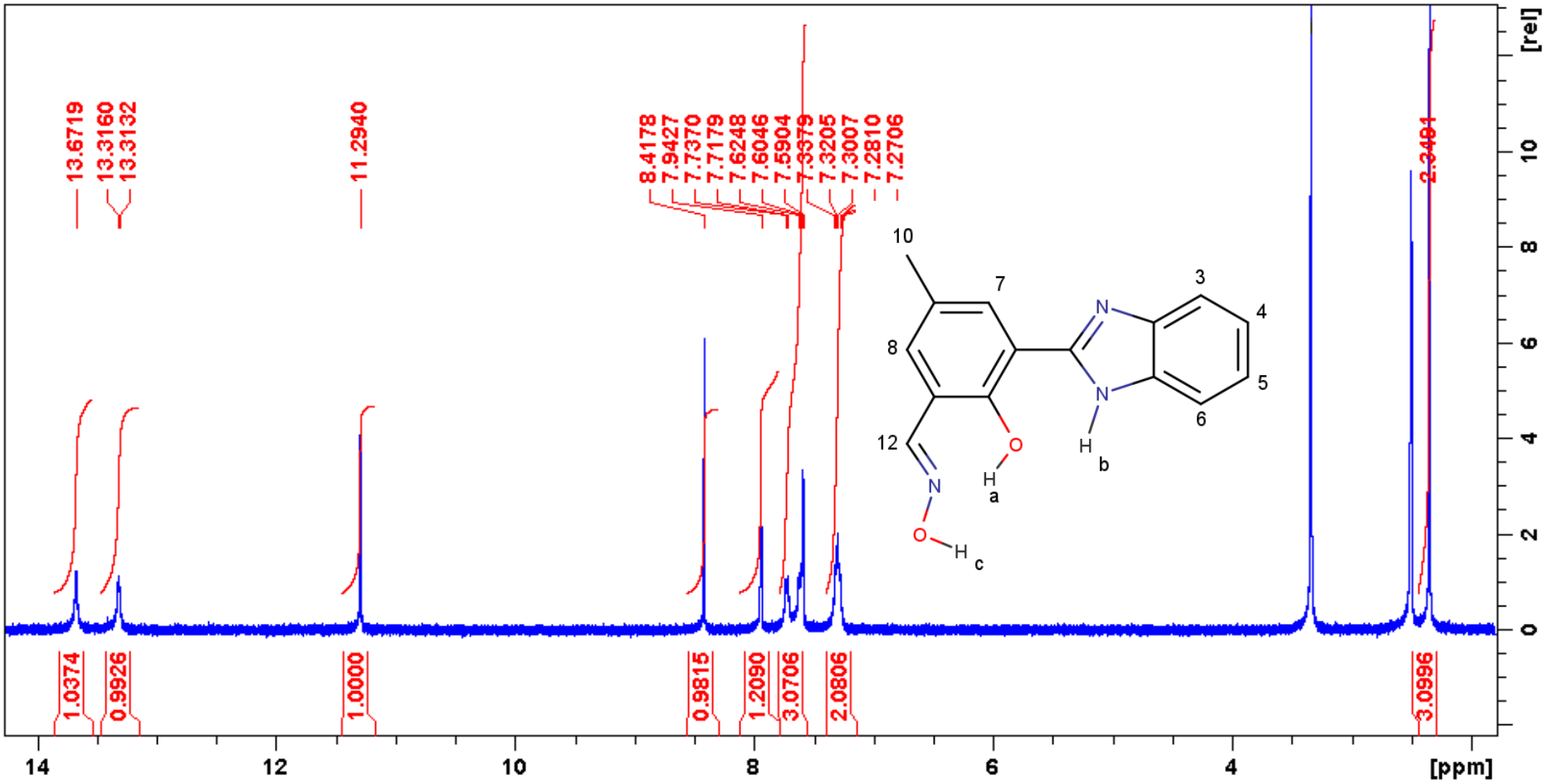

Figure 68. ^{1}H-NMR (DMSO-d_6, 400 MHz) spectrum of **M4**.

2.2.5 Characterization of M5

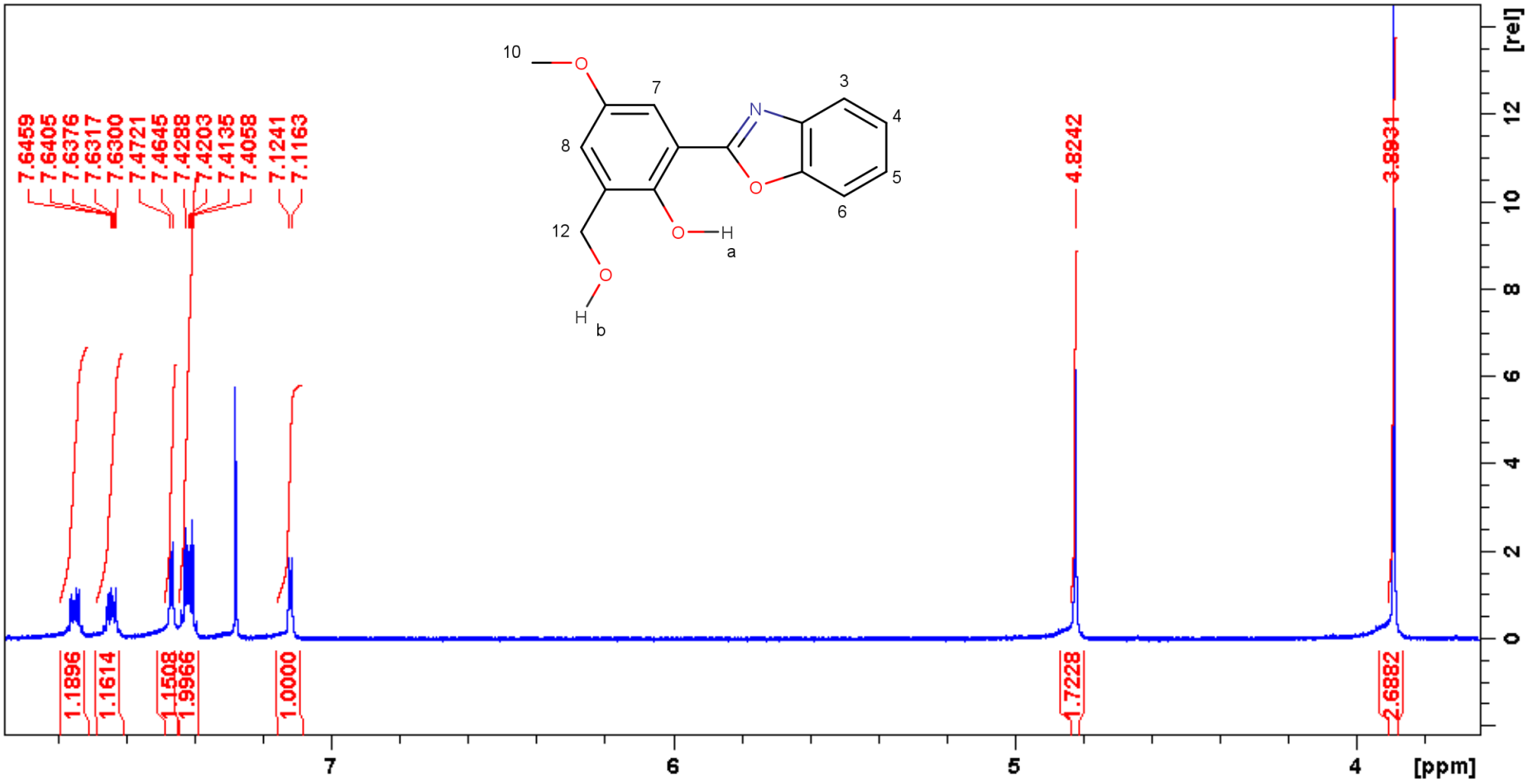

Figure 69. ^{1}H-NMR spectrum ($CDCl_3$, 400 MHz) of **M5**.

2.2.6 Characterization of M6

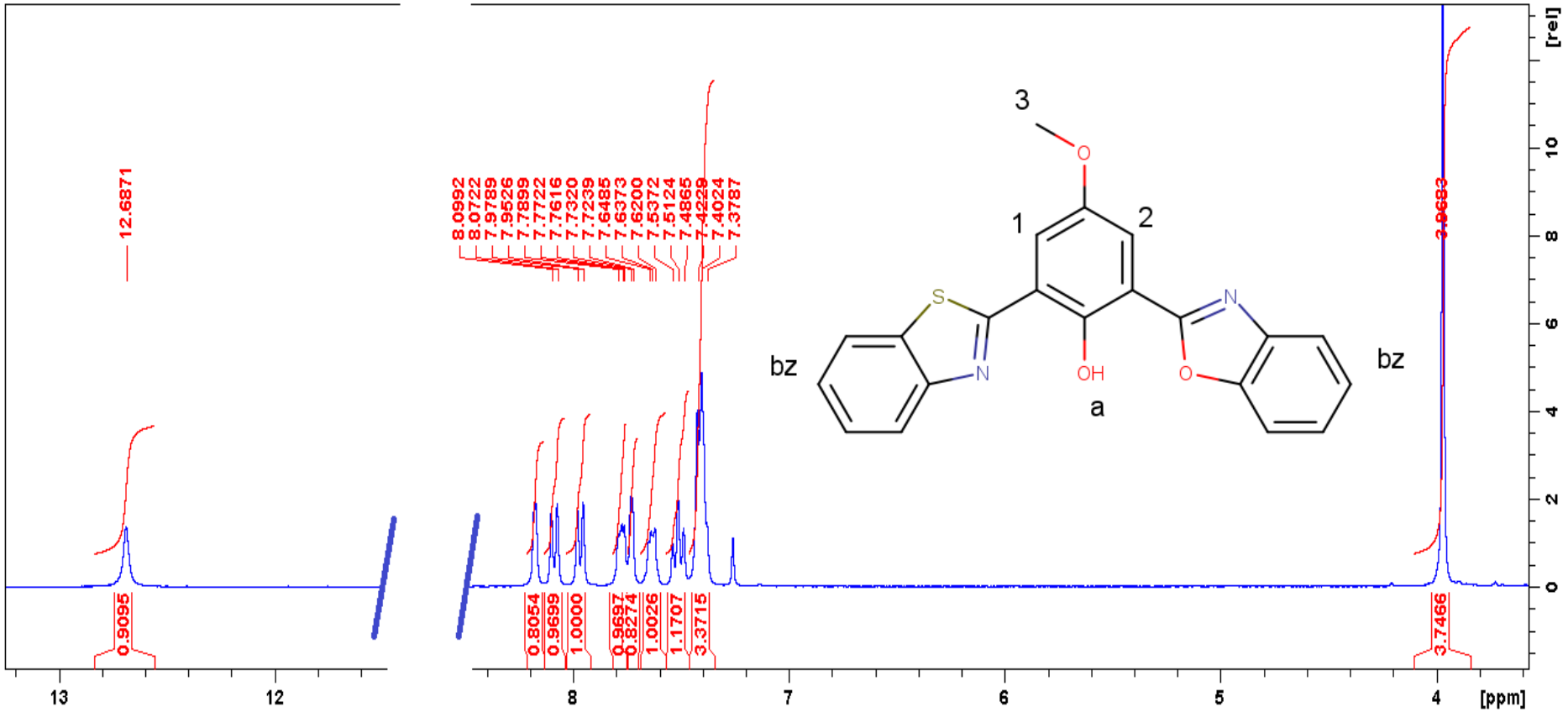

Figure 70. ^{1}H-NMR spectrum ($CDCl_3$, 300 MHz) of **M6**.

2.2.7 Characterization of M7

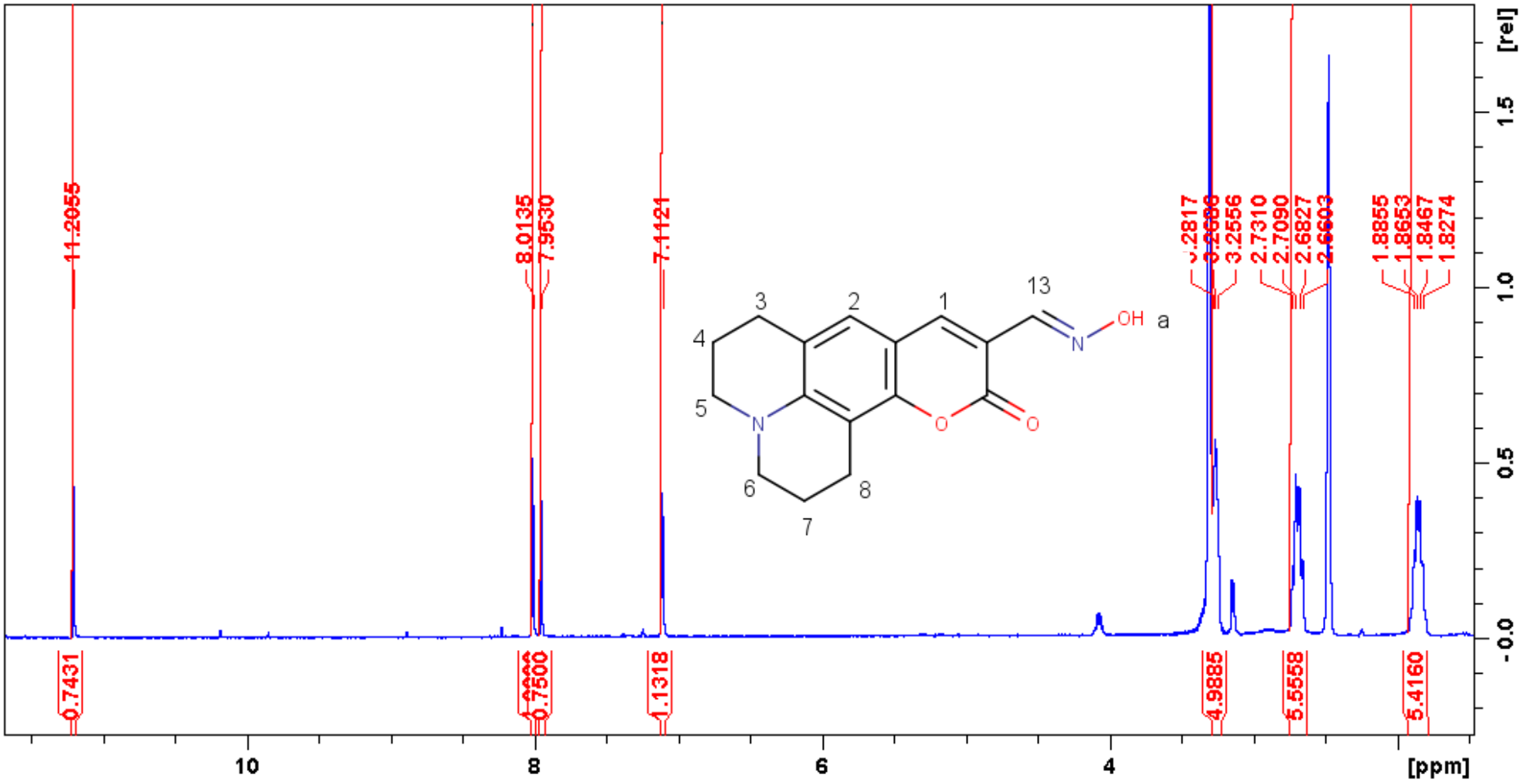

Figure 71. ^{1}H-NMR spectrum (DMSO-d_6, 300 MHz) of **M7**.

2.2.8 Characterization of M8

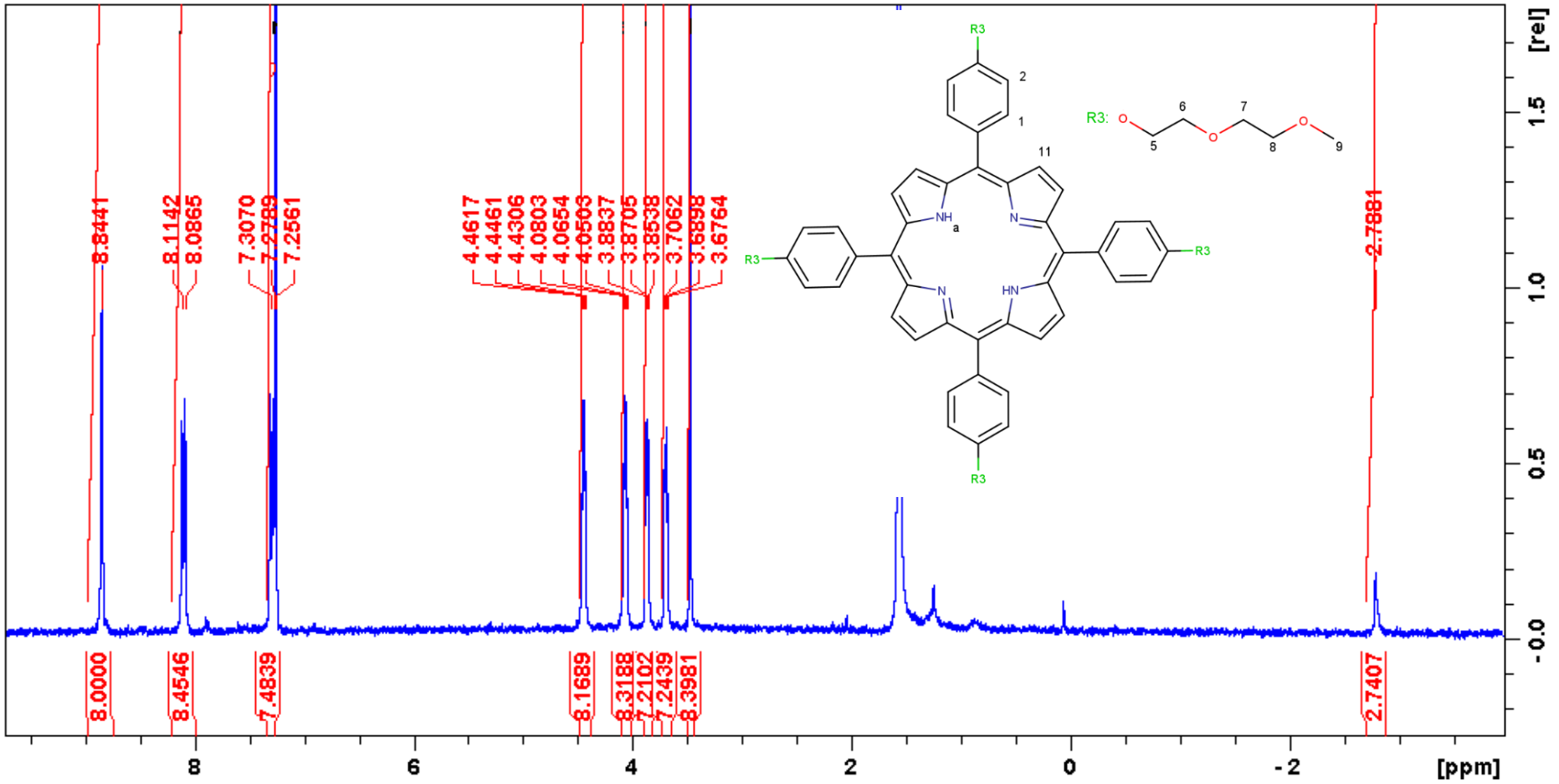

Figure 72. ^{1}H-NMR spectrum ($CDCl_3$, 300 MHz) of **M8**.

2.2.9 Characterization of M9

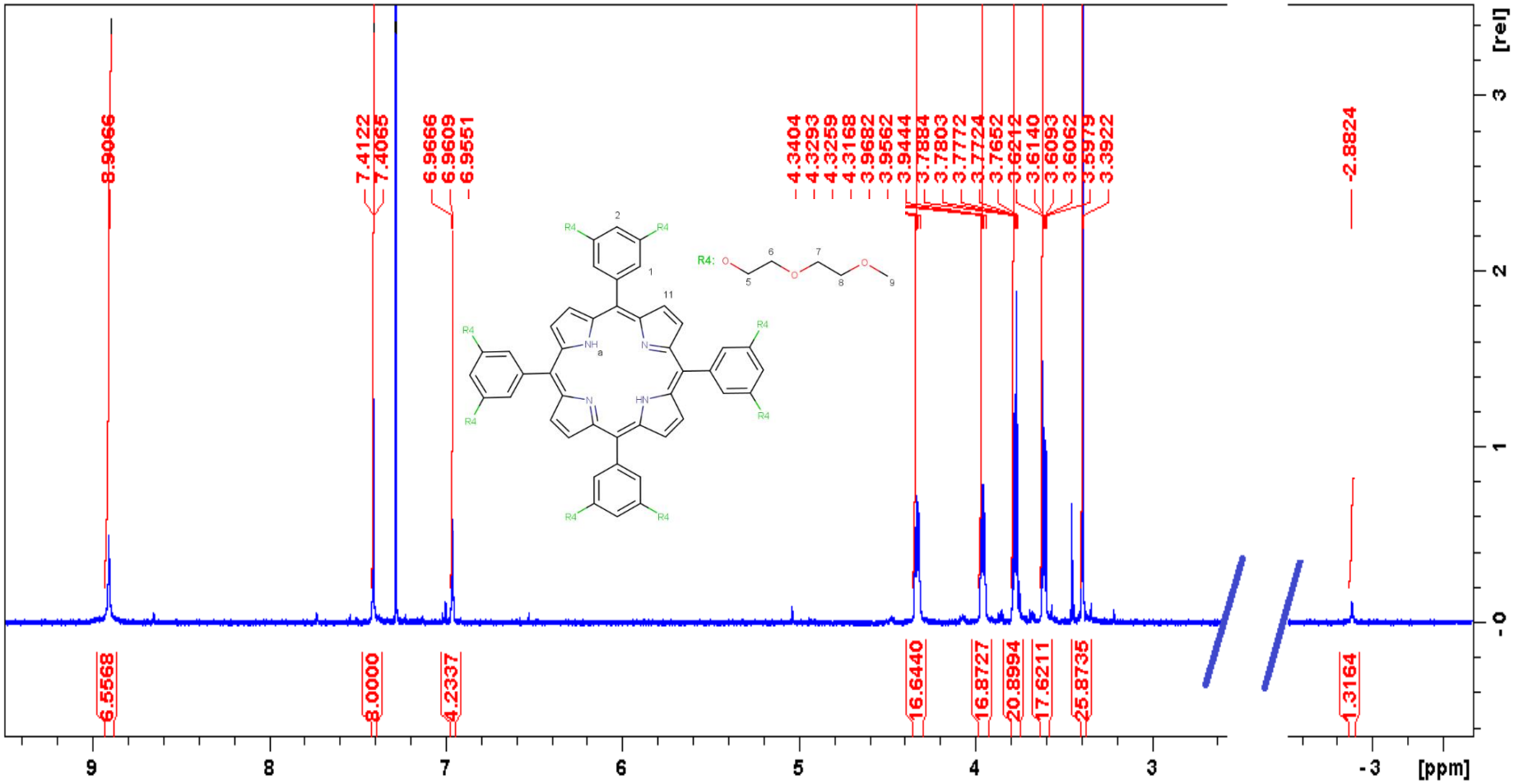

Figure 73. ^{1}H-NMR spectrum ($CDCl_3$, 400 MHz) of **M9**.

2.2.10 Characterization of M8-Pd

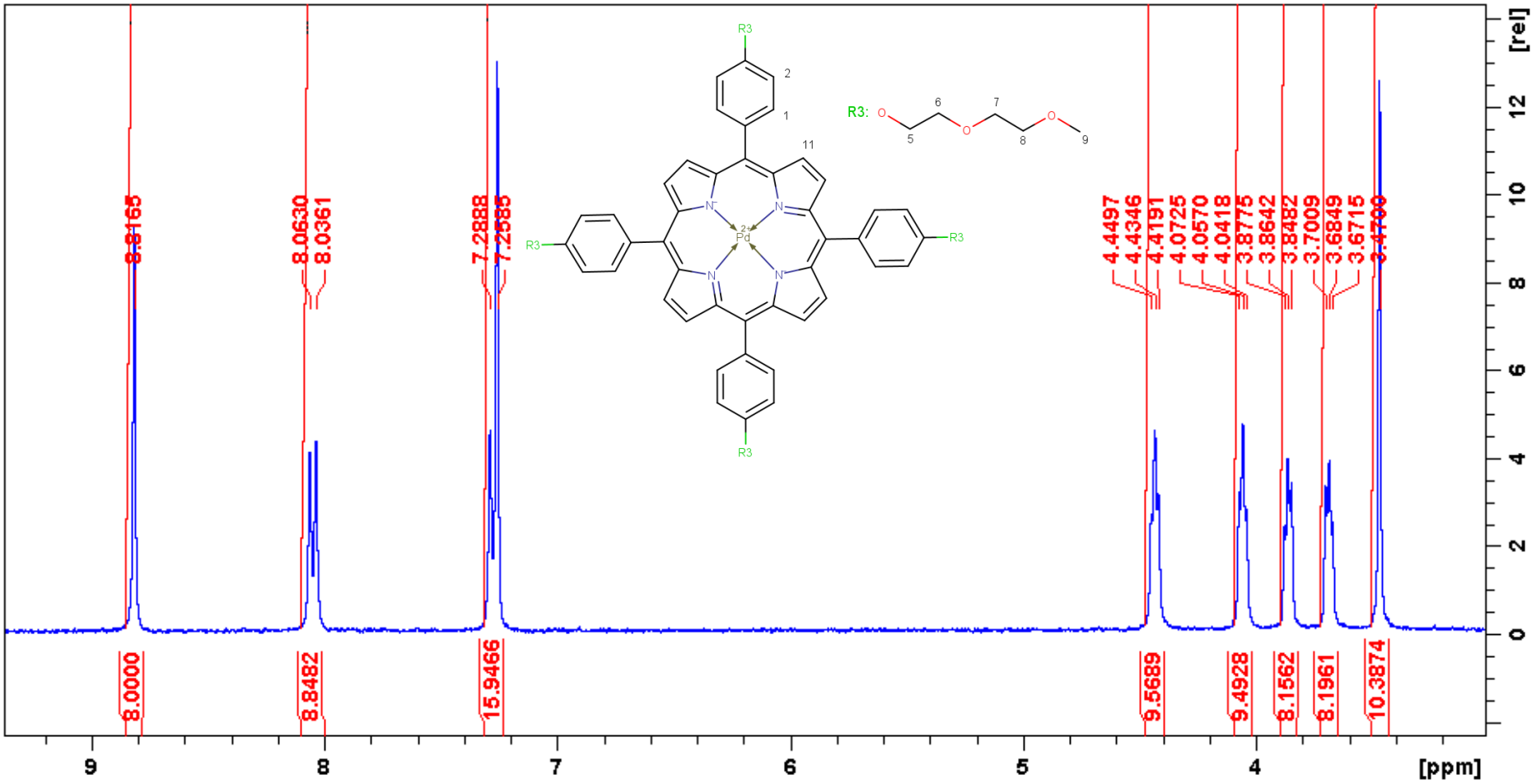

Figure 74. ^{1}H-NMR spectrum ($CDCl_3$, 300 MHz) of **M8-Pd**.

2.2.11 Characterization of M9-Pd

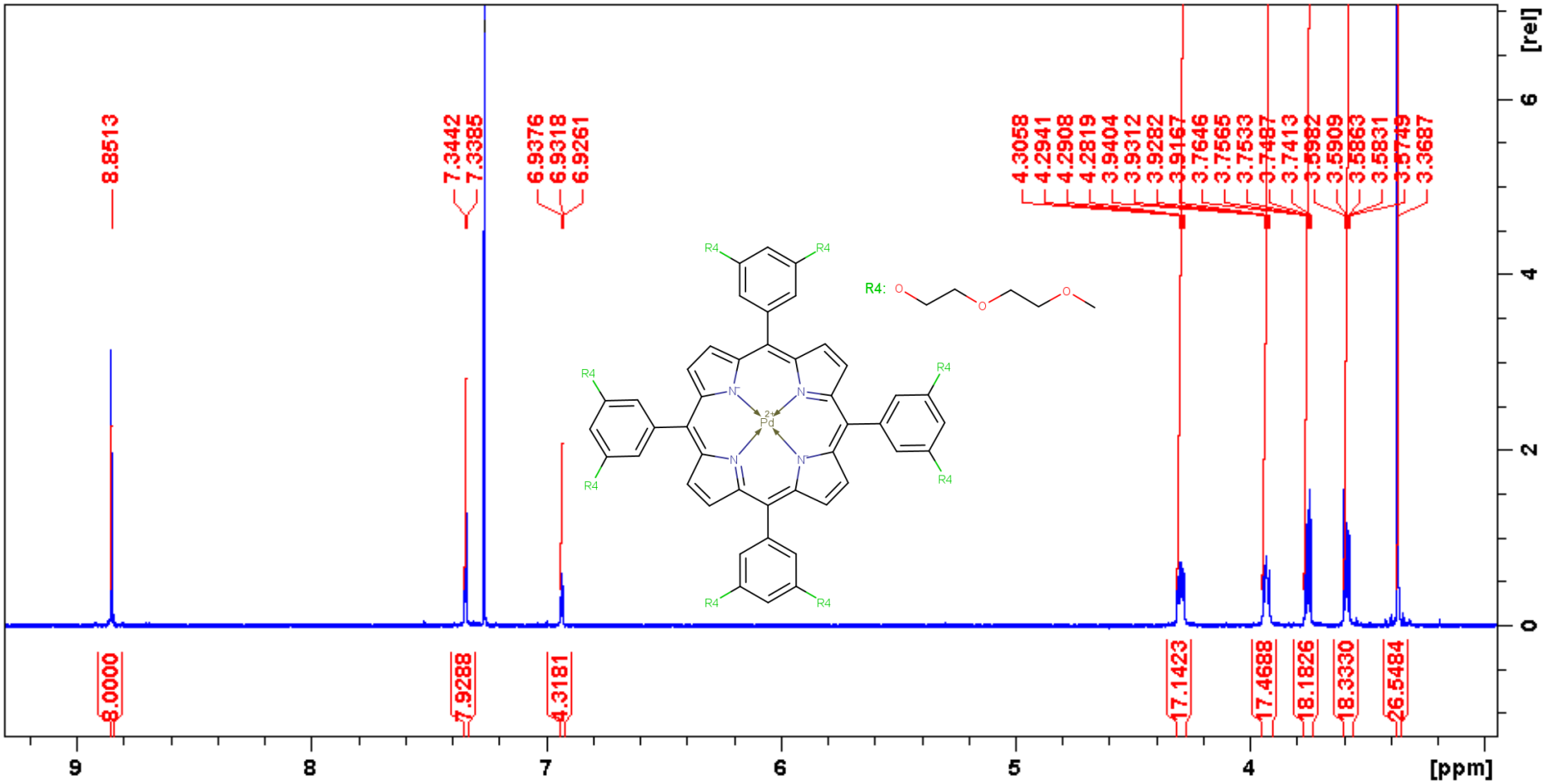

Figure 75. ^{1}H-NMR spectrum ($CDCl_3$, 400 MHz) of **M9-Pd**.

2.2.12 Characterization of M8-Pt

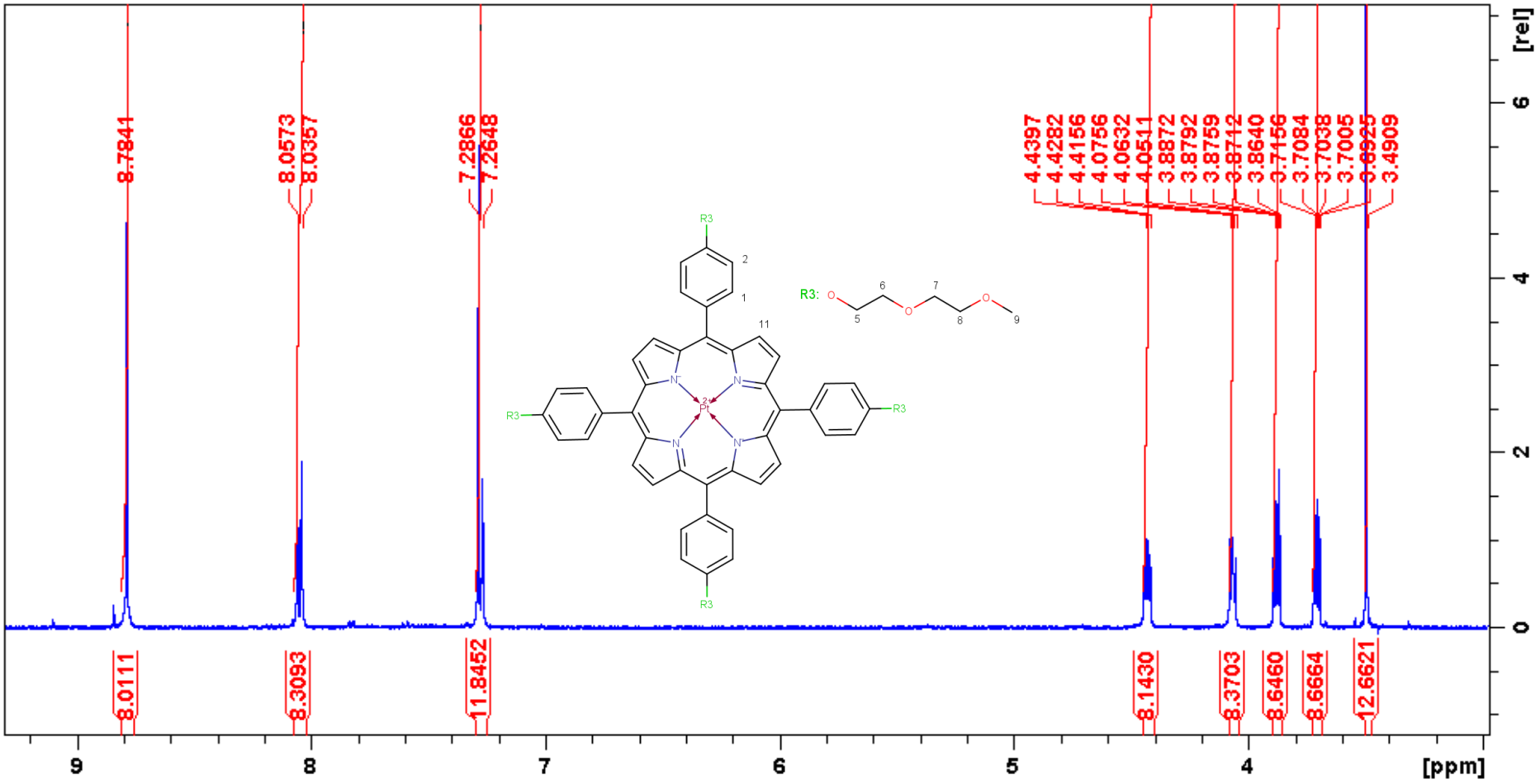

Figure 76. ^{1}H-NMR spectrum ($CDCl_3$, 400 MHz) of **M8-Pt**.

2.2.13 Characterization of M9-Pt

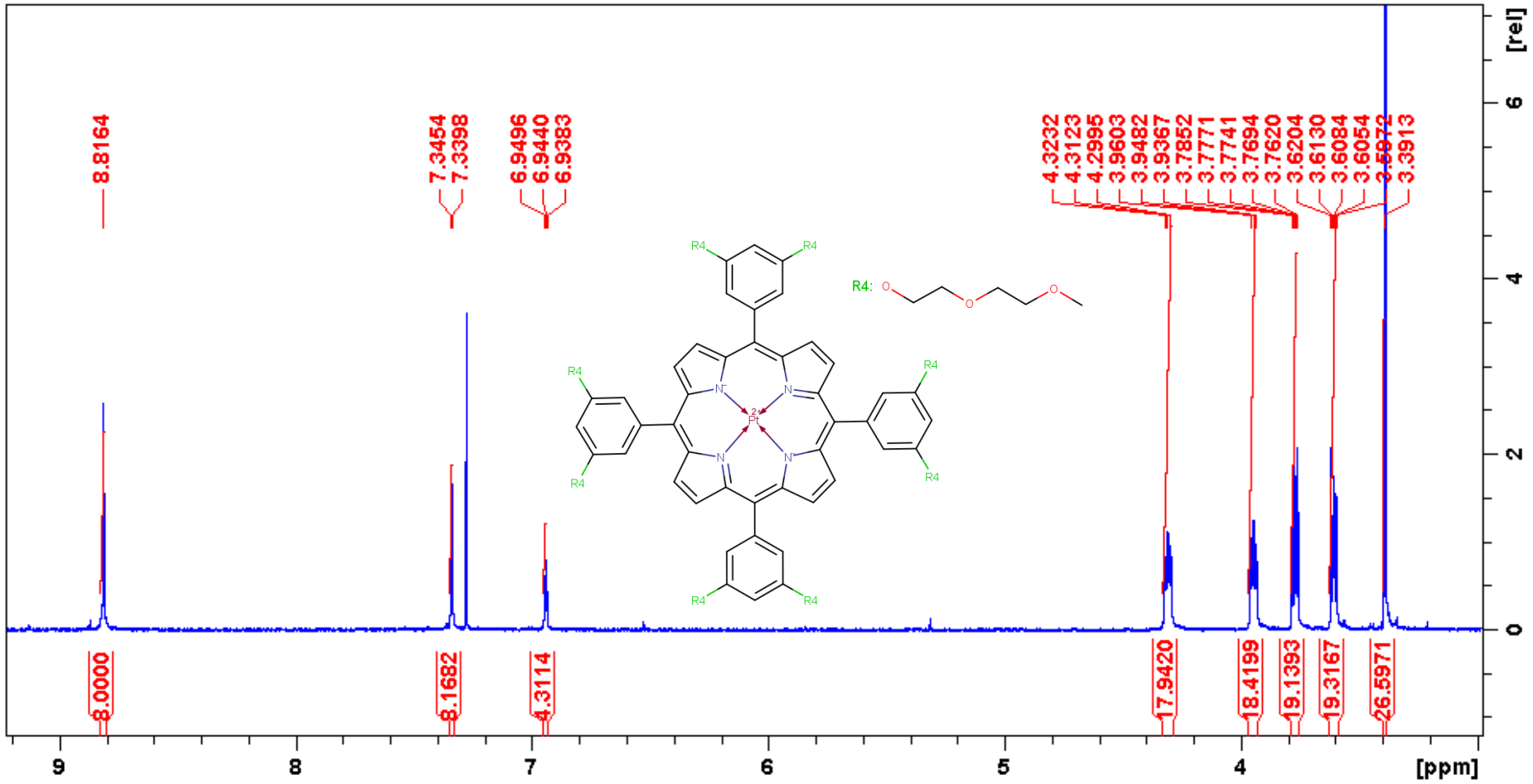

Figure 77. ^{1}H-NMR spectrum ($CDCl_3$, 400 MHz) of **M9-Pt**.

2.3 Other experimental procedures

2.3.1 General procedure for preparing probe solutions for spectroscopic measurements

The general procedure to obtain a solution of the ligand with appropriate concentration involved the preparation of a high concentration stock solution of the compounds, and then diluting these solutions between 200 and 250 times in the selected solvent or solvent mixture so that the final working concentration fall into the domain for which the concentration is directly proportional to the intensity of the emission. This testifies for a solution without aggregation. The exact concentration and solvent information will be given in each particular case. It is important to mention that for each working day, fresh solutions were always prepared. Also, it should be considered that the vast majority of emission spectra were recorded using 2 nm / 2 nm slits. The bandwidths will only be mentioned in the cases where a different size was used.

2.3.2 Quantum yield measurements

The fluorescence quantum yield (Φ_F) is the fraction of the number of photons emitted with respect to the number of photons absorbed by a species. Getting a grasp on the quantum yield values of ligands is critical for their use as chemosensors, owing to the fact that their transduction mechanism operates via the conversion of excitation energy into light [232].

Relative quantum yield values of the synthesized ligands were measured according to the procedure “A guide to recording fluorescence quantum yields” elaborated by Horiba[7], the manufacturer of the fluorimeter used for all the measurements shown in this manuscript. The method involves the use of well-characterized standard samples with established Φ_F values, the condition being that the standard and the ligand samples have similar absorbance values at the excitation wavelength of the ligand. It involves the following steps:

1. Preparation of a solution of a compound with an absorbance value that does not exceed 0.1 at and above the excitation wavelength to be used. This absorbance value accounts for the use of 10 mm cuvettes.

[7] https://www.chem.uci.edu/~dmitryf/manuals/Fundamentals/Quantum%20yield%20determination.pdf

2. Recording the UV-vis absorption of this solution to determine the absorbance at the excitation wavelength that is going to be used. Then, measuring the fluorescence spectrum of this same solution and integrating it (*i.e.* the area under the fluorescence spectrum).
3. Repeating point 2 of this procedure with at least 4 more solutions of the same compound, each one being at different and lower concentration than the first one.
4. Plotting a graph of integrated fluorescence intensity *vs.* absorbance and obtaining a linear fit with an intercept of zero (0). Then, determining the slope of this curve.
5. Repeat points 1 to 5 with all samples, which includes ligand and standard solutions.
6. Finally, obtain the quantum yield value using the following equation:

$$\Phi_F = \Phi_{ST}\left(\frac{Slope_X}{Slope_{ST}}\right)\left(\frac{\eta_X^2}{\eta_{ST}^2}\right)$$

In which F and ST denote ligand and standard, respectively; slope is the value found in point 4; η is the refractive index of the solvent used; and Φ_{ST} is the reported quantum yield value of the standard.

As this method involves the obtention of the quantum yield relative to those of known standards, it is important to ensure that they are suitable to be used at the excitation wavelength of the ligand. Thus, a cross-calibration between them needs to be done. This means that 1) at least two standards need to be used for each Q.Y. measurement and 2) the quantum yield of each one of these standards needs to be calculated relatively to the others. If the values of Φ_F for both standards calculated this way match the literature values with an error of ± 10 %, they can be considered suitable for the Q.Y. of the sample at the selected excitation wavelength.

Then, the Φ_F of each compound can be calculated relatively to at least two different standards and the value is the average of these.

2.3.3 Ligand – analyte bulk tests

To assess the sensing capabilities of the different compounds (with the exception of the porphyrin metallocomplexes), as far as sensitivity and selectivity are concerned, their response towards a large number of anionic and cationic species was screened. The rationale behind this is that, besides the target species each ligand is designed to detect, they could also be sensitive towards species that are always present in water samples

(ranging from ppm concentrations to trace levels) or towards analytes that are considered interferents of the desired detection.

As the compounds were designed with groups that could potentially lead to electrostatic interactions, a library of positively and negatively charged analytes was constructed, which included the following species: NO_3^-, SO_4^{2-}, SO_3^{2-}, HSO_4^-, F^-, I^-, Cl^-, Br^-, *N*-(phosphomethyl)glycine (glyphosate), aminomethylphosphonic acid, PO_4^{3-}, HPO_4^{2-}, OCl^-, CN^-, CH_3COO^-, AsO_2^-, $HAsO_4^{2-}$, Fe^{2+}, Fe^{3+}, Cu^{2+}. Zn^{2+}, Hg^{2+}, Ni^{2+}, Al^{3+}, Cd^{2+}, Ca^{2+} and Mg^{2+}. In all cases, 0.01 mol/L aqueous solutions were prepared. All the solutions of anions were prepared from their respective sodium salts, with the exception of OCl^- and $HAsO_4^{2-}$, which were already commercially available as solutions with sodium as the counter cation; and CH_3COO^-, that was prepared from its tetrabutylammonium salt. In a similar way, all the solutions of cations were prepared from their respective chloride salts.

The standard bulk tests then implied the following steps:

1. Preparation of the solution of the ligand as described in Section 2.3.1.
2. Recording the emission spectrum of this sample.
3. Adding at least 4 equivalents of an analyte in a way that its final concentration sits at around 100 μmol/L. Gentle agitation for two minutes and recording the emission spectrum.
4. Repeating points 1 to 3 with all the analytes.

The exact concentrations and stoichiometric ratios of ligand and analyte will be provided for each particular case in Chapter 4, as well as the solvent medium in which the test was carried out. In some cases, it will be noted that some analytes were not used, the reason being their lack of availability at that given time.

Also, it is important to mention that the logic behind using an excess of the analytes in these tests was to ensure a fluorescence response (or lack thereof) of the chemosensor towards them. This means that if an analyte is not able to change the fluorescence properties of the ligand even when being present in a moderate excess, that particular species is transparent towards the chemosensor and their interaction, if any, will not be further explored.

Finally, in order to assess for a possible pH-dependent response, the ligands were also screened by adding acidic and basic solutions of HCl and NaOH, respectively, following the same procedure described above. The exact concentrations will be given in each case.

2.3.4 Ligand – analyte titrations

Fluorescence and absorption titrations were carried out following the standard procedure:

1. Preparation of the solution of the ligands as described in Section 2.3.1.
2. Preparation of the solutions of the analyte in the range of 0.0001 to 0.005 mol/L.
3. Measurement of the absorption and emission spectra of the free ligand.
4. Addition of a small volume, ranging from 1 to 10 μL of the solution of the analyte to the solution of the ligand to have a negligible dilution effect. Gentle stirring for two minutes and recording the absorption and emission spectra.
5. Repeating step 4 at least 6 times, ensuring that the final point of the titration is such in which there is an excess of at least 2.5 equivalents of the analyte in respect to the ligand.

The exact concentrations and stoichiometric ratios of ligand and analyte will be provided in each particular case in Chapter 4, as well as the solvent medium in which the test was carried out.

With these data, a calibration curve that plots response *vs.* concentration is obtained. Note that “response” can be emission intensity, absorbance, ratio between two different emission intensities, among other parameters obtained from the spectroscopic measurements.

2.3.5 Limit of detection

The limit of detection (LoD) is defined as the minimum concentration of analyte that a ligand can detect distinguishing its response from the background signal of the machine [233]. In fluorescence and absorption studies, it can be calculated using the following equation:

$$\mathrm{LoD} = \frac{3 \times \sigma}{\mathrm{k}}$$

Where σ is the standard deviation of the blank and k is the slope of the calibration curve from the ligand – analyte titration obtained as explained in Section 2.3.4 [233]. The standard deviation of the blank is simply the SD of the plotted response (emission intensity, absorbance, etc.) of the ligand. For assessing this value, 10 to 15 emission or absorption measurements of the free ligand are taken and the SD is calculated using the response values at the working wavelengths.

2.3.6 Job's method of continuous variations

The Job's method of continuous variations, or more simply, the Job Plot, is a method widely used in fluorescence sensing research, among other fields, to obtain the stoichiometry between the ligand and the analyte.

The Job's method is considered since a few years to be outdated for providing results with low confidence values, mostly for supramolecular host-guest systems. However, for the study of inorganic complexes, and in particular those with a 1 to 1 stoichiometric ratio, it may still be valid [234].

The procedure involves preparing 10 different solutions of ligand (L) + analyte (A) in which the total concentration is always the same, with the molar percentage of the ligand in these solutions varying between 10 and 100 %. Then, the absorption and emission spectra of each solution is measured and the absorbance (Abs) or emission intensity (I) value at a selected wavelength is plotted against the molar percentage of the analyte to obtain a $\mathrm{I}\ vs\ \frac{[\mathrm{A}]}{[\mathrm{A}]+[\mathrm{L}]}$ or $\mathrm{Abs}\ vs\ \frac{[\mathrm{A}]}{[\mathrm{A}]+[\mathrm{L}]}$ graphic. Finally, the molar percentage at the inflection point of the curve represents the stoichiometric value [235].

2.3.7 Benesi-Hildebrand method

The Benesi-Hildebrand (BH) method is a linear regression-type technique that, in the field of fluorescence sensing, allows for the obtention of the association constant (K) of a ligand-analyte interaction using titration data. For the same reasons as the Job Plot method, the BH has been deemed outdated and unreliable, particularly for calculating K values of species in which the stoichiometry is different than 1 to 1 [236]. However, it still holds some utility when used for inorganic complexes.

The linear regression that needs to be solved to obtain a BH plot is the following:

$$\frac{1}{\mathrm{I}-\mathrm{I}_0}=\frac{\mathrm{BH}}{\mathrm{K_a}\times[\mathrm{Ligand}]\times[\mathrm{Analyte}]^{\mathrm{n}}}+\frac{\mathrm{BH}}{[\mathrm{Ligand}]}$$

Where I is the emission intensity (or absorbance) of the ligand upon addition of the analyte; I_0 is the emission intensity (or absorbance) of the free ligand; BH is the Benesi-Hildebrand constant; K_a is the association constant; [Ligand] is the concentration of the ligand, that should stay constant; [Analyte] is the concentration of the analyte; and n is the stoichiometric ratio.

Thus, after performing a titration following the procedure detailed in Section 2.3.4, the values of I_0 and I are found. Then, in the equation, I_0, BH, and [Ligand] remain constant; n is a known value; and I and [Analyte] vary. Then, by plotting $\frac{1}{I-I_0}\ vs\ \frac{1}{[Analyte]^n}$, the slope $\frac{BH}{K_a \times [Ligand]}$ and the intercept $\frac{BH}{[Ligand]}$ can be found. After solving a two-variable equation, the value of K_a is obtained [236].

2.3.8 Interference tests

To check if an analyte interferes with the detection of the ligand towards a species that generates a change in its emission intensity, interference tests are run. They consist in the following steps:

1) Preparation of a solution of the ligand following the procedure described in Section 2.3.1 and recording its emission spectrum.
2) Adding a quantity of the interferent species. Gentle stirring for two minutes and recording the emission spectrum.
3) Adding an equimolar amount of the analyte (the species the ligand has been deemed to detect), gentle stirring for two minutes and recording the emission spectrum.

The exact concentrations and stoichiometric ratios of ligand and interferent/analyte will be provided in each particular case in Chapter 4, as well as the solvent medium in which the test was carried out.

2.4 Equipment and materials

2.4.1 Equipment

2.4.1.1 Nuclear magnetic resonance

^{1}H- and ^{13}C-NMR spectra were recorded on a Bruker Advance 300 MHz spectrometer and in a Bruker Advance 400 MHz spectrometer. The chemical shifts are expressed as parts per million (ppm) relative to tetramethylsilane (TMS) at δ = 0 ppm.

2.4.1.2 Emission spectra

Steady-state fluorescence spectra were recorded in a HORIBA Jobin Yvon spectrofluorometer model Fluoromax-4 and in an Edinburgh Instruments spectrofluorometer model FS5. All measurements were carried at room temperature.

2.4.1.3 Absorption spectra

UV-vis spectra were recorded in an Agilent Technologies Cary 60 spectrophotometer. All measurements were carried out at room temperature.

2.4.1.4 High-resolution mass spectra

Mass spectra experiments were performed on a Bruker Tims-TOF mass spectrometer. Confirmation of the isotopic composition of the samples was made using the MarvinSketch software.

2.4.2 Materials

All commercial reagents were purchased from Sigma-Aldrich or VWR and, unless stated otherwise, were used without prior purification or pretreatment. Dry DMF, PhCN and $CHCl_3$ were obtained *via* distillation over CaH_2 and stored over 3 Å molecular sieves. All spectroscopic-grade solvents were purchased from Sigma-Aldrich.

3 Photophysical properties

The study of the photophysical properties of the 11 compounds presented in Chapter 2 will be shown in this Chapter. The analysis will focus on the description and interpretation of their steady-state fluorescence and absorption spectra, with emphasis on the elucidation of the mechanism that governs their excited states.[8]

3.1 Pyrene derivatives: M1, M2 and M3

The UV-vis absorption, excitation and emission spectra of **M1** and **M2** were recorded in 100 % THF medium with a concentration of each ligand set at 11.6 μmol/L and 14.8 μmol/L, respectively. They are shown in Figure 78.

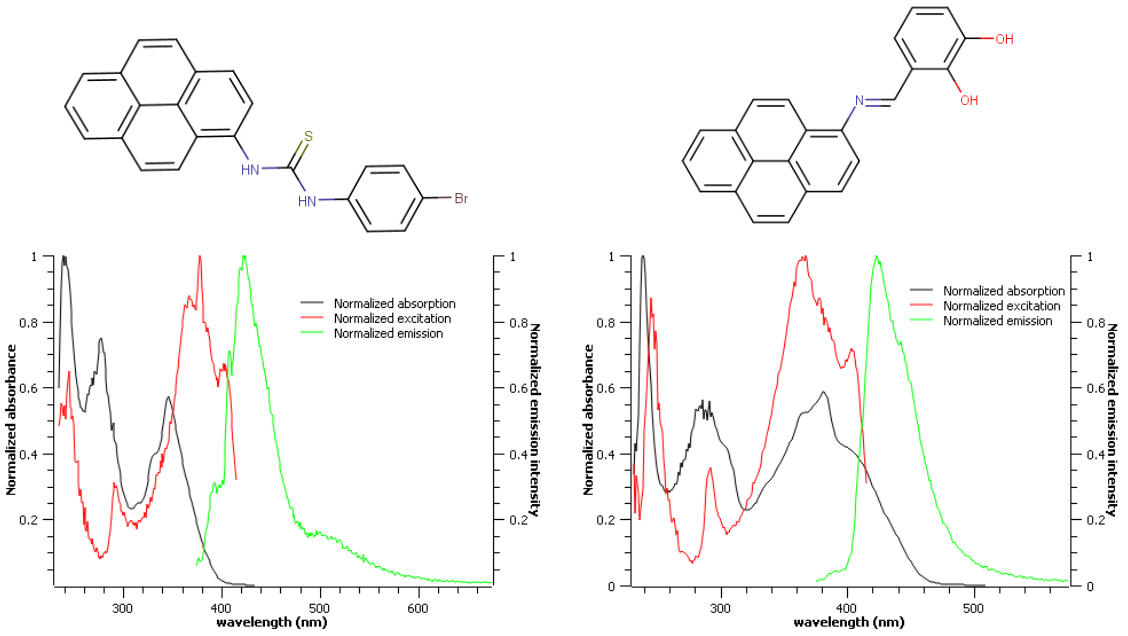

Figure 78. (left) Normalized absorption (black), normalized excitation (red, λ_{em} = 425 nm) and normalized emission (green, λ_{exc} = 364 nm) spectra of **M1** in 100 % THF medium. (right) Normalized absorption (black), normalized excitation (red, λ_{em} = 425 nm) and normalized emission (green, λ_{exc} = 365 nm) spectra of **M2** in 100 % THF medium. ε(**M1**) = 32 420 L.mol^{-1}.cm^{-1}. ε(**M2**) = 26 940 L.mol^{-1}.cm^{-1}. The chemical structures of both compounds are presented on top of their corresponding spectra.

[8] It is important to mention that the extinction coefficient values presented in this chapter were calculated using the absorbance of the excitation wavelength for each particular molecule.

The UV-vis absorption, excitation and emission spectra of **M3** were recorded in a mixture of THF : EtOH 0.5 : 99.5 with a concentration of the ligand at 12.1 μmol/L. They are reported in Figure 79.

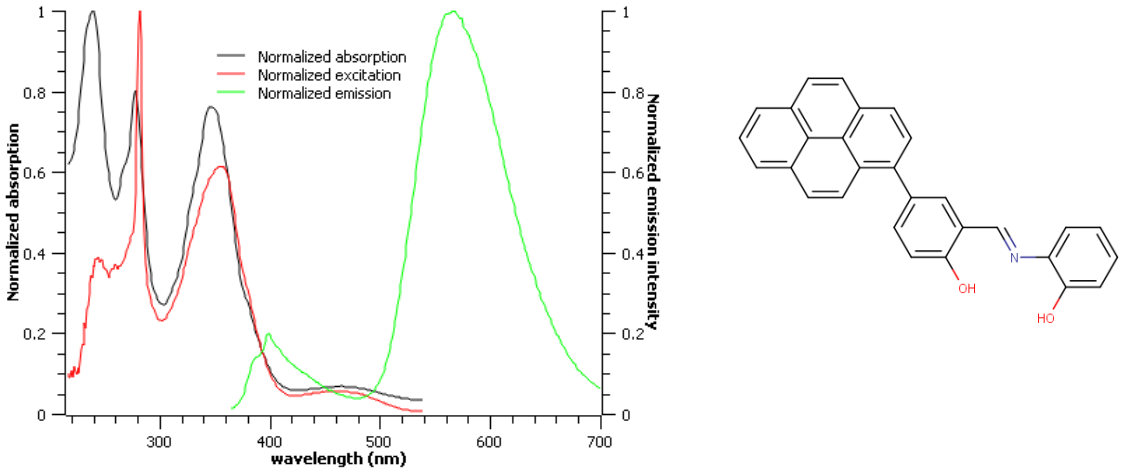

Figure 79. Normalized absorption, normalized excitation (red, λ_{em} = 563 nm) and normalized emission (green, λ_{exc} = 357 nm) spectra of **M3** in THF : EtOH 0.5 : 99.5 medium. ε(**M3**) = 41 190 L.mol^{-1}.cm^{-1}. The chemical structure of **M3** is presented on the right.

The notorious difference in the solvent systems used for **M1** and **M3** in comparison with **M3** is due to the fact that, starting with the latter molecule, it was decided, were possible, to switch away from using THF as the main working medium for the sensing studies. The reason behind was the search for solvent media that were chemically closer to H_2O in the sense that they have a high degree of hydrogen bonding capabilities, thus resembling the real conditions in which the molecules were meant to be used. Also, there was the desire for using more environmentally friendly options, such as alcohols or water itself.

The UV-vis absorption spectra of these three ligands show the typical absorption bands of pyrene derivatives. For **M1**, the bands at 346 and 277 nm can be assigned to $B_{3u} \leftarrow A_g$ transitions, while the shoulder at 331 nm and the band at 239 nm can be assigned to the $B_{2u} \leftarrow A_g$ transitions [237]. For **M2**, the bands at 382 and 287 nm should correspond to the $B_{3u} \leftarrow A_g$ transitions and those at 366 nm and 239 nm, to the $B_{2u} \leftarrow A_g$ transitions. With respect to the shoulder at 403 nm, it is present in several pyrene-Schiff base compounds and could arise due to the isomerization of the C=N bond [237] [238] [239]. Finally, for the **M3** ligand, the bands at 348 and 240 nm should also correspond to the $B_{3u} \leftarrow A_g$ transitions, and the band at 278 nm, to the second $B_{2u} \leftarrow A_g$ transition. The first

band of this transition cannot be seen, but could be merged with the band at 348 nm. **M3** also shows an absorption band at 464 nm that is thought to be due to an anionic form present in equilibrium in the protic solvent used [240] [241]. To verify this claim, the absorption spectrum of **M3** was recorded in a wide array of solvents. It can clearly be seen in Figure 80 that the aforementioned low energy band appears strongly in ethanol and water, which are media in which an acid-base equilibrium can occur.

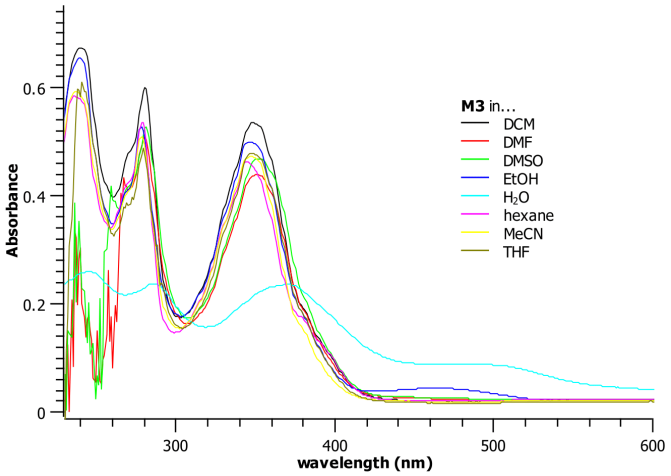

Figure 80. Absorption spectra of **M3** in different solvents (0.5 : 99.5 THF : solvent). In all cases, the concentration of the ligand was 12.1 μmol/L.

As for the emission spectra, the λ_{max} is situated at 423, 422 and 566 nm for **M1**, **M2** and **M3**, respectively. In the first two cases, it is of no surprise that these ligands emit in the blue and, as predicted due to their design, with very low intensity. In the first case, this could be attributed to the lack of proper conjugation between the pyrene unit and the thiourea entity due to the twist that exists between these moieties. While the crystal structure of **M1** has not been obtained, it can be found in the literature that, commonly, diarylthioureas do not exhibit a preformed planarity [242], which hinders the emission of these molecules probably because of radiationless deactivation processes due to the free rotation of the aryl-thiourea bond in solution. In the case of **M2**, the low emission can be attributed to the free isomerization process of the C=N bond, as explained in Section 2.1.1.4. Also, as expected for pyrene derivatives, a significant fine structure due to vibronic transitions can be observed [243]. Moreover, a possible excimer band can be seen at 503 nm in the spectrum of **M1**.

The situation is completely different for **M3**, however. In first place, this ligand shows two emission bands in 99.5 % ethanol: at 400 nm and at 566 nm. While the emission intensity of these bands is expected due to the predicted C=N isomerization mechanism, the

extremely high Stoke's shift of the band at 566 was surprising. As the dilution used to record the emission and absorption spectra was high, the possibility of the red shifted belonging the excimer species of the ligand was not very likely. Nonetheless, considering the chemical structure of this ligand in which an acidic proton of a phenol is in close proximity to the basic nitrogen atom of the imine, then led to postulate the possibility of this molecule to also have an active ESIPT mechanism, as described in Section 2.1.2.1 for the proposed benzazole derivatives. In the particular case of **M3**, the band at 400 nm could correspond to the emission of the [enol]* tautomer, while the one centered at 566 nm, to the emission of the [keto]* tautomer. The proposed ESIPT phototautomerization process can be seen in Figure 81. It is important to mention that quite few examples of pyrene-based ESIPT-type molecules for sensing applications are reported in the literature [244].

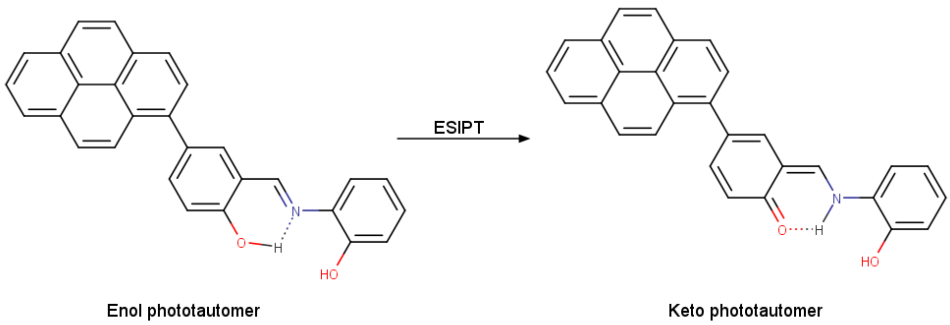

Figure 81. Proposed ESIPT mechanism for **M3**.

Also, the fluorescence relative quantum yield value of **M1** and **M2** in 100 % THF were determined using quinine sulfate and norhamane as standards following the procedure described in Section 2.3.1. The average results obtained are 0.0018 (0.18 %) and 0.0023 (0.23 %), which are consistent with the fact that the molecule is basically non emissive in this solvent. The quantum yield plots can be seen in Figure 82. The quantum yield of **M3** was not obtained due to reasons that will be described in Section 4.1.3.

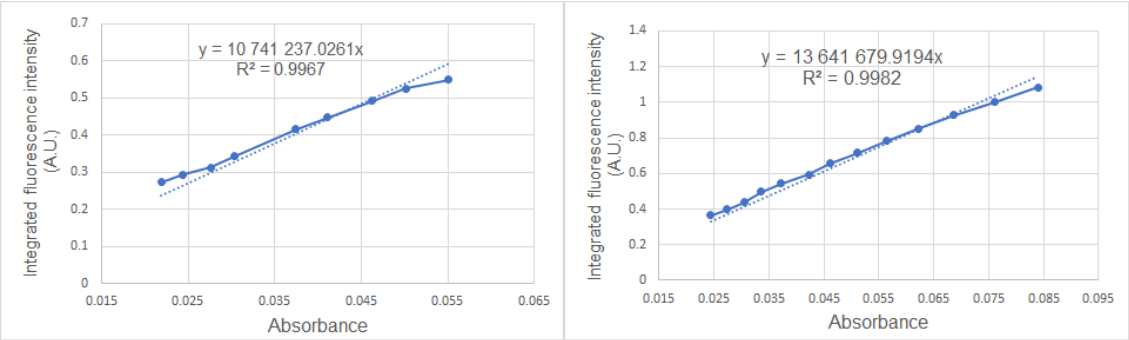

Figure 82. Plots used to calculate the fluorescence quantum yield value of **M1** (left) and **M2** (right). Average fluorescence quantum yield values are 0.0018 ± 0.0001 and 0.0023 ± 0.0002, respectively.

3.2 Benzazole derivatives: M4, M5 and M6

The UV-vis absorption, excitation and emission spectra of **M4** were recorded in a mixture of THF : H_2O 0.5 : 99.5 with a concentration of the ligand at 15 μmol/L. For its part, these same spectra for **M5** were recorded using with a concentration of 14.7 μmol/L in a mixture of EtOH : H_2O 0.1 : 0.4. Finally, for **M6**, the spectra were recorded in a mixture of THF : EtOH : H_2O 0.4 : 49.8 : 49.8 while its concentration was set at 13.4 μmol/L.

The UV-vis absorption spectra of the three benzazole derivatives are characteristic for ESIPT ligands of this family of compounds. The low energy bands at 343 nm in both **M4** and **M5**, and at 377 – 386 nm in **M6** should correspond to a $\pi \leftarrow \pi^*$ transition that can be assigned to the closed conformer or enol form of the ligand, this is, with an intramolecular hydrogen bonding. The red shift observed in the absorption spectrum of **M6** in respect to the other two ligands could be due to it bearing a benzothiazole group. Owing to the presence of a sulfur atom, benzothiazoles have an increased aromatic character in comparison with its oxygen and nitrogen analogs, accounting for an increased π-delocalization and a reduced band gap [245]. Then, the higher energy bands between 290 and 300 nm in the three cases should correspond to the open conformers [246] [247]. For **M4** and **M6**, the bands at 380 and 447 nm, respectively, are thought to correspond to the phenolate anion that may have formed in solution and is in equilibrium with the protonated form in the ground state [167] [176]. The presence of this band is a clue of the elevated acidity of the phenolic proton of these two molecules.

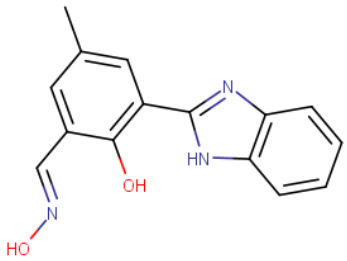
N
HN
OH
N
HO

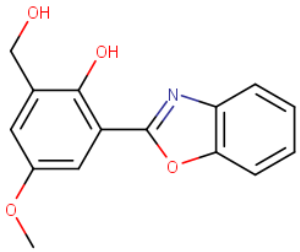
OH
OH
N
O
O

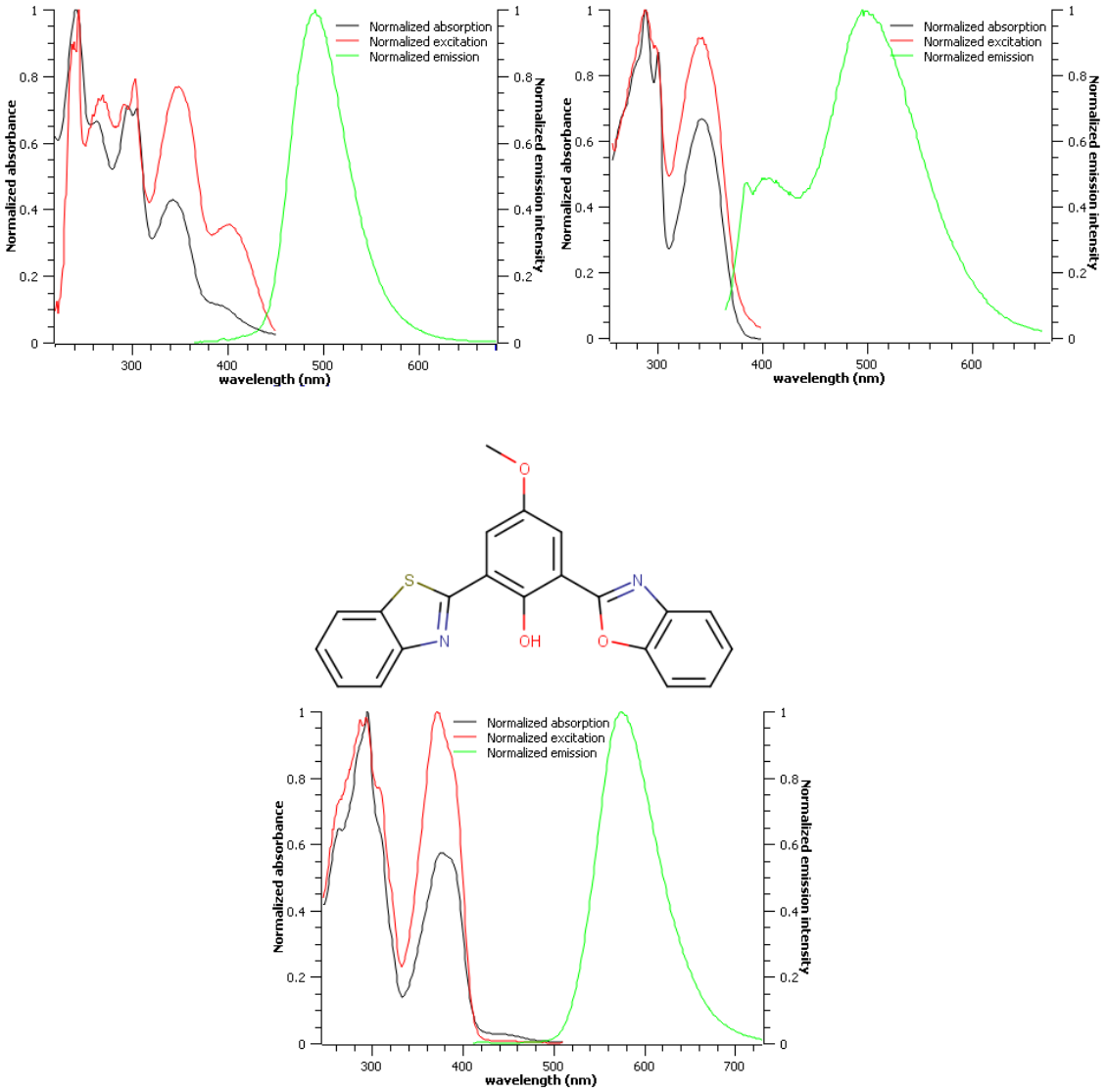

Figure 83. (top left) Normalized absorption (black), normalized excitation (red, λ_{em} = 490 nm) and normalized emission (green, λ_{exc} = 349 nm) spectra of **M4** in a THF : H_2O 0.5 : 99.5 medium. (top right) Normalized absorption (black), normalized excitation (red, λ_{em} = 504 nm) and normalized emission (green, λ_{exc} = 340 nm) spectra of **M5** in a EtOH : H_2O 1 : 4 medium. (bottom) Normalized absorption (black), normalized excitation (red, λ_{em} = 574 nm) and normalized emission (green, λ_{exc} = 372 nm) spectra of **M6** in a THF : EtOH : H_2O 0.4 : 49.8 : 49.8 medium. ε(**M4**) = 8 000 L.mol^{-1}.cm^{-1}. ε(**M5**) = 5 330 L.mol^{-1}.cm^{-1}. ε(**M6**) = 14 360 L.mol^{-1}.cm^{-1}. The chemical structures of the three benzazole derivatives are shown on top of their corresponding spectra.

In regards to this, it is of particular notoriety that the band corresponding to the phenolate forms is not seen in **M5**. The difference between the benzimidazole and the benzoxazole can be explained by the difference in pK_a of both molecules as the solvent media used in both cases is mainly H_2O. With his own 2-(2-hydroxyphenylbenzazole) derivatives,

Henary calculated that the pK_a that corresponds to the deprotonation of the phenolic oxygen (which is the most acidic hydrogen in the ligand) is 9.28 for an oxazole and 8.63 for an imidazole in HEPES buffer [176], meaning that the formation of a phenolate anion is much easier for the latter molecule. While the pK_a values of our ligands are not the same as those of Henary, some approximations can be made. In the present case, no buffer was used and the pH of the medium was measured to be in the 6 – 7 range, meaning that a small fraction of dissolved **M4** molecules were going to be found in their phenoxide form. For **M5**, however, this is not the case as its pK_a could be up in one order of magnitude in comparison with the benzimidazole, thus it can easily be inferred that all molecules of this oxazole will be in the phenol form.

To finalize the analysis of the absorption spectra, it is important to mention that the tails that extend to the visible part of in the absorption spectra of these three derivatives could be a consequence of Mie Scattering observed for organic chromophores in water [248].

When excited at 349 nm, **M4** shows a single emission in the THF/H_2O mixture used with a maximum at 490 nm, which can be assigned to the radiative relaxation of its keto tautomer and has a high Stock's shift as expected due to the ESIPT capabilities of the molecule [160] [249]. Interestingly, it was found that the emission of the enol tautomer appears at 365 nm and is superimposed with the Raman band of the solvent. Thus, in order to correctly visualize it, as in Figure 84, the ligand was excited at 300 nm maintaining all other experimental conditions. This high energy enol band is consistent with published literature [164] [249] [250].

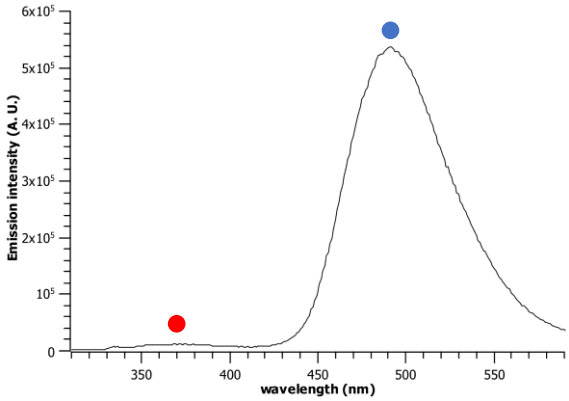

Figure 84. Emission spectrum of **M4** when excited at 300 nm ([**M4**]: 18.7 μmol/L). The emission of the keto tautomer is seen at 490 nm (blue mark) and the one of the enol tautomer, at 365 nm (red mark).

The observed fact that **M4** shows a [keto]* emission that is up until two orders of magnitude stronger than that of its [enol]* emission, especially in a 99.5 % H_2O solvent medium, is a notorious feature for this ligand and few similar reports can be found [164] [251]. In fact, it has been widely reported in other ESIPT systems that protic solvents – such as H_2O, EtOH or MeOH – normally quench the [keto]* tautomer emission and favor the [enol]* tautomer emission due to the promotion of intermolecular hydrogen bonding between the solvent and the phenolic O-***H*** of the ligand, which disrupts the intramolecular H-bonding required for an ESIPT process to occur and destabilizes the planar conformation [55] [160] [176], as schematized in Figure 85 with a generic ESIPT-type molecule. There, it is shown how methanol, a protic solvent, can actively form hydrogen bonding interactions between itself and the O-H group of the molecule, thus greatly diminishing the proton transfer rate and making the [enol]* tautomer emission the predominant one.

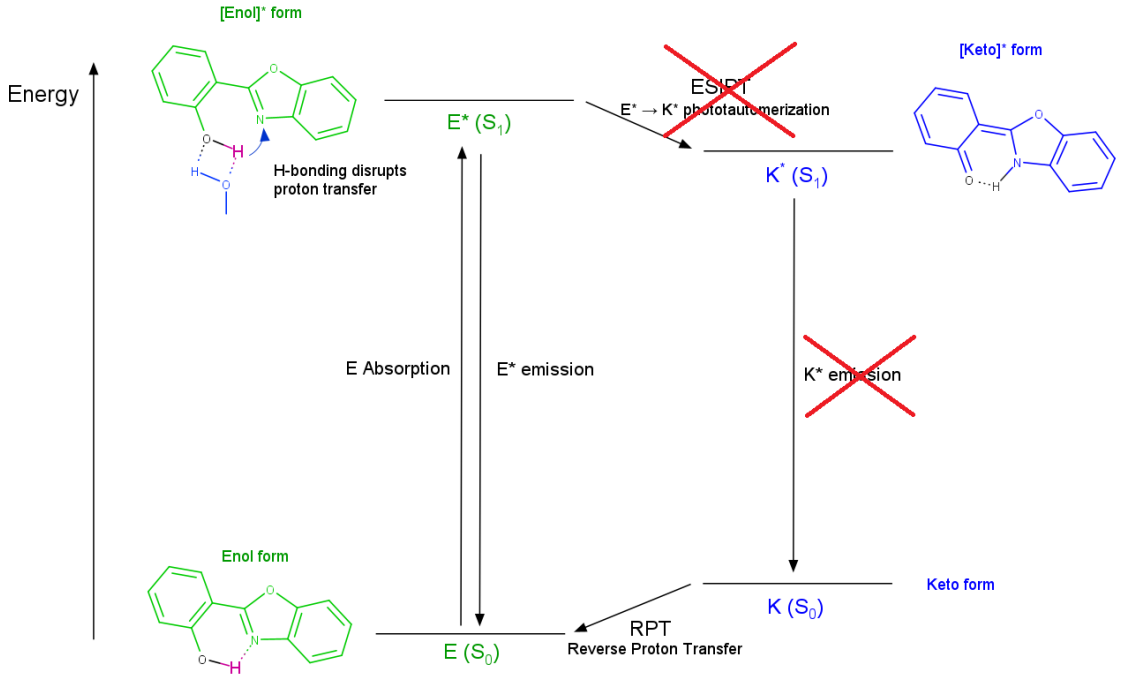

Figure 85. Schematic representation of the inhibition of the ESIPT mechanism of an oxazole derivative in a protic solvent.

It is clear that the solvent-induced inhibition of ESIPT does not occur in the case of **M4** and the reason may rely on its particular chemical structure. It has been reported that electron-donating substituents in the hydroxyphenyl entity of 2-(2-hydroxyphenyl)benzazoles diminish the acidity of the ***H*** atom of the *OH* group, with the consequence of decreasing the ESIPT rate and promoting the [enol]* emission [159]. It

can therefore be postulated that electron-withdrawing entities linked to this group, such as the oxime group and the benzimidazole moiety present in **M4**, have the opposite effect, meaning that they increase the acidity of the phenolic proton and thus promote the [keto]* tautomer emission instead.

Then, as mentioned in Section 2.1.2.2, the ESIPT process that governs the excited state of **M4** can produce *a priori* two different keto forms. For both of them, the proton is transferred from the O-***H*** group of the phenol moiety, but the receiving atom could be either the nitrogen of the benzimidazole moiety or the nitrogen of the oxime group. It has been reported that the pK_a values for the deprotonation of the nitrogen atom of benzimidazoles and of oximes are in the range of 5 to 6 and 4.5 to 5, respectively [176] [252], so it is not possible to make an accurate prediction of the directionality of the proton transfer based solely on this.

As mentioned in Section 2.1.2.1, a prerequisite for the ESIPT process to occur is to have preformed intramolecular hydrogen bonds in the molecular structure. Hence, although not entirely accurate due to being in two different states, the crystal structure of **M4** could give a clue about towards which nitrogen between the oximic and the benzimidazolic ones, the phenolic proton could be preferably linked to.

Crystals of **M4** were therefore obtained by slow evaporation of an ethanolic solution and the structure is shown in Figure 86, where it can be seen that the unit cell contains an additional molecule of ethanol. Noteworthy is that two internal hydrogen bonds take place. The first one being between the ***N*** atom of the oxime group and the ***O*** atom of the phenol group, while the second one occurs between the N-**H** atom of the benzimidazole and the ***O*** atom of the phenol group, the distances being 1.912 Å and 2.132 Å, respectively. These values reveal that these hydrogen bonds are relatively strong, especially the one formed between the phenolic proton and nitrogen group of the oxime.

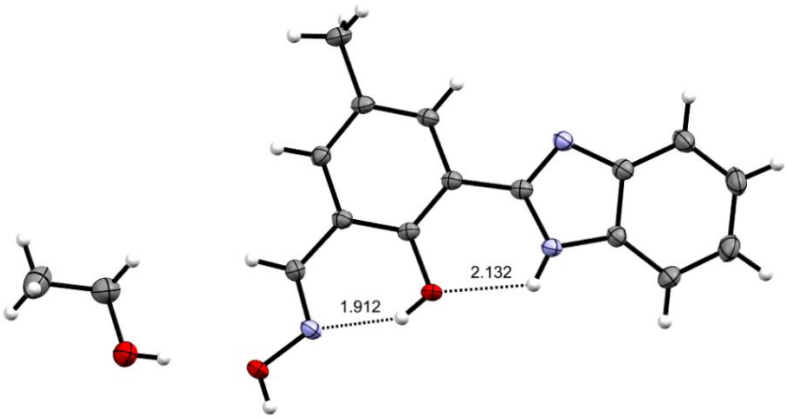

Figure 86. X-ray crystal structure of **M4**.EtOH showing intramolecular hydrogen bonds with dashed lines. Color code: grey for carbon; white for hydrogen; mallow for nitrogen; and red for oxygen.

Based on this information, an ESIPT phototautomerization process can be proposed and it is shown in Figure 87.

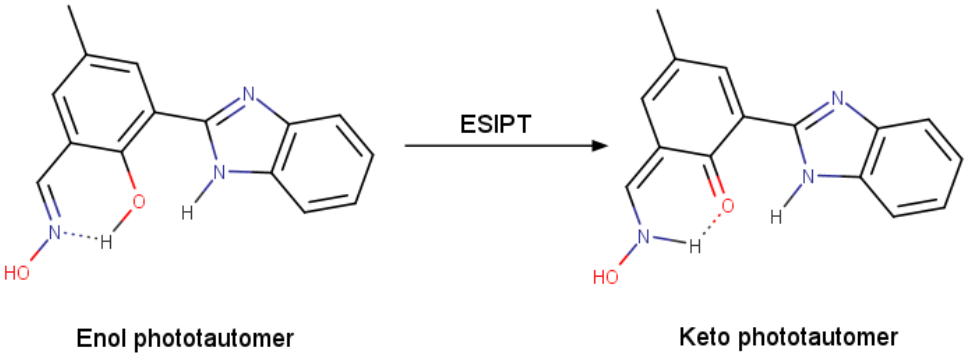

Figure 87. Proposed ESIPT mechanism for **M4**.

By its side, excitation of **M5** at 340 nm in EtOH : H_2O 1 : 4 resulted in three emission bands. The highest energy band at 386 nm is attributed to Raman scattering of the solvent and is clearly visible owing to the low emission intensity of this ligand (compared to other benzoxazoles) probably due to an active PET mechanism as predicted by the molecular design. Among the two other bands, the one shown at shorter wavelengths (405 nm) can be assigned to the emission of the [enol]* tautomer, while the broad red-shifted band with a high Stokes Shift centered at 496 nm can be attributed to the emission of the [keto]* tautomer as a consequence of the ESIPT process in the same fashion as already described for **M4**. In Figure 88, the proposed ESIPT phototautomerization process for **M5** can be appreciated along with the possible PET mechanism.

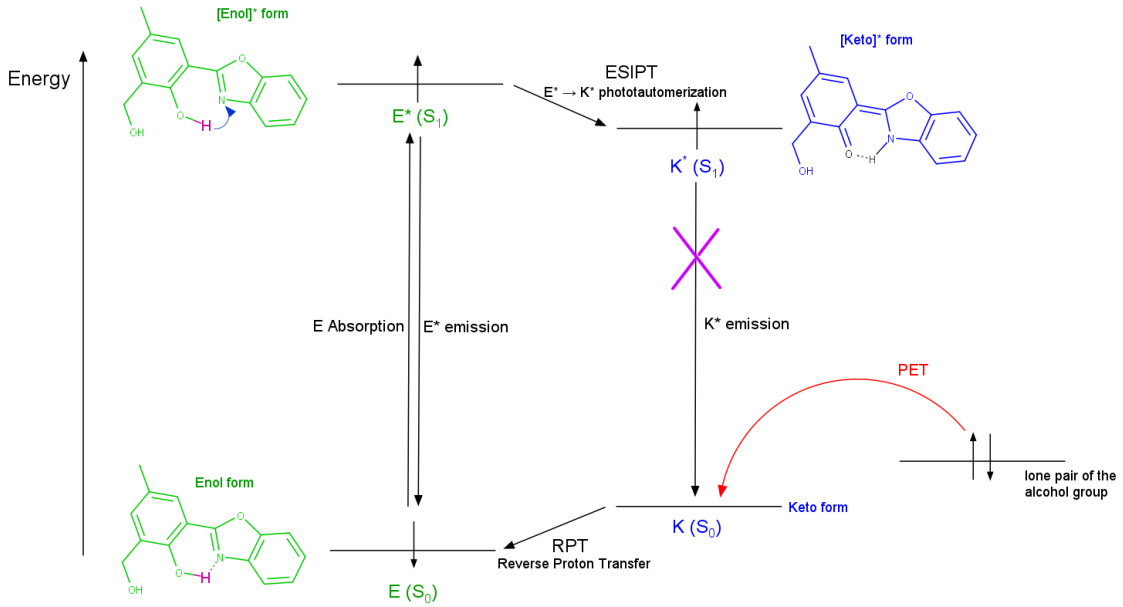

Figure 88. Proposed ESIPT and PET mechanisms for **M5**.

As mentioned in Section 2.1.2.4, the design of this ligand was based on a similar molecule reported by Shang [177], the difference being that the previously reported molecule possesses two hydroxymethyl groups, in *ortho* and *para* positions to the hydroxyphenyl, while **M5** possesses an hydroxymethyl group in *ortho* and a methoxy group in *para*. It can be noted that Shang's molecule only shows one emission band at 471 nm in HEPES buffer with a very low emission intensity. Unfortunately, it is not possible to compare the emission spectra in the same solvent because **M5** phases out in pure water medium; however, it is evident that the presence of a methoxy group completely altered the emission properties of the molecule, diminishing the ESIPT rate constant as expected. As mentioned before, electron-donating groups, such as methoxy, tend to decrease the ESIPT process due to a decrease in the acidity of the phenolic proton and this could explain why the emission of the [enol]* tautomer is seen in the present case and not for Shang's compound [159].

Finally, excitation of **M6** at 372 nm yielded an emission band centered at 575 nm. Similarly to our two previous benzazole derivatives, the very large Stoke's shift confirms the ESIPT capabilities of this ligand. The fact that the [enol]* tautomer cannot be seen in the emission spectrum could also be explained by the fact that there are two-electron withdrawing substituents in *ortho* position to the hydroxyphenyl group, thus greatly increasing the acidity of the phenolic proton.

In a similar fashion as that observed for **M4**, **M6** has the possibility to undergo two proton transfers: from the O-***H*** group of the phenol entity towards either the nitrogen atom of the benzoxazole unit or the nitrogen atom of the benzothiazole moiety, the basicity of these two nitrogen atoms determining the one that is favored. It is found in the literature that the pK_a of the nitrogen-protonated 2-(2-hydroxyphenyl)benzoxazole is 1.3 [253] and that of benzothiazole is 4.51 [185]. While it was not possible to find a reliable value for the pK_a of the nitrogen-protonated 2-(2-hydroxyphenyl)benzothiazole, it should not be far away from the one the non-derivatized molecule[9]. These pK_a values indicate that the nitrogen atom of the benzothiazole unit is more basic, which allows to propose the ESIPT phototautomerization process for **M6** seen in Figure 89.

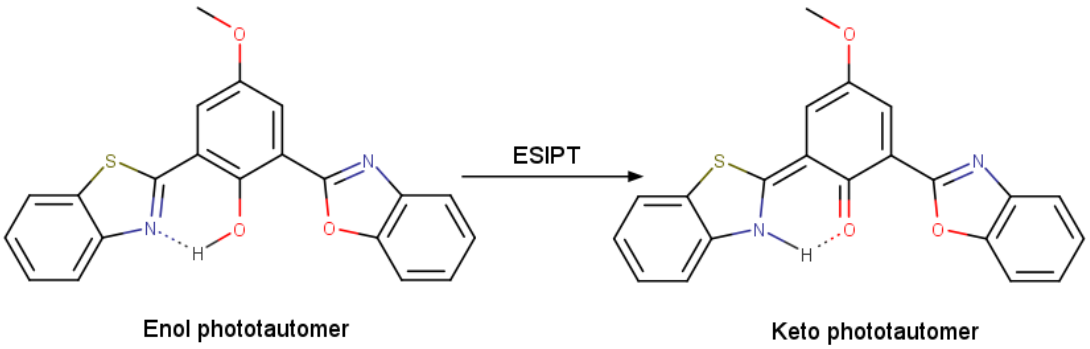

Figure 89. Proposed ESIPT mechanism for **M6**.

Comparing the spectral properties of **M6** with the similar molecule synthesized by Li [186], the difference being that they used a 2-hydroxynaphtyl instead of a 5-methoxy-2-hydroxyphenyl, two aspects can be highlighted. Firstly, the emission intensity of **M6** is higher than Li's molecule, even though the solvent system used in the present case contains almost 50 % water in comparison with only 10 % in the reported case. This difference can be explained thanks to a more planar conformation of our molecule, as, in Li's case, the bulky naphthyl group twists the benzazole moieties. Secondly, there is a ~25 nm red shift of the emission of **M6** in comparison with the reported molecule, owing probably to the increased planar nature of our compound.

For the three compounds, **M4**, **M5** and **M6**, the fact that ESIPT is strictly an excited state phenomenon can be emphasized by the very close similarity of their excitation and

[9] For instance, the pK_a of the nitrogen-protonated pure benzoxazole is -0.13. Also, the pK_a values of the nitrogen-protonated benzimidazole and 2-(2-hydroxyphenyl)benzimidazole are 5.53 and 5.48, respectively [246]

absorption spectra, ensuring that both emission bands originate from the same species in the ground state [254].

Finally, the fluorescence relative quantum yield value of **M4** in THF : H_2O 0.5 : 99.5 and of **M5** in EtOH : H_2O 1 : 4 were calculated using quinine sulfate and 9,10-diphenylanthracene, and quinine sulfate and norhamane as standards, respectively, following the procedure described in Section 2.3.1. The average results obtained are 0.1252 (12.52 %) for **M4** and 0.0215 (2.15 %) for **M5**.

In the case of **M6**, unfortunately, the cross-calibration of the standards described in Section 2.3.1 could not be made because only one standard in our chemical library is suitable for measuring quantum yields at an excitation wavelength of 372 nm. Due to this limitation, it can be said that the confidence value of the calculated QY value for **M6** will be lower than for the other two benzazole derivatives. Nonetheless, the fluorescence relative quantum yield value of this ligand in THF : EtOH : H_2O 0.4 : 49.8 : 49.8 medium was still obtained and found to be 0.1397 (13.97 %) using 9,10-diphenylanthracene as standard[10]. The three quantum yield plots can be seen in Figure 90.

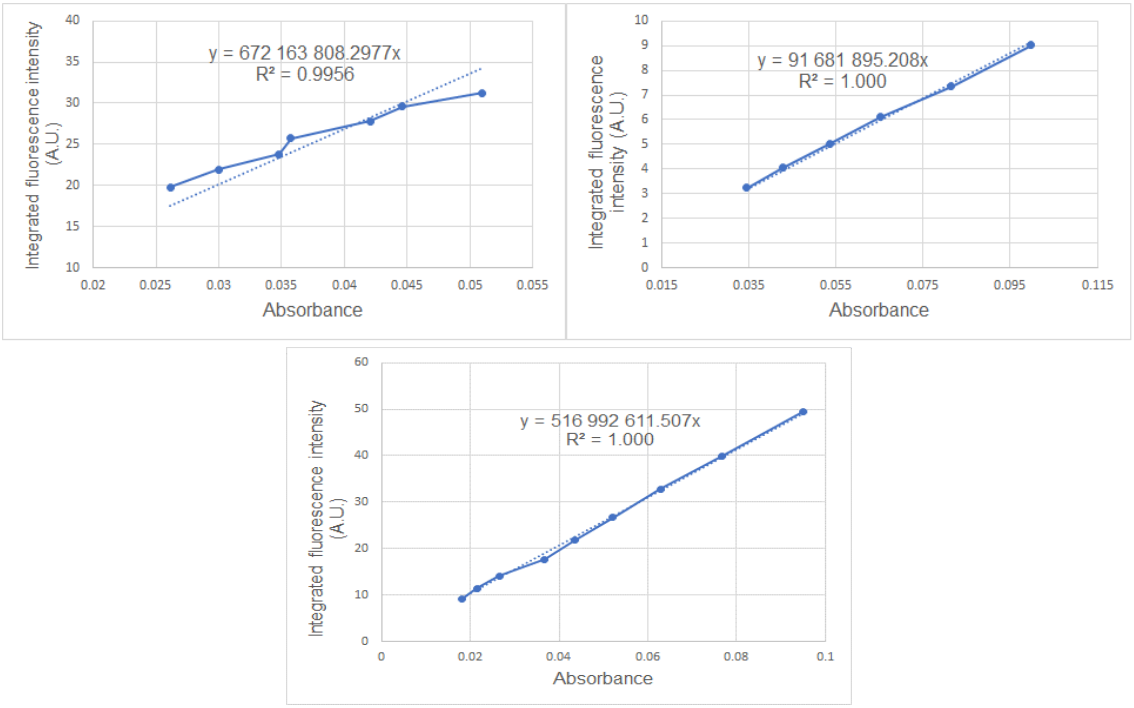

[10] Also, the refractive index was calculated only considering water and ethanol as constituents of the solvent mixture.

Figure 90. Plots used to calculate the fluorescence quantum yield values of **M4** (top left), **M5** (top right) and **M6** (bottom). Average fluorescence quantum yield values are 0.1252 ± 0.013, 0.0215 ±0.002 and 0.1397 ± 0.014, respectively.

3.3 Coumarin derivative: M7

The UV-vis absorption, excitation and emission spectra of **M7** were recorded in a mixture of THF : EtOH 1 : 51 with its concentration set at 17.1 μmol/L. They can be seen in Figure 91.

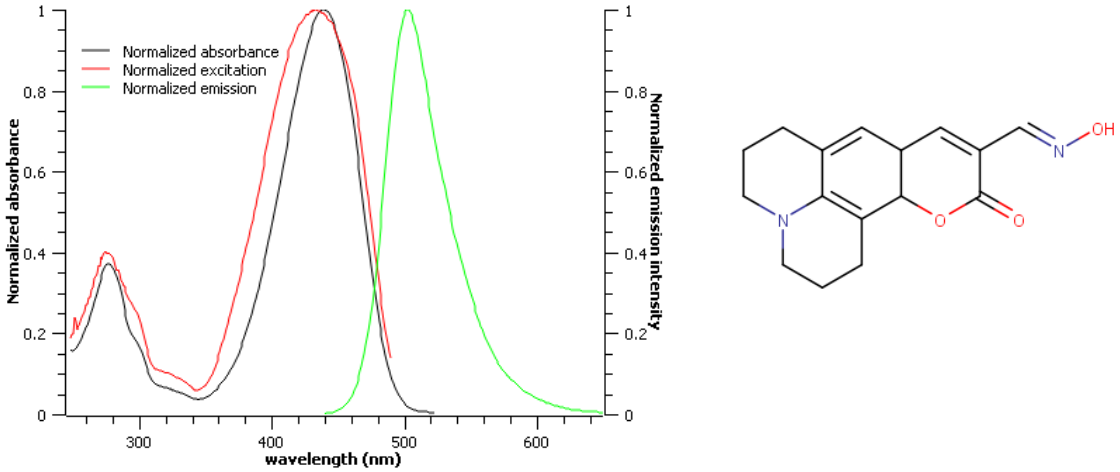

Figure 91. Normalized absorption (black), normalized excitation (red, λ_{em} = 503 nm) and normalized emission (green, λ_{exc} = 431 nm) spectra of **M7** in THF : EtOH 1 : 51 medium. ε(**M7**) = 6 500 L.mol^{-1}.cm^{-1}. The chemical structure of **M7** can be seen on the right.

The UV-vis absorption spectrum of this coumarin derivative shows two main bands. The one at lower energy (440 nm) corresponds to the typical charge transfer band of coumarins when they are substituted by an electron-donating group in their 7 position and it is particularly red shifted owing to the greater donating power of the nitrogen atom of the julolidine entity thanks to the inductive effect +I of their aliphatic rings [194] [255] [256].

Then, when excited at 431 nm, **M7** shows a narrow emission band centered at 503 nm with a very high emission intensity. This band is attributed to the internal charge transfer mechanism that governs the excited state of the ligand, as schematized in Figure 92. It is important to mention that the rigidification of the amino group in the julolidine entity prevents the so called twisted intramolecular charge transfer (TICT), which is a

mechanism in which radical species in the excited state are formed and accounts for the non-radiative decaying pathways [192] [257].

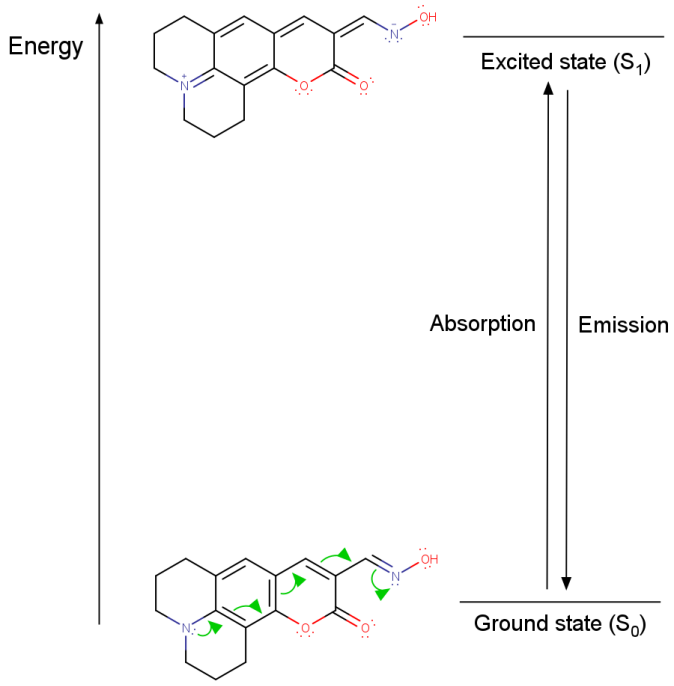

Figure 92. Internal charge transfer mechanism for **M7**.

The measurement of the absorption and emission spectra of **M7** in a near perfect aqueous medium (98 % H_2O) was explored in order to compare them with those of the coumarin analog derivative that possesses a diethylamino group in place of the julolidine moiety [195] [258]. Unfortunately, the ligand aggregates in this medium, which is evidenced by the strong diffusion of the absorption spectrum. Probably, the rigidity of the julolidine entity hampers the compatibility of our coumarin with H_2O.

3.4 Porphyrin derivatives: M8, M9 and their Pt(II) and Pd(II) metallocomplexes

3.4.1 M8 and M9

The UV-vis absorption, excitation and emission spectra of **M8** and **M9** were recorded in 100 % $CHCl_3$ with a concentration of 3.7 μmol/L in both cases. They can be seen in Figure 93 and Figure 94, respectively.

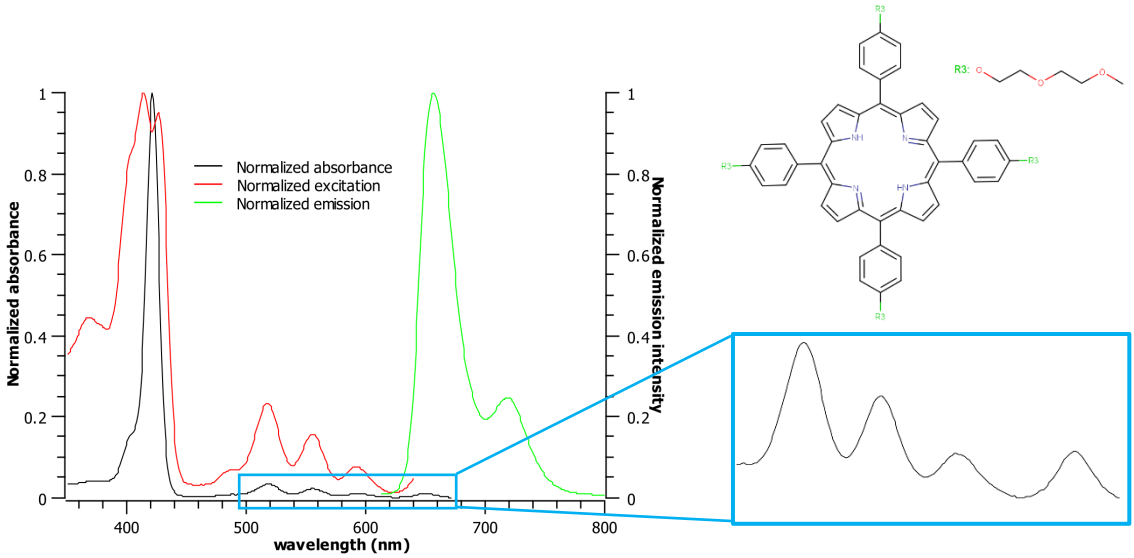

Figure 93. Normalized absorption (black), normalized excitation (red, λ_{em} = 657 nm) and normalized emission (green, λ_{exc} = 422 nm) spectra of **M8** in 100 % $CHCl_3$ medium. ε(**M8**) = 524 200 L.mol^{-1}.cm^{-1}. Inset: zoom of the absorption spectrum in the range from 495 to 675 nm showing the Q bands of the macrocycle. The chemical structure of **M8** can be seen on the right. The slits used were 5 nm / 5 nm.

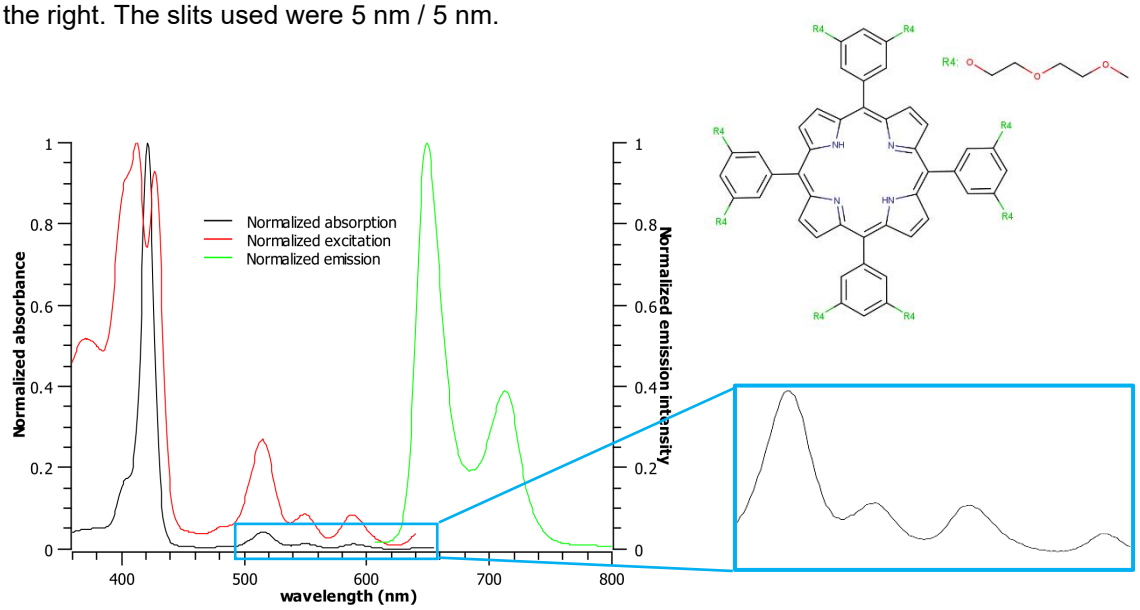

Figure 94. Normalized absorption (black), normalized excitation (red, λ_{em} = 649 nm) and normalized emission (green, λ_{exc} = 420 nm) spectra of **M8** in 100 % $CHCl_3$ medium. ε(**M9**) = 596 630 L.mol^{-1}.cm^{-1}. Inset: zoom of the absorption spectrum in the range from 495 to 660 nm showing the Q bands of the macrocycle. The chemical structure of **M9** can be seen on the right. The slits used were 5 nm / 5 nm

The UV-vis absorption spectra of both porphyrin derivatives are consistent with what has been extensively reported in the literature for this family of molecules. The high energy band at 422 nm (for **M8**) and 421 nm (for **M9**) is called the Soret or B(0,0) band and is assigned to the $S_2 \leftarrow S_0$ transition. The additional four bands located in the visible region of the spectra (zoomed in the inlets of Figure 93 and Figure 94) at 519, 556, 594 and 649 nm, and 515, 551, 589 and 645 nm for **M8** and **M9**, respectively, are the so-called Q bands and correspond to four different $S_1 \leftarrow S_0$ transitions that arise due to the asymmetry of the central core of the porphyrin macrocycle. From lower to higher energy, the nomenclature of these bands is $Q_x(0,0)$, $Q_x(1,0)$, $Q_y(0,0)$ and $Q_y(1,0)$ [259] [260] [261] [262] [263].

In the same manner, the emission spectra of **M8** and **M9** are also consistent with previous reports. When excited at the corresponding excitation wavelength of their Soret bands, both molecules show an intense and high energy fluorescence band at 657 and 649 nm, respectively, that is assigned to the $Q_x(0,0)$ $S_0 \leftarrow S_1$ transition and a second band at 720 and 713 nm, respectively, assigned to the $Q_x(1,0)$ $S_0 \leftarrow S_1$ transition [260] [261].

Finally, it can be noticed that the emission of **M9** is slightly blue shifted in comparison to that of **M8**. As seen in the structures of the molecules (Figure 54), the difference between these macrocycles is that the former has the phenyls substituted at the *meta* position while they are at the *para* position for the latter. While this observation cannot be adequately explained, it is consistent with the reviewed literature. For example, Ormond reported a similar behavior with *para*-hydroxyphenyl and aminophenyl porphyrins having an emission at lower energies than the corresponding *meta* derivatives [259].

3.4.2 M8-Pd, M8-Pt, M9-Pd and M9-Pt

The UV-vis absorption, excitation and emission spectra of the four porphyrin complexes were recorded in 100 % $CHCl_3$ solutions that were previously bubbled with Ar for 10 minutes, all at a concentration of 3.7 μmol/L. They can be seen in Figure 95 (**M8-Pd**), Figure 96 (**M9-Pd**), Figure 97 (**M8-Pt**) and Figure 98 (**M9-Pt**).

The absorption spectrum of all these compounds is characteristic for Pd and Pt-metalated porphyrins. In the first place, they all exhibit the classic Soret band in the ultraviolet region and the two Q bands in the visible. The λ_{abs} values are summarized in Table 2.The decrease in the number of Q bands in comparison with the free ligands are a result of the increased molecular symmetry of the porphyrin complexes, owing to the loss of the two hydrogen atoms from their central core [260] [264]. Also, the general blue

shift of the absorption bands accounts for the hypsochromic effect of palladium(II) and platinum(II) [265] [266].

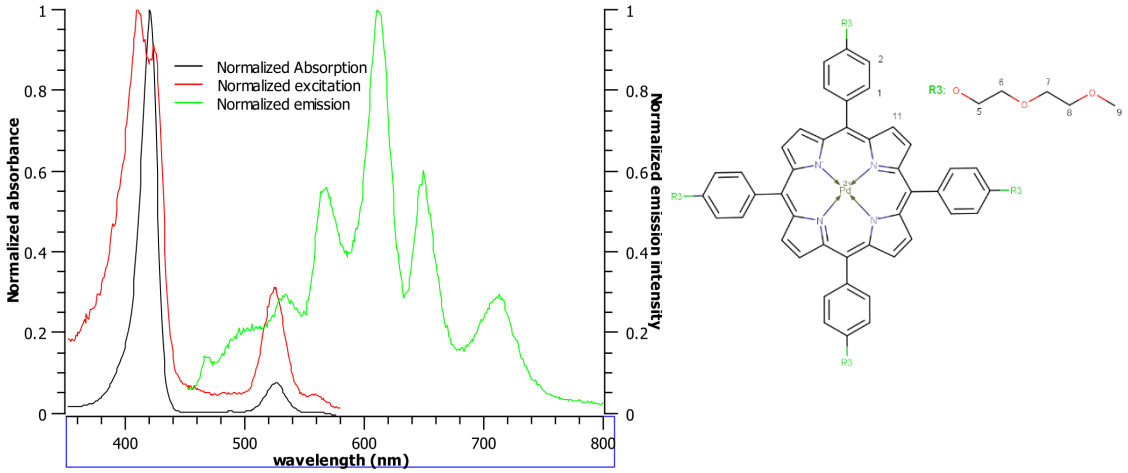

Figure 95. Normalized absorption (black), normalized excitation (red, λ_{em} = 613 nm) and normalized emission (green, λ_{exc} = 410 m) spectra of **M8-Pd** in 100 % $CHCl_3$ medium. ε(**M8-Pd**) = 398 360 L.mol^{-1}.cm^{-1}. The chemical structure of **M8-Pd** can be seen on the right. The slits used were 5 nm / 5 nm.

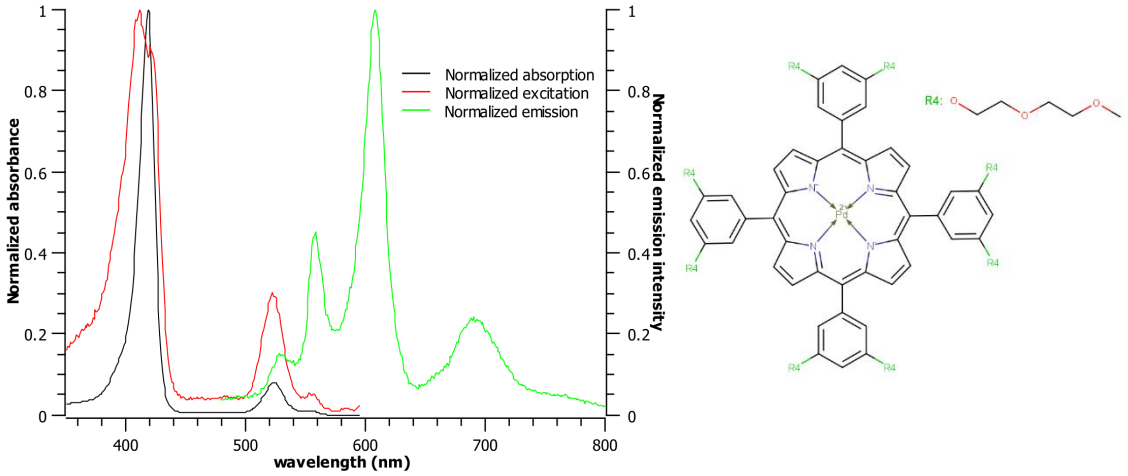

Figure 96. Normalized absorption (black), normalized excitation (red, λ_{em} = 609 nm) and normalized emission (green, λ_{exc} = 410 m) spectra of **M9-Pd** in 100 % $CHCl_3$ medium. ε(**M9-Pd**) = 379 390 L.mol^{-1}.cm^{-1}. The chemical structure of **M9-Pd** can be seen on the right. The slits used were 5 nm / 5 nm.

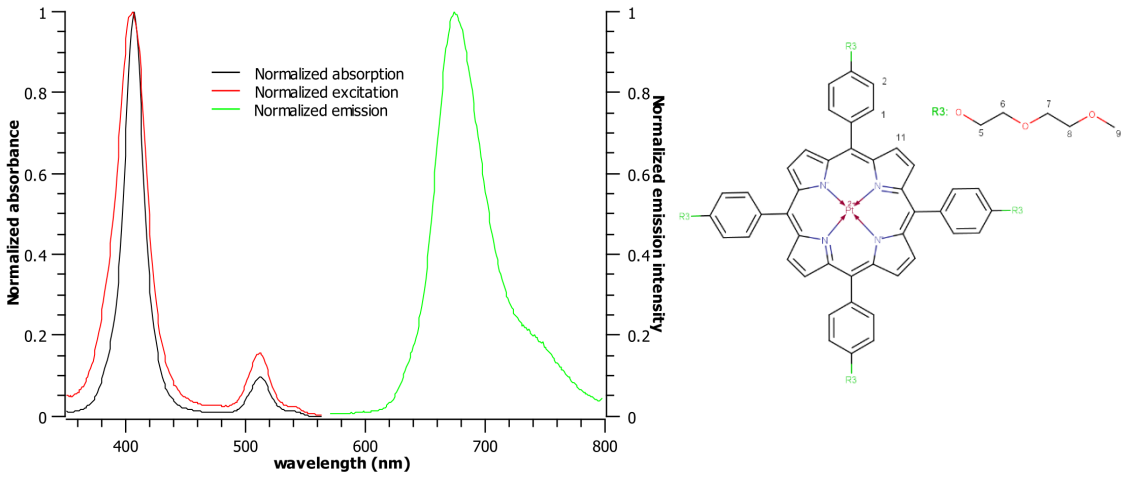

Figure 97. Normalized absorption (black), normalized excitation (red, λ_{em} = 677 nm) and normalized emission (green, λ_{exc} = 405 m) spectra of **M8-Pt** in 100 % $CHCl_3$ medium. ε(**M8-Pt**) = 206 050 L.mol^{-1}.cm^{-1}. The chemical structure of **M8-Pt** can be seen on the right. The slits used were 5 nm / 5 nm.

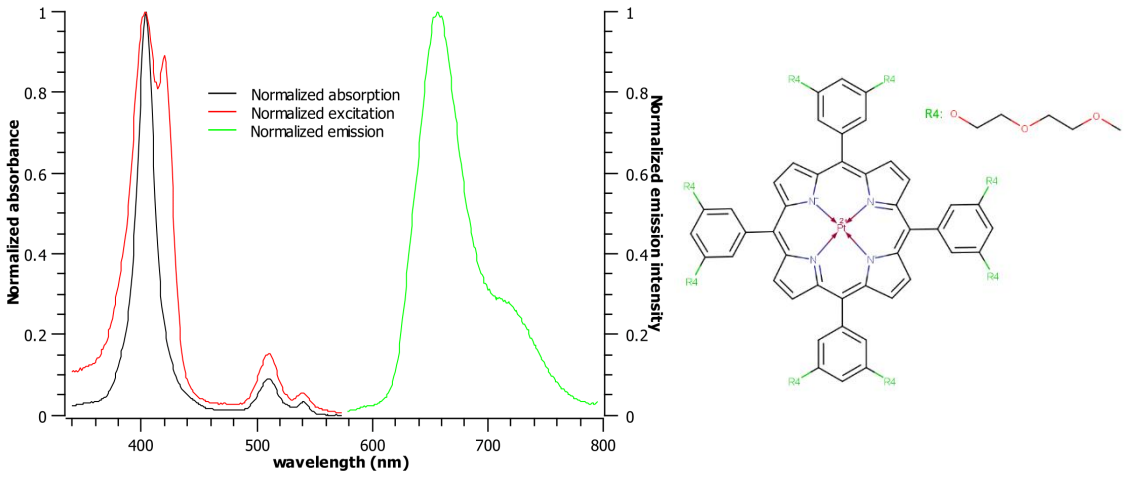

Figure 98. Normalized absorption (black), normalized excitation (red, λ_{em} = 656 nm) and normalized emission (green, λ_{exc} = 404 m) spectra of **M9-Pt** in 100 % $CHCl_3$ medium. ε(**M9-Pt**) = 167 280 L.mol^{-1}.cm^{-1}. The chemical structure of **M9-Pt** can be seen on the right. The slits used were 5 nm / 5 nm.

Table 2. λ_{abs} values for the four porphyrin complexes in 100 % $CHCl_3$

Complex	λ_{abs} Soret band (nm)	λ_{abs} Q bands (nm)
M8-Pd	420	526, 560
M9-Pd	418	524, 555
M8-Pt	407	512, 541
M9-Pt	404	511, 541

The emission spectrum of the four metalloporphyrins also comply with previous reports. For instance, **M8-Pd** (Figure 95) shows four emission bands at 566, 611, 648 and 712 nm. The two bands at higher energy can be assigned to the $S_0 \leftarrow S_1$ transition, in a similar way as in the corresponding ligand. The two additional low energy bands, for their part, are assigned to the $S_0 \leftarrow T_1$ phosphorescence transition. In the case of **M9-Pd** (Figure 96), however, only three high intensity bands can be seen, with those at 558 and 609 nm assigned to the $S_0 \leftarrow S_1$ and the one at 690 nm, to the $S_0 \leftarrow T_1$ transition [265] [266] [267] [268] [269]. It is not clear why the second phosphorescence band cannot be observed in this complex, but it is possible that it lies under the band at 609 nm. Moreover, in these two compounds a low emissive blue shifted band at 533 (**M8-Pd**) and 527 nm (**M9-Pd**) can also be seen which may account for an E-type delayed fluorescence [265] or to the bleaching of the ground state [270].

The emission spectra of the platinum(II) analogs **M8-Pt** and **M9-Pt** are simpler, as they are both completely dominated by the $S_0 \leftarrow T_1$ phosphorescence transitions at 674 and 742 nm (shoulder), and 657 and 716 nm, respectively [265] [266].

These results show that there is an active intersystem crossing mechanism from the first singlet excited state (S_1) to the first triplet excited state (T_1) in the four complexes. It is in fact the presence of platinum(II) and palladium(II), owing to their 'heavy' nature because of their high number of protons, that enhances the rate of the intersystem crossing by an increase in the spin-orbital interactions between the π^* orbitals of the porphyrin and the *d* orbitals of the metal. As these orbitals are closely located, their singlet and triplet states are efficiently combined [266] [271]. As the Pt^{2+} cation is heavier than the Pd^{2+} one, it could be expected that it promotes a higher rate of triplet state formation, which explains the predominance of the $S_0 \leftarrow T_1$ emission over the $S_0 \leftarrow S_1$ one [272].

4 Sensing studies

In this Chapter, the sensing performance of the 11 molecules whose photophysical properties were described previously will be presented. For the pyrene, benzazole and coumarin derivatives, in general terms, the study will be divided in 4 sections. In the first one, bulk test to probe the sensitivity of the compounds against a wide variety of analytes will be presented and discussed, along with tests in acidic and basic media, which will be particularly and thoroughly analyzed. As mentioned in Section 2.3.3, these bulk tests are made to obtain a first clue about the capabilities of the molecules to detect species at high concentration values. That logic that has been applied is that, if there is no change in the luminescence properties of our compounds when exposed to an analyte in these conditions, it can be considered that they are transparent towards that species and they will no longer be investigated. Next, the emission and/or absorption titrations of the probes against the analytes they are sensitive to will be shown and the limits of detection will be presented. These values carry importance as they allow to set the thresholds in which the molecules can be used in potential real-life assessments. Thirdly, the sensing mechanisms by which the compounds can detect their correspondent target analytes will be investigated to be elucidated and discussed. In these sections, it will be explored how the probe-analyte interaction affects the photophysical properties of the free molecule and, when possible, how these two species interact in terms of structure, stoichiometry and strength. Finally, the interference tests will be shown and discussed. As described in Section 2.3.8, these tests are made with the rationale of verifying how other common species present in solution can affect the sensitivity of the probes.

As for the four porphyrin derivatives, the results of their sensitivity towards O_2 and their potential to elaborate recyclable sensors will be provided and discussed.

4.1 Pyrene derivatives: M1, M2 and M3

4.1.1 M1

As mentioned in 2.1.1.2, the new molecule **M1**, which chemical structure is shown in Figure 99, was designed with the principal objective of detecting Hg^{2+} and/or Cu^{2+}, possibly along with anionic species such as F^-. Moreover, it was expected that it could act as a chemodosimeter for hypochlorite sensing.

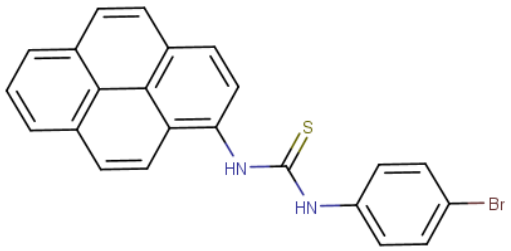

Figure 99. Chemical structure of **M1**.

Mercury is one of the most toxic heavy metals in the environment, where it can be found in three different species: elemental (Hg^0), inorganic (Hg^{2+}) and organic (alkyl or aryl-Hg species), the middle form being the detection target in the present thesis work. Mercury(II) is mainly found in soil and water, from where it can enter the human body *via* consumption of contaminated liquids or food. In the human body, it can accumulate causing damage in the gastrointestinal tract, collapse of kidney functions, stomatitis, gastroenteritis and immune system disorders [273].

Copper is a trace element considered as an essential micronutrient as it is necessary for a wide array of enzymatic processes in proto and eukaryote. However, as its ionic form Cu^{2+} is readily soluble and bioaccumulated in plants, it can enter the human body with relative ease [274]. There, if present above certain concentration thresholds, it has been linked to the most common neurodegenerative disorders, such as Alzheimer's, Parkinson's, Huntington's and Wilson's diseases, among others [275].

It is then evident that the detection of these two metallic cations in water systems is of great importance because of the danger they possess to human beings and, in general terms, to the environment.

Finally, as mentioned in Section 1.2.2.5, hypochlorite is widespread used as a domestic disinfectant agent and its presence is linked to microbial absence and, by consequence, of good water quality. Moreover, its presence in water media rich in organic matter promotes the discharge of toxic byproducts, such as chloramines, owing to its oxidizing capabilities. Hence, its constant detection and monitoring are necessary as a quality control parameter of water.

4.1.1.1 Bulk tests

Bulk tests in 100 % THF were carried out following the procedure described in Section 2.3.3. The cation and anion bulk test results are shown in Figure 100 and Figure 101, respectively.

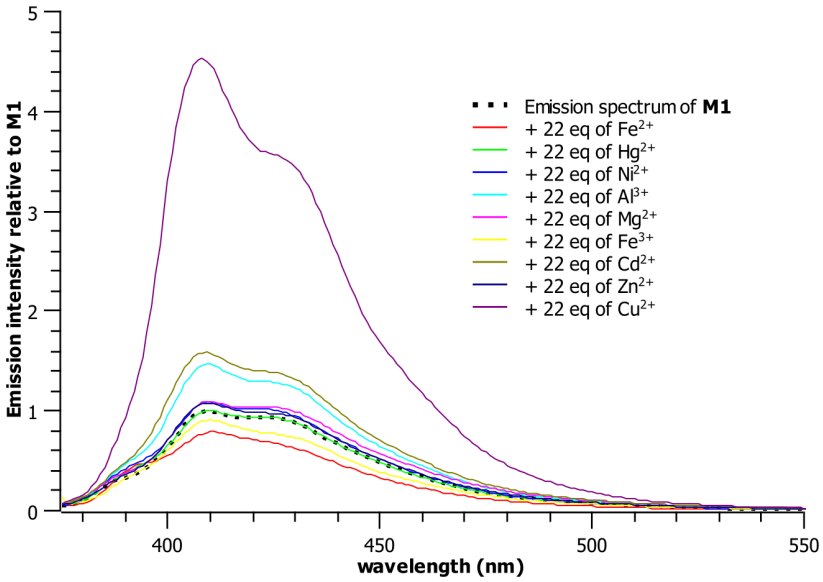

Figure 100. Emission spectrum of **M1** (4.6 μmol/L in 100 % THF) in presence of an excess (22 equivalents) of several metallic cations; λ_{exc} = 364 nm. The slits used were 5 nm / 5 nm.

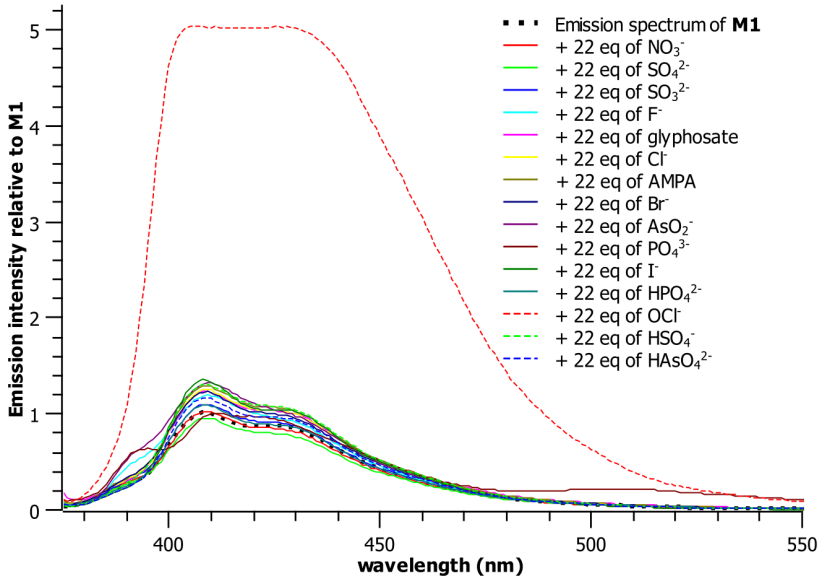

Figure 101. Emission spectrum of **M1** (4.6 μmol/L in 100 % THF) in presence of an excess (22 equivalents) of several anions; λ_{exc} = 364 nm. The slits used were 5 nm / 5 nm.

It can be clearly seen in both Figures that **M1** is relatively highly sensitive to OCl^- and Cu^{2+} by straight enhancement of its fluorescence emission. However, the enhancement that these ions caused to the fluorescence of the ligand was so drastic that apparently the detector of the spectrophotometer got saturated and thus the observed shape of the new emission band is very broad, especially in the case of OCl^-. The reason why this happened was that slits initially set at 5 nm/5 nm were used. In order to obtain better spectra, the bulk test was remade with optimized experimental conditions and the results (Figure 102) verified that the emission of the ligand experiences a huge enhancement in both cases: 40-fold in presence of Cu^{2+} and 70-fold in presence of OCl^-. This confirmed the prediction that was made in the design of the molecule (Section 2.1.1.2). When comparing these sensing results with those of Lin [117], who used a very similar ligand (the difference being a methyl instead of a bromide group) claiming it was sensitive to Hg^{2+} and Cu^{2+}, it can be seen that **M1** is not sensitive to the former cation. The reason may rely on the solvent medium used for the tests: while in the present case, a 100 % THF medium was used, Lin used a DMSO/H_2O mixture[11].

Also, it is noteworthy that this compound is not sensitive to any other anion tested. The reasons may rely on the high solvation energies of these species, which is an impediment for efficient sensing [276].

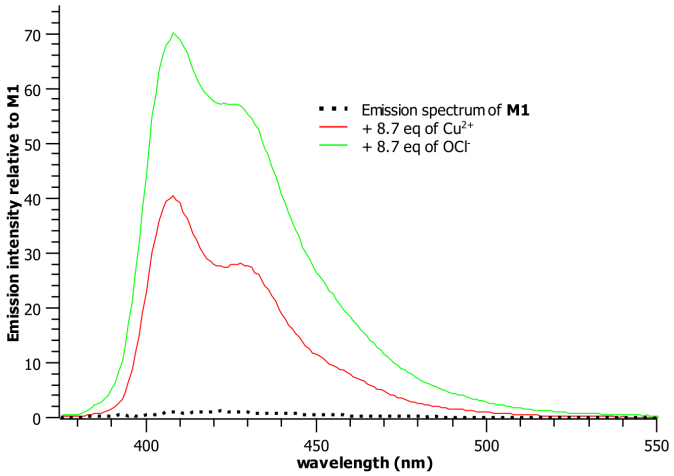

Figure 102. Bulk test of **M1** (11.6 μmol/L in 100 % THF) against Cu^{2+} and OCl^- using optimized conditions; λ_{exc} = 364 nm.

As **M1** has groups that could react either in acidic or basic medium, the response of this compound upon addition of different aqueous solutions of different pH was carried out.

[11] Due to time constraints, the solvent system used by Lin was not applied with our molecule.

The results can be seen in Figure 103 and indicate that there is also a huge enhancement of the emission intensity when protonation and deprotonation processes occur, with a new band centered at ~390 nm in the latter case. Interestingly, while only around 9 equivalents of OH^- were enough to drastically change the emission spectrum of **M1**, a much higher amount of H^+ was needed for a change to occur.

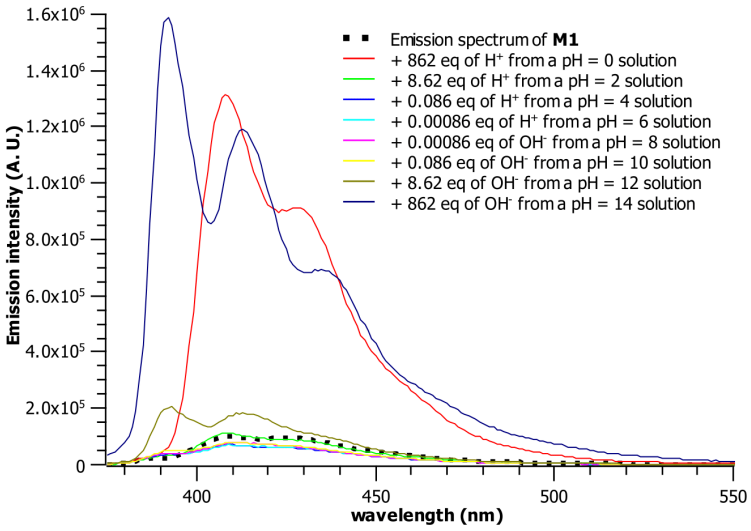

Figure 103. Emission spectrum of **M1** (11.6 μmol/L in 100 % THF) in presence of different quantities of acid or base; λ_{exc} = 364 nm.

The changes in the emission spectrum of **M1** upon addition of an acid or a base can be explained owing to the protonation and deprotonation capabilities of the molecule in the sulfur and nitrogen atoms, respectively. It is stated in literature that thioureas are firstly protonated at the sulfur atom in acidic conditions (and not at the nitrogen atoms as in urea) [277], so the enhancement observed in Figure 103 is the consequence of this reaction. However, as the equivalent amount of acid needed for a change to happen is extremely high (> 800 equivalents), it can be stated that the pK_aH value of this process is probably very low and negative. Thus, its effect is not representative of the acidity levels of the medium in which this molecule intends to be used. On the other hand, the deprotonation of the molecule most possibly occurs at one of the two N-**H** atoms of the thiourea moiety. According to Jakab *et al*, typical pK_a values for substituted thioureas range between 8 and 20 in DMSO. Interestingly, for diphenyl thiourea, which is somewhat structurally similar to **M1**, the pK_a value is around 13 and it further decreases when electron withdrawing groups are introduced to the adjacent benzene rings [278]. It can therefore be expected that not much base is needed to promote this process, which explains the lower number of equivalents of OH^- needed (in comparison with H^+) to

generate an appreciable change of the emission. A scheme with the proposed protonation and deprotonation reactions can be seen in Figure 104. Also, the effect of an acidified or basified medium in the sensing capabilities of **M1** towards Cu^{2+} will be analyzed in Section 4.1.1.4.

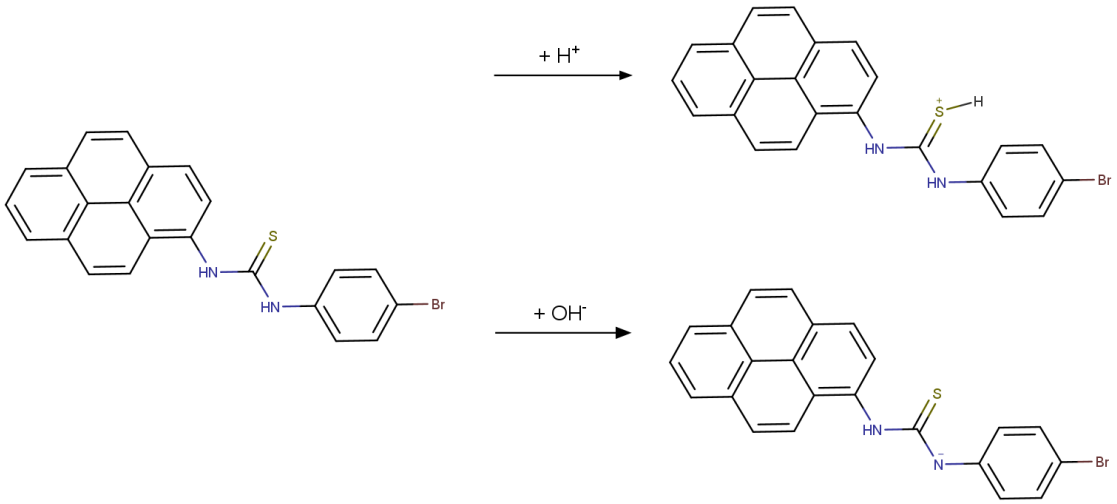

Figure 104. Proposed protonation and deprotonation reactions of **M1** in acidic and basic conditions[12].

All this being said, it is important to note that since the responses in acidic and basic media are different, **M1** could be a candidate for an effective pH sensor, with a special sensitivity at higher pH values due to the new and unique band that arises at these conditions. It can hence be proposed that **M1** can detect basic solutions starting at pH 10 onwards and acidic solutions starting at pH 2 downwards.

4.1.1.2 Calibration curves

Emission titrations of **M1** in 100 % THF were carried out against Cu^{2+} and OCl^- following the procedure described in Section 2.3.4. In all cases, the concentration of the ligand was 11.6 μmol/L and the final point of the titration occurs upon addition of a total of 4.31 equivalents of the analyte into the solution. The emission titration profiles of **M1**-Cu^{2+} and **M1**-OCl^-, and their corresponding calibration curves are shown in Figure 105 and Figure 106, respectively. It is important to mention that the small dilution generated by the addition of the analyte solution was taken into account to obtain the calibration curves.

[12] It is also possible that the deprotonated nitrogen atom is the one adjacent to the pyrene entity.

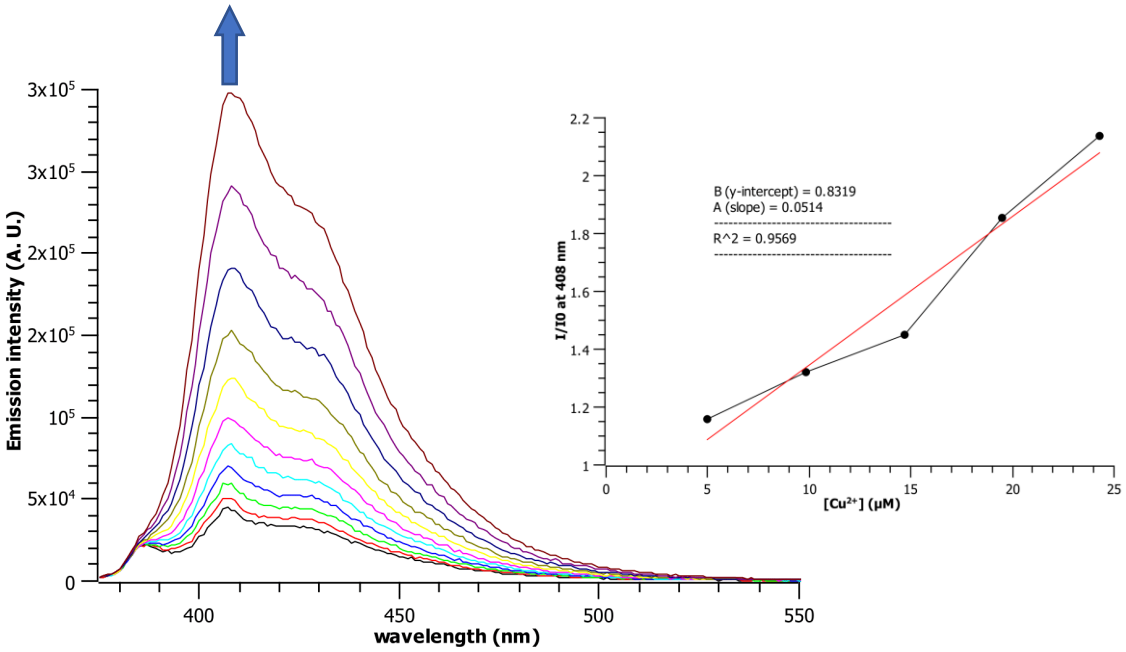

Figure 105. (left) Emission titration profile of **M1** against incremental quantities of Cu^{2+}. [**M1**] = 11.6 μmol/L; λ_{exc} = 364 nm. (right) Calibration curve for this titration (I/I_0 at 408 nm *vs*. [Cu^{2+}]. Each point has a calculated error of 12 %.

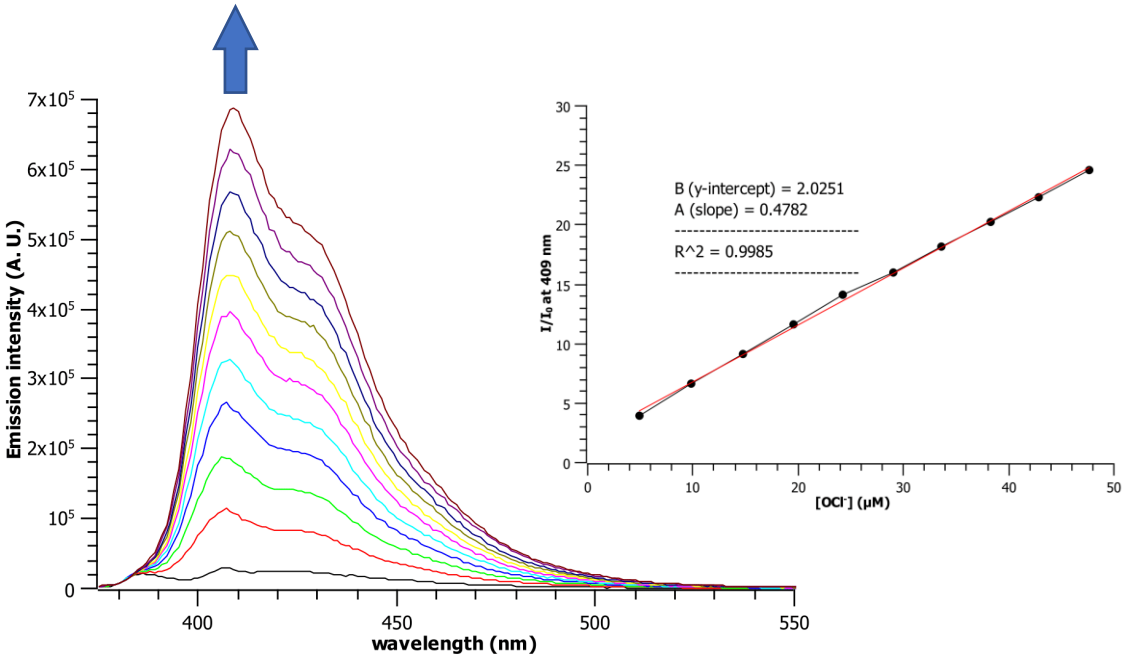

Figure 106. (left) Emission titration profile of **M1** against incremental quantities of OCl^-. [**M1**] = 11.6 μmol/L; λ_{exc} = 364 nm. (right) Calibration curve for this titration (I/I_0 at 409 nm *vs.* [OCl^-]). Each point has a calculated error of 12 %.

It is important to mention that the calibration curves presented in the insets of Figure 105 and in Figure 106, and in all the calibration curves that will be presented next in this manuscript, only show the points that account for a linear and continuous Emission intensity *vs* Concentration response, which means that not all the spectra plotted in the emission profiles are used. The reasons why linearity is not maintained in the whole titration could be due to changes in the concentration of the molecule (as with each titration point the volume of the medium increases and the dilution effect correction made may not be sufficient), changes in pH/acidity/basicity of the medium at higher concentration of the analytes, among others. For instance, the calibration curve that represents the whole titration process of **M1** against Cu^{2+} can be seen in Figure 107, where it is evident that linearity in only obtained in the first 5 points (which are shown in Figure 105 inset). Due to this, each time that a calibration curve is presented, it will be clearly stated in which titration range the response is linear.

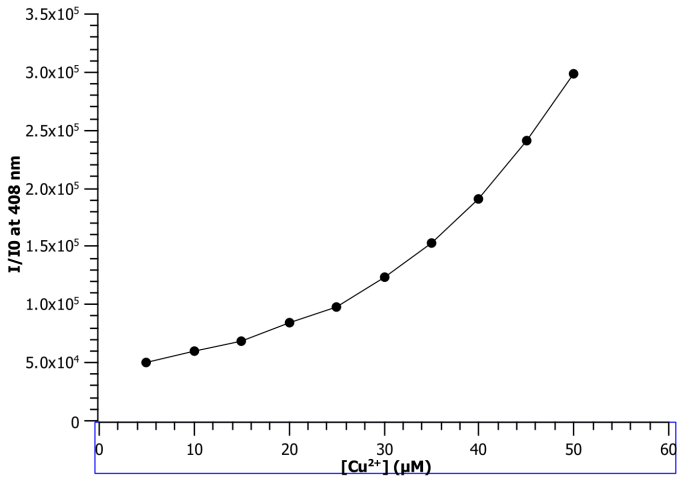

Figure 107. Complete calibration curve for the **M1**-Cu^{2+} titration.

This being said, it can be seen in Figure 105 that there is a linear response of **M1** towards the copper cation in the ~5 to ~25 μmol/L range for the concentration of the analyte. For its part, Figure 106 shows a linear response of the ligand towards the hypochlorite anion in the ~5 to ~50 μmol/L of OCl^- concentration range. Using the information obtained from these titration profiles, the limits of detection towards these analytes were calculated using the 3σ method (Section 2.3.5). The results are 9.71 ± 1.17 μmol/L and 1.01 ± 0.23 μmol/L for Cu^{2+} and OCl^-, respectively.

According to the European Union Council Directive 98/83/EC on the quality of water intended for human consumption[13], the acceptable limit of Cu in this medium is 31.47 μmol/L. Since the limit of detection of **M1** towards the corresponding metallic cation lies below the EU limits, it could be considered as a good candidate to be used in real-life water quality assessment.

As for the detection of OCl^-, it is worth to note that the NaOCl salt is the main active agent in commercially available bleach, and that it is sold in aqueous solutions at concentrations that typically range from 2 % to 10 % of OCl^-[14,15]. Thus, at the lowest, its concentration is around 0.3 mol/L. Moreover, the Center for Disease and Control Prevention (CDC) and the World Health Organization suggest that the concentration of hypochlorite in piped water treatment systems for an effective removal of bacteria should be in the range from 0.2 to 0.5 mg/L (4 – 10 μmol/L)[16,17]. As the limit of detection of OCl^- by **M1** is as low as 1.01 μmol/L, it can be said that this molecule is an excellent candidate to be used in bleach detection and monitoring.

4.1.1.3 Sensing mechanism

The sensing mechanism of **M1** towards the hypochlorite and copper ions was investigated. Firstly, towards OCl^-, in the reviewed literature, it is interesting to note that, basically, each author proposes a different sensing mechanism of thiourea-based chemosensors towards this analyte. For example, P. Zhang [115] and So [120] propose a desulfurization reaction, which oxidizes the thiourea group into urea disabling the PET mechanism of the ligand and with an enhancement of the emission. Lin [113] and X. Zhang [116] also propose this mechanism, but they postulate that a cyclization reaction then occurs between an adjacent nitrogen atom and the carbon of the recently formed urea group. Finally, Lee [112] and Pham [114] indicate that the thiourea moiety is cleaved from the ligand, thus regenerating the amine or forming an iminium ion, respectively. Some of these reaction mechanisms can be seen in Figure 108. In all reported cases, there is a desulfurization reaction which, as explained in Section 1.2.2.5, means that thiourea-based ligands act as chemodosimeters towards the hypochlorite anion.

---

[13] https://www.lenntech.com/applications/drinking/standards/eu-s-drinking-water-standards.htm

[14] https://assets.publishing.service.gov.uk/government/uploads/system/uploads/attachment_data/file/561017/sodium_hypochlorite_general_information.pdf

[15] https://www.uwo.ca/animal-research/doc/bleach-sop.pdf

[16] https://www.cdc.gov/safewater/publications_pages/chlorineresidual.pdf

[17] http://apps.who.int/iris/bitstream/handle/10665/44584/9789241548151_eng.pdf;jsessionid=7A2BD988C6737DB20B72C62B6E418806?sequence=1

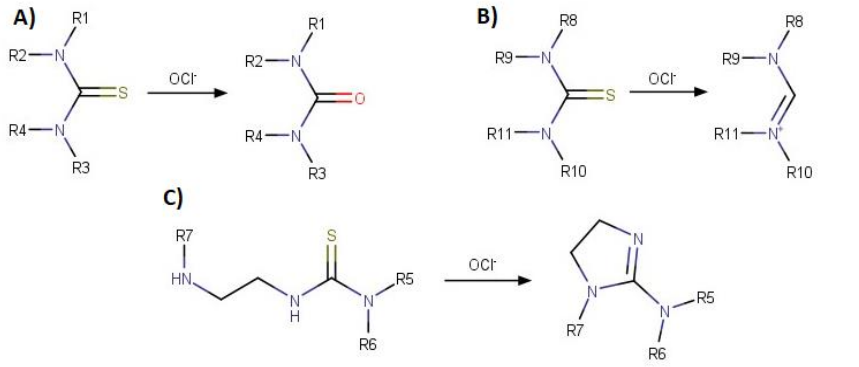

Figure 108. Proposed reaction mechanisms between the thiourea moiety with OCl^- according to A) P. Zhang [115] and So [120], B) Pham [114] and C) Lin [113].

To figure out if **M1** interacts with OCl^- in a manner similar to what has been reported in literature, firstly an ^{1}H-NMR titration was performed. The results are shown in Figure 109, where it can be seen that the two original signals corresponding to the thiourea protons (circled in brown) are shifted downfield and merged into a single peak that still integrates for two, relative to the phenylic protons. The opposite behavior happens with the protons from the bromobenzene group, as now the two pairs can be distinguished from one another (circled in orange).

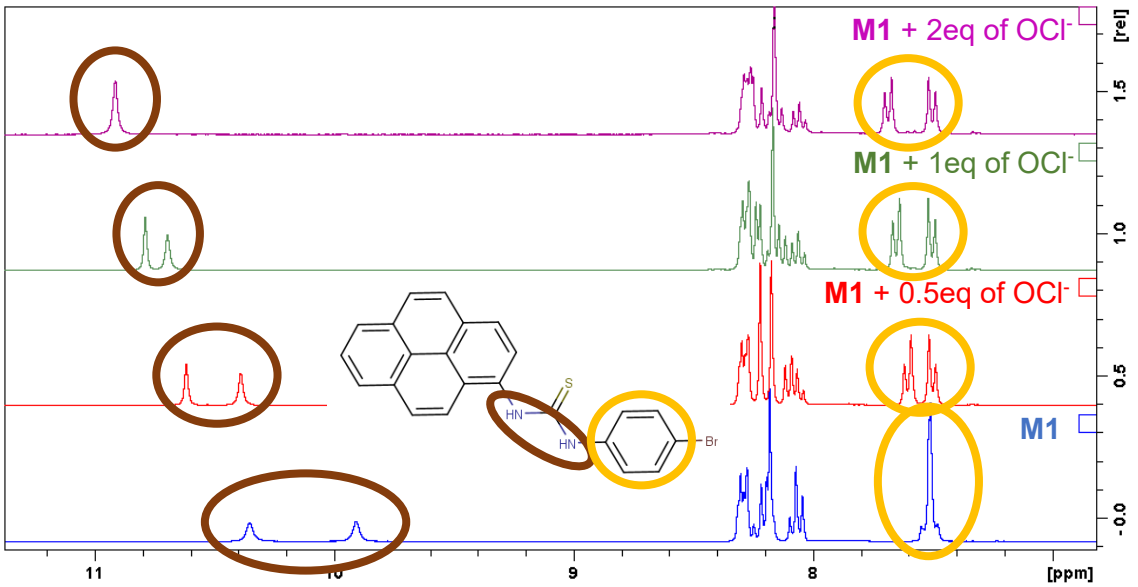

Figure 109. ^{1}H-NMR (DMSO-d_6, 300 MHz) titration of **M1** against OCl^-. The inset shows the chemical structure of the free ligand.

At this point, taking into account both luminescence and NMR data, a deprotonation reaction between **M1** and OCl^- owing to the basicity of the hypochlorite anion could be discarded because 1) the integration of the downfield proton signal is still 2H, which means that no hydrogen atom is lost, and 2) the emission spectrum of **M1** + OCl^- is very different from that of **M1** + OH^-, as in the second case, a new band at 395 nm appears (Figure 102 *vs.* Figure 103).

To completely understand the nature of the product formed, it was decided to isolate it from the chemical reaction itself. For this, 1eq of **M1** was reacted with approximately 2eq of NaOCl in the least possible amount of THF. After 16 h of reaction time, a precipitate formed, which separated from the reactant medium and was analyzed with ^{1}H-NMR (in DMSO-d_6), but it did not give any signals, meaning that it could be possibly a salt. Then, the solvent was evaporated from the reactant medium and the residue was column chromatographed. A lone blue emissive spot was isolated and its mass spectrum (Figure 110) was obtained, which showed a mass that exactly corresponds to the product that is generated by the proposed desulfurization reaction to yield a urea group in place of thiourea (ESI-MS: urea product + H^+ (m/z), calculated: 415.0446; found: 415.0435). This experimental way of characterizing the reaction product between the thiourea probe and the hypochlorite anion is the same as the one that Zhang and So used in their respective researches [115] [120].

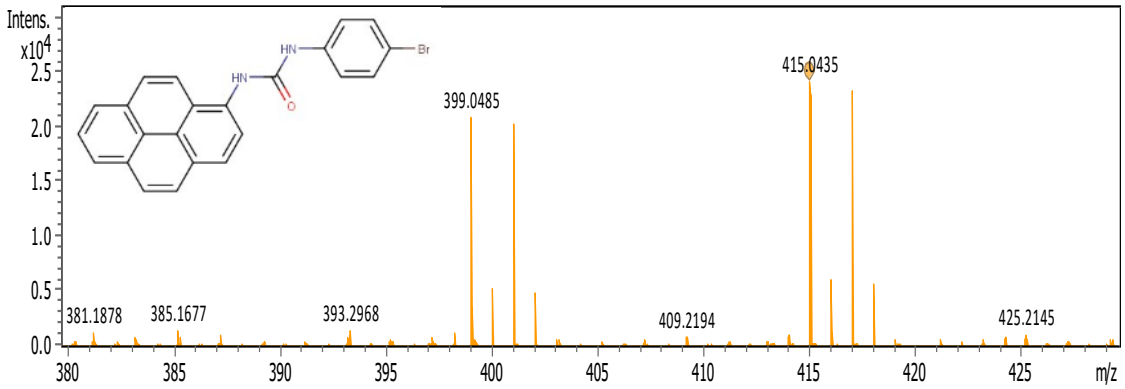

Figure 110. Zoom of the ESI-MS spectrum of the isolated reaction product between **M1** and OCl^-.

Finally, a pyrene-urea derivative of similar structure than **M1** (Figure 111 top left) was synthesized to compare its emission and ^{1}H-NMR spectra with those obtained when exposing our ligand to hypochlorite. As can be seen, this urea compound is very highly emissive at similar concentrations than **M1** (Figure 111 top right), and the two sets of

protons belonging to the phenyl ring and a single signal corresponding to the N-**H** urea protons are observed in the ^{1}H-NMR circled in brown and orange, respectively (Figure 111 bottom). These three observations are in close resemblance with those obtained in the **M1**-OCl^{-} reaction. While it is true that the λ_{exc} and the chemical shifts are not exactly the same, the differences could be attributed to the presence of a fluorine atom in place of the bromine.

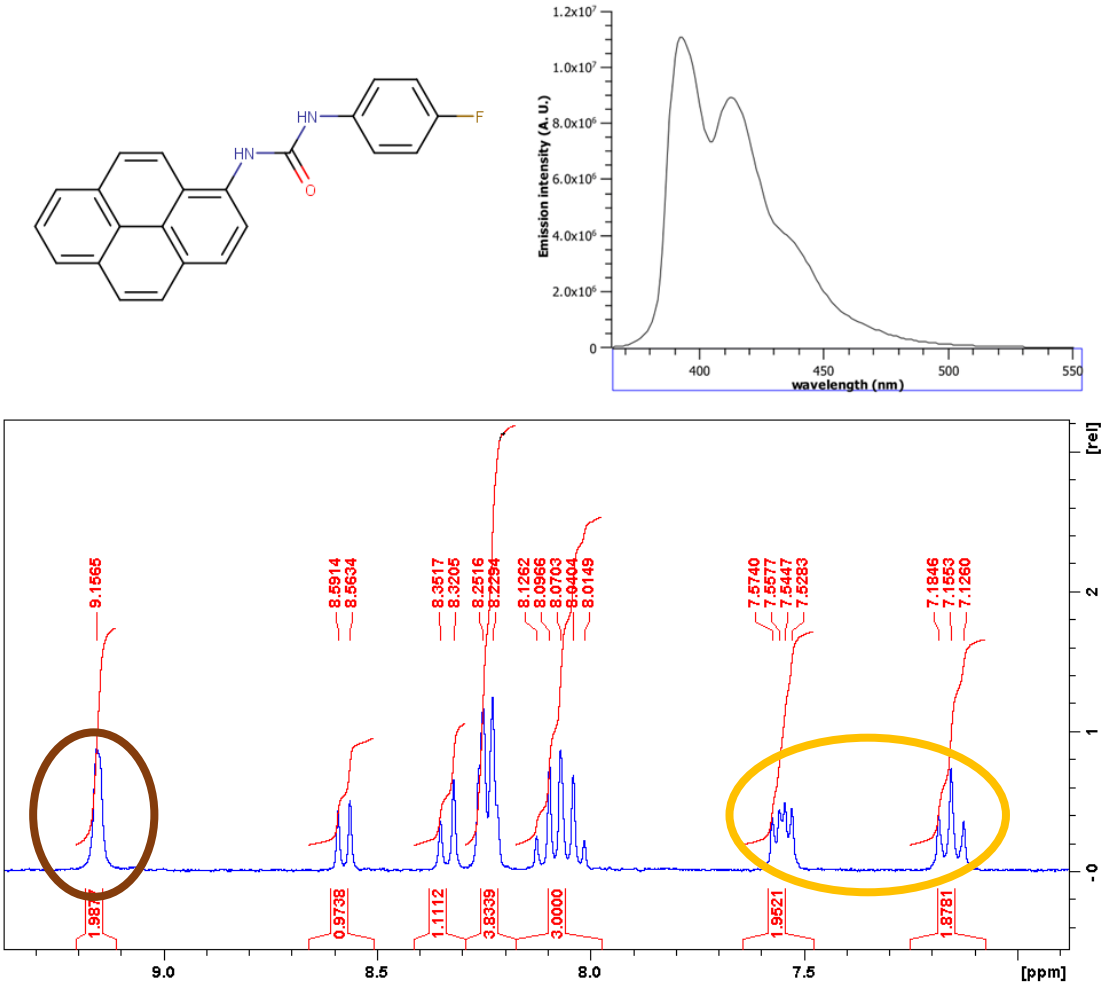

Figure 111. (top left) chemical structure of a urea analog of **M1**. (top right) Emission spectrum of this analog. Concentration: 14.1 μmol/L; λ_{exc} = 353 nm; solvent: 100 % THF. (bottom) ^{1}H-NMR (DMSO-d_6, 300 MHz) of this analog.

Taking all what has been presented before, it can therefore be concluded that the recognition event between **M1** and OCl^{-} is a chemical reaction that involves the oxidation of the thiourea group into a urea group, as seen in Figure 112, the latter being highly emissive in contrast with the original ligand.

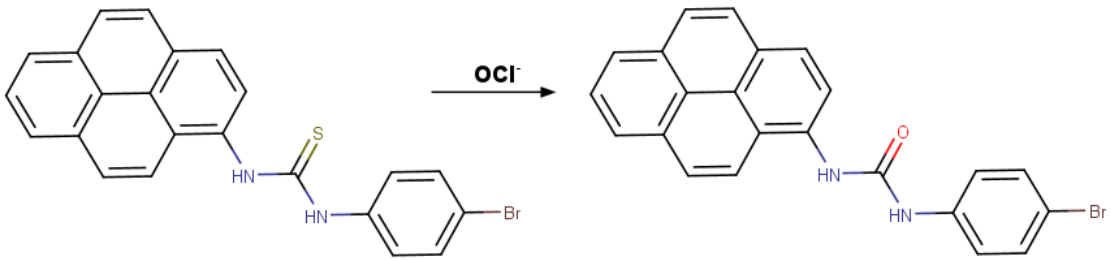

Figure 112. Proposed chemical reaction between **M1** and OCl^-.

As for the interaction between a thiourea entity and Cu^{2+} in sensing applications, it is clear that a complex is formed according to published literature. The different complexation ways have been reported and they are schematized in Figure 113. For instance, Lin [117] stated that the complex is formed between the copper cation, and the sulfur atom of the thiourea moiety and a proton from the benzene ring. This possibility is hard to believe due to the general incapability of protons to form complexes due to their lack of basicity. Chen [279] reported a complex in which the copper cation is bound by the two nitrogen atoms and the sulfur atom of the thiourea group, while Udhayakumari [280] described a complex formed by the metal cation connected with only the sulfur atom of the thiourea, but also with an adjacent nitrogen atom located in close proximity, meaning that the nitrogen atoms of the thiourea do not participate in the complexation process. In any of these cases, however, the corresponding X-ray crystal structures were obtained so a definite conclusion about the coordination mode of the molecules with Cu^{2+} cannot be provided.

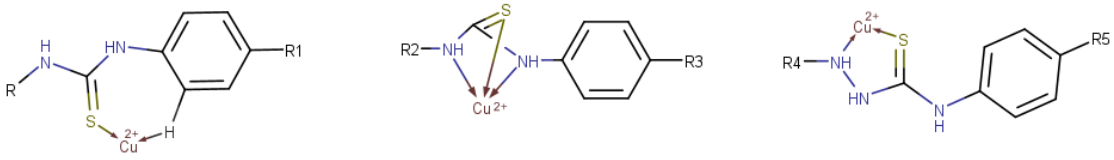

Figure 113. Complexation of the copper ion with the thiourea group according to Lin [117], Chen [279] and Udhayakumari [280].

Attempts to obtain the Job Plot to assess the **M1** : Cu^{2+} stoichiometry failed. However, the mass spectrum of the formed complex could be acquired (Figure 114) and it clearly showed a peak corresponding to the compound [2**M1** + Cu]$^+$ (ESI-MS (m/z), calculated: 922.9574; found: 922.9561), implying that the ligand – analyte stoichiometry is 2 : 1 without the loss of protons in this process. Also importantly, this implies a possible reduction of the copper cation from +2 to +1 with the consequent oxidation of thiourea

into formamidine disulphide. It has been reported that the remaining non-reacted thiourea then complexes the Cu(I) cation [281]. With this information, it is possible to suggest a coordination mode shown in Figure 114 (inset).

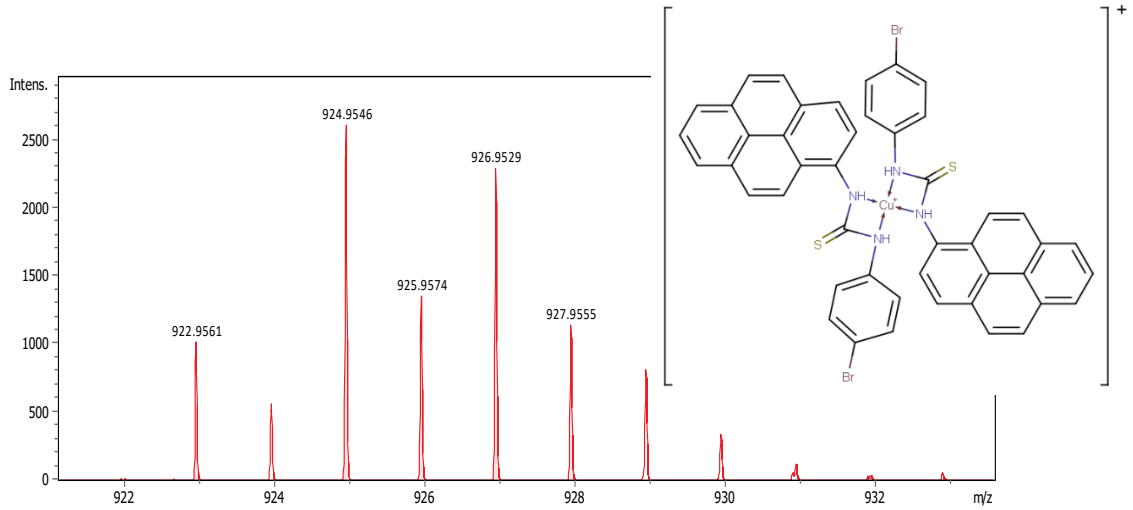

Figure 114. Zoom of the ESI-MS spectrum of the **M1** – Cu^{+} complex and its proposed structure.

As the **M1** : Cu^{2+} stoichiometric ratio is 2 : 1, the Benesi-Hildebrand equation cannot be applied in this particular case. Other titration methods for calculating the value of K_a exist, such as the double logarithm method [281]. However, none of them are reliable because they employ on the so called “local analysis” when a broad “global analysis” should be used instead [236]. Unfortunately, attempts to obtain single crystals of this complex were unsuccessful.

Finally, considering the results reported above, a sensing mechanism for the $[Cu(\mathbf{M1})_2]^{2+}$ species can be proposed. Considering that **M1** is low emissive due to the free rotation of the pyrene-thiourea bond, it can be postulated that the complexation of Cu^{2+} rigidifies the structure of the probe, blocking the radiationless de-excitation pathways and turning ON its emission.

4.1.1.4 Interference tests

Next, interference tests of the detection of Cu^{2+} by **M1** were made according to the procedure described in Section 2.3.8. The concentration of the ligand was 11.6 μmol/L in 100 % THF, and 8.62 equivalents of each of the interferent and the copper cation were added. The results are shown in Figure 115, where the emission intensity at 407 nm relative to that of the free ligand is shown (λ_{exc} = 364 nm).

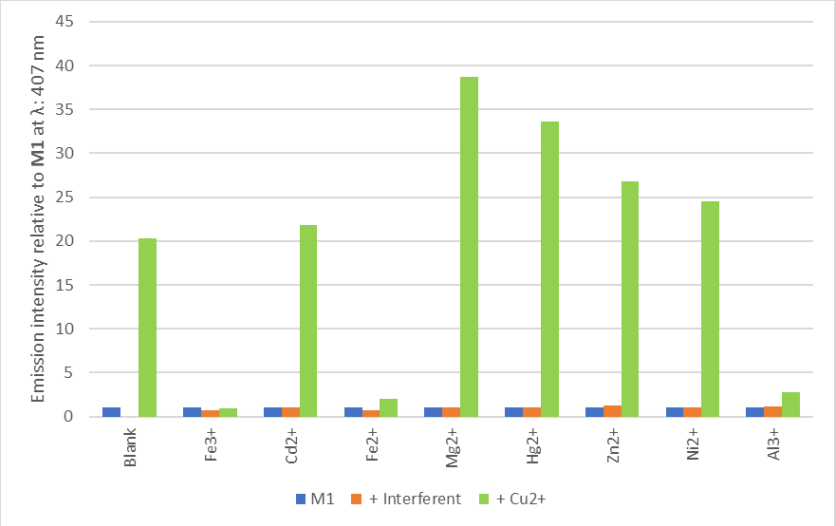

Figure 115. Interference test results for the detection of Cu^{2+} by **M1**. The blue boxes represent the emission intensity of **M1** normalized to 1; the orange ones, the relative emission intensity when an interferent is subsequently added; and the green ones, the relative final emission intensity when Cu^{2+} is added to the mixture.

As can be seen in the above figure, the presence of Fe^{2+}, Fe^{3+} and Al^{3+} inhibits the detection of Cu^{2+} by **M1**, even though these three cations do not generate a noticeable change in the emission spectrum of the probe by themselves (as showed in Figure 100). This could be explained in two different ways. Firstly, it can be postulated that the binding affinity of **M1** towards $Fe^{2+/3+}$ and Al^{3+} is higher than that towards Cu^{2+}, or that the formation of the copper complex is kinetically less favorable. If correct, this explanation evidences that the luminescence mechanism of the resulting complex of this molecule and $Fe^{2+/3+}$ and Al^{3+} is of different nature than that with Cu^{2+}. Secondly, it could also be stated that the slight acidity of the aqueous iron and aluminum solutions[18] influences the sensing capabilities of **M1** in a way that it makes the complexation event of the molecule with copper more difficult.

To try to further understand these interactions, the reverse interference tests were performed: instead of firstly adding the interferent and then, the copper cation, the test was made in the exact reverse order. The results are shown in Figure 116 and indicate that once the complex between **M1** and Cu^{2+} is formed, the addition of $Fe^{2+/3+}$ or Al^{3+} aqueous solutions does not break it.

[18] The measured pH of the original 0.01 mol/L solutions from which aliquots of these cations are taken from is between 4 and 5. It should be noted that in the interference tests, 20 μM of these solutions are added into 2 mL of THF, meaning that the THF medium becomes only slightly acidic.

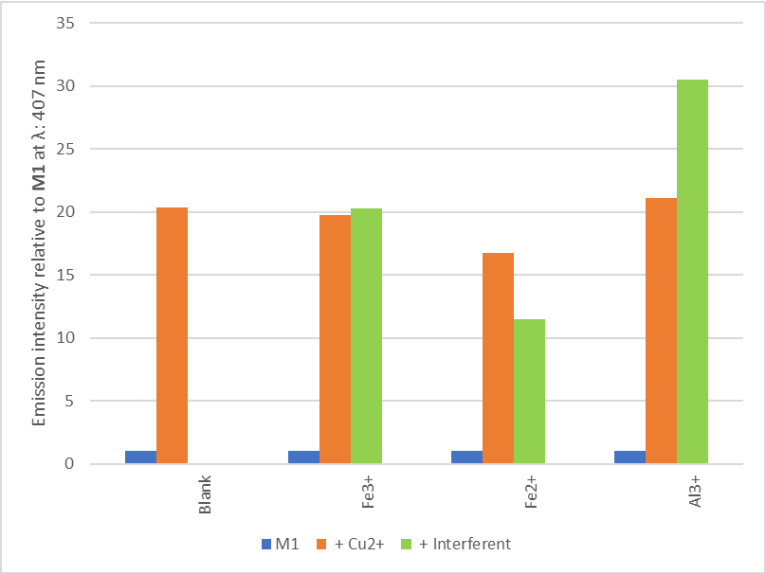

Figure 116. Reverse interference test results of **M1** against its inhibitors for the detection of copper. The blue boxes represent the emission intensity of **M1** normalized to 1; the orange ones, the relative emission intensity when Cu^{2+} is added to the solution; and the green ones, the relative final emission intensity when the inhibitor is added to the mixture. [**M1**]: 11.6 μmol/L in 100 % THF; cations added: 8.62 equivalents; λ_{exc} = 364 nm.

To wrap up these qualitative studies, another test was performed in which an equimolar amount of Cu^{2+} and each of the three interferents was added into the cuvette *prior* to the ligand. Then, after its addition, which yielded a ratio of **M1** : Cu^{2+} : inhibitor at 1 : 8.62 : 8.62, the emission spectrum was recorded. These results are shown in Figure 117 and, as can be seen, under these conditions the probe is not able to detect Cu^{2+}. This result confirms the complete inhibition of the detection of copper(II) by **M1** when solutions of aluminum(III) or both iron cations are present in the medium.

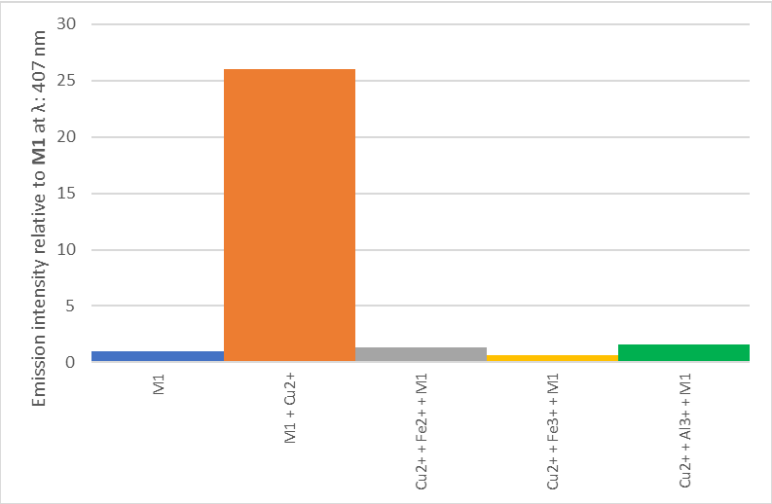

Figure 117. Double cation interference test results. The blue box represents the emission intensity of **M1** normalized to 1 and the orange one, the relative emission intensity of **M1** + Cu^{2+} (depicted for comparison purposes). The grey, light orange and light blue boxes represent the relative emission intensities of **M1** when it is added to a solution containing the indicated inhibitor cations. [**M1**]: 11.6 μmol/L in 100 % THF; cations added: 8.62 equivalents; λ_{exc} = 364 nm.

Finally, tests to directly verify if a mildly acidified or basified THF medium affects **M1** sensing capabilities towards Cu^{2+} were carried out following the same procedure as with the cationic interferents (Section 2.3.8). The results are shown in Figure 118.

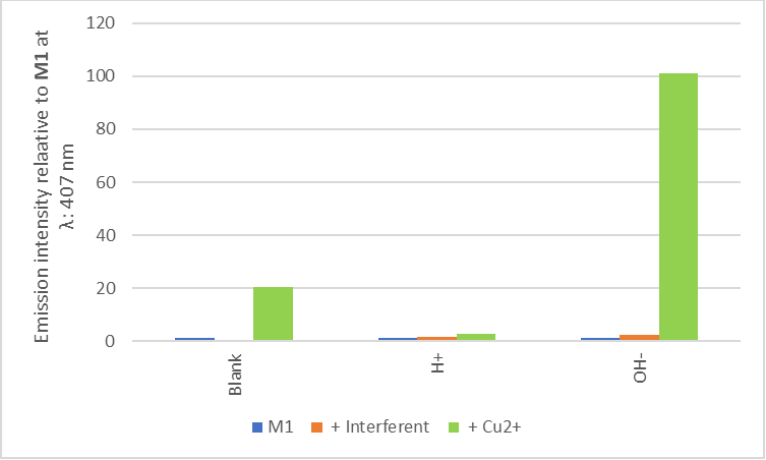

Figure 118. Interference test results for the detection of Cu^{2+} by **M1** upon addition of acidic and basic solutions. The blue boxes represent the emission intensity of **M1** normalized to 1; the orange ones, the relative emission intensity when H^+ or OH^- is subsequently added; and the green ones, the relative final emission intensity when Cu^{2+} is added to the mixture. [**M1**]: 11.6 μmol/L in 100 % THF; acid, base and Cu^{2+} added: 8.62 eq equivalents; λ_{exc} = 364 nm.

As can be seen in Figure 118, an acidified THF medium inhibits the fluorescence detection of Cu^{2+} by **M1**. Even though, as mentioned in Section 4.1.1.1, a big excess of H^+ is needed to protonate the sulfur atom of the thiourea group and generate a change in the emission spectrum, it is apparent that a mild acidic THF medium diminishes the coordinating capabilities of the thiourea entity. This result, along with the ones shown in the reverse interference (Figure 115) and double interference (Figure 116) essays tend to indicate that it is the slight acidic medium induced by the addition the Fe^{2+}, Fe^{3+} and Al^{3+} solutions, and not the cations themselves, that also inhibits the detection of copper. However, an inhibition due to a possible complex formation with these three species that is more stable than that with Cu^{2+} cannot be ruled out.

On the other hand, it can be seen in the same figure that a basified THF medium promotes an even higher enhancement of the fluorescence emission when Cu^{2+} is added. As discussed previously, it is likely that thioureas lose the N-**H** proton under basic conditions, thus it can be considered that the addition of OH^- enhances the deprotonation of **M1**. The effect that this deprotonation has in the sensing capabilities of **M1** towards Cu^{2+} can be explained in terms of the increased basicity of the nitrogen atoms. As the basicity of a species grows with increasing of the negative charge, the removal of a proton at the ***N*** atom of the thiourea enhances the complexing properties and possibly promotes the formation of a more stable **M1**-Cu^{2+} entity.

4.1.1.5 Conclusion

In conclusion, **M1** is a new pyrene-thiourea derivative that can detect aqueous Cu^{2+} and OCl^- in a 100 % THF medium. In the first case, it is thought that the sensing mechanism relies on rigidification of the molecule owing to the complexation of copper(II) in a 1 : 2 ratio, which generates an enhancement of the emission of the molecule. In the second case, it has been determined that hypochlorite reacts irreversibly with **M1** to form a urea entity in place of the original thiourea, which generates the concomitant enhancement of the emission of the probe. The calculated limits of detection are 9.71 μmol/L and 1.01 μmol/L for Cu^{2+} and OCl^-, respectively. These values are such that make **M1** an interesting candidate for real-life water quality assessment of these two species.

4.1.2 M2

The new compound **M2**, which structure can be seen in Figure 119, was designed with the objective to study the C=N isomerization mechanism and with the goal of detecting preferably the aluminum(III) cation thanks to the suitable size of the cavity generated by

the *OH* group in *ortho* position to an imine moiety, as discussed in Section 2.1.1.4. However, as the selectivity of this cavity is poor, it is also possible that this molecule could detect Zn^{2+}, Fe^{2+}, Fe^{3+} or Cu^{2+}.

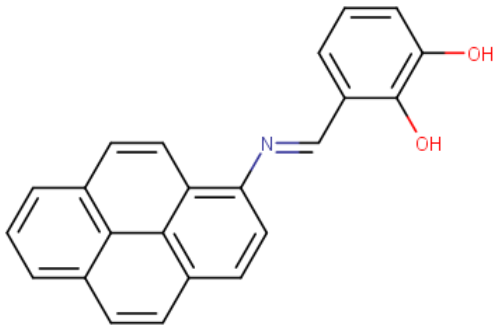

Figure 119. Chemical structure of **M2**.

The interest about aluminum detection relies on the fact that it is the most common metal on Earth's crust and its cationic species is a readily soluble in water systems. If ingested in large quantities, it can potentially bioaccumulate in bones, parathyroids, liver and spleen and kidneys of human beings. Aluminum(III) has been linked with osteomalcia, hypoparathyroidism anemia, among other diseases [282]. Moreover, recently, elevated content of aluminum has been detected in the brains of patients with Alzheimer's disease, which accounts for a potential link of the metal with this neurodegenerative disorder [283]. For the mentioned reasons, fast and effective detection of this metal is of great significance, especially in drinking water.

4.1.2.1 Bulk tests

Bulk tests in 100 % THF were carried out following the procedure described in Section 2.3.3. The cation and anion bulk test results are shown in Figure 120 and Figure 121, respectively. Also, the response of **M2** against the addition of acidic and basic solutions was probed and the results can be seen in Figure 122.

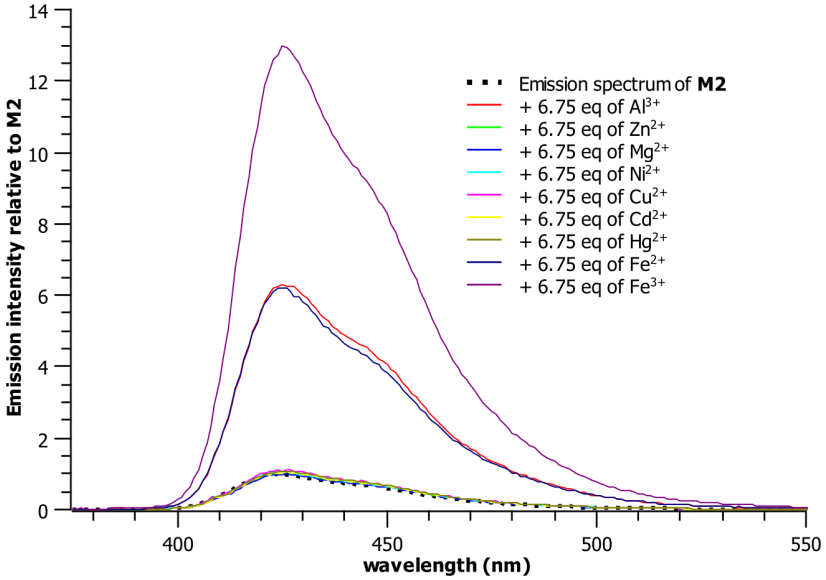

Figure 120. Emission spectrum of **M2** (14.8 μmol/L in 100 % THF) in presence of an excess (6.75 equivalents) of several metallic cations; λ_{exc} = 365 nm.

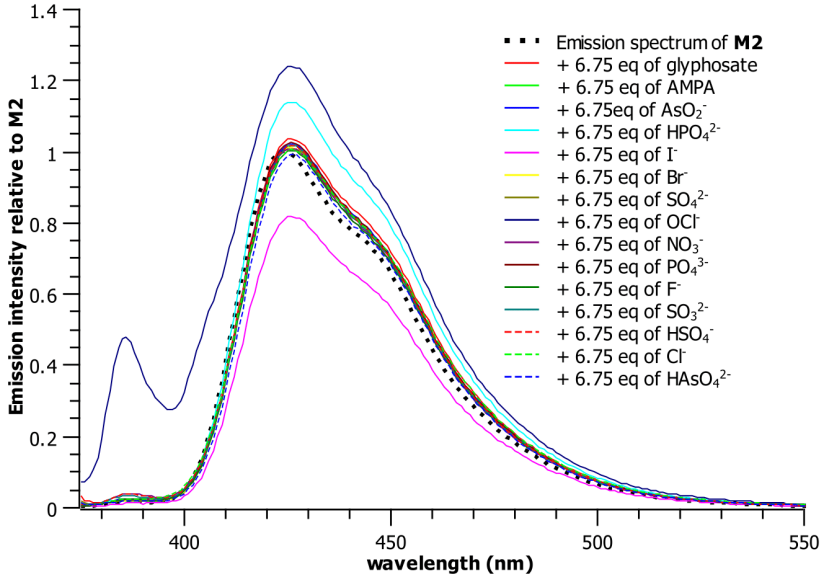

Figure 121. Emission spectrum of **M2** (14.8 μmol/L in 100 % THF) in presence of an excess (6.75 equivalents) of several anions; λ_{exc} = 365 nm.

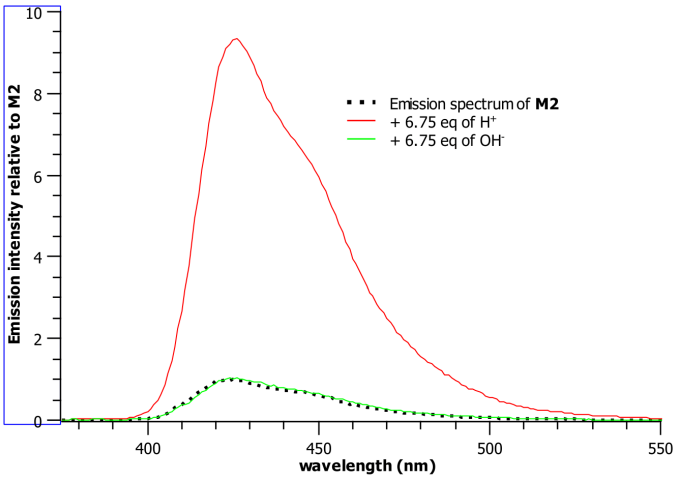

Figure 122. Emission spectrum of **M2** (14.8 μmol/L in 100 % THF) in acidified and basified THF; λ_{exc} = 365 nm.

As can be seen in Figure 120, **M2** is sensitive to Fe^{2+}, Fe^{3+} and Al^{3+} by a straight enhancement of the emission intensity. Under the conditions used, in presence of the aluminum and iron(II) ions, the emission of the ligand is enhanced 6-fold and in presence of the iron(III) ion, it is enhanced 13-fold. These results are consistent with what was expected according to the ligands design (Section 2.1.1.4). As for the bulk test with anionic species, it can be seen in Figure 121 that, interestingly, the presence of the hypochlorite anion promotes the appearance of a new band centered at 386 nm.

Finally, the addition of OH^- yielded no appreciable change in the emission spectrum of **M2**. On the other hand, upon presence of H^+ a 10-fold straight enhancement of the emission was observed. This could be explained due to protonation of the nitrogen atom of the imine moiety, which has a pK_aH between 5 and 7 [284], that could eventually lead to the cleavage of the imine bonding [285]. The effect of an acidified or basified medium on the sensitivity of **M2** against the three cations, Al^{3+}, Fe^{2+} and Fe^{3+}, will be analyzed in Section 4.1.2.4.

4.1.2.2 Calibration curves

Emission titrations of **M2** in 100 % THF were carried out against OCl^-, Fe^{2+}, Fe^{3+} and Al^{3+} following the procedure described in Section 2.3.4. In all cases, the concentration of the ligand was 14.8 μmol/L and the final point of the titration occurs upon addition of a total of 3.38 equivalents of the analyte into the solution.

As the appearance of a new band at 386 nm in the presence of OCl^- was not expected and a similar behavior is not reported in the literature, it was decided to explore this interaction first. The titration profile can be seen in Figure 123.

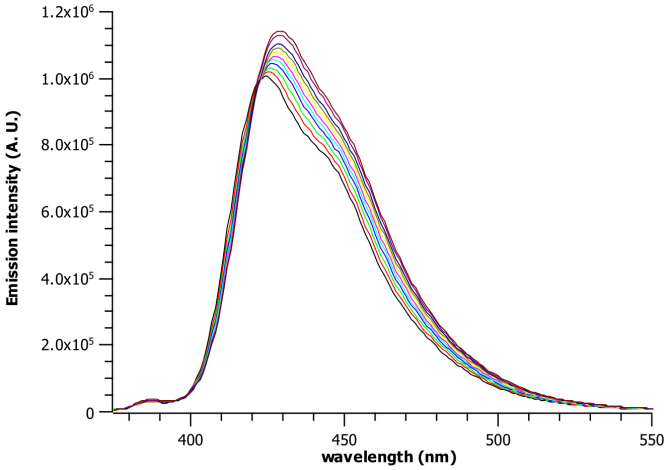

Figure 123. Emission titration profile of **M2** against incremental quantities of OCl^-. [**M2**] = 14.8 μmol/L; λ_{exc} = 365 nm.

As can be seen, there is basically no change in the emission spectrum of **M2** when titrating it against OCl^- and the new band that appeared when performing the bulk test cannot be seen at all. In fact, the small redshift in the titration profile is comparable to the one generated by the addition of the same incremental volumes of H_2O (Figure 124), which could be considered as a “blank” titration.

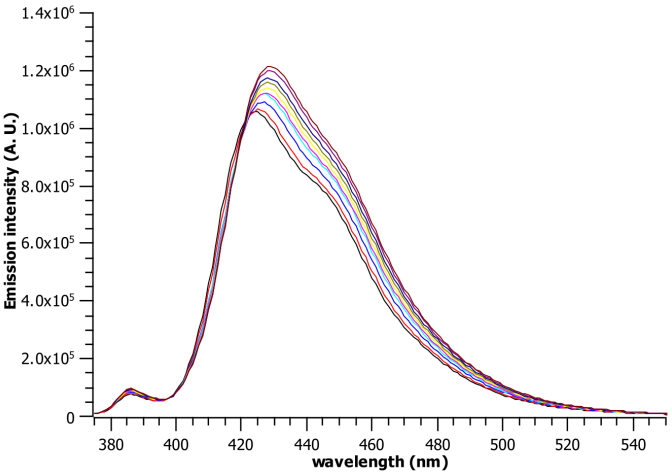

Figure 124. Emission profile for the titration of **M2** against incremental quantities of H_2O. [**M2**] = 14.8 μmol/L; λ_{exc} = 365 nm.

These results may indicate that hypochlorite can interact with the **M2** molecule, but in order for a change to be seen in the emission spectrum, the concentration of this analyte needs to be substantially high, in the mmol/L range. As mentioned in Section 4.1.1.2, target concentrations for hypochlorite sensing need to be in the *µ*mol/L range, thus, as these high concentration values are uninteresting for adequate water quality assessments, it was decided to no further explore this sensitivity pathway and to focus instead on the metal cations.

The emission titration profiles of **M2**-Fe^{2+}, **M2**-Fe^{3+} and **M2**-Al^{3+}, and their corresponding calibration curves, are shown in Figure 125, Figure 126 and Figure 127, respectively. It is important to mention that the small dilution generated by the addition of the solution of the analyte was considered to obtain the calibration curves by subtracting the emission spectra

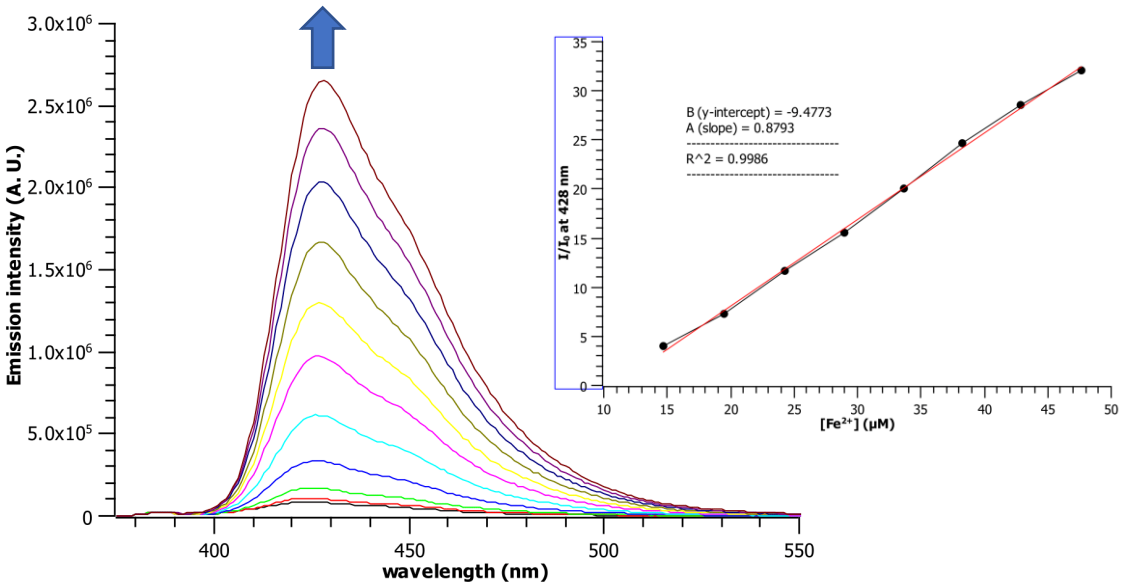

Figure 125. (left) Emission titration profile of **M2** against incremental quantities of Fe^{2+}. [**M2**] = 14.8 *µ*mol/L; λ_{exc} = 365 nm. (right) Calibration curve for this titration (I/I_0 at 428 nm *vs.* [Fe^{2+}]. Each point has a calculated error of 1 %.

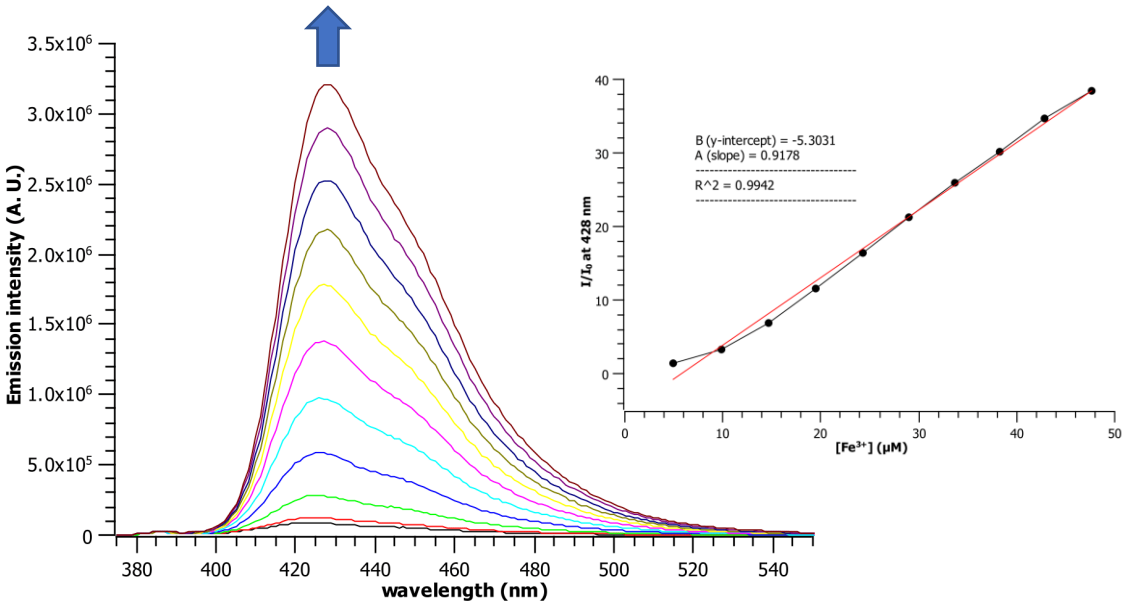

Figure 126. (left) Emission titration profile of **M2** against incremental quantities of Fe^{3+}. [**M2**] = 14.8 μmol/L; λ_{exc} = 365 nm. (right) Calibration curve for this titration (I/I_0 at 428 nm *vs.* [Fe^{3+}]. Each point has a calculated error of 1 %.

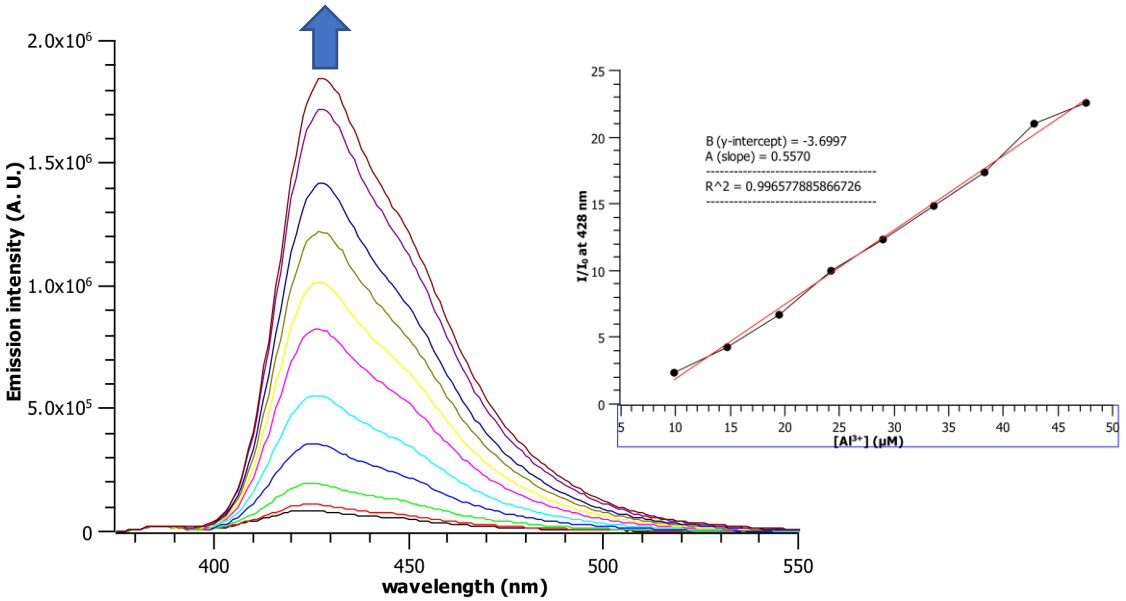

Figure 127. (left) Emission titration profile of **M2** against incremental quantities of Al^{3+}. [**M2**] = 14.8 μmol/L; λ_{exc} = 365 nm. (right) Calibration curve for this titration (I/I_0 at 428 nm *vs.* [Al^{3+}]. Each point has a calculated error of 1 %.

It can be seen in the above figures that there is a linear response of the **M2** ligand towards the Fe^{2+} cation in the ~15 to ~50 μmol/L range; towards the Fe^{3+} cation in the ~5

to ~50 μmol/L range; and towards the Al^{3+} cation in the ~10 to ~50 μmol/L range. Using the information from the titration profiles, the limits of detection for these interactions were calculated using the 3σ method (Section 2.3.5) and the obtained values are 0.03 ± 0.0003 μmol/L, 0.04 ± 0.0004 μmol/L and 0.06 ± 0.0006 μmol/L for Fe^{2+}, Fe^{3+} and Al^{3+}, respectively.

According to the European Union Council Directive 98/83/EC on the quality of water intended for human consumption[19], the acceptable limits of Fe and Al are, respectively, 3.58 μmol/L and 7.41 μmol/L. Thus, **M2** could be considered as an interesting candidate to be used for real-life water quality assessment.

4.1.2.3 Sensing mechanism

The enhancement of the emission intensity that both iron cations and Al^{3+} generate is consistent with the predicted sensing mechanism of this molecule (Section 2.1.1.4). In fact, the emission intensity of the free **M2** molecule is low due to the rapid C=N isomerization process that actively occurs in solution and that allows the energy to dissipate in non-radiative ways, as already explained. It is upon complexation of the aforementioned cationic species that the rotation of the N=C-Phenyl bond is inhibited, rigidifying the structure with the concomitant "turning-on" effect on the emission of the ligand. This sensing mechanism is classic for chemosensors containing an *OH* group in *ortho* position to a Schiff base [125] [126].

In order to obtain more clues about the exact nature of the complexes formed, an ^{1}H-NMR titration was carried out between **M2** and Al^{3+} and the result can be seen in Figure 128. The first thing that pops out when analyzing that figure is that none of the signals assigned to the phenolic protons disappear upon addition of Al^{3+}. Also, it can be seen that the titration promotes a new signal at 9.72 ppm, which could correspond to the iminic proton of the complex. Unfortunately, the broadening of the signals corresponding to the pyrene and the phenyl units does not allow for a proper integration to reliably obtain the relative ratio with the iminic proton signal of the free ligand.

At this point, it is worth to describe an observation: in several articles published in literature about aluminum(III) sensing, researchers report ^{1}H-NMR titrations in which their molecules are dissolved in DMSO-d_6 and the added Al^{3+} comes from either $AlCl_3$, $AlNO_3$ or $Al(ClO_4)_3$ dissolved in DMSO-d_6 or in D_2O. However, while trying to replicate these tests, it was experimentally demonstrated in blank essays that, at least the first two

[19] https://www.lenntech.com/applications/drinking/standards/eu-s-drinking-water-standards.htm

aluminum salts, and also other organic aluminum salts tested, are completely insoluble in DMSO or DMSO-d_6 and, moreover, when dissolved in D_2O, CD_3OD or CD_3CN, they precipitate instantly when added into a DMSO-d_6 solution. This generates the practical disadvantage of not being able to properly carry out ^{1}H-NMR titrations as reported in the literature because it is not possible to account for the aluminum lost due to precipitation.

In the particular case of the **M2**-Al^{3+} ^{1}H-NMR titration, it was observed that some aluminum compound precipitated when added to the solution, either the salt or the complex. Thus, the results reported could have some intrinsic error as some aluminum precipitated before actually getting complexed by the ligand. An alternative to bypass this problem involves the use of deuterated methanol or ethanol; however, they possess labile protons that rapidly exchange with the phenolic protons of the ligand, thus limiting the analysis.

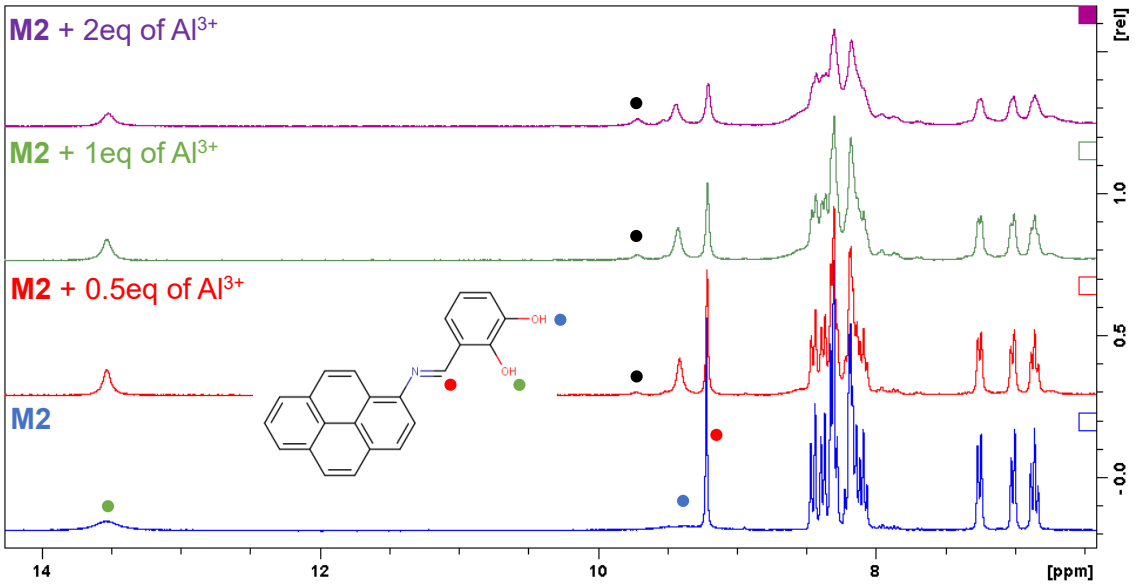

Figure 128. ^{1}H-NMR (DMSO-d_6, 300 MHz) titration of **M2** against Al^{3+}. The cation was prepared in a D_2O solution. The inset shows the chemical structure of the free ligand. Protons in the spectrum are assigned with colored circles.

In any case, two conclusions can be extracted from this experiment: 1) the phenolic protons do not seem to be lost in the complexation with Al^{3+} and 2) a new signal, probably belonging to the iminic proton of the complex (marked with a black circle in Figure 128), appears. Unfortunately, due to the open-shell nature of Fe^{2+} and Fe^{3+}, the ^{1}H-NMR experiment using these cations is not suitable.

Also, efforts to obtain the Job Plots of the **M2**-$Fe^{2+/3+}$ and **M2**-Al^{3+} interactions failed. In a similar way, mass spectra results yielded very complex spectra with a big amount of multimeric and multicharged species, rendering the detection of the peaks corresponding to the likely 1 : 1 or 1 : 2 stoichiometry impossible. This, in turn, does not allow the calculation of the binding constant with the Benesi-Hildebrand method.

Despite these limitations, and based on the already cited literature reports consisting of ligands that possess the similar structural motif of a Schiff base with an *OH* in ortho position and the emission enhancement effect that iron(II), iron(III) and aluminum(III) generate in the emission of **M2**, a chemical structure for the complexes formed could be in principle proposed (Figure 129). Independently of the stoichiometric ratio (which could be different than 1 : 1), it is believed that the interaction between the metal and the ligand happens at the nitrogen atom of the imine and the oxygen atom of the phenol in *ortho* position to the Schiff base.

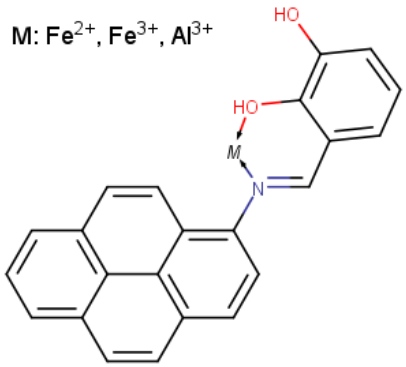

Figure 129. Proposed chemical structure for the **M2**-metal complexes using a 1 : 1 stoichiometric ratio.

4.1.2.4 Interference tests

Next, interference tests of the detection of the three cations by **M2** were made according to the procedure described in Section 2.3.8. The concentration of the molecule was 14.8 μmol/L in 100 % THF, and 6.75 equivalents of each of the interferent and the target cation (Fe^{2+}, Fe^{3+} or Al^{3+}) were added. The results are shown in Figure 130, Figure 131 and Figure 132, where the emission intensity at 425 nm relative to that of the free ligand is shown (λ_{exc} = 365 nm).

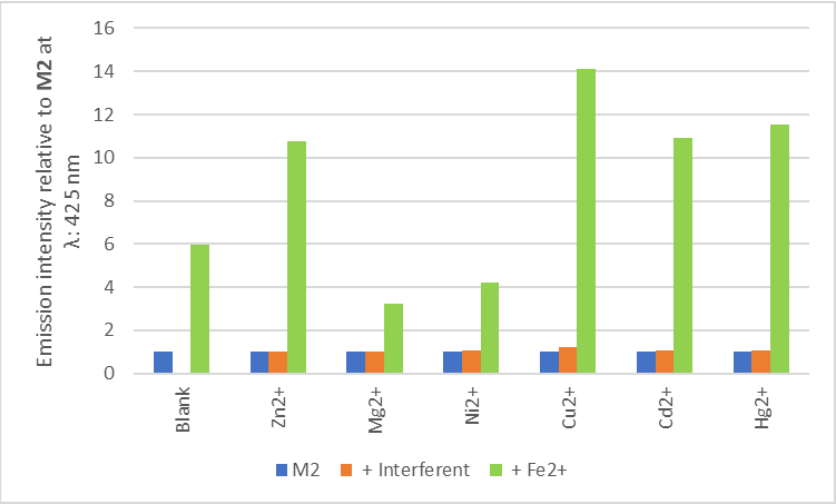

Figure 130. Interference test results for the detection of Fe^{2+} by **M2**. The blue boxes represent the emission intensity of **M2** normalized to 1; the orange ones, the relative emission intensity when an interferent is subsequently added; and the green ones, the relative final emission intensity when Fe^{2+} is added to the mixture.

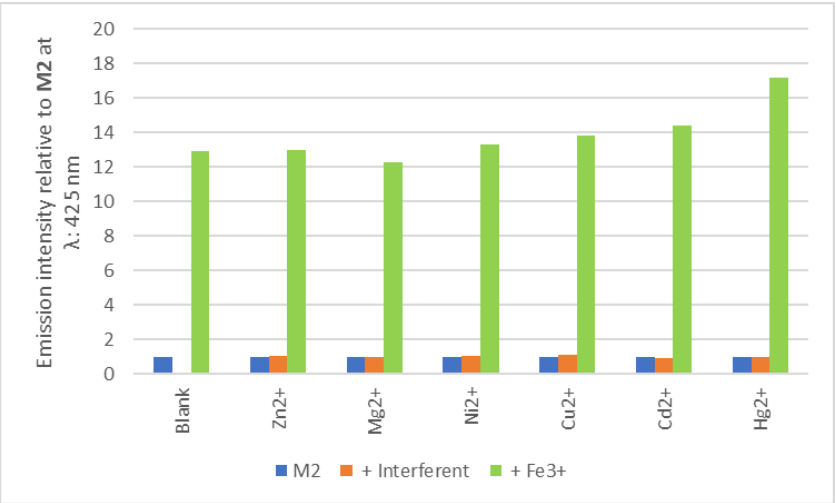

Figure 131. Interference test results for the detection of Fe^{3+} by **M2**. The blue boxes represent the emission intensity of **M2** normalized to 1; the orange ones, the relative emission intensity when an interferent is subsequently added; and the green ones, the relative final emission intensity when Fe^{3+} is added to the mixture.

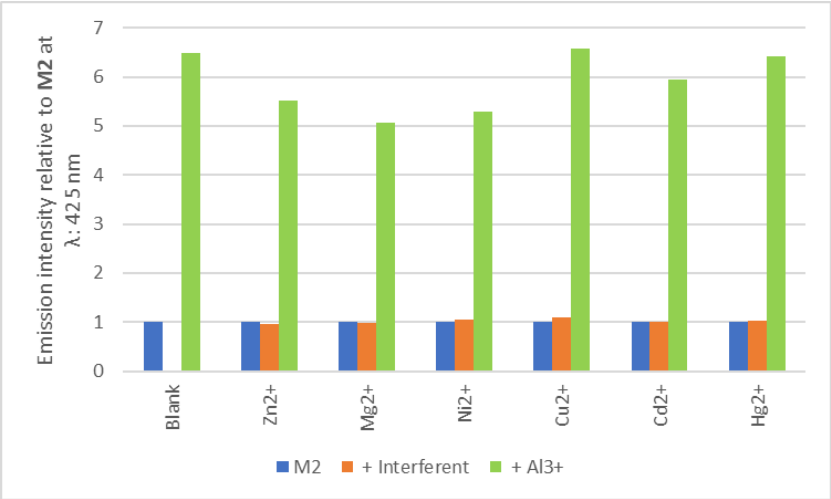

Figure 132. Interference test results for the detection of Al^{3+} by **M2**. The blue boxes represent the emission intensity of **M2** normalized to 1; the orange ones, the relative emission intensity when an interferent is subsequently added; and the green ones, the relative final emission intensity when Al^{3+} is added to the mixture.

As can be seen in these figures, none of the metal cations tested act as inhibitors for the detection of either Al^{3+}, Fe^{2+} or Fe^{3+} by **M2**, although the only case worth of mention is that when Mg^{2+} or Ni^{2+} are present in the medium, the enhancement of the emission of the ligand by Fe^{2+} is not as pronounced as it is in their absence.

Finally, tests to verify if a mildly basified THF medium affects the sensing capabilities of **M2** towards the three cations in neat conditions were carried out following the same procedure as with the cationic interferents (Section 2.3.8). As presented in Figure 133, a basified medium slightly decreases the expected emission enhancement of the ligand – analyte interaction, but without compromising the detection.

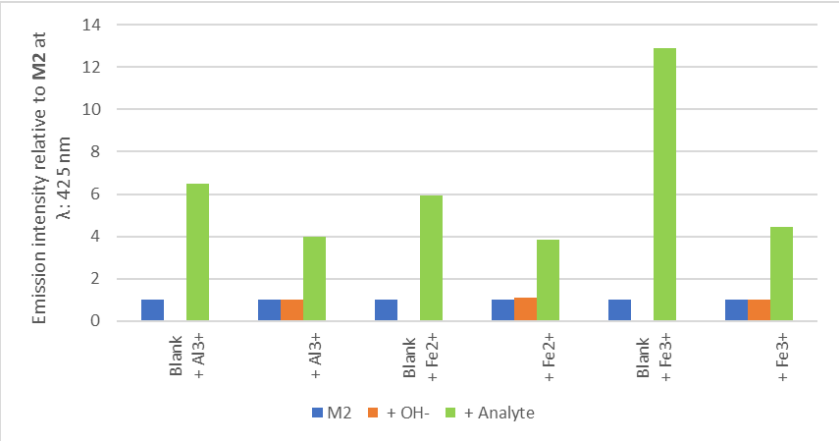

Figure 133. Interference test results for the detection of Al^{3+}, Fe^{2+} and Fe^{3+} by **M2** upon addition of a basic solution. The blue boxes represent the emission intensity of **M2** normalized to 1; the orange ones, the relative emission intensity when OH^- is subsequently added; and the green ones, the relative final emission intensity when Al^{3+}, Fe^{2+} or Fe^{3+} are added to the mixture. [**M2**]: 14.8 μmol/L in 100 % THF; base and Cu^{2+} added: 6.75 equivalents; λ_{exc} = 365 nm.

It should be noted that tests to verify the interference of an acidified THF medium into the sensing of the three metal cations were not carried out. The reason was that the response of these species is exactly the same as the one obtained when adding H^+: a straight enhancement of the emission spectrum. While literature reports support the complex structure proposed in Figure 129, the similar effect that is observed when adding acid could mean that it is the added protons, and not the cations themselves, that generates the change in the emission spectrum of the molecule, because aqueous solutions of Al^{3+}, Fe^{2+} and Fe^{3+} are slightly acidic in nature. Unfortunately, attempts to prepare aqueous solutions of these cations in a pH 7 buffered medium to rule out the acidic interference were not successful due to the insolubility of the metallic species at this pH.

It should be mentioned at this point that the pH of the metal solutions from which aliquots were taken to perform the bulk tests (Figure 120) was measured to be between 4 and 6. For their part, the titrations (Section 4.1.2.2) were made using 10 times more diluted solutions. While it is true that these solutions are acidic in nature, their acidic strength is fairly low, and they are further diluted in the THF medium when performing the aforementioned analysis. Moreover, the fact that an enhancement of the emission spectrum of **M2** in basified THF in presence of these three cations is clearly observed further supports the assessment that the fluorescence change is due to a complex formation and not due to the presence of protons: if the spectral changes were due to

the acidification of the medium, a response should not be obtained under basified conditions.

4.1.2.5 Conclusion

In conclusion, **M2** is a pyrene-Shiff base-hydroxyphenyl derivative that can detect Fe^{2+}, Fe^{3+} and Al^{3+} in a 100 % THF medium. In the three cases, and based on literature reports, it is proposed that the mechanism involves the inhibition of the C=N isomerization of the free molecule in solution owing to the cations being complexed *via* the nitrogen atom of the Schiff base and an oxygen atom of the hydroxyphenyl entity. The limits of detection for these three analytes are 0.03 μmol/L, 0.04 μmol/L and 0.06 μmol/L, respectively, which make the ligand a suitable candidate for real-life water quality control.

4.1.3 M3

The new ligand **M3** was designed aiming at a direct detection of glyphosate owing to its chemical structure (Figure 134) with plenty of available hydrogen bonding positions. As described in Section 1.1.2.2, glyphosate is currently widespread in the environment because it is the most common pesticide used in agriculture, but at the same time it poses several health risks in human beings. It is then urgent to find ways to detect and quantify its concentration, especially considering that, to the best of our knowledge, no report of its direct fluorescent sensing has been published in the literature.

Also, as it contains a phenolic group in *ortho* position to a Shiff base, it was expected that this molecule could detect metal cations such as Al^{3+}, Zn^{2+} or Cu^{2+}.

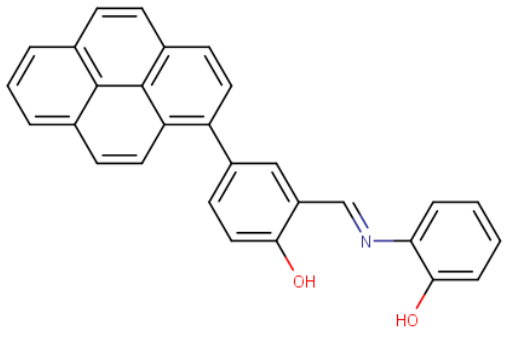

Figure 134. Chemical structure of **M3**.

It is important to mention that, at this stage of the thesis work, it was decided to stop using THF as the main solvent for preparing solutions of the ligands. While it is true that

THF offers advantages such as readily dissolving most of our compounds and being miscible with water, which is the medium in which the solutions of the analytes are prepared, it is in reality not a solvent that is normally used in real-life applications. In fact, in the majority of the recent literature cited in this manuscript, researchers tend to utilize solvent media that are as close as possible to water systems, which are more environmentally friendly and yield more close-to-reality results. Thus, the main solvents that will be used starting with **M3** are going to be DMSO, methanol, ethanol and water itself[20]. Moreover, these organic solvents and particularly water generate a strong solvation effect for cations and anions [276], meaning that if a fluorescence change is observed in these media, the strength of the probe-analyte interaction is significant and could reveal a specific interaction.

4.1.3.1 Bulk tests

Bulk tests were carried out following the procedure described in Section 2.3.3. The cation and anion bulk test results are shown in Figure 135 and Figure 136, respectively. Also, the response of **M3** against the addition of acidic and basic solutions was probed and the results can be seen in Figure 137.

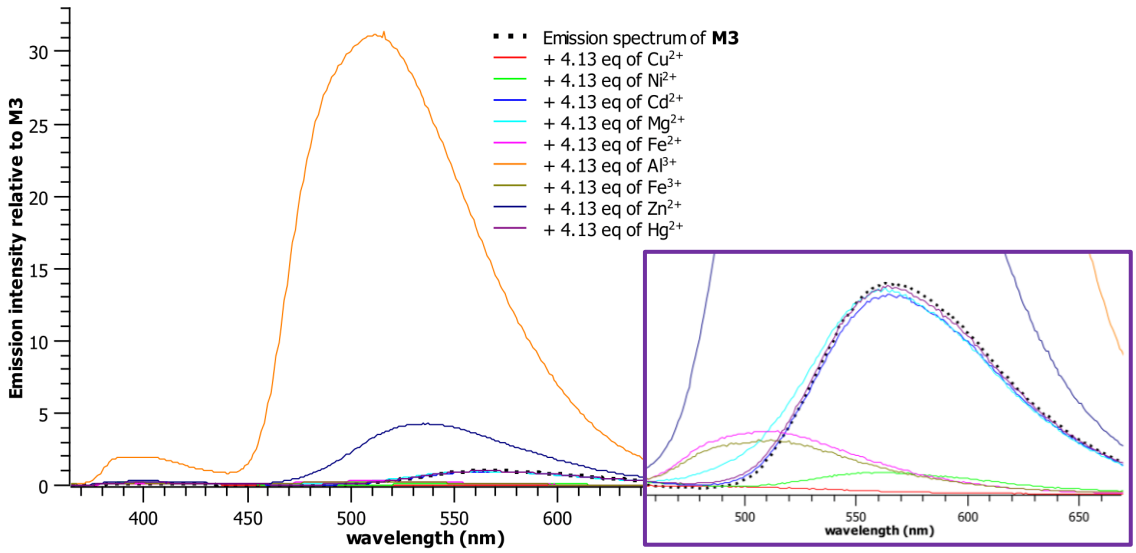

Figure 135. Emission spectrum of **M3** (12.1 μmol/L in THF : EtOH 0.5 : 99.5) in presence of an excess (4.13 equivalents) of several metallic cations; λ_{exc} = 356 nm. Inset (right bottom): zoom of the region from 450 to 675 nm and 0 to 1.2 relative emission intensity.

[20] It is important to mention that, in some cases, like with the **M3** molecule, THF will be used in very low quantities (< 0.5 % of the volume of the solvent mixture) in order to help to solubilize the probes.

It can be seen in Figure 135 that Al^{3+} has a dramatic impact on the emission spectrum of **M3**: it enhances 20-fold the band at 400 nm, also promoting a new band centered at around 510 nm, with an intensity that is more than 30-fold in comparison with the more intense band of the free ligands which was centered at 566 nm. Also, the addition of the same amount of zinc has a similar but lesser effect: it enhances 3-fold the band at 400 nm, while promoting a new and more intense band at 535 nm. Moreover, both iron cations (Fe^{2+} and Fe^{3+}) quench the emission intensity of the band at 566 nm and generate a new but low emissive band centered at 500 nm. Finally, the copper and nickel cations completely quench the emission intensity of the low-energy emission band of **M3**.

All these bulk test results indicate that **M3** lacks selectivity towards a specific metallic cation in the solvent medium used in terms on coordination. This result was expected owing to the chemical structure of the molecule, as mentioned in Section 2.1.1.6. Nonetheless, the change in the emission spectrum generated by the aluminum cation is impressive by itself and unique in terms of the enhanced intensity and can be anticipated as a selective way for the detection of Al^{3+}.

By its side, Figure 136 shows that the emission of **M3** is impacted by several anionic species. Particularly, it can be mentioned that the phosphate anion promotes a new band that is blue shifted from the most emissive one of the free molecule and has a 2.5-fold higher emission intensity. A similar but less impressive effect happens upon addition of $HAsO_4^{2-}$, AsO^{2-}, and CN^-. Owing to their strong Brønsted base nature, it could be postulated *a priori* that these anions are able to deprotonate the phenolic protons of **M3**, particularly the one that undergoes ESIPT as seen in Figure 81 in Section 3.1, which have a pK_a of around 10 [286].

The hypochlorite anion, for its part, generates a 7-fold enhancement of the emission band of the ligand at 400 nm while also having the same effect as the last three anions mentioned. Finally, the same amount of glyphosate has the effect of enhancing 7-fold the band at 400 nm and quenching by 50 % the band at 566 nm. Combining this last observation with the fact that CH_3COO^- does not induce any change in the emission spectrum of **M3**, it can be thought that the interaction of glyphosate with the molecule may not occur *via* carboxylate group. Moreover, the lack of shift of the band at 566 nm could indicate that a deprotonation *via* the phosphonate group does not take place, as the result of this interaction should be a blue shifted band as in the case with PO_4^{3-}.

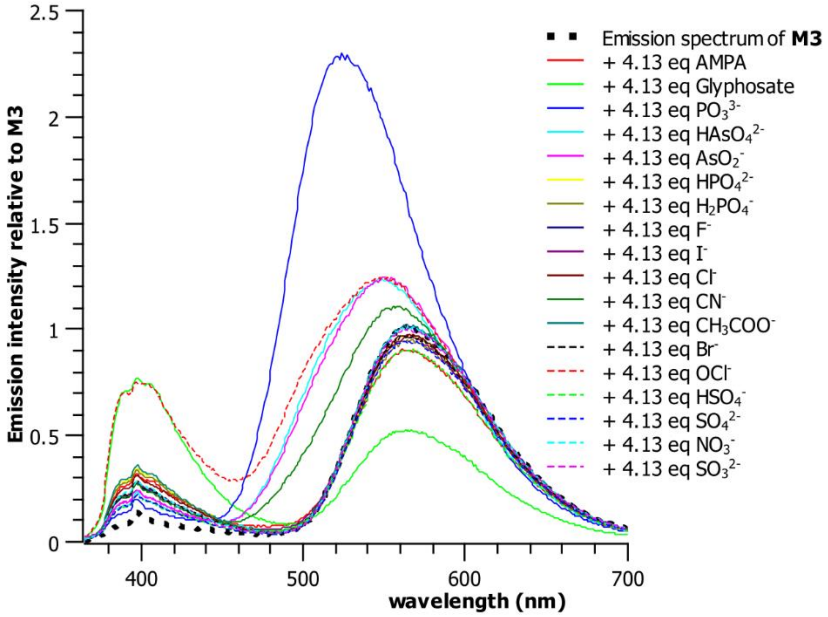

Figure 136. Emission spectrum of **M3** (12.1 μmol/L in THF : EtOH 0.5 : 99.5) in presence of an excess (4.13 equivalents) of several anions; λ_{exc} = 356 nm.

All these results clearly exhibit a lack of selectivity of **M3** towards a single anion; however, upon closely examining the responses, an interesting conclusion can be extracted: glyphosate is the only species that generates an enhancement in the band at 400 nm and, at the same time, a quenching of the band at 566 nm in ethanolic medium. This unique response towards the pesticide could be the basis of a ratiometric chemosensor.

To finalize the description of the bulk tests, it can be seen in Figure 137 that **M3** has a different response depending on the pH of the solution added. In the solvent medium tested (THF : EtOH 0.5 : 99.5), the addition of a few equivalents of HCl generates the quenching of the band at 566 nm and a 15-fold enhancement of the band at 400 nm. Also, the addition of a few equivalents of NaOH generates a new band centered at 533 nm, which is 1.5-fold enhanced in comparison with the original most intense band of the ligand.

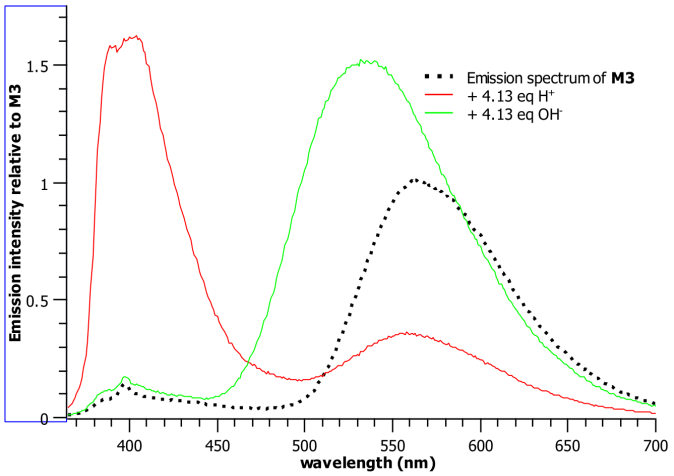

Figure 137. Emission spectra of **M3** when adding acidic or basic solutions. [**M3**] = 12.1 μmol/L in THF : EtOH 0.5 : 99.5; λ_{exc} = 356 nm.

The effect observed upon addition of a base can be explained by the deprotonation of the phenolic groups, thus the resulting emission spectrum at these conditions might correspond to the phenolate anion of **M3**. This tends to confirm the initial assessment that the most basic anionic species, PO_4^{3-}, $HAsO_4^{3-}$ and CN^-, the former in particular, could also deprotonate the ligand because the response is similar, although not exactly the same. This hints that, in reality, owing to the labile nature of the phenolic protons, **M3** is susceptible of deprotonation, thus the response that was observed with these analytes depends on the strength of the base and not to a particular interaction with an anionic species.

On the other hand, the effect of adding an acid to the ethanolic solution of the ligand could have the effect of protonating the nitrogen atom of the imine group, which could hamper the ESIPT mechanism because the basicity of this atom is reduced, thus limiting the proton transfer [287]. Also, as mentioned before, an acidic medium can eventually lead to the cleavage of the imine bond [285]. Then, it can be concluded that the enhanced emission band observed at 400 nm could be due to the cationic form of **M3**, with the quenching of the band at 566 nm, which was assigned to the keto tautomer, as the logic consequence of a diminished ESIPT rate. Interestingly, the addition of glyphosate has this same effect on the emission spectrum of **M3**, which may indicate that the imine group interacts with the pesticide.

At this point, unfortunately, a non-expected behavior of **M3** in the solvent medium used was noticed: the band at 400 nm experienced a notorious and spontaneous self-

enhancement over time while the band at 566 get slightly quenched, as can be seen in Figure 138.

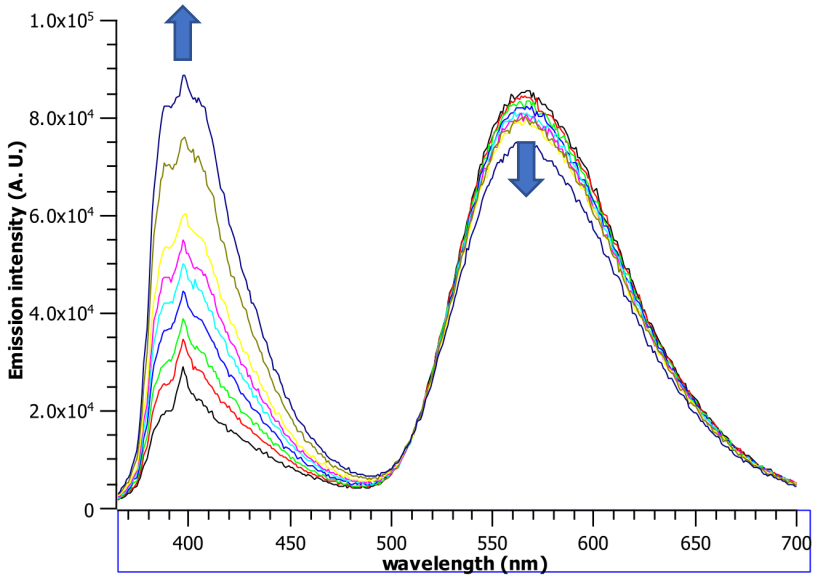

Figure 138. Emission spectra of **M3** in THF : EtOH 0.5 : 99.5 solvent medium over time. The first 6 spectra were measure 1 minute apart. The second to last, 10 minutes after, and the last one, 15 minutes after. [**M3**] = 12.1 μmol/L; λ_{exc} = 356 nm.

To verify if this effect was solvent-dependent, the emission spectrum of **M3** in near perfect MeOH, CH_2Cl_2, DMSO and MeCN medium was recorded over time. The results can be seen in Figure 139.

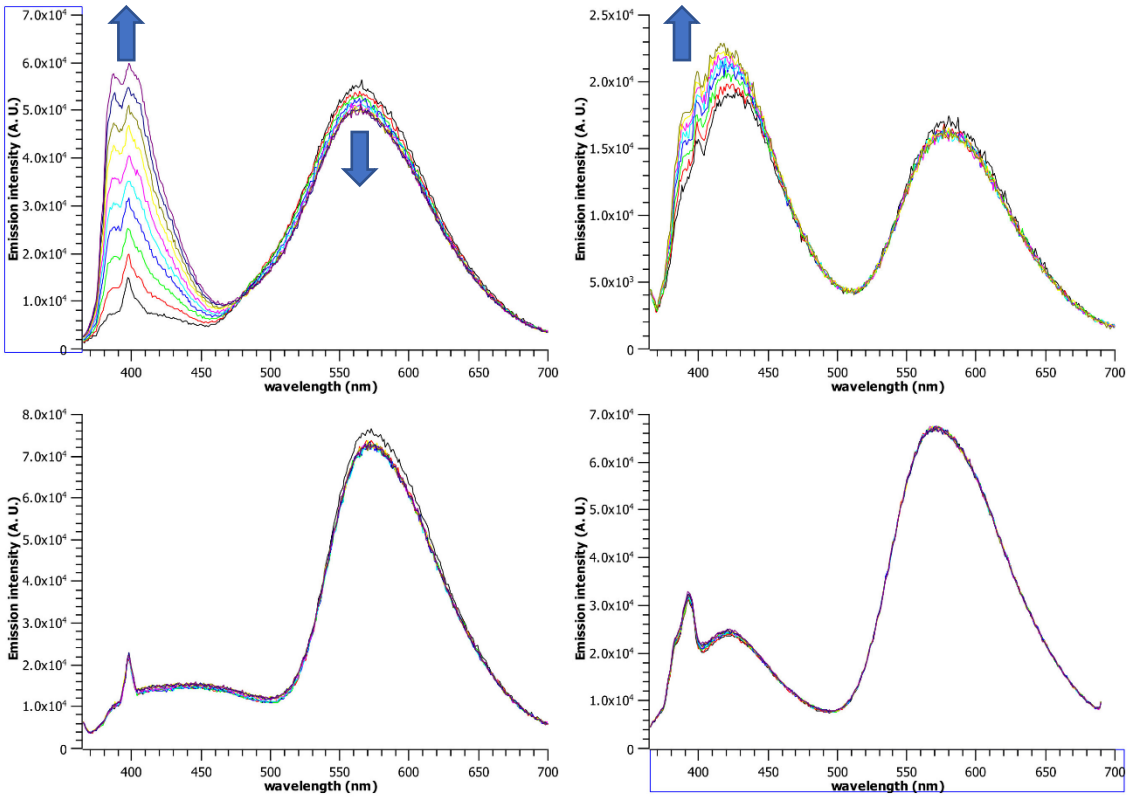

Figure 139. Evolution of the emission spectrum of **M3** in different solvent media ([**M3**] = 12.1 μmol/L). Each spectrum was taken 2 minutes apart. (top left) solvent medium: THF : MeOH 0.5 : 99.5; λ_{exc} = 356 nm. (top right) solvent medium: THF : CH_2Cl_2 0.5 : 99.5; λ_{exc}: 356 nm. (bottom left) solvent medium: THF : DMSO 0.5 : 99.5; λ_{exc} = 356 nm. (bottom right) solvent medium: THF : MeCN 0.5 : 99.5; λ_{exc} = 352 nm. Note that the y-axis scale is different in each case.

Firstly, it can be seen that the position and relative intensity of both bands vary depending on the solvent. As mentioned in 2.1.2.1, ESIPT is a solvent-dependent process and its rate depends, among other factors, on the proticity and polarity of the medium [55], thus this observation confirms the presence of this mechanism in **M3**. Also, due to the low emission intensity of the molecule, the band corresponding to the Raman scattering of the solvent can be seen as a sharp peak in the 390 – 400 nm region in the four cases.

As for the evolution of the spectrum over time, in THF : MeOH 0.5 : 99.5 medium, the band assigned to the emission of the [enol]* tautomer gets enhanced by 300 % in twenty minutes. For THF : $CHCl_3$, THF : DMSO and THF : MeCN 0.5 : 99.5 media in the same time, the enhancement of this band is of only by around 15 %, 8 % and 5 %, respectively.

It is then clear that protic solvents have the effect of rapidly enhancing the band assigned to the emission of the [enol]* tautomer. While this process seems to also occur in aprotic solvents, the effect is noticeably much retarded, probably because the solvent-probe

interaction is less efficient. This observation allows these solvents to be used as suitable medium for sensing applications of **M3**, considering that the detection and concomitant change of the fluorescence needs to be a fast process.

Gathering all the results together, it can be stated that it is the effect of H^+, protic solvents and glyphosate that generate an enhancement in the band corresponding to the [enol]* tautomer emission and a concomitant quenching of the band corresponding to the [keto]* tautomer, probably due to interaction with the iminic nitrogen of **M3** that decreases the ESIPT rate in the ligand.

Then, in order to verify if the sensitivity of the ligand was maintained using a non protic solvent, the bulk tests were carried out in a mixture of THF : MeCN 0.5 : 99.5 following the procedure described in Section 2.3.3. The results can be seen in Figure 140, Figure 141 and Figure 142.

As for the cations, it is evident that **M3** loses the particular sensitivity towards aluminum(III) in a non-protic solvent. In THF : MeCN 0.5 : 99.5, it can be seen that the ligand is sensitive towards Cu^{2+}, Al^{3+}, Zn^{2+} and Hg^{2+}, all by the promotion of a new band, which is more intense and at higher energies than the original band corresponding to the emission of the [keto]* tautomer. Moreover, Fe^{2+} and Fe^{3+} quench the emission of the ligand at 570 nm and promote a new and low intense band centered at around 510 nm.

Also, **M3** unfortunately loses the sensitivity to glyphosate in an ethanolic medium. Under the new solvent conditions, emission of the molecule changes upon addition of PO_4^{3-}, CN^- and F^-, all by a promotion of a new and more intense blue shifted band in comparison with the one assigned to the [keto]* tautomer of **M3**. Finally, it can detect the hypochlorite anion by a 30-fold enhancement of the band assigned to the emission of the [enol]* tautomer and the promotion of a new band that is blue shifted from the original highest emissive one.

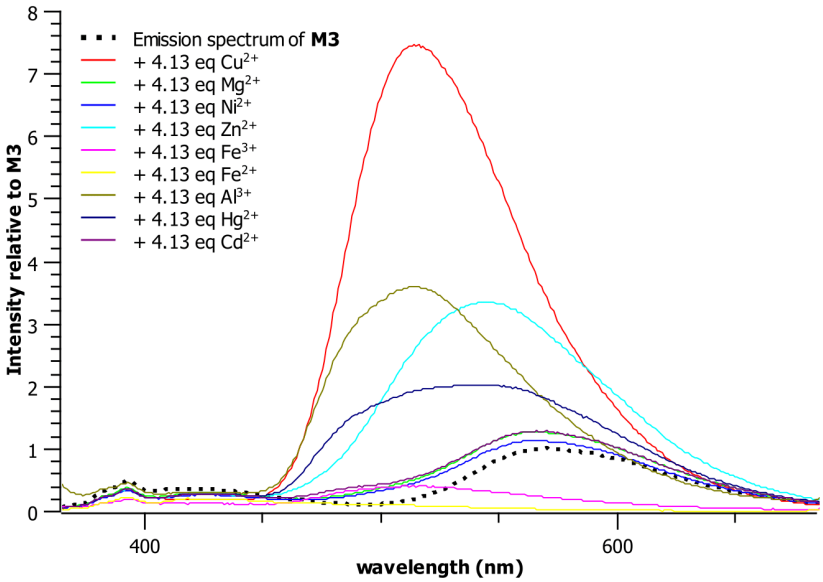

Figure 140. Emission spectrum of **M3** (12.1 μmol/L in THF : MeCN 0.5 : 99.5) in presence of an excess (4.13 equivalents) of several metallic cations; λ_{exc} = 352 nm.

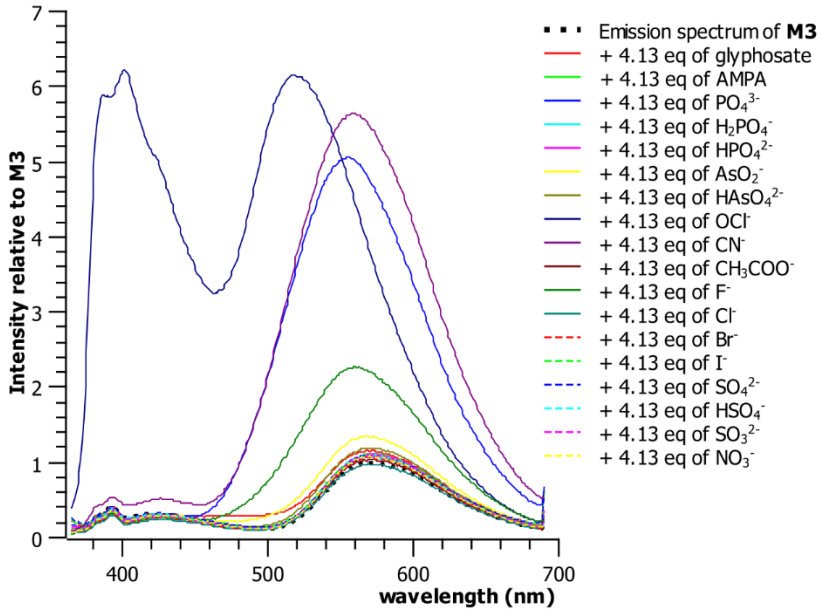

Figure 141. Emission spectrum of **M3** (12.1 μmol/L in THF : MeCN 0.5 : 99.5) in presence of an excess (4.13 equivalents) of several anions; λ_{exc} = 352 nm.

Upon addition of an acid or a base into the solvent medium, it can be seen that OH^- has the effect of enhancing and slightly blue shifting the low energy band of **M3**, while H^+ only generates a quenching of the emission.

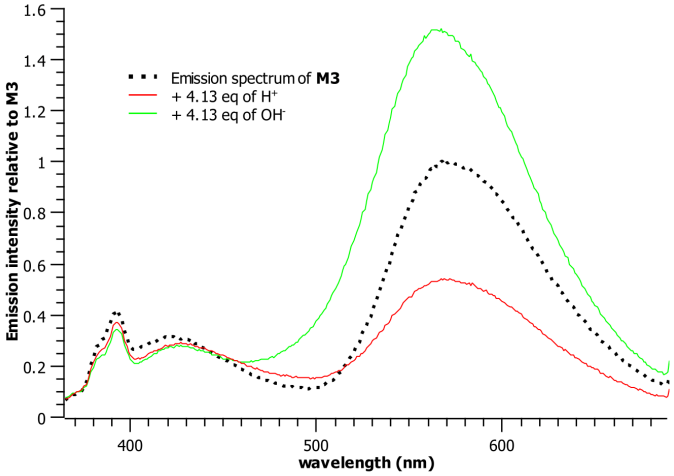

Figure 142. Emission spectra of **M3** when adding acidic or basic solutions. [**M3**] = 12.1 μmol/L in THF : MeCN 0.5 : 99.5; λ_{exc} = 352 nm.

All these results show that **M3** is not a selective luminescent probe for the detection of cations in a THF : MeCN 0.5 : 99.5 medium and the only species that generates a unique change of the emission is the hypochlorite anion. Considering this aspect and the fact that **M3** lost the sensitivity to the particular species it was designed to detect in a solvent medium that did not promote a self-change in the emission, it was decided to halt further research on this compound[21]. However, it has been demonstrated that the design of this molecule, which carries both acidic and basic groups intercalated one from the other, could be the base for the development of other ligands with direct sensing aptitudes towards the aforementioned pesticide because there was a unique response against it in an ethanolic medium. Tuning the sensitivity of the ligand towards glyphosate could involve, for example, avoiding the use of phenol groups in *ortho* position to a Schiff base that make it able to detect metallic cations. Also, further research on the solvent-dependent emission of this ligand could be worth to pursue in the future, for instance, as it might be an interesting candidate for alcohol detection.

4.1.3.2 Conclusion

The molecule **M3**, which intercalates in its chemical design acidic and basic groups capable of forming hydrogen bonding interactions with glyphosate, exhibits a unique, fast and direct response towards this pesticide in a EtOH : THF 99.5 : 0.5 solvent medium even when the analyte is dissolved in water. Unfortunately, the emission of this compound evolves spontaneously over time in this system, which makes it unsuitable

[21] This includes not obtaining the value of the fluorescence quantum yield of this molecule.

for quantitative sensing applications. Despite this drawback, **M3** could be an interesting candidate for immediate glyphosate detection acting as a qualitative indicator of its presence in aqueous environments.

Additionally, in a solvent medium in which the emission of **M3** is more stable, namely MeCN : THF 99.5 : 0.5, the sensitivity towards glyphosate is completely lost and the molecule does not exhibit a marked selectivity towards any species among the ones tested. Nonetheless, the particular design of **M3** could be the base for the development of future chemosensors able to not only directly detect, but to quantify this dangerous species.

4.2 Benzazole derivatives: M4, M5 and M6

4.2.1 M4

The new ligand **M4** (Figure 143) was designed with the objective of using its ESIPT capabilities to obtain a ratiometric detection of metallic cations, particularly aluminum(III) taking advantage of the reported suitable size of the preformed cavity formed by the *OH* of the phenol group and the oxime unit. As mentioned in Section 2.1.2.1, this response, which arises as the consequence of the inhibition of ESIPT that will be explained later, carries several advantages such as better sensitivity and better quantification results. Moreover, the presence of an oxime group in the structure of the molecule was thought to induce a chemical reaction upon exposure of OCl^-, making this compound a chemodosimeter against this analyte. The importance of the detection of aluminum(III) and hypochlorite have already been outlined in previous sections of this chapter.

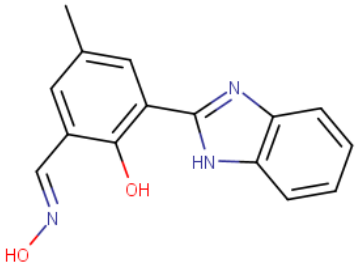

Figure 143. Chemical structure of **M4**.

4.2.1.1 Bulk tests

Bulk tests in THF : H_2O 0.5 : 99.5 medium were carried out following the procedure described in Section 2.3.3. The cation and anion bulk test results are shown in Figure 144 and Figure 145, respectively. Also, the response of **M4** against the addition of acidic and basic solutions was probed and the results can be seen in Figure 146.

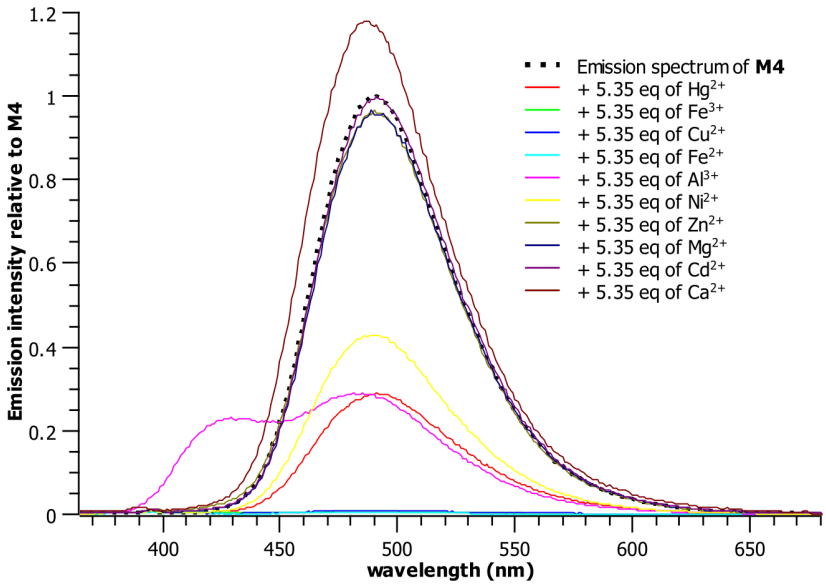

Figure 144. Emission spectrum of **M4** (18.7 μmol/L in THF : H_2O 0.5 : 99.5) in presence of an excess (5.35 equivalents) of several metallic cations; λ_{exc} = 349 nm.

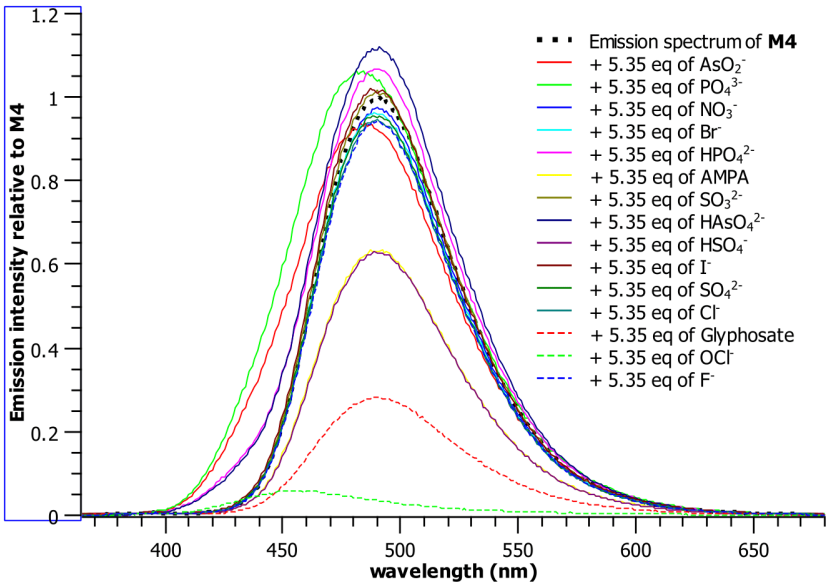

Figure 145. Emission spectrum of **M4** (18.7 μmol/L in THF : H_2O 0.5 : 99.5) in presence of an excess (5.35 equivalents) of several anions; λ_{exc} = 349 nm.

It can be extracted from the cation bulk test that the emission of **M4** gets partially quenched by Ni^{2+} and Hg^{2+}, and completely quenched by Fe^{2+}, Fe^{3+} and Cu^{2+}. More importantly, the addition of Al^{3+} originates a new band centered at 427 nm and a concomitant quenching of the original emission band of the ligand assigned to the emission of the [keto]* tautomer as discussed in Section 3.2.

As for the anion bulk test, it can be seen that OCl^- generates a dramatic decrease in intensity of the emission of the ligand with a slight blue shift to 455 nm. Other anionic species also seem to interact with the ligand, such as glyphosate, AMPA and HSO_4^-, all by partially quenching the emission, but without any shift. Finally, it can be seen that PO_4^{3-}, being basic in nature, generates a slight blue shift in the emission band of the ligand.

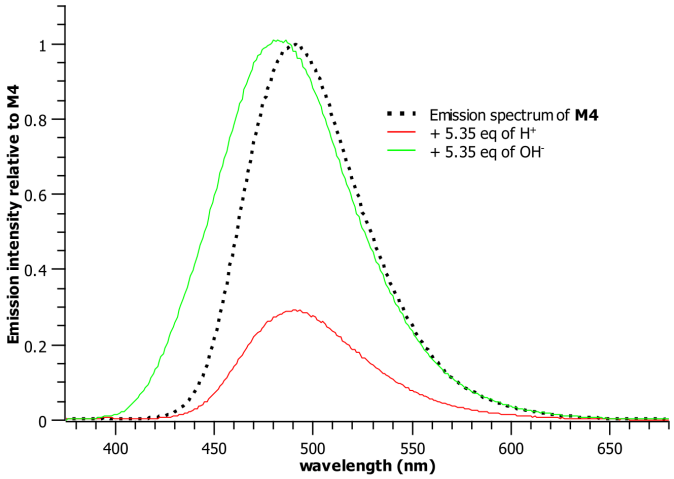

Figure 146. Emission spectra of **M4** in acidic or basic medium. [**M4**] = 12.1 μmol/L in THF : H_2O 0.5 : 99.5; λ_{exc} = 349 nm.

Finally, the pH tests show that the addition of an acid into the solvent mixture, which has been calculated to be at pH ≈ 4 after this addition, quenches the emission of **M4**, while the addition of base (giving a final pH of ≈ 10) slightly blue shifts it. This last effect is analog as what was observed with PO_4^{3-}, and it can be proposed that this blue shifted band corresponds to an anionic species of **M4**, formed as a consequence of the deprotonation promoted by the Brønsted base capabilities of these two species. It is important to mention that the pK_a values for the deprotonation of the phenol of 2-(hydroxyphenyl)benzimidazoles, the hydroxy unit of a benzaldoxime and the N-**H** of the benzimidazole are ~9.2 [163], ~10.7 [288] and ~17 [289], respectively, meaning that the first species to lose a proton is the phenolic O-***H***, closely followed by the oximic O-***H***.

Thus, the first anionic species formed by addition of base is the phenoxide anion of the hydroxyphenyl, which at pH 10 should be the most predominant species in solution. This result indicates that the response of **M4** towards phosphate accounts for the basicity of this species and not due to a particular interaction.

As for the effect of adding an acid, in the first place, it needs to be considered that the pK_a values for the protonation of the nitrogen of benzimidazoles and of oximes are both in the 4.5 to 6 range, which means that a solution of **M4** at pH ~4 it is expected to have a mixture of mono-, di- and non-protonated species. It has been mentioned in Section 4.1.3.1 that an acidic solution reduces the ESIPT rate constant and allows to see the band corresponding to the emission of the [enol]* tautomer. This, however, is true for alcoholic solutions. In aqueous environments, an ultrafast deprotonation process has been proposed to occur in the excited state, in which the [cation]* rapidly transfers its most acidic proton to the solvent medium forming the neutral [keto]* tautomer [287]. It is then consistent that the observed emission of **M4** in acidic conditions only comprises the band corresponding to the [keto]* tautomer of the ligand, although with lower emission intensity due to the quenching nature of the H^+ ions in aqueous ESIPT systems [290].

The effect that an acidic or basic medium on the sensing aptitudes of **M4** will be analyzed in Section 4.2.1.4.

Finally, it can be concluded that **M4** shows a particular and specific response when treated with aluminum(III) and hypochlorite, different in each case. Indeed, no other species among those tested gave rise to new bands at 527 nm or 427 nm as observed for the Al^{3+} and OCl^- ions, respectively.

As for the species that totally quench the emission of the ligand, namely Fe^{2+}, Fe^{3+} and Cu^{2+}, their effect could be explained by the paramagnetic fluorescence quenching mechanism [61]. Apparently, in some particular complexes with these cations, among others, the forbidden intersystem crossing ($T_1 \leftarrow S_1$) becomes faster thanks to the complexation event itself. Then, the triplet state of the fluorophore is deactivated by a bimolecular non-radiative process. Ligands that exhibit this mechanism have been found in the literature [64] [177] [291] [292] [293] [294]. Due to being of a different nature than the ESIPT mechanism that was the subject of study with this benzazole derivative, it was decided to leave the fluorescence quenching mechanism out of the scope of the present

thesis work and thus, the interaction of **M4** with Fe^{2+}, Fe^{3+} and Cu^{2+} will not be analyzed in more detail[22].

Finally, although there are other species that partially quench the emission of **M4** such as Ni^{2+} or glyphosate, the response they promote is not unique as only a partial quenching of the emission is observed. So, they cannot lead to a possible differentiation when these species are present along with Fe^{2+}, Fe^{3+} or Cu^{2+}. In consequence, they will not be further analyzed. Nonetheless, it should be noted that the response of this ligand towards glyphosate is consistent with the observed results with the **M3** molecule: **M4** has in its structure several hydrogen bonding positions that can interact with the mentioned herbicide, which could then lead to a change in its emission spectrum. These both results offer a glimpse into the future design of other molecules able to directly detect glyphosate as the evidence suggests that they i) need several acidic or basic entities to obtain a good interaction and b) should avoid containing phenol groups in close proximity to Schiff bases to circumvent potential cation sensitivity.

4.2.1.2 Calibration curves

Emission titrations of **M4** in THF : H_2O 0.5 : 99.5 medium against Al^{3+} and OCl^- were carried out following the procedure described in Section 2.3.4. The results of the titration with the former analyte, as well as its calibration curve, can be seen in Figure 147. It is clear that Al^{3+} generates a ratiometric response: the gradual quenching of the band assigned to the emission of the [keto]* tautomer is accompanied by the enhancement of a new band centered at 428 nm. Upon addition of 1 600 equivalents of Al^{3+}, the original band of **M4** is completely quenched and the new band is not further enhanced.

[22] Despite deciding to not analyze these interactions with greater detail, experimental work has been carried out. The obtained results are the following:

- For the **M4**-Fe^{2+} interaction. Limit of detection (3σ method): 0.54 μmol/L; Stoichiometry (ESI-MS): 1 : 1; Binding constant (Benesi-Hildebrand equation): 1.69 x 10^5 M^{-1}.
- For the **M4**-Fe^{3+} interaction. Limit of detection (3σ method): 0.27 μmol/L; Stoichiometry (ESI-MS): 1 : 1; Binding constant (Benesi-Hildebrand equation): 1.83 x 10^5 M^{-1}.
- For the **M4**-Cu^{2+} interaction. Limit of detection (3σ method): 0.68 μmol/L; Stoichiometry (ESI-MS): 1 : 1; Binding constant (Benesi-Hildebrand equation): 2.64 x 10^4 M^{-1}.

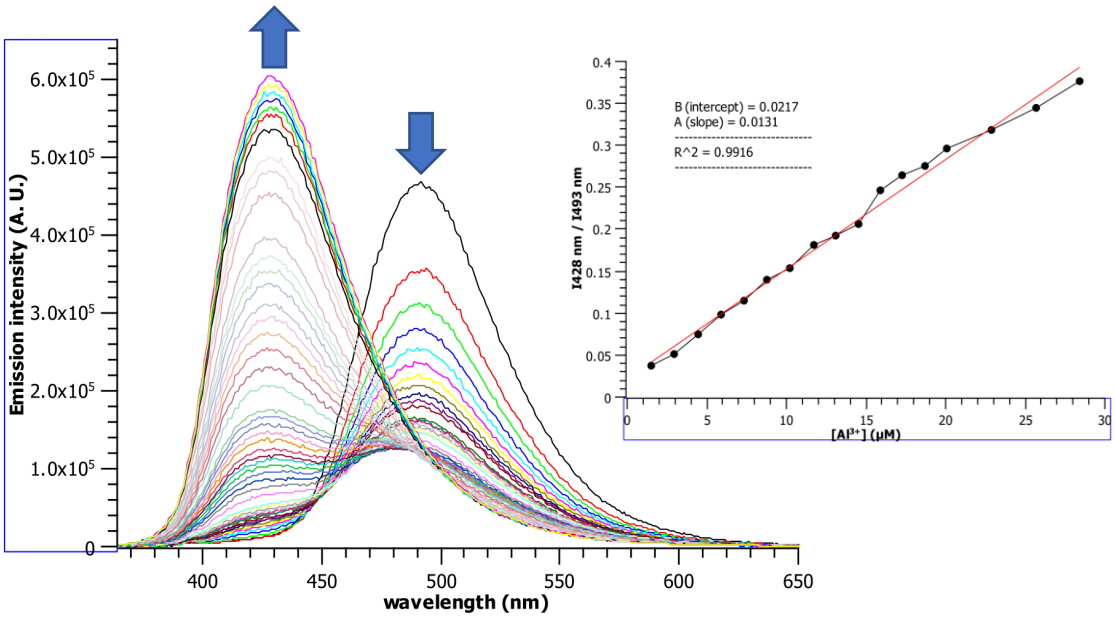

Figure 147. Emission titration profile of **M4** against incremental quantities of Al^{3+}. [**M4**] = 14.7 μmol/L; λ_{exc} = 349 nm. (right) Calibration curve for this titration ($I_{429\ nm}/I_{493\ nm}$ *vs.* [Al^{3+}]). Each point has a calculated error of 2 %.

The calibration curve for this titration shows that there is a linear ratiometric response of the ligand towards aluminum(III) in the ~2 to ~30 μmol/L range of the concentration of the analyte with the limit of detection being calculated at 0.14 ± 0.003 μmol/L using the 3σ method (Section 93).

The emission titration profile of **M4** towards OCl^- can be seen in Figure 148, where it is also clear that there is a ratiometric response: the quenching of original band of the ligand at 493 nm gives rise to a new band centered at 453 nm. The end point of this titration happens upon addition of 3.2 equivalents of OCl^-.

Unfortunately, due to the close proximity of the two bands, it was not possible to accurately use the emission intensity values to calculate the limit of detection of **M4** towards hypochlorite. Thus, the absorption titration was carried out (Figure 149). It can be seen that the response of the ligand towards OCl^- is also ratiometric: the absorbance of the band at 340 nm decreases while that of the band at 399 nm increases with a clear isosbestic point at 365 nm that evidences the presence of two species in solution. It was found that **M4** exhibits a linear response in the range of ~5 to ~30 μmol/L of concentration of the analyte, which allowed for the calculation of the limit of detection using the 3σ method (Section 2.3.5). The obtained value is 1.08 ± 0.03 μmol/L.

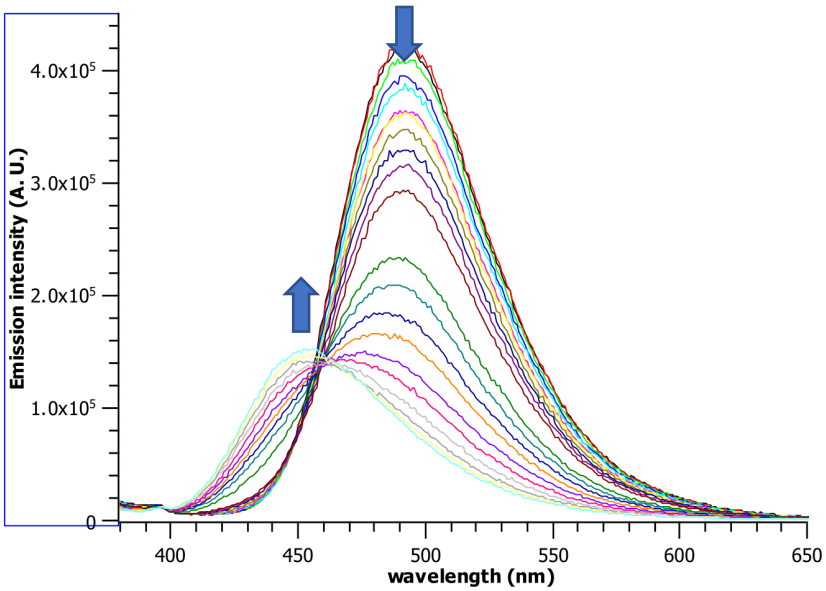

Figure 148. Emission titration profile of **M4** against incremental quantities of OCl^-. [**M4**] = 14.7 μmol/L; λ_{exc} = 349 nm. Each point has a calculated error of 2 %.

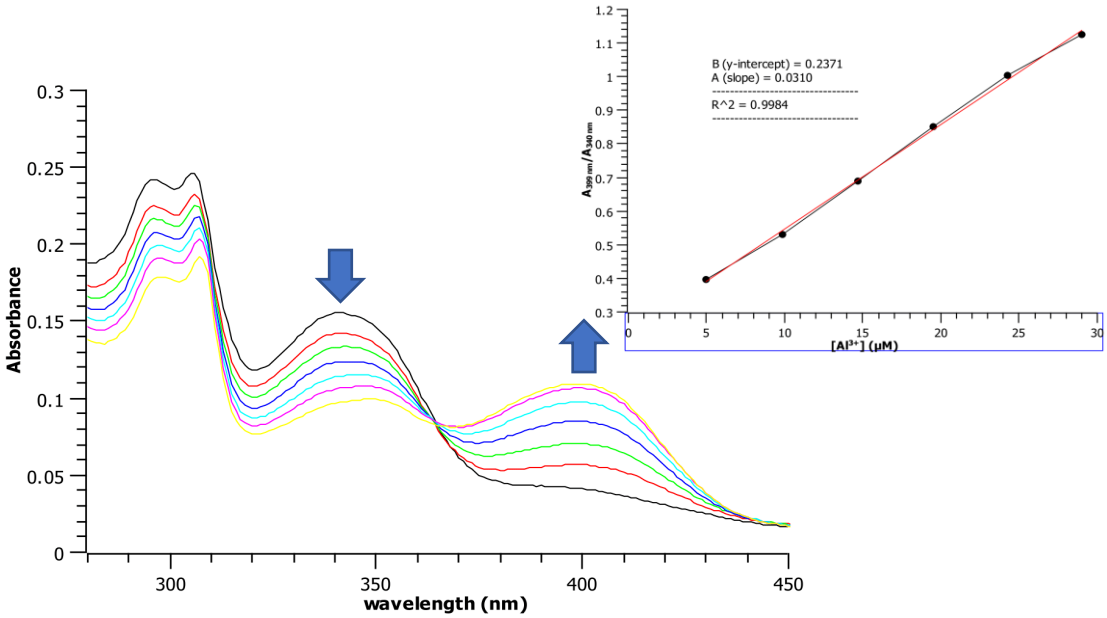

Figure 149. Absorption titration profile of **M4** against incremental quantities of OCl^-. [**M4**] = 18.7 μmol/L. (right) Calibration curve for this titration ($A_{399\ nm}/A_{340\ nm}$ *vs*. [Al^{3+}]). Each point has a calculated error of 3 %.

To finalize this analysis, it can be said that while the values of the limits of detection of **M4** for Al^{3+} (0.14 μmol/L) and OCl^- (1.08 μmol/L) are a little higher than those of **M2** towards Al^{3+} (0.06 μmol/L) and **M1** towards OCl^- (1.01 μmol/L), they are still well under the threshold of acceptability, making the ligand a good candidate for real-life water

quality assessment. Moreover, this ligand has the advantage to detect both species in a near perfect aqueous environment, making it even more suitable for monitoring applications.

4.2.1.3 Sensing mechanism

As mentioned in Section 2.1.2.1, the general recognition event of an ESIPT-based ligand involves the inhibition of this mechanism by blocking the proton transfer. Thus, to verify if this applies to the present case and understand the detection of Al^{3+} by **M4**, first a ^{1}H-NMR titration was carried out, albeit with the limitations described in Section 4.1.2.3 due to the poor solubility of the aluminum salt in DMSO. The results can be seen in Figure 150.

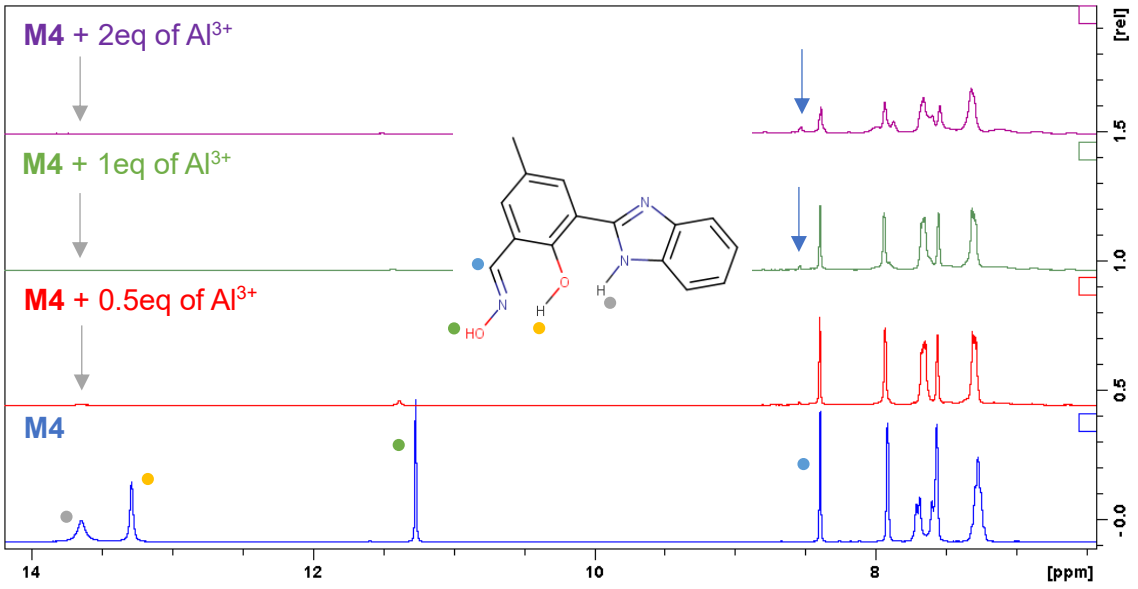

Figure 150. ^{1}H-NMR (300 MHz) titration of **M4** against Al^{3+}. The ligand was dissolved in DMSO-d_6 and the aluminum salt, in D_2O. Protons in the spectrum are assigned with colored circles.

While it is true that some of the aluminum salt that was added phased out of the solution, some interesting observations can still be made. First, it is seen that upon addition of Al^{3+}, the signal corresponding to the ***H*** atom of the C=N-O-***H*** oxime group at 11.27 ppm undergoes a slight downfield shift (from 11.27 ppm to 11.51 ppm) with a pronounced decrease in its intensity, almost completely disappearing. Also, a new peak appears next to the one assigned to the N=C-**H** proton of the oxime moiety at 8.40 ppm (pointed with a blue arrow). This could indicate that the oxime group actively takes part in the complexation event. Moreover, the peaks assigned to the benzimidazolic N-***H*** and the phenolic O-***H*** at 13.64 and 13.28 ppm, respectively, also seem to disappear upon

addition of Al^{3+}. However, zooming in the spectrum reveals that while the phenolic proton is completely lost, the intensity of the benzimidazolic one has just greatly decreased (grey arrow). It is important to consider that the loss of these labile protons in the ^{1}H-NMR spectra could also be due to exchange with the added D_2O. In fact, it has been empirically demonstrated that their intensity diminishes when adding the same amounts of only D_2O (without aluminum) into a DMSO-*d*$_6$ solution of **M4** as a reference test, although not as much as when aluminum(III) is present.

Also, while an ^{1}H-NMR titration cannot be done in CD_3OD because the labile protons cannot be seen in this solvent, a test that consisted in the addition of 1eq of Al^{3+} dissolved in CD_3OD to a methanolic solution of **M4** was done. The resulting spectrum is presented in Figure 151 and it clearly shows a small shift of the N=C-**H** proton, as well as a complete rearrangement of the chemical shifts of the benzimidazole unit, probably because of a change in the electronic structure of the ligand upon complexation.

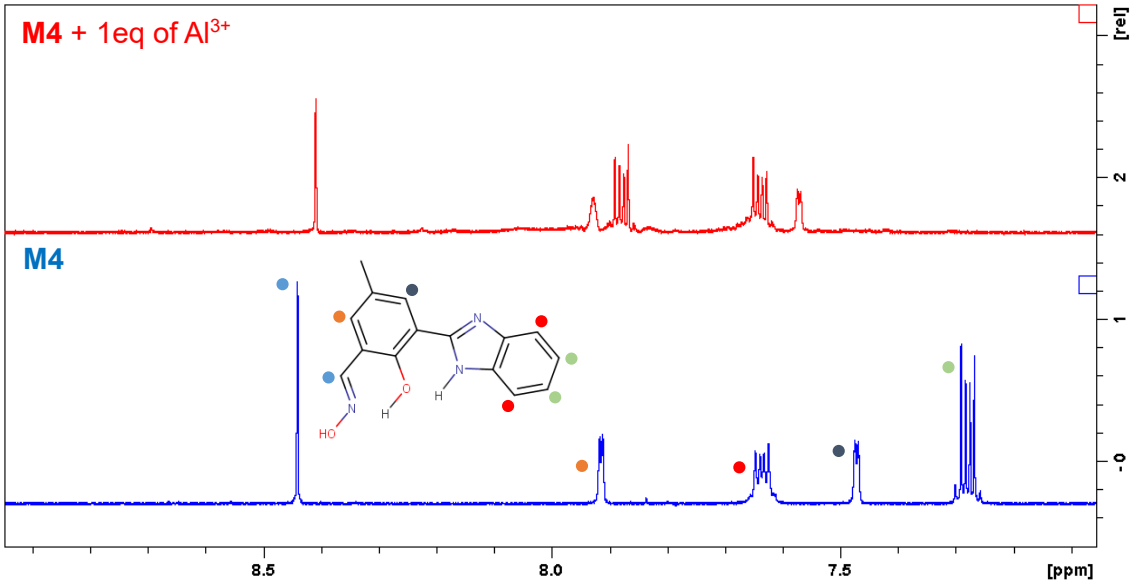

Figure 151. ^{1}H-NMR spectrum (CD_3OD, 400 MHz) of **M4** and **M4** + 1eq of Al^{3+} in deuterated methanol. Protons in the spectrum are assigned with colored circles.

Then, the Job's method of continuous variations was used to obtain the complexation ratio between **M4** and the aluminum cation following the procedure described in Section 2.3.6. The experiment was carried out in 1 : 9 DMSO : H_2O solution to eliminate the slight Mie Scattering effect present in the 99.5 % aqueous environment used for the titrations. The result, which can be seen in Figure 152, suggests a 1 to 1 complexing stoichiometry.

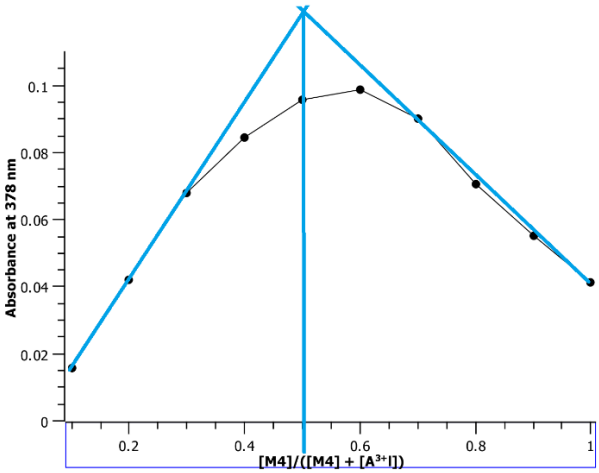

Figure 152. Job plot for the **M4**-Al^{3+} complex.

To verify this result, the ESI-MS spectrum of the complex[23] was obtained (Figure 153). It undoubtedly shows the presence of a mono-charged species that corresponds to the formula [**M4** – 2$\mathbf{H^+}$ + $\mathbf{Al^{3+}}$]$^+$ (ESI-MS (m/z), calculated: 292.0667; found: 292.0649). This result confirms the 1 to 1 stoichiometry obtained by the Job method and suggests the loss of two protons upon complexation.

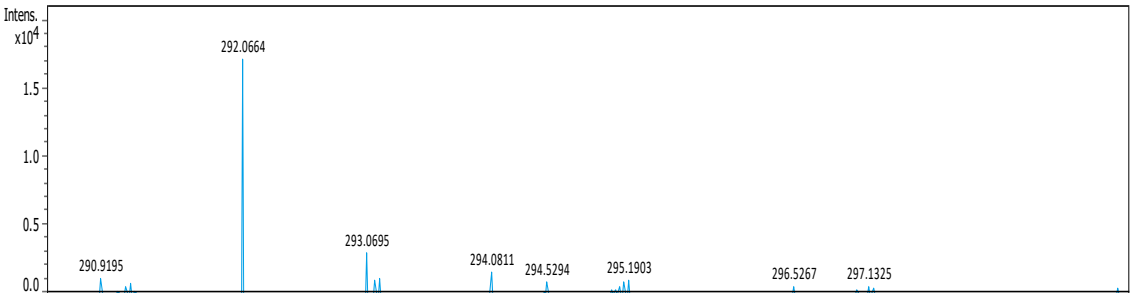

Figure 153. Zoom of the ESI-MS spectrum of the complex between **M4** and aluminum(III).

Several efforts were made to obtain crystals for X-ray diffraction analysis, but they all were unsuccessful.

All these results seem to confirm the original claim that the complexation of Al^{3+} by **M4** inhibits the ESIPT mechanism. At first, it can be proposed that the new band centered at 427 nm corresponds to the complexed phenoxide anion of **M4**. Indeed, it has been widely reported in the literature that blue shifted bands with respect to the emission of the [keto]*

[23] The complex was obtained using the following procedure: To a solution of **M4** in refluxing MeCN, 1eq of Al^{3+} was added. A yellow solid immediately precipitated, which was filtered, washed with hot MeCN and hexane, and dried under reduced pressure.

tautomer belong to such anions of 2-(2-hydroxyphenyl)benzazole ligands [250] [293] [294] [295]. Combining these facts with the ESI-MS results that indicate the loss of two protons in the complexation process and considering that the phenolic proton of **M4** is the most acidic one in the molecule, it can be postulated that it is this proton one of those who have been removed, leading to the formation of the phenoxide species observed during the emission titration. The lack of this phenolic proton in the complex then suppresses ESIPT simply because there is no proton to be transferred.

Then, the other proton that has been lost should be, according to the ^{1}H-NMR titration results and to the fact that it is the second most acidic proton in the ligand (Section 4.2.1.1), the one corresponding to the O-***H*** unit of the oxime.

At this point, it is reasonable to propose a possible complex structure for the [**M4**-Al^{3+}] complex as well as the mechanism of the ESIPT inhibition effect. Both can be seen in Figure 154.

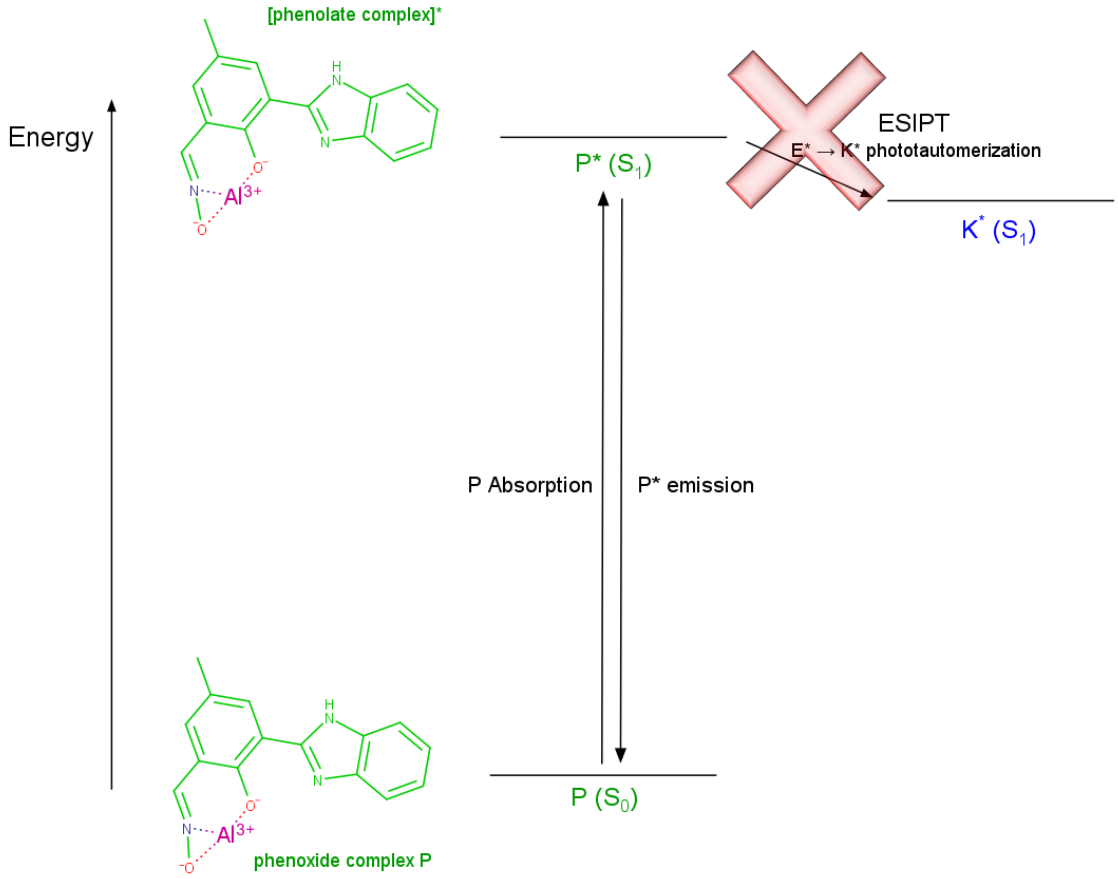

Figure 154. Proposed mechanism for the inhibition of the ESIPT mechanism in **M4** by the complexation of Al^{3+}.

Finally, because of the 1 : 1 stoichiometric ratio, it was decided to use the Benesi-Hildebrand equation to calculate the association constant of this interaction. Following the procedure detailed in section 2.3.7, the K_a was calculated to be 1.43 x 10^6 M^{-1}. With probes that have a similar structure as **M4**, it has been found that the typical association constant values lie between 3.31 x 10^4 M^{-1} [296] and 2 x 10^7 M^{-1} [132], showing that the value obtained for **M4** – Al^{3+} sits well in the upper part of that range.

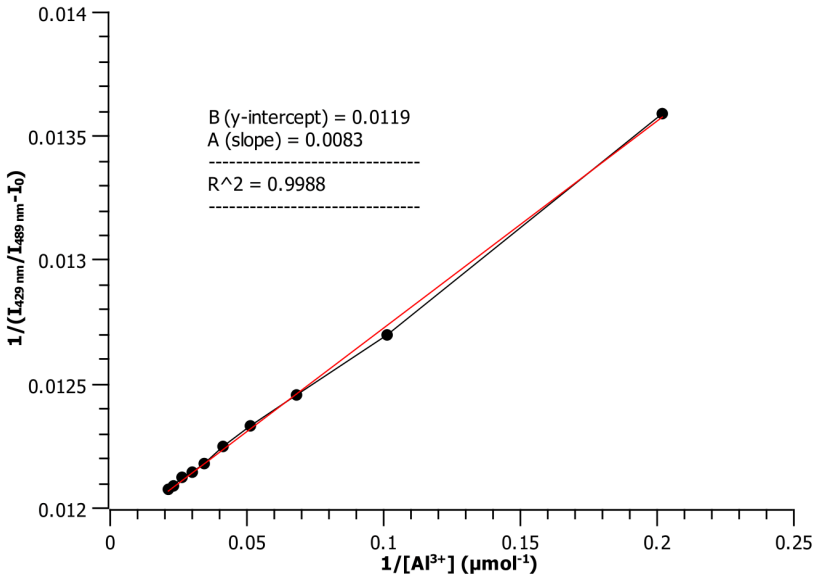

Figure 155. Benesi-Hildebrand plot for the **M4**-Al^{3+} interaction.

Concerning the sensing mechanism with OCl^-, as mentioned in Section 2.1.2.2, it was expected that the C=N bond of the oxime group of **M4** could react with this anion. According to the reviewed literature, there are two possibilities: either the formation of an aldehyde or of a nitrile oxide, the latter being a highly unstable group that may undergo further reactions [82] [87] [168] [169] [170] [171].

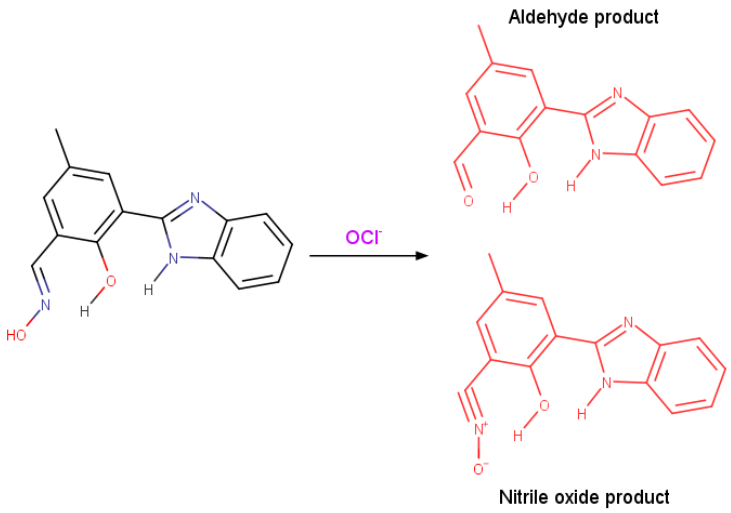

Figure 156. Possible reaction products of **M4** with OCl^- according to the reviewed literature.

The quickest way to verify the possible deoximation reaction into an aldehyde was to compare the emission spectra of this species and that obtained by adding OCl^- to a solution of **M4**. The aldehyde, which was synthesized as the precursor of **M4** (Section 2.1.2.3.2) shows an emission band centered at 525 nm, as can be seen in Figure 157. This band is completely different from that of **M4** (493 nm) and that obtained when OCl^- is added (455 nm). This result gave a first clue that the recognition event does not involve the formation of an aldehyde.

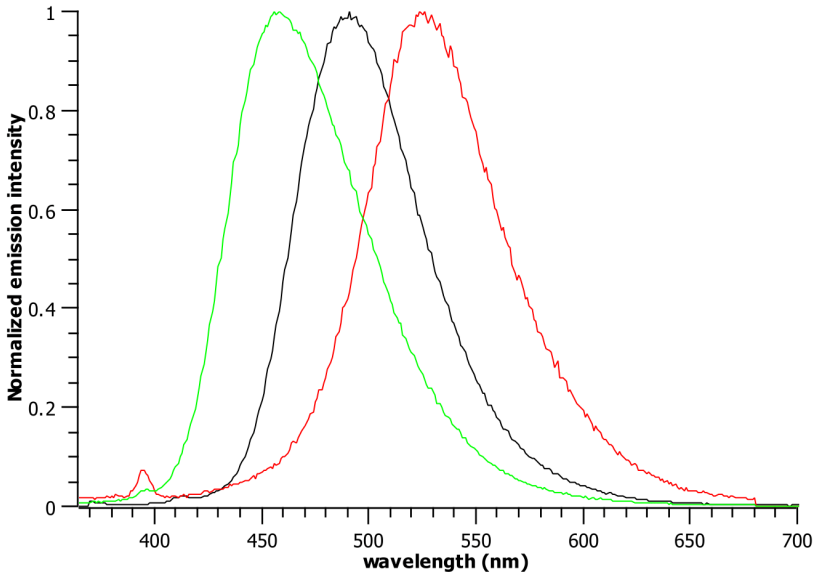

Figure 157. Comparison of the normalized emission spectrum of **M4** (black), the corresponding aldehyde (red) and the product of the interaction between **M4** and OCl^- (green) in THF : H_2O 0.5 : 99.5 solvent medium.

Then, the ^{1}H-NMR titration of **M4** against hypochlorite was performed in DMSO-d_6 with $Ca(OCl)_2$ as the source of the anion as this compound is soluble in DMSO at low concentrations. The results can be seen in Figure 158 and they show the partial disappearance of the signal corresponding to the oxime N-O-***H*** proton, the apparent loss of the signal assigned to the phenolic O-***H***, and the broadening of the signal that corresponds to the benzimidazolic N-***H***.

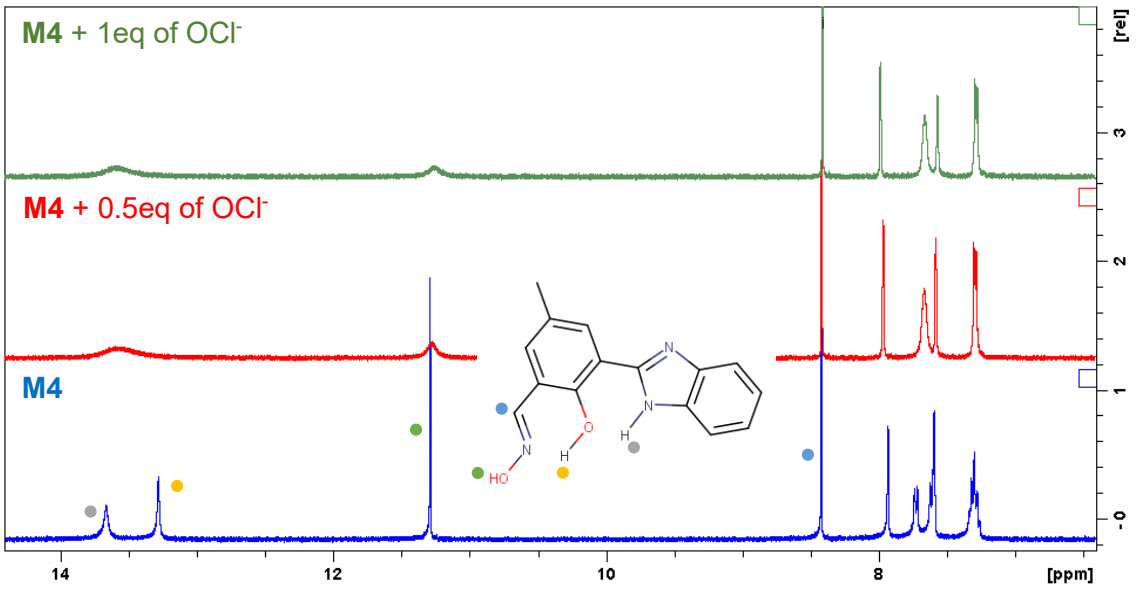

Figure 158. ^{1}H-NMR titration (DMSO-d_6, 400 MHz) of **M4** with OCl^-. Protons in the spectrum are assigned with colored circles.

Besides the changes in the spectra, the most important observation that can be done from this test is that no signal corresponding to the presence of an aldehyde was observed. If this compound were to be formed, the signal of the **H**-C=O proton would have been observed *δ* 10.47 ppm (Section 2.1.2.3.2). Also, as the signal corresponding to the **H**-C=N proton of the oxime was still present without any change, the formation of the nitrile oxide could also be discarded.

At that point, however, an interesting observation arose. When integrating the signals of the spectra shown in Figure 158, it was noticed that the one corresponding to the oxime N-O-***H*** still gave a value of 1 ***H*** (relatively to the ***H***-C=N proton of the oxime) and the broad signal in the area of the benzimidazolic N-***H*** proton integrated for 2 ***H***, hinting that the signal of the phenolic O-***H*** was not lost and had coalesced with that of the benzimidazolic proton.

Hence, it was decided to study more precisely the evolution of the ^{1}H-NMR spectra over time in order to better understand the ligand-analyte interaction. As seen in Figure 159, the signal corresponding to the C=N-O-***H*** proton of the oxime moiety at 11.27 ppm, after a fast broadening upon addition of OCl^-, tends to go back to the sharp signal that was originally observed in the free **M4** molecule. As with the signals corresponding to the ***H*** atoms of the hydroxybenzene-O-***H*** and the benzimidazole-N-***H*** groups, the situation is somewhat similar: after a fast coalescence, they tend to eventually split. More importantly, it is observed that after 5 – 6 days, signals at 10.47 (blue circumference) and 8.18 ppm (grey circumference) start to appear and they get bigger as time passes. As can be seen in Section 2.1.2.3.2, these two signals correspond to the aldehyde. In fact, it was calculated at the 11th day of the experiment that the ratio between **M4** and the corresponding aldehyde was ~6 : 1, while at the 20th day, the ratio was ~2 : 1. At this point, it should be mentioned that decomposition of the molecule could already be detected.

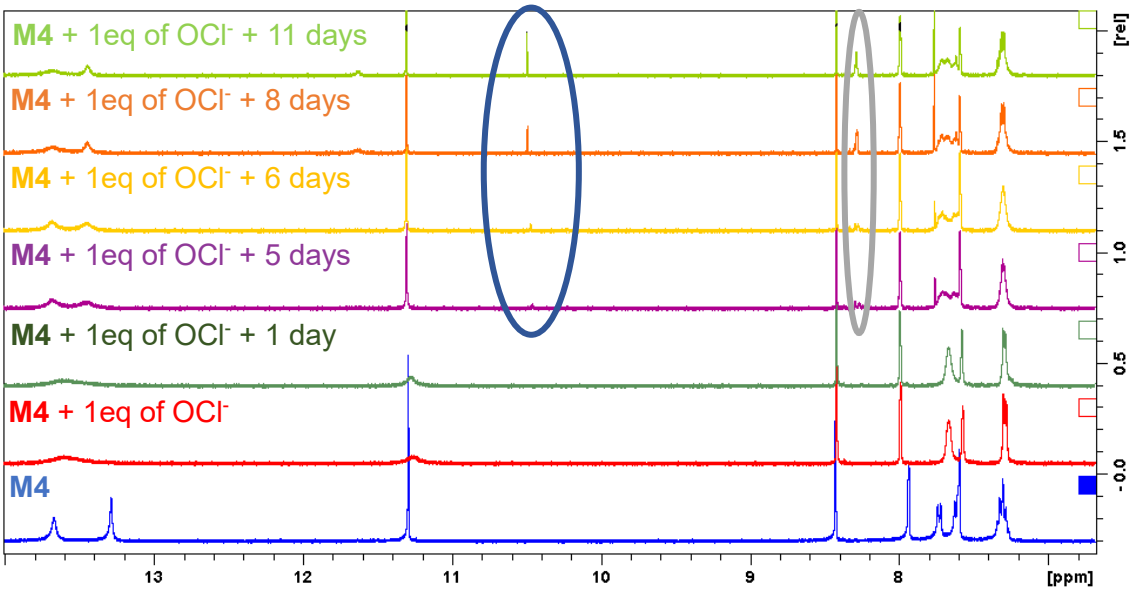

Figure 159. Evolution of the interaction between **M4** and OCl^- over time monitored by ^{1}H-NMR spectrum (DMSO-d_6, 400 MHz).

Also, the same test was carried out maintaining the samples at 60 °C (except when recording the ^{1}H-NMR spectra) to verify if the deoximation reaction could be accelerated. The results show (Figure 160) that it is only at the 9th day, that the oxime group is completely lost in favor of the aldehyde (blue circumference), but with heavy decomposition of the molecule as well as seen with the additional signals in the aromatic area of the spectrum (7 – 8 ppm).

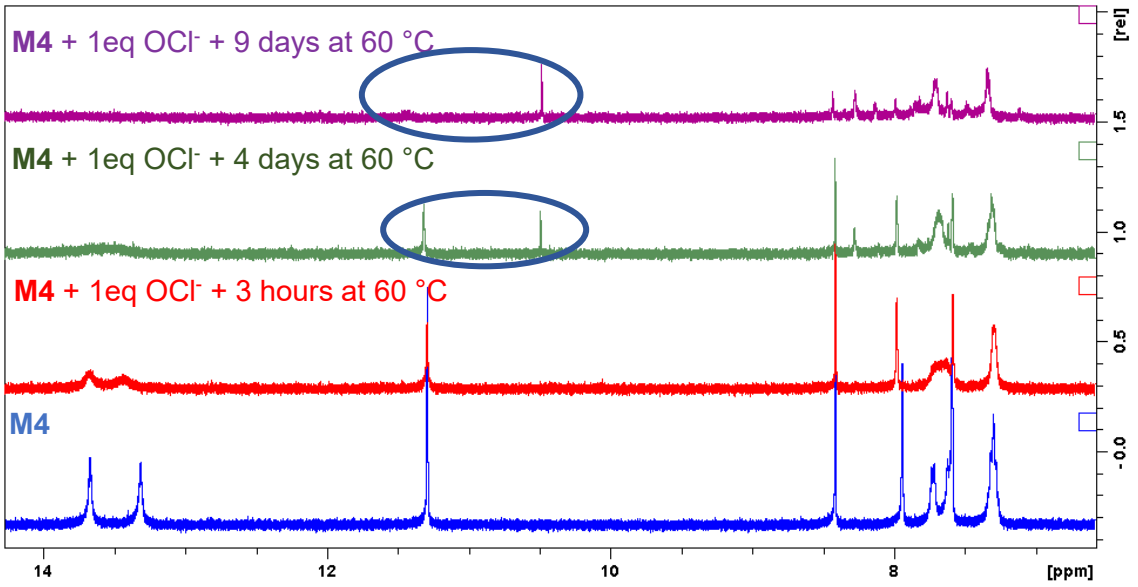

Figure 160. Evolution of the interaction at 60 °C between **M4** and OCl^- over time monitored by ^{1}H-NMR spectrum (DMSO-d_6, 400 MHz).

In conclusion, all these results tend to indicate that, for the particular case of **M4**, the interaction of the oxime group with the hypochlorite ion does not immediately generate an irreversible chemical reaction that would result in the formation of an aldehyde or a nitrile oxide, as described by the literature. While the aldehyde-formation reaction indeed occurs, it is detectable by NMR only at the 5th day of exposure of **M4** to OCl^- at room temperature. This timeframe is extremely long and out of interest, as only chemosensors with fast response times are pursued.

As for the initial and almost instant change observed in the emission spectrum (the quenching of the band at 493 nm and the promotion of a new band at 455 nm), it can be postulated that it is similar in nature to the one observed upon addition of Al^{3+}: due to the basicity of the OCl^- solution, and thanks to its Brønsted base capabilities, this analyte may be able to interact with the acidic protons of the ligand, particularly with the phenolic O-***H***, with the consequence of weakening this bond. This interaction completely inhibits the original ESIPT process of the molecule, as the proton cannot be transferred because it is interacting with the hypochlorite anion, and allows to see the emission band of a species that lies in the middle between the phenoxide ion (a fully deprotonated ligand) and the hydroxyphenyl (a fully protonated ESIPT-active ligand), meaning that the O-H bond has weakened, but is not completely broken. This same interaction could be occurring with the other two labile protons of **M4**. Based on this hypothesis, it is possible to postulate an initial interaction between **M4** and OCl^-, which is represented in Figure 161.

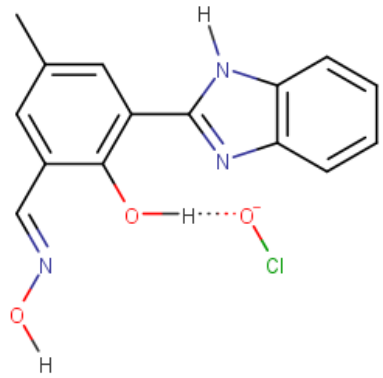

Figure 161. Proposed interaction for the immediate species formed between **M4** and OCl^-.

4.2.1.4 Interference tests

Next, interference tests of the detection of Al^{3+} by **M4** were made according to the procedure described in Section 2.3.8. The concentration of the ligand was 18.7 μmol/L in a 0.5 : 99.5 THF : H_2O solvent medium. In the tests, 5.35 equivalents of each of the interferent and the aluminum cation were added.

As the response of the ligand towards Al^{3+} involves the unique appearance of a band assigned to the complex at ~430 nm, the focus of this series of tests was to verify if such band still appears in presence of other cationic species. The results are shown in Figure 162.

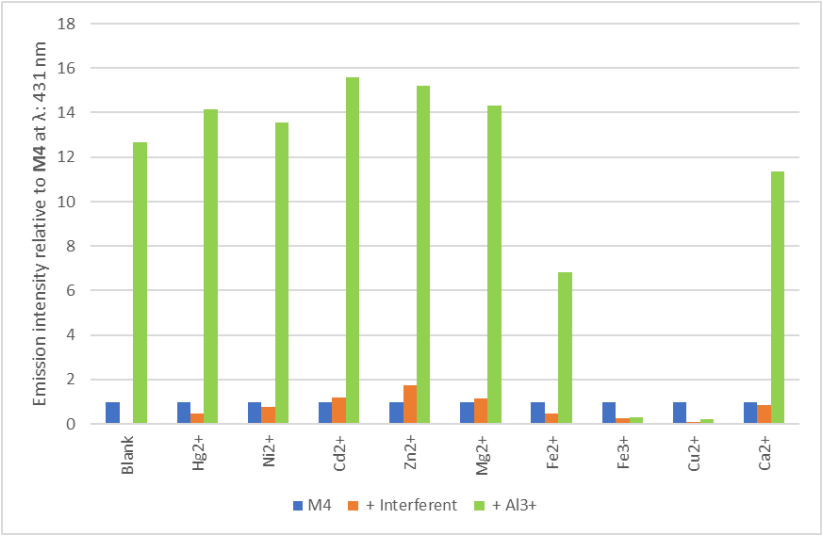

Figure 162. Interference test results for the detection of Al^{3+} by **M4**. The blue boxes represent the normalized emission intensity of **M4**; the orange ones, the relative emission intensity when an interferent is subsequently added; and the green ones, the final relative emission intensity when Al^{3+} is added to the mixture. λ_{exc} = 349 nm.

As can be seen, the presence of Fe^{3+} or Cu^{2+} completely inhibits the observation of the new band centered at ~430 nm that is the signature of the interaction between **M4** and Al^{3+}. Moreover, the presence of Fe^{2+}, while not totally inhibiting this new band, prevents it to be enhanced as it normally would in its absence. This might mean that the strength of the interaction between this trio of cations and the ligand is higher than the corresponding one with aluminum(III).

To further assess this interference mechanism, the same analysis was performed, but in a reverse order, meaning that instead of adding the interferent species first and then the aluminum cation, the Al^{3+} was first and then the interferents. As before, the focus was only on the unique band at ~430 nm. The results in Figure 163 show that addition of both iron cations to the **M4** – Al^{3+} solution partially quenches the emission of the new band, while the addition of Cu^{2+} completely quenches it. This means that the interaction of the ligand with this trio of interferents is strong enough to partially (for Fe^{2+} and Fe^{3+}) or completely (for Cu^{2+}) displace the Al^{3+} from the previously formed complex.

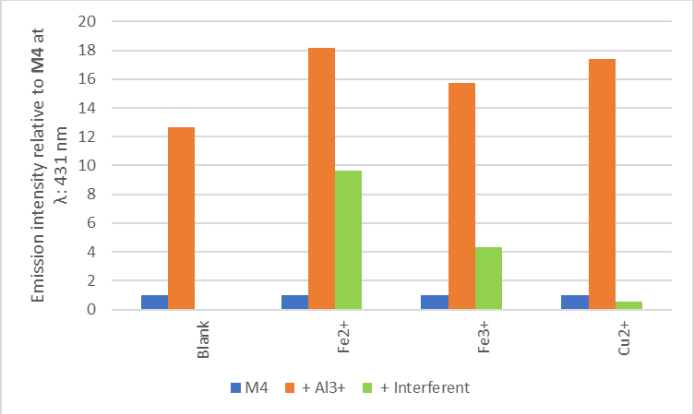

Figure 163. Reverse interference test results of **M4** against its inhibitors for the detection of aluminum. The blue boxes represent the normalized emission intensity of **M4**; the orange ones, the relative emission intensity when Al^{3+} is added to the solution; and the green ones, the final relative emission intensity when the inhibitor is added to the mixture. λ_{exc} = 349 nm.

From these results it can be confidently conclude that the presence of Cu^{2+} in the medium completely inhibits the formation of the new band at ~430 nm and thus, the recognition of Al^{3+} by **M4**. As for both iron species, it can be concluded that they also act as inhibitors of this recognition event, but their effect is not as strong as the one generated by copper.

Finally, tests to verify if mildly acidic or basic media affect **M4** sensing capabilities towards Al^{3+} were carried out following the same procedure as with the cationic interferents

(Section 2.3.8). As seen in the bulk tests with addition of OH^- (Figure 146), a basic environment has the effect of widening and blue shifting the emission band of **M4** in a way that it overlaps with the band generated by the interaction of the ligand with the aluminum cation, so a visual comparison of the spectra, as presented in Figure 164, is better suited for this analysis. Also, in Figure 165, the emission spectra of **M4** and its aluminum complex in different pH media are presented to visually compare the final intensity of the band at ~430 nm.

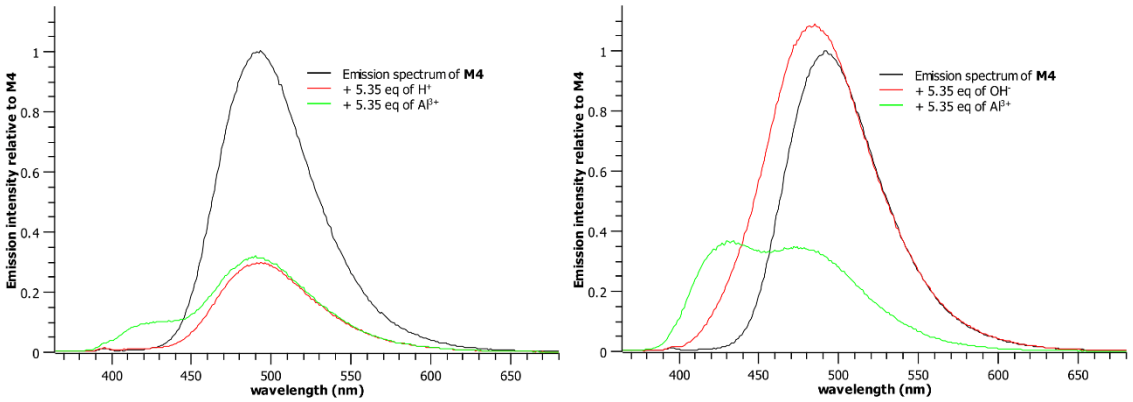

Figure 164. Emission spectra showing the interference of acidic (left) and basic (right) medium in the detection of Al^{3+} by **M4**. [**M4**]: 18.7 μmol/L in THF : H_2O 0.5 : 99.5 medium; λ_{exc} = 349 nm.

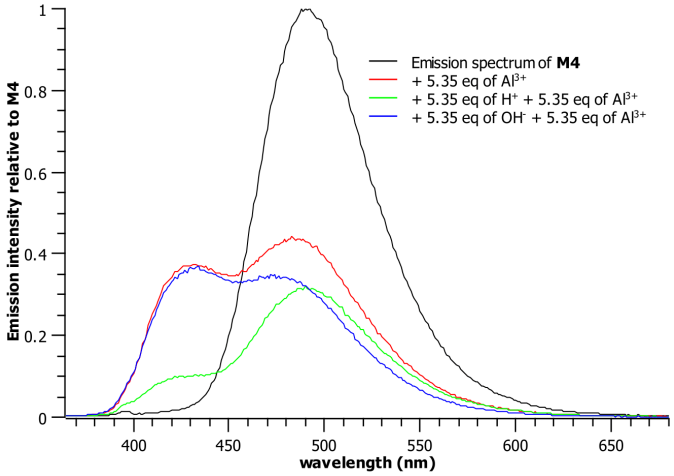

Figure 165. Comparison of the emission spectra of **M4**, **M4** + Al^{3+}, **M4** + Al^{3+} in acidic medium, and **M4** + Al^{3+} in basic medium. [**M4**]: 18.7 μmol/L in THF : H_2O 0.5 : 99.5 medium; λ_{exc} = 349 nm.

As can be observed in Figure 164, an acidic medium partially inhibits the appearance of the new band at ~430 nm, while a basic medium, although having by itself the effect of widening the emission spectrum, does not have any consequence in the aluminum

recognition. This result is consistent with the explanation given for the sensing mechanism of **M4** towards Al^{3+}: a basic medium facilitates the deprotonation of the phenolic O-***H*** proton, promoting the complexation of the aluminum cation and thus allowing the inhibition of the ESIPT mechanism. On the other hand, an acidic medium makes the complexation harder, as the acid-base equilibrium that allows for the formation of the phenoxide anion that needs to be formed in the complexation is displaced to the protonated form. This has the consequence of decreasing the rate of inhibition of the ESIPT mechanism.

4.2.1.5 Conclusion

In conclusion, **M4** is a 2-(2-hydroxyphenyl)benzimidazole-oxime ESIPT derivative that is able to selectively detect Al^{3+} and OCl^- in a 99.5% aqueous medium. For the metallic cation, this molecule exhibits a ratiometric fluorescence response as a consequence of the inhibition of ESIPT that can be visualized by the quenching of the emission assigned to the [keto]* tautomer and the appearance of a new blue shifted emission band assigned to the deprotonated complex. The limit of detection for this interaction is 0.14 μmol/L, the stoichiometry is 1 : 1 and the binding constant has been calculated at 1.43×10^6 M^{-1}.

As for the response of the molecule towards the hypochlorite anion, it has been determined that the response is also ratiometric and involves the quenching of the [keto]* tautomer band and the enhancement of another blue shifted band that has been assigned to a **M4**-OCl^- adduct that inhibits ESIPT. Moreover, it has been proved that a chemical reaction does not take place in the timeframe and conditions normally used in fluorescence sensing studies. To the best of our knowledge, this is the first time that a probe is able to rapidly detect OCl^- without involving a structural change. The limit of detection for this interaction is 1.08 μmol/L.

These results suggest that **M4** could be effectively used as a chemosensor for real-life water quality assessments, particularly for the fast detection of hypochlorite.

4.2.2 M5

The novel compound **M5** (Figure 166) was designed with similar purposes than **M4**: to attain a ratiometric response towards target cations, particularly Al^{3+} and Zn^{2+}, by taking advantage of the ESIPT capabilities.

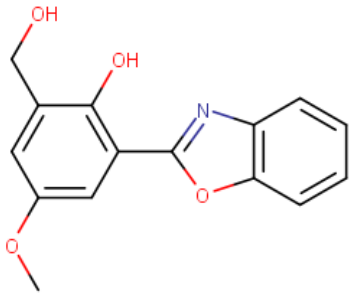

Figure 166. Chemical structure of **M5**.

Zinc does not pose a substantial threat to the environment or to human beings. However, it is an essential trace metal for mammals and its deficit in humans can cause growth deficiency, an increase in the risk of infections and of degenerative diseases, among others [297]. Hence, its detection and quantification are of great importance, particularly for children.

4.2.2.1 Bulk tests

Bulk tests in an EtOH : H_2O 1 : 4 medium were carried out following the procedure described in Section 2.3.3. Particularly for this compound, as it was designed specifically for the detection of cations, it was decided to limit the scope of the bulk tests to only this group and thus no anion bulk test was performed. The results of the cation bulk tests are therefore shown in Figure 167. Also, the response of **M5** against the addition of acidic and basic solutions was probed and the results can be seen in Figure 168.

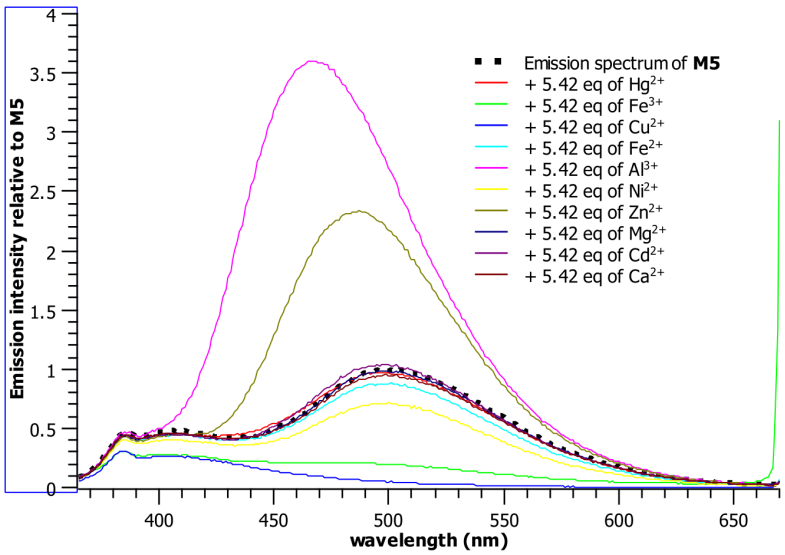

Figure 167. Emission spectrum of **M5** (14.7 μmol/L in EtOH : H_2O 1 : 4) in presence of an excess (5.42 equivalents) of several metallic cations; λ_{exc} = 340 nm.

It can be seen in the cation bulk test that **M5** has a particular response towards Al^{3+}: it promotes the appearance of a new band centered at 467 nm, 30 nm blue shifted and 3.5 times more intense than the band assigned to the [keto]* tautomer emission of the ligand. Also, this molecule can detect Zn^{2+} by a similar but lesser effect, as the new band is blue shifted by 10 nm and is only 2.3 times more intense with respect to the aforementioned [keto]* band of the free molecule.

Moreover, it can be noticed in Figure 167 that Cu^{2+} and Fe^{3+} completely quench the emission of the ligand. This effect can be attributed to their paramagnetic quenching properties, as explained in Section 4.2.1.1, and thus their interaction will not be further studied. A slight quenching effect can also be distinguished between **M5** and the Fe^{2+} and Ni^{2+} cations (10 and 30 % quenching, respectively).

These results indicate that **M5** possesses a particular response when treated with aluminum(III) and zinc(II), with the former being more intense and bluer shifted than the second one. Hence, it can be hypothesized that there is a partial selective recognition towards these two cations.

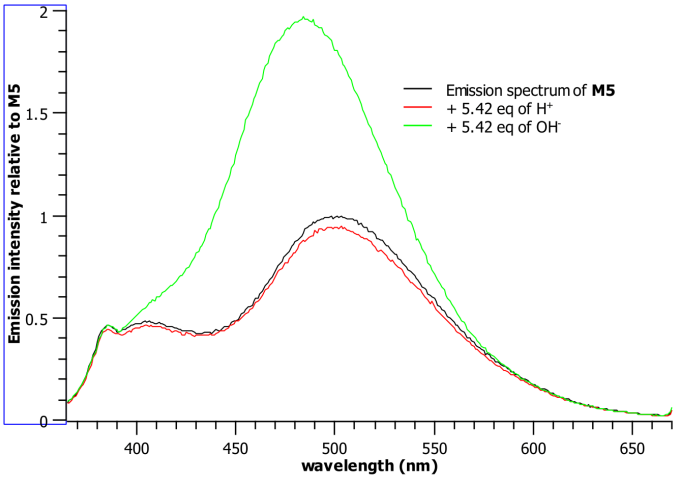

Figure 168. Emission spectra of **M5** when adding acidic or basic solutions. [**M5**] = 14.7 μmol/L in EtOH : H_2O 1 : 4; λ_{exc} = 340 nm.

As for the tests in different pH solutions, the results are expected and consistent with literature. An acidic medium (pH ~4) is not strong enough to protonate the nitrogen atom of a 2-(2-hydroxyphenyl)benzoxazole unit (pK_aH = 1.3 [253]), which explains the lack of impact on the emission spectrum. On the other hand, a basic medium (pH ~10) is in the pK_a range of the phenolic O-***H*** of the ligand (pK_a = 9 – 10 [176]), meaning that the predominant species at these conditions is the phenoxide anion of **M5**. This allows to

assign the emission band centered at 484 nm that appears in a basic medium to this anionic species. The impact of an acidic or basic medium upon the detection of Al^{3+} and Zn^{2+} will be discussed in Section 4.2.2.4.

4.2.2.2 Calibration curves

Emission titrations of **M5** in EtOH : H_2O 1 : 4 against Al^{3+} and Zn^{2+} were carried out following the procedure described in Section 2.3.4. The results of the titration with the former analyte, as well as its calibration curve, can be seen in Figure 169. For this titration, the concentration of the ligand was 14.7 μmol/L and the final point represents the addition of a total of ~4 equivalents of the analyte into the solution. While it can be inferred that there is a ratiometric response of the ligand when treated with Al^{3+} owing to the appearance of a new blue shifted emission band, it is in fact difficult to visualize because the emission intensity of the band corresponding to the [keto]* tautomer is very low and it is quickly superimposed with the new broad emission of the complex. Moreover, the absorption titration was also performed, but a ratiometric response was not observed. For this reason, the calibration curve could not allow a ratiometric analysis.

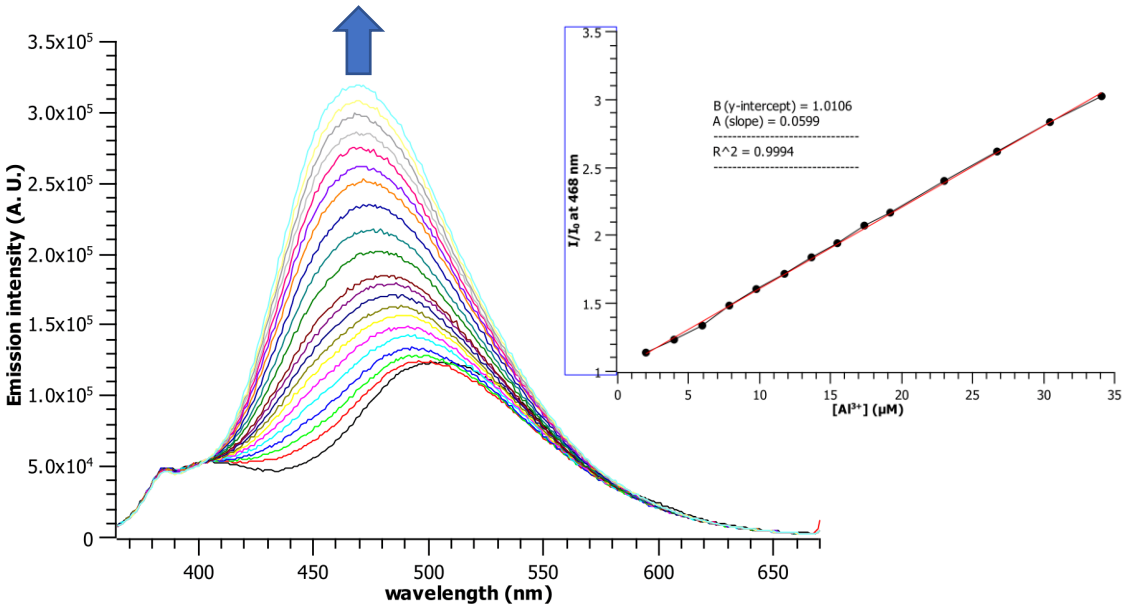

Figure 169. Emission titration profile of **M5** against incremental quantities of Al^{3+}. [**M5**] = 14.7 μmol/L; λ_{exc} = 340 nm. (right) Calibration curve for this titration (I/I_0 at 468 nm *vs.* [Al^{3+}]). Each point has a calculated error of 1 %.

The calibration curve shows that there is a linear response of the ligand towards aluminum(III) at λ_{em} = 468 nm in the ~2 to ~34 μmol/L range of the concentration of the

analyte, with the limit of detection calculated to be 0.30 ± 0.003 μmol/L using the 3σ method (Section 2.3.5).

The results of the titration against Zn^{2+} are shown in Figure 170. In this case, it is not evident that a ratiometric response of the ligand towards zinc(II) occurs due to the close proximity of the [keto]* tautomer emission band of the free ligand and that of the **M5**-Zn^{2+} complex. Nonetheless, the calibration curve for this titration shows a linear response of **M5** towards Zn^{2+} at λ_{em} = 492 nm in the [Zn^{2+}] range from ~4 to ~65 μmol/L. Then, using the 3σ method (Section 93), the limit of detection for this cation was calculated to be at 3.43 ± 0.10 μmol/L.

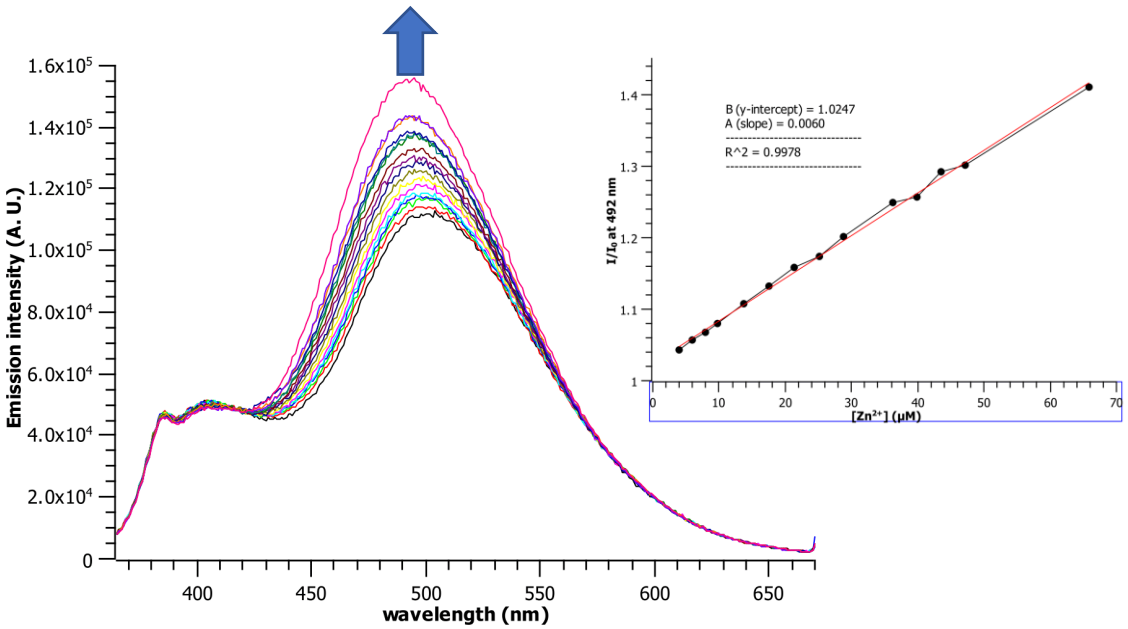

Figure 170. Emission titration profile of **M5** against incremental quantities of Zn^{2+}. [**M5**] = 14.7 μmol/L; λ_{exc} = 340 nm. (right) Calibration curve for this titration (I/I_0 at 492 nm *vs*. [Zn^{2+}]). Each point has a calculated error of 1 %.

While the limit of detection of **M5** towards Al^{3+} is higher than the values found with **M2** and **M4** against this same analyte, the value is still below the threshold of acceptability on the quality of water intended for human consumption[24]. As for the limit of detection towards Zn^{2+}, the World Health Organization has set the acceptable limit in drinking water at 76 μmol/L [25,26], meaning that **M5** can detect this cation at levels far below the threshold.

[24] https://www.lenntech.com/applications/drinking/standards/eu-s-drinking-water-standards.htm
[25] https://www.lenntech.com/periodic/water/zinc/zinc-and-water.htm
[26] https://www.canada.ca/en/health-canada/services/publications/healthy-living/guidelines-canadian-drinking-water-quality-guideline-technical-document-zinc.html

As mentioned before, the detection of zinc(II) is more important in terms of detecting its deficiency in the human body. It has been established that the lower limit concentration of zinc in blood plasma and serum for an adult not to be considered at risk of Zn-deficiency is ~11 μmol/L [297], which lies above the limit of detection of our ligand.

Then, it can be concluded that the capability of **M5** to detect aluminum(III) and zinc(II) below important thresholds make it a good candidate for real-life water quality assessment and for potential biological analysis of zinc in human cells.

4.2.2.3 Sensing mechanism

Based on the results obtained from the **M4**-Al^{3+} interaction detailed in Section 4.2.1.3, it is expected that the recognition event between **M5** and this same analyte involves the inhibition of the ESIPT mechanism of the compound due to the removal of the phenolic proton, thus allowing to visualize the emission spectrum of the complexed phenoxide form of the ligand, which is redshifted in comparison with the emission of its [keto]* tautomer.

Attempts were made to obtain the Job Plot for the **M5**-Al^{3+} interactions, but they were not successful. Also, due to the plethora of problems that the lack of solubility of the aluminum salts bring into the analysis of the ^{1}H-NMR titrations with them, it was decided not to perform this test and instead, record the mass spectrum of the complex[27]. The results can be seen in Figure 171.

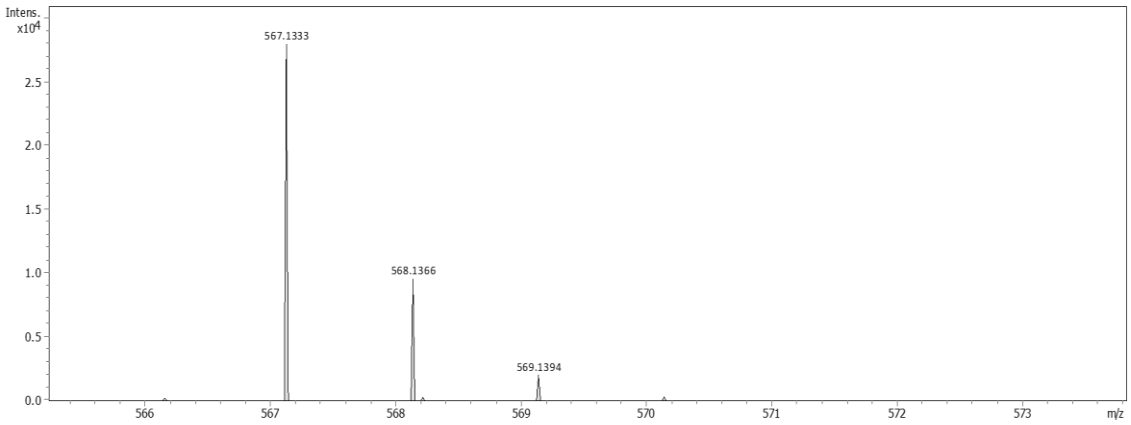

Figure 171. Zoom of the ESI-MS spectrum of the complex between **M5** and aluminum(III).

[27] The complex for ESI-MS analysis was obtained using the following procedure: To a solution of **M5** in MeOH at room temperature, 2eq of Al^{3+} were added. The mixture was stirred for two hours and the complex solution was directly analyzed.

The spectrum unequivocally shows the presence of a mono-charged species labeled that corresponds to the formula [2(**M5** – $\mathbf{H^+}$) + $\mathbf{Al^{3+}}$]$^+$ (ESI-MS (m/z), calculated: 567.1359; found: 567.1333). This result suggests a 2 : 1 stoichiometry and the loss of one proton from each of the ligands that form the complex.

Comparing the pK_a values of the hydroxy groups of ethanol (pK_a = 16[28]) and 2-(2-hydroxyphenil)benzoxazoles (pK_a = 9 – 10 [176] [298]), it is clear that the proton that is lost should correspond to the hydroxyphenyl entity, forming a phenoxide anion. The loss of this proton also justifies the inhibition of the ESIPT mechanism that was previously proposed simply because there is no longer a proton to be transferred. Also, this corroborates the initial hypothesis that the new band centered at 467 nm corresponds to the aluminum(III) complex of the phenoxide form of **M5**. These conclusions are consistent with the reviewed literature [250] [293] [294] [295].

It has been previously reported for other 2-(2-hydroxyphenyl)benzoxazole ligands that they act as bidentate ligands towards the complexation of Al^{3+} through the deprotonated oxygen atom and the nitrogen atom of the oxazole unit being the second donor [299] [300]. In the present case, the comparison of the pK_aH values of the 2-(2-hydroxybenzoxazole) (pK_aH = 1.3 [253]) and of hydroxyethyl (pK_aH = -2.4[29]) indicates that the basicity of the nitrogen atom of the benzoxazole is higher than that of the oxygen atom of the hydroxyethyl group, meaning that it should be the preferred second atom that participates in the complexation. It is thus reasonable to postulate the complex structure seen in Figure 172 for the **M5**-Al^{3+} interaction.

[28] https://owl.oit.umass.edu/departments/OrganicChemistry/appendix/pKaTable.html

[29] https://www.as.wvu.edu/~jpenn/Chem%20231/Bruice%20Essential%20Organic%20Chemistry%202nd%20Edition%20Chapter%202.pdf

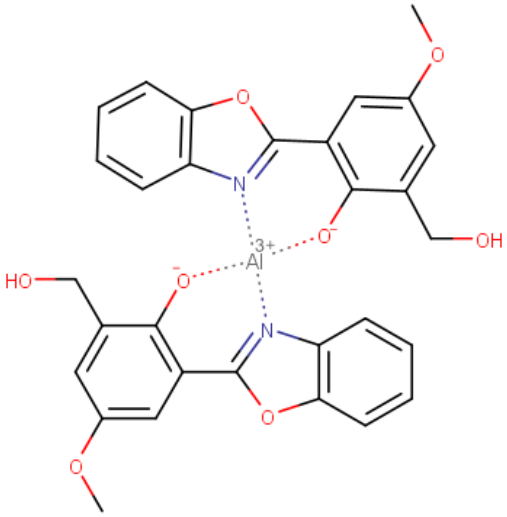

Figure 172. Proposed chemical structure of complex between **M5** and Al^{3+}.

Then, the lack of participation of the hydroxyethyl entity in the complexation event could be the reason of the general low emission intensity of the ligand even in presence of aluminum: the PET mechanism proposed in Section 2.1.2.4 may still be active.

Unfortunately, due to the 2 : 1 stoichiometry, the Benesi-Hildebrand method for calculating the association constant could not be applied [236].

As for the interaction with the Zn^{2+} cation, taking advantage of the fact that both $ZnCl_2$ and **M5** are readily soluble in DMSO, an ^{1}H-NMR titration was performed DMSO-d_6. The results are presented in Figure 173.

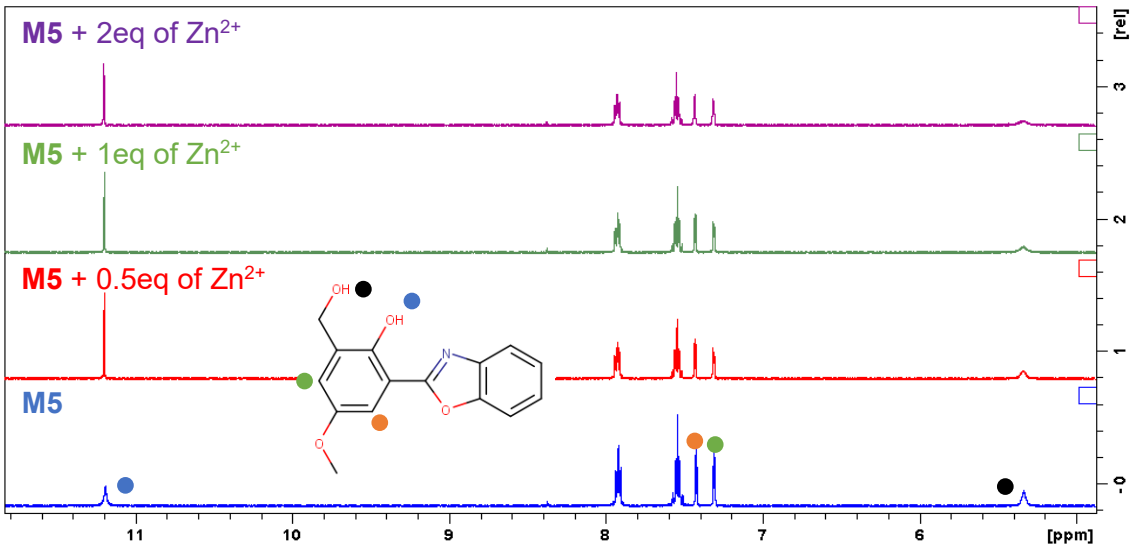

Figure 173. ^{1}H-NMR titration (DMSO-d_6, 400 MHz) of **M5** against Zn^{2+}. Protons in the spectrum are assigned with colored circles.

As can be seen, neither the phenolic nor the ethanolic proton of **M5** are lost upon addition of incremental quantities of Zn^{2+} under the conditions used. Particularly for the phenolic proton, this result is supported by that obtained with the titration experiment (Figure 170), in which an enhancement of the emission was observed, but without the appearance of a new red shifted band that is assigned to the phenoxide anion of the molecule. This allows to postulate that the interaction of this molecule with zinc(II) does not involve the inhibition of ESIPT.

Even though the majority of the reviewed literature proposes that the complexation of 2-(2-hydroxyphenyl)benzoxazoles with Zn^{2+} involves the loss of the phenolic proton and the concomitant inhibition of ESIPT, a complexation mode in which a 2-(2-hydroxyphenyl)benzoxazole does not lose its phenolic proton has been reported before, although in that particular case, the ESIPT process is still inhibited [301].

The most likely explanation for the fact that Al^{3+} is able to deprotonate the phenolic O-***H*** of **M5** and Zn^{2+} does not relies on the Lewis acid strength and hardness of both cations, which greatly favors the aluminum species [302] [303]. As Zn^{2+} is softer and only a borderline Lewis acid, it thus lacks the strength to promote the removal of the phenolic proton, which implies a weaker interaction between the ligand and this analyte, and corresponds to the smaller change in the emission spectra. Also, comparing this result with other reports in which Zn^{2+} is able to deprotonate the phenolic O-***H*** of 2-(2-hydroxyphenyl)benzoxazole derivatives, it can be postulated that the difference between these results and the ones obtained in the present case might depend on the strength of the O-H bond itself due to the design of **M5**. As explained in Section 3.2, the strength of this bond is enhanced in our molecule thanks to the electron donating methoxy group, which has the effect of reducing the rate of ESIPT in the free ligand. This means that the O-H bond is strong enough to not be broken by the complexation of the weak Zn^{2+} Lewis acid to the molecule.

Unfortunately, the Job plot essays to obtain the stoichiometry of the **M5**-Zn^{2+} interaction failed and the mass measurements yielded a mixture of 1 : 1 and 2 : 1 ligand : metal complexes in solution, thus the ratio between them cannot be properly assessed, and the binding constant using the Benesi-Hildebrand equation cannot be calculated.

4.2.2.4 Interference tests

Next, interference tests of the detection of the two cations by **M5** were made according to the procedure described in Section 2.3.8. The concentration of the ligand was 14.7

μmol/L in EtOH : H_2O 1 : 4, and 5.42 equivalents of each the interferent and the target cation (Al^{3+} or Zn^{2+}) were added.

As the response of **M5** towards both species involves appearance of new blue shifted bands at ~465 and ~495 nm, the focus of this series of tests was to verify if such bands still appear in presence of other cationic species. The results are shown in Figure 174 and Figure 175.

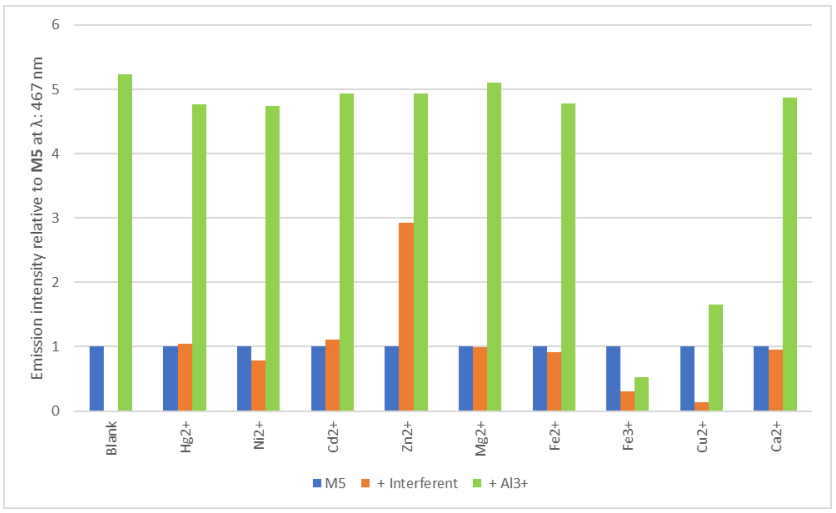

Figure 174. Interference test results for the detection of Al^{3+} by **M5**. The blue boxes represent the normalized emission intensity of **M5**; the orange ones, the relative emission intensity when an interferent is subsequently added; and the green ones, the final relative emission intensity when Al^{3+} is added to the mixture. λ_{exc} = 340 nm.

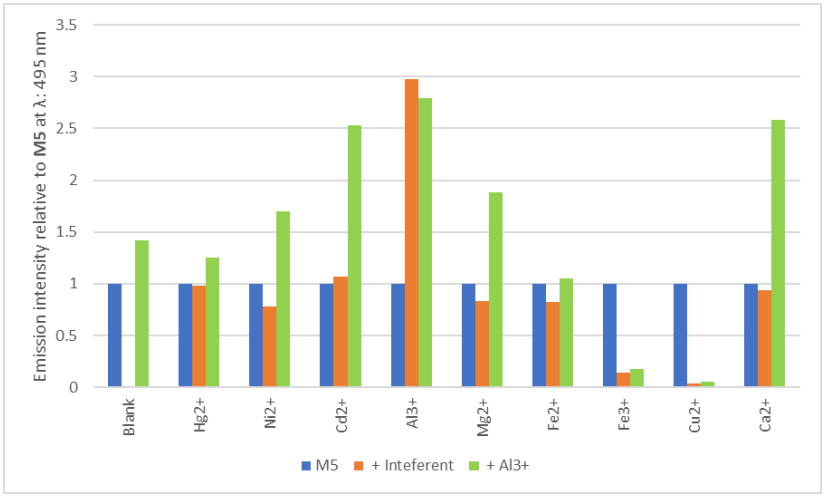

Figure 175. Interference test results for the detection of Zn^{2+} by **M5**. The blue boxes represent the normalized emission intensity of **M5**; the orange ones, the relative emission intensity when an interferent is subsequently added; and the green ones, the final relative emission intensity when Zn^{2+} is added to the mixture. λ_{exc} = 340 nm.

It can be seen in Figure 174 that Fe^{3+} and Cu^{2+} completely inhibit the detection of Al^{3+} by **M5**, probably by a similar mechanism than the one hampering the detection of aluminum by the benzimidazole derivative **M4** (4.2.1.4). As for the detection of Zn^{2+}, it can be seen in Figure 175 that Fe^{2+}, Fe^{3+} and Cu^{2+} ions completely inhibit the sensitivity of the ligand towards Al^{3+}. It is worth to mention that there are some species that seem to enhance the detection of Zn^{2+} even if they, by themselves, do not generate any change in the emission spectrum of the ligand such as Cd^{2+}, Mg^{2+} and Ca^{2+}. This behavior was not further analyzed, but could be worth of future research.

Also, it is clear in both figures that the presence of Zn^{2+} does not interfere with the detection of Al^{3+}. In fact, when these two analytes are present, independently on the order in which they are added to the solution, the response of the ligand is such as if it was transparent towards the zinc cation. This observation supports the possible weaker interaction between **M5** and Zn^{2+} in comparison with Al^{3+} as mentioned in Section 4.2.2.3.

Finally, tests to verify if mildly acidic or basic media affect the sensing capabilities of **M5** towards Al^{3+} or Zn^{2+} were carried out following the same procedure as with the cationic interferents (Section 2.3.8). As it was observed in Figure 168 that a basic medium has the effect of generating a new blue shifted band, a visual comparison of the emission spectra observed upon addition of an acid or a base is better suited, and they are presented in Figure 176 and Figure 178. Also, in Figure 177 and Figure 179, a comparison of the emission spectra of **M5** and its metallic complexes in different pH media is presented to visually contrast the final intensity of the new band that is formed.

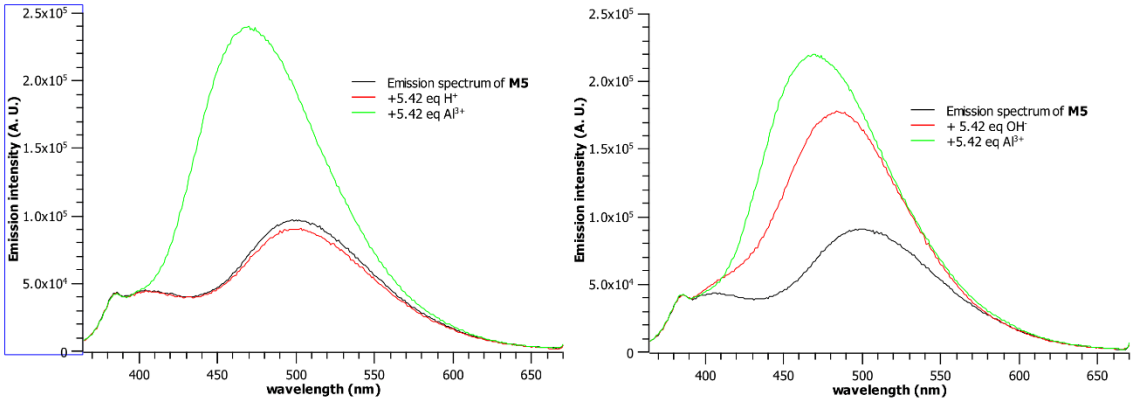

Figure 176. Emission spectra showing the interference of acidic (left) and basic (right) medium in the detection of Al^{3+} by **M5**. [**M5**]: 14.7 μmol/L in EtOH : H_2O 1 : 4 medium; λ_{exc} = 340 nm.

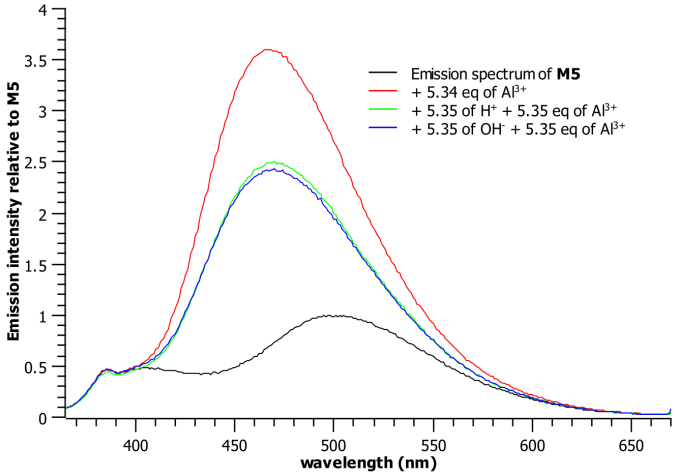

Figure 177. Comparison of the emission spectra of **M5**, **M5** + Al^{3+}, **M5** + Al^{3+} in acidic medium, and **M5** + Al^{3+} in basic medium. [**M5**]: 14.7 μmol/L in EtOH : H_2O 1 : 4 medium; λ_{exc} = 340 nm.

It can be seen in Figure 176 that neither an acidic (pH ~4) nor a basic (pH ~10) medium interfere with the detection of Al^{3+} by **M5**, as in both media the characteristic band of the complex is seen at 467 nm. However, the intensity of this band under the test conditions is lower than the one obtained without modifying the pH of the medium. In acidic conditions, this can be explained by the fact that added protons make the complexation harder due to partially hindering the deprotonation of the phenol, which has the consequence of diminishing the inhibition rate of ESIPT. It is evident, however, that, even at these conditions, the aluminum cation can still deprotonate the ligand, although at a lesser rate than at pH ~6 – 7. On the other hand, in basic conditions, this result was surprising and a reliable explanation cannot be provided as this medium is thought to enhance the detection by promoting the deprotonation of the phenolic proton of the ligand.

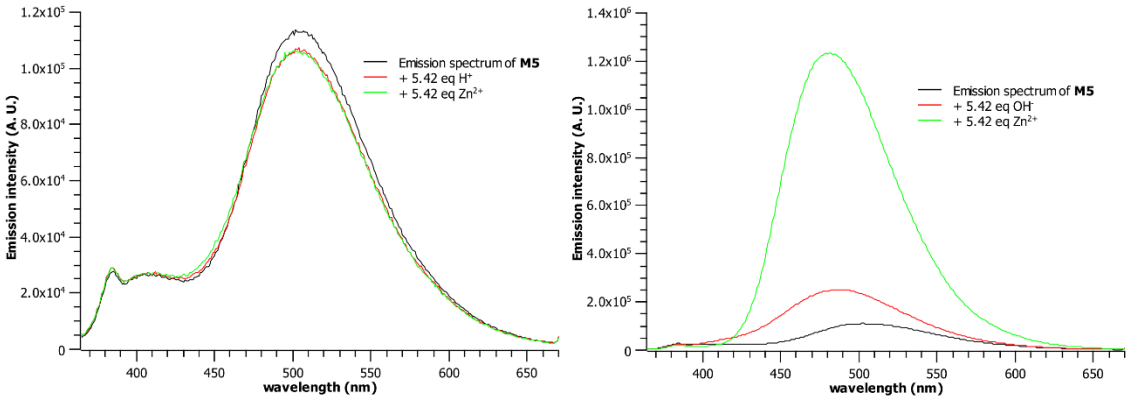

Figure 178. Emission spectra showing the interference of acidic (left) and basic (right) medium in the detection of Zn^{2+} by **M5**. [**M5**]: 14.7 μmol/L in EtOH : H_2O 1 : 4 medium; λ_{exc} = 340 nm.

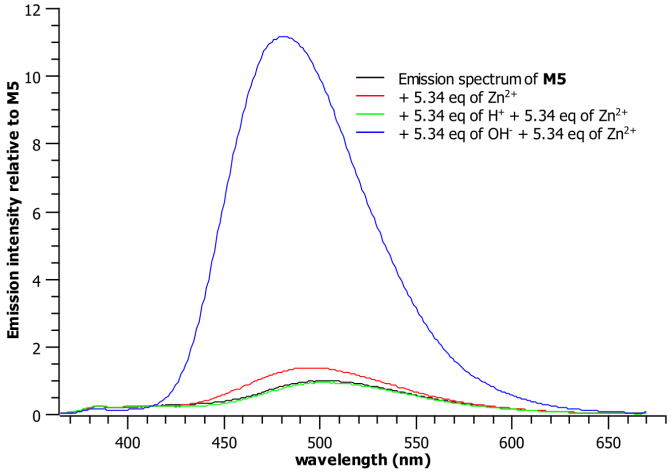

Figure 179. Comparison of the emission spectra of **M5**, **M5** + Zn^{2+}, **M5** + Zn^{2+} in acidic medium, and **M5** + Zn^{2+} in basic medium. [**M5**]: 14.7 μmol/L in EtOH : H_2O 1 : 4 medium; λ_{exc} = 340 nm.

The results about the detection of Zn^{2+} at different pH media are also interesting. In the first place, it can be seen in Figure 178 that an acidic medium completely inhibits the detection of this cation. A plausible explanation could be that the acidified medium either decreases the already low Lewis acid capabilities of Zn^{2+} or limits the availability of the phenolic oxygen atom lone pairs by the formation of hydrogen bonds, rendering the complexation reaction ineffective.

Comparing the results obtained for Al^{3+} and Zn^{2+} in an acidic medium, it can be seen that the former cation is detected while the latter is not. This difference is consistent with the superior Lewis acid and hardness of Al^{3+}, as mentioned in Section 4.2.2.3.

Finally, it can be seen that a basic medium greatly enhances the emission band corresponding to the **M5**-Zn^{2+} complex. This result indicates that once the phenolic proton is removed from the ligand, the complexation of Zn^{2+} is greatly favored and the resulting effect could be justified by the Chelation Induced Enhancement of Fluorescence (CHEF) mechanism, which accounts for a minimization of non-radiative decaying channels that subsequently enhances the emission intensity of the complex [254]. This observation tends to support the idea that the sensing mechanism of the interaction between **M5** and Al^{3+} and Zn^{2+} are different in nature: the removal of the phenolic proton in the first case accounts for the inhibition of the ESIPT mechanism of the ligand, while the soft interaction between **M5** and the analyte in the second case accounts for an enhancement of the emission band (with a small blue shift) due to CHEF.

4.2.2.5 Conclusion

In conclusion, **M5** is a 2-(2-hydroxyphenyl)benzoxazole molecule that is able to detect Al^{3+} and Zn^{2+} in an 80 % aqueous ethanol medium. In the first case, the detection mechanism relies on the inhibition of the ESIPT mechanism promoted by the complexation of Al^{3+} and the concomitant loss of the phenolic proton of the ligand. The limit of detection for this interaction is 0.30 μmol/L and the stoichiometry has been found to be 2 : 1. For the second cation, the proposed sensing mechanism does not involve the inhibition of ESIPT, but a CHEF effect, which accounts for the lower Lewis acidity of zinc(II) in comparison with Al(III). For this interaction, the limit of detection has been calculated at 3.43 μmol/L. These results make **M5** an interesting candidate for real-life water quality assessment and, in particular, for the possible detection of low concentration levels of Zn^{2+} in human cells.

4.2.3 M6

The last benzazole derivative synthesized within the scope of the present thesis work is **M6**, which chemical structure can be seen in Figure 180. The objective with this molecule was to obtain a ligand that could preferably detect Zn^{2+} *via* a ratiometric response, once again owing to the inhibition of the ESIPT mechanism and to try to improve previous reports in which, with a similar molecule, only a turn-ON effect was observed. Moreover, if a ratiometric response was indeed to be obtained, this result could be an improvement over that obtained with the **M5**-Zn^{2+} interaction in terms of specificity of the detection and better LoD.

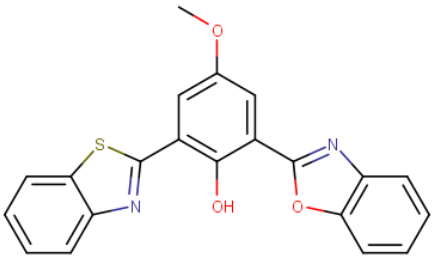

Figure 180. Chemical structure of **M6**.

4.2.3.1 Bulk tests

Bulk tests in a THF : EtOH 0.5 : 99.5 medium were carried out following the procedure described in Section 2.3.3. The cation and anion bulk test results are shown in Figure

181 and Figure 182, respectively. Also, the response of **M6** against the addition of acidic and basic solutions was probed and the results can be seen in Figure 183.

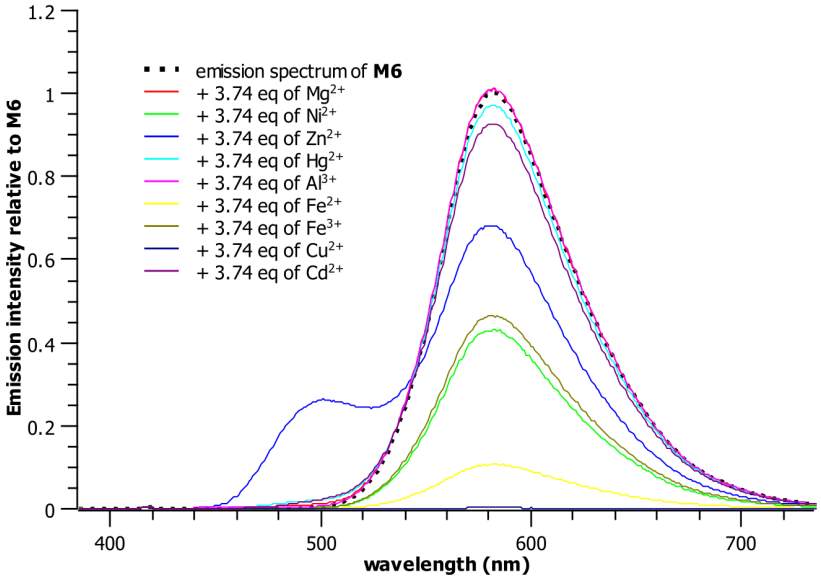

Figure 181. Emission spectrum of **M6** (13.4 μmol/L in THF : EtOH 0.5 : 99.5) in presence of an excess (3.74 equivalents) of several metallic cations: λ_{exc} = 372 nm.

The bulk cation test shows that upon addition of Zn^{2+}, a new band centered at 500 nm, 80 nm blue shifted with respect to the band assigned to the [keto]* tautomer emission of the ligand, appears. While the sensitivity towards this cation was expected by taking into consideration the already discussed report by Li [186] with a similar molecule, it is noteworthy that the present result seems to indicate a ratiometric response and not a simple “turn-ON” one as in the reported work. Also, the ligand shows sensitivity towards several other cations, such as Cu^{2+} (99 %), Fe^{2+} (90 %), Fe^{3+} (45 %) and Ni^{2+} (42 %), but their effect is just a quenching, to a greater or lesser extent, of the emission of **M6** without promoting the appearance of a new band. Thus, in a similar way as what was stated with **M4** and **M5**, these interactions will not be further explored.

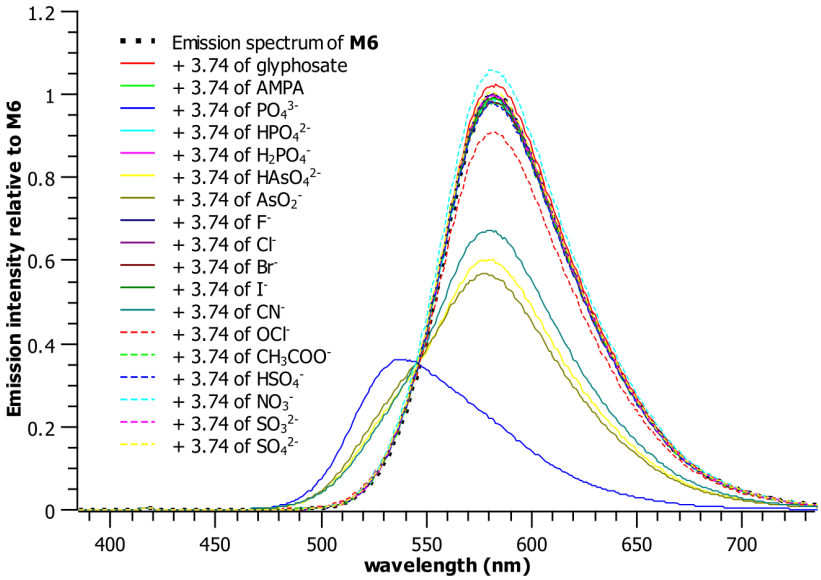

Figure 182. Emission spectrum of **M6** (13.4 μmol/L in THF : EtOH 0.5 : 99.5) in presence of an excess (3.74 equivalents) of several anions: λ_{exc} = 372 nm.

Concerning the response of the probe towards anions, it can be seen in Figure 182 that PO_4^{3-} promotes a new band centered at 538 nm while quenching the original emission band of the ligand. Also, F^-, AsO_2^- and $HAsO_4^{2-}$ seem to broaden the emission spectrum of **M6** into this region, probably because of the overlap of two bands. These results can be attributed to the Brønsted base capabilities of these species that have the capability of removing an acidic proton from the molecule to form an anion, which in this case should correspond to the phenoxide.

Then, in Figure 183, it can be seen how the addition of a base into the medium quenches the emission corresponding to the [keto]* tautomer and in turn, enhances a new band at ~540 nm. This result is consistent with reports about other bis-benzazole molecules [304] and can be assigned to the formation of the phenoxide anion of **M6**. Then, it is confirmed that the effect of the strong base PO_4^{3-} is similar than the one of OH^-: it abstracts a proton and hence the resulting emission spectrum corresponds to the phenoxide form of the ligand[30]. For the other species, the effect is similar, although smaller due to being weaker bases than phosphate.

[30] For instance, the pK_a values of phosphoric acid are 2.2, 7.2 and 12.3 (https://chem.libretexts.org/Bookshelves/Organic_Chemistry/Book%3A_Organic_Chemistry_with_a_Biological_Emphasis_v2.0_(Soderberg)/07%3A_Acid-base_Reactions/7.08%3A_Polyprotic_Acids)

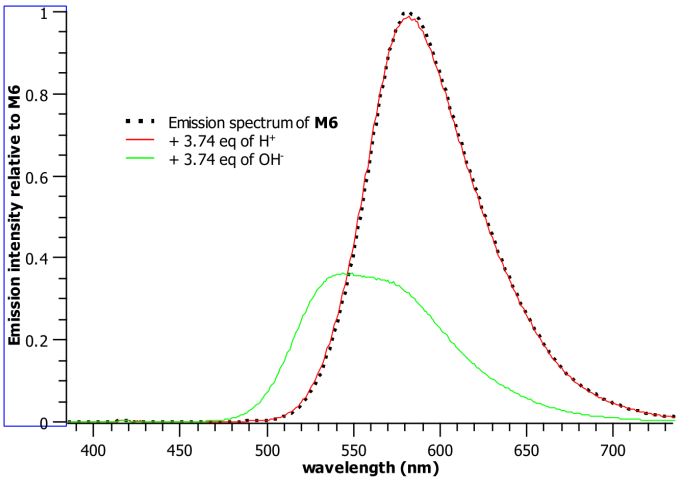

Figure 183. Emission spectra of **M6** when adding acidic or basic solutions. [**M6**] = 13.4 μmol/L in THF : EtOH 0.5 : 99.5 medium; λ_{exc} = 372 nm.

Finally, it can be seen that an acidified ethanolic medium does not generate any change in the emission spectrum of **M6**. This result is surprising considering what has been reported about the promotion of the [enol]* tautomer emission band under the conditions of the test [287] and it could be worth of further investigation. One possible explanation is that the acidified medium is not strong enough to protonate any of the nitrogen atoms of the ligand, particularly the benzothiazole one that is attributed to being the hydrogen accepting atom in the ESIPT mechanism (Section 3.2). As mentioned before, the pK_aH of benzoxazole and benzothiazole analogs are around 1.3 [253] and 4.51 [185], respectively. These results are true for an aqueous medium, however, they are expected to be lower in an ethanolic solution. Then, if there is no protonation of these atoms, the ESIPT mechanism is not hampered and there should be no change in the emission spectrum under these conditions. The other possibility could simply be that, even though the ***N*** atom of the benzothiazole is protonated, it does not affect the ESIPT mechanism of the molecule.

Owing to the interesting and unique result obtained when probing **M6** against zinc in a near perfect ethanolic medium, it was then decided to verify if this sensitivity and selectivity could be maintained in an aqueous environment. Unfortunately, **M6** tends to phase out in near perfect water systems, so a 1 to 1 mixture of H_2O and ethanol was used with 0.4 % of THF. The results of the bulk test against cations carried out using these conditions can be seen in Figure 184. Also, the emission spectra of the molecule in acidic and basic solutions are reported in Figure 185.

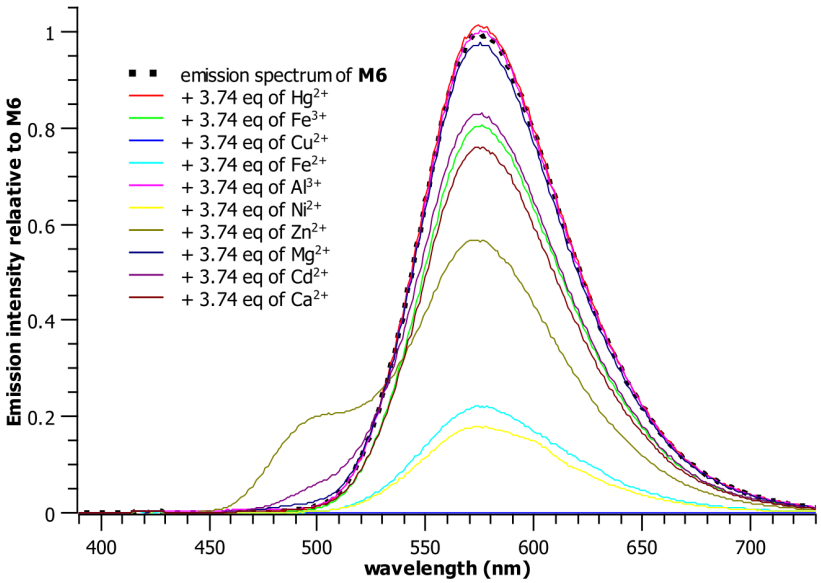

Figure 184. Emission spectrum of **M6** (13.4 μmol/L in THF : EtOH : H_2O 0.4 : 49.8 : 49.8) in presence of an excess (3.74 equivalents) of several metallic cations: λ_{exc} = 372 nm.

The cation bulk test in a partially aqueous medium shows that the sensitivity and selectivity of **M6** towards Zn^{2+} is maintained. All the other cationic species investigated either do not promote a change in the emission spectrum of this compound or directly quench it, similarly to what has already been described in Figure 181 in the near perfect ethanolic medium. The only possible exception is Cd^{2+}, which presence seems to generate a low emissive tail at higher energy in comparison with the band corresponding to the free molecule.

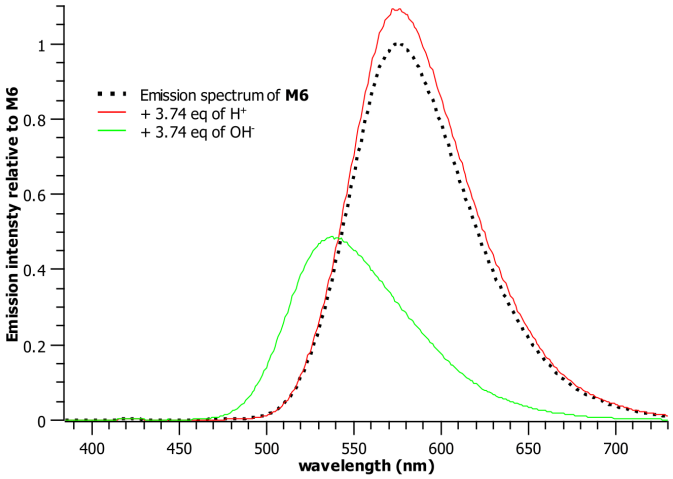

Figure 185. Emission spectra of **M6** when adding acidic or basic solutions. [**M6**] = 13.4 μmol/L in a THF : EtOH : H_2O 0.4 : 49.8 : 49.8 medium; λ_{exc} = 372 nm.

As for the emission of **M6** in acidic or basic media, it can be seen in Figure 185 that the former environment generates only a small enhancement of the emission intensity. As explained before, this could be due to the medium (pH ~4) not being acidic enough to protonate the ***N*** atom of the benzothiazole or benzoxazole moieties, with the consequence of having no effect in the ESIPT mechanism. As for the result in a basic medium, it can be seen that a new and less intense band than the one corresponding to the emission of the [keto]* tautomer of **M6** appears at 537 nm. This is consistent with all previous observations that a basic medium (pH ~10 in this case) is able to deprotonate the phenolic O-***H*** of 2-(2-hydroxyphenyl)benzazole groups. Thus, this new band can be assigned to the emission of the phenoxide form of the molecule.

The specific effect of an acidic or basic medium on the detection of Zn^{2+} by **M6** will be further analyzed in Section 4.2.3.4.

4.2.3.2 Calibration curves

The emission titration of **M6** in a THF : EtOH : H_2O 0.4 : 49.8 : 49.8 medium against Zn^{2+} was carried out following the procedure described in Section 2.3.4. These results, as well as the calibration curve for this interaction, can be seen in Figure 186. It is evident that zinc(II) generates a ratiometric response to the emission of the compound as the gradual quenching of the band assigned to the emission of the [keto]* tautomer is accompanied by the enhancement of a new band centered at 503 nm. When adding ~2 250 equivalents of Zn^{2+}, the initial band of **M6** is completely quenched and the new band is not further enhanced.

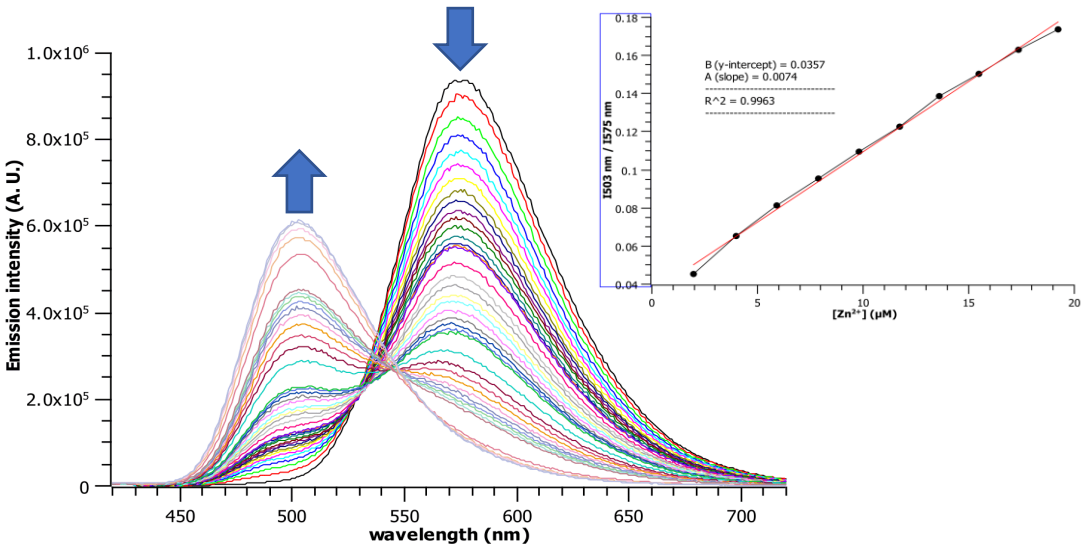

Figure 186. Emission titration profile of **M6** against incremental quantities of Zn^{2+}. [**M6**] = 10.7 μmol/L; λ_{exc} = 372 nm. (right) Calibration curve for this titration ($I_{503\ nm}/I_{575\ nm}$ *vs.* [Zn^{2+}]). Each point has a calculated error of 3 %.

The calibration curve for this titration shows that there is a linear ratiometric response of **M6** toward Zn^{2+} in the ~2 to ~19 μmol/L range of concentration of the metal cation with the limit of detection being calculated at 0.29 ± 0.009 μmol/L using the 3σ method (Section 2.3.5).

As expected, due to fact that the detection of zinc(II) by **M6** is ratiometric in nature, this result is better than the one obtained in the **M5**-Zn^{2+} case (LoD: 3.43 μmol/L). As explained in Section 4.2.2, the importance of the detection of zinc is mainly due to it being an essential trace metal, which concentration must be above certain levels in the human body. Hence, the ability of **M6** to detect Zn^{2+} at lower concentrations that **M5** makes it an even better candidate applications in zinc-deficiency assessments in human cells.

4.2.3.3 Sensing mechanism

Owing to the fluorescence response obtained when exposing **M6** to Zn^{2+}, and based on the previous results with **M4**-Al^{3+} and **M5**-Al^{3+}, it was expected that the sensing mechanism in this case would also involve the inhibition of ESIPT. Then, it could be hypothesized that the new band that appears at ~500 nm corresponds to the deprotonated form of **M6**, which is forming a complex with the zinc(II) cation.

Unfortunately, the ^{1}H-NMR titration could not be carried out because of solubility issues: while $ZnCl_2$ is very soluble in DMSO-d_6, **M6** is completely insoluble in this solvent; and

while **M6** is very soluble in $CDCl_3$, the salt is not. Efforts were made to use a $CDCl_3$ - DMSO-d_6 solvent mixture to perform the aforementioned titration, but they were unsuccessful as they did not provide any meaningful result.

Following the procedure described in Section 2.3.6, the Job's method of continuous variations was thereafter applied to get a glimpse about the complexation ratio between **M6** and Zn^{2+}. The experiment was carried out in a THF : EtOH : H_2O 0.4 : 49.8 : 49.8 medium and the result, which can be seen in Figure 187, shows an inflection point at ~0.66, which accounts for a 2 : 1 **M6** : Zn^{2+} stoichiometry. However, this result cannot be taken as a prove of the real metal:ligand ratio due to the limitations of this technique.

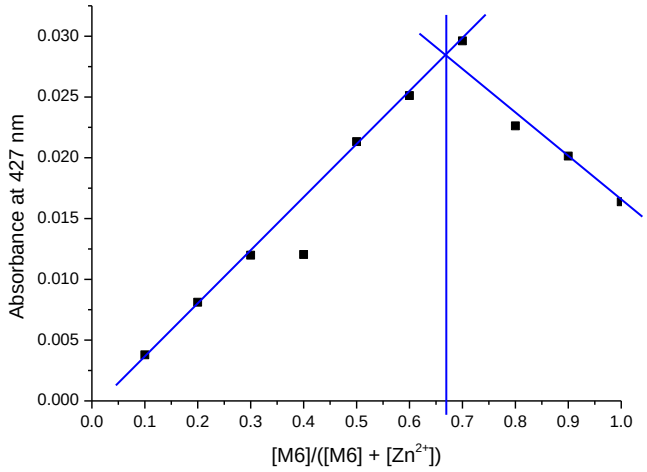

Figure 187. Job plot for the **M6**-Zn^{2+} complex.

It was then decided to record the mass spectrum of the **M6**-Zn species[31]. The resulting spectrum can be seen in Figure 188, where the mass corresponding to the species [**M6** + Zn^{2+} + Cl^-]$^+$ (ESI-MS (m/z), calculated: 472.9700; found: 472.9700) was found.

[31] The complex for ESI-MS analysis was obtained using the following procedure: To a solution of **M6** in THF at room temperature, 2eq of Zn^{2+} in DMSO were added. The mixture was stirred for 30 minutes and the complex solution was directly analyzed.

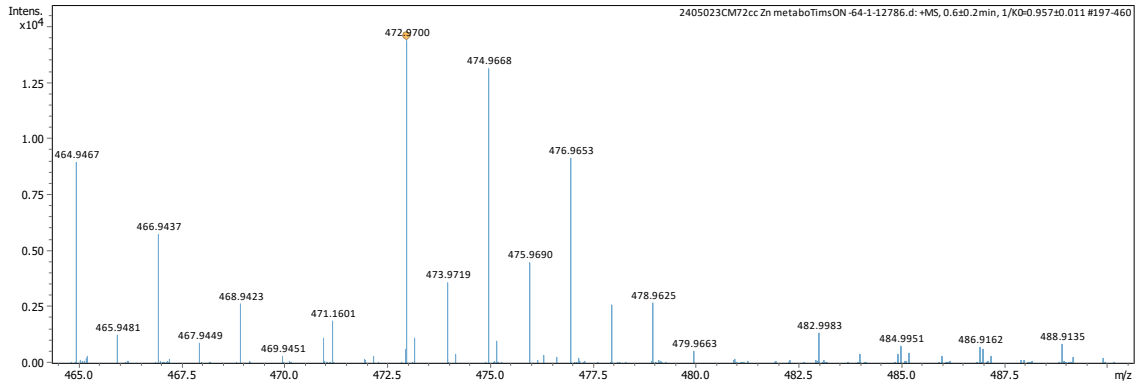

Figure 188. Zoom of the ESI-MS spectrum of the complex between **M6** and zinc(II).

Two important conclusions can be extracted from this result. Firstly, it indicates the formation of a 1 : 1 complex between our compound and Zn^{2+}, with the additional presence of a chloride anion that was introduced because $ZnCl_2$ was the salt used in the reaction. Secondly, the mass indicates a complexation mode in which there is no loss of protons by the ligand. While this result is surprising because all previous evidences point to the loss of a proton due to the complexation event, it is important to note that the possibility exists for the compound to be protonated inside the instrument where the mass is measured.

Finally, computational studies were performed using the density functional method (DFT) at the ub3lyp/6-31g + EmpiricalDispersion=GD2 (Grimm 2) level to obtain further insight into the complex formed by **M6** and Zn^{2+}. Firstly, these results show that the preferred complexing site for the Zn cation is the cavity generated by the deprotonated hydroxyphenyl and the nitrogen atom of the benzothiazole. Moreover, the calculations suggest that the structure corresponding to the complex 2**M6**-H^++Zn is more stable than that corresponding to **M6**-H^++Zn^{2+} by a difference of energy of 0.8 eV, which implies that a 2 : 1 ligand : metal stoichiometry is favored. The proposed ligand structure is shown in Figure 189.

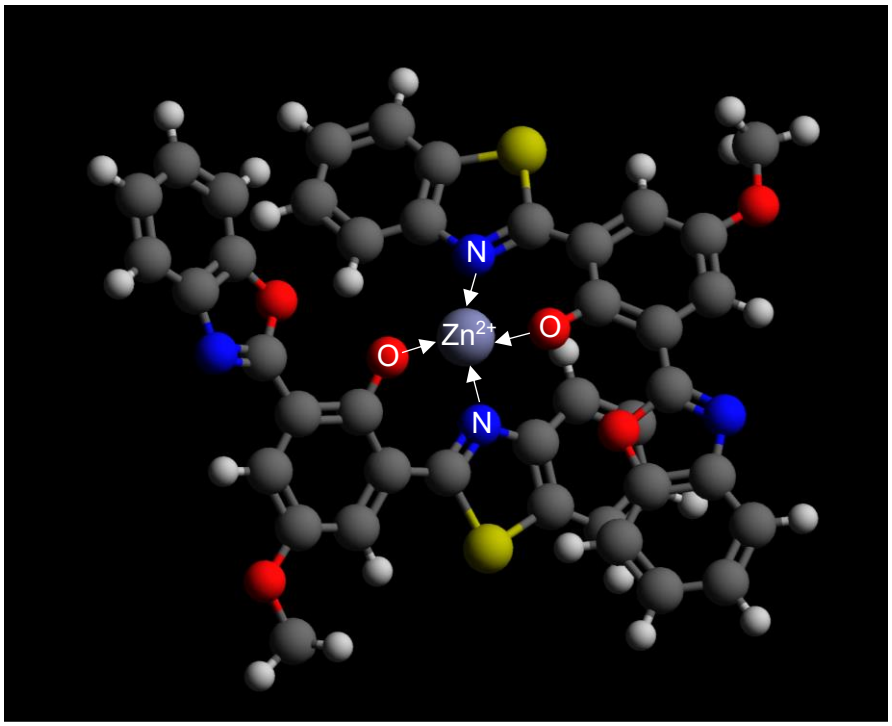

Figure 189. Optimized calculated structure for the M6-Zn^{2+} complex.

Attempts to obtain crystals of the **M6**-Zn^{2+} complex were unsuccessful.

4.2.3.4 Interference tests

Next, interference tests of the detection of Zn^{2+} by **M6** were made according to the procedure described in Section 2.3.8. The concentration of the ligand was 13.4 μmol/L in a 0.4 : 49.8 : 49.8 THF : EtOH : H_2O solvent medium. In the tests, 3.74 equivalents of each of the interferent and the zinc cation were added.

As the response of the ligand towards Zn^{2+} involves the unique appearance of a band assigned to the complex at ~503 nm, the focus of this series of tests was to verify if such band still appears in presence of other cationic species. The results are shown in Figure 190.

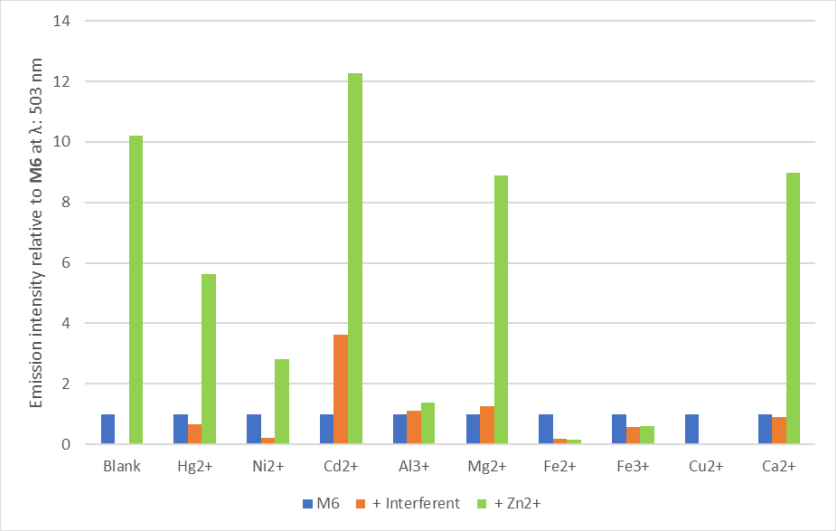

Figure 190. Interference test results for the detection of Zn^{2+} by **M6**. The blue boxes represent the normalized emission intensity of **M6**; the orange ones, the relative emission intensity when an interferent is subsequently added; and the green ones, the final relative emission intensity when Zn^{2+} is added to the mixture. λ_{exc} = 372 nm.

The interference test results show that the recognition of Zn^{2+} is completely inhibited by the presence of Al^{3+}, Fe^{2+}, Fe^{3+} and Cu^{2+}, and partially inhibited by Ni^{2+}. In the iron(II), copper(II) and nickel(II) cases, this result could be expected because these cations, by themselves, quench the emission of **M6**. It can then be postulated that the stability of the complex formed between the ligand and these species is higher than that with the zinc cation. Moreover, it can also be seen that the presence of aluminum(III) and iron(III) inhibit the detection of Zn^{2+} despite the fact that these two cations do not have a pronounced effect on the emission of the free ligand by themselves.

Finally, tests to verify if mildly acidic or basic media affect **M6** sensing capabilities towards Zn^{2+} were carried out following the same procedure as with the cationic interferents (Section 2.3.8). Once again, as a basic environment deprotonates the compound and generates a blue shifted band centered at 537 nm, a visual comparison of the spectra is better suited for this analysis. The results can be seen in Figure 191.

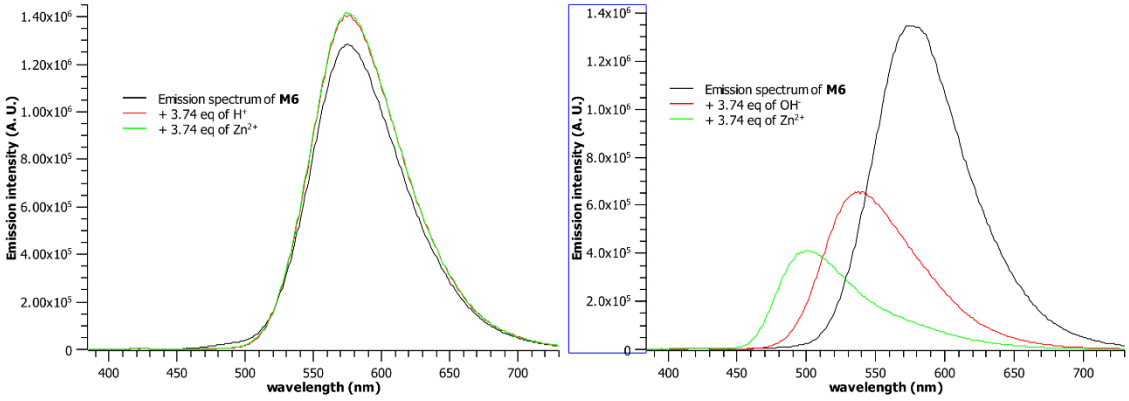

Figure 191. Emission spectra showing the interference of acidic (left) and basic (right) medium in the detection of Zn^{2+} by **M6**. [**M6**]: = 13.4 μmol/L in THF : EtOH : H_2O 0.4 : 49.8 : 49.8 medium; λ_{exc} = 372 nm.

It can be seen that an acidic medium completely inhibits the detection of zinc(II) by **M6** while a basic medium, although changing by itself the emission of the molecule, does not have any negative effect in the recognition of this cation. The result in a basic medium can be explained in a similar way as in the **M4**-Al^{3+} and **M5**-Al^{3+} cases: the medium facilitates the deprotonation of the phenolic O-***H***, enhancing the complexation of Zn^{2+} and, as a consequence, favoring the inhibition of the ESIPT mechanism of the molecule while giving rise to a new band assigned to the phenoxide species of **M6** that forms a complex with zinc(II). In fact, comparing the response towards the same amount of zinc in neutral (Figure 184) and basic media (Figure 191), it is clear that, in the latter, the complex is favored because the phenolic proton has already been displaced, which makes the complexation easier. On the other hand, it is also clear that an acidic medium makes the complexation not possible, as the acid-base equilibrium that allows the formation of the phenoxide anion necessary for the complexation is displaced to the protonated form.

At first, it was thought that this result in acidic medium could also help to understand the inhibition of the recognition of Zn^{2+} when Al^{3+} or Fe^{3+} are present in the solution. As mentioned in Section 4.1.1.4, the aqueous solutions of these cations are slightly acidic in nature, which means that it is possible that the inhibition towards the detection of zinc(II) observed in Figure 190 is due to them faintly acidifying the solution of **M6**, displacing the equilibrium to the protonated form of the molecule, and not due to the cations themselves. If this hypothesis was true, then the addition of base into a solution containing **M6**, Zn^{2+} and either Fe^{2+}, Fe^{3+} or Al^{3+} would displace the equilibrium to higher pH values and allow the complexation of zinc, which can be observed in the emission

spectrum by the characteristic band at ~500 nm. This test was carried out and, as can be seen in Figure 192, the addition of an excess of base does not influence the emission spectrum when Al^{3+} is present in the solution. It can thus be confidently proposed that it is the effect of the cations, and not of the medium, that inhibits the detection of zinc(II) by **M6**. This probably means that a complex with higher binding constant is formed between the ligand and these three species, and also that these complexes do not affect the ESIPT mechanism of the molecule, which is still active. It is then plausible to postulate that both the complexation and the luminescence mechanisms are different than those with Zn^{2+}.

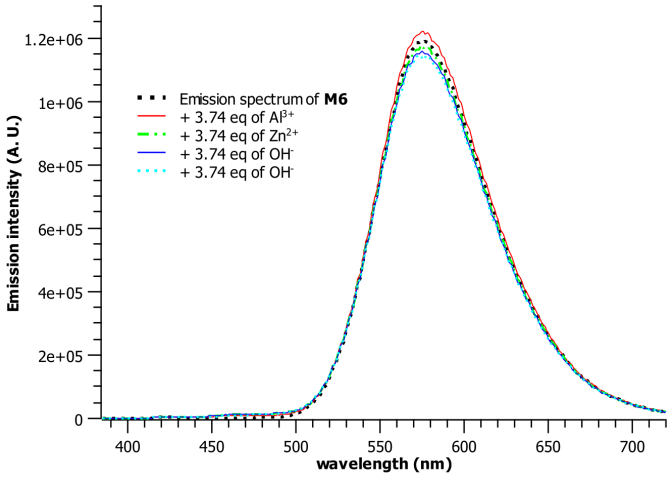

Figure 192. Comparison of the emission spectrum of **M6** upon subsequent additions of 3.74 equivalents of Al^{3+}, Zn^{2-} and OH^-. [**M6**] = 10.7 μmol/L in THF : EtOH : H_2O 0.4 : 49.8 : 49.8 medium; λ_{exc} = 372 nm.

4.2.3.5 Conclusion

In conclusion, **M6** is a 2-(2-hydroxyphenyl)benzoxazole/benzothiazole derivative that is able to detect Zn^{2+} in almost 50 % aqueous medium. The detection mechanism towards this metal is based on the inhibition of the ESIPT mechanism of the free ligand, which is promoted by the complexation of Zn^{2+} accompanied with the loss of the phenolic proton. The limit of detection for this interaction is 0.29 μmol/L and the stoichiometry is thought to be 1 : 1 according to the mass spectrum. These results show a clear improvement in the detection of zinc(II) in comparison with what has been reported in literature for a similar compound and with **M5** thanks to the ratiometric response of **M6** against this metal cation, which makes it a promising candidate for real-life assessment of low concentration levels of Zn^{2+} in human cells.

4.3 Coumarin derivative: M7

The novel molecule **M7** (Figure 193) was synthesized aiming for an indirect detection of glyphosate. As mentioned in Section 1.2.2.4, the most common strategy usually employed for sensing this pesticide is an indirect detection in which in the first place a metal cation is complexed by the ligand, changing the original emission. Then, the addition of glyphosate breaks this complex and restores the emission of the free chemosensor. For this indirect detection to be effective, the bond between the molecule and the metal cation should not be strong.

Inspired by the results obtained with **M4** (Section 4.2.1), which has a hydroxyphenyl in *ortho* position to an oxime group, it was thought that changing the phenol group to a carbonyl could yield a molecule in which the strength of the ligand-cation interaction could be smaller as it is widely known that the oxygen atom of carbonyls are much weaker bases than the oxygen atom of phenoxides (like the one present in **M4** upon complexation)[32]. This weaker interaction could then be the base for an indirect glyphosate sensor and hence it was decided to take advantage of the carbonyl group present in coumarins to achieve such a detection.

Particularly in the case of **M7**, it is expected that this molecule could complex Cu^{2+} following a report by Hu [258] with a similar derivative, and also OCl^- owing to the presence of an oxime group, as already described in detail before.

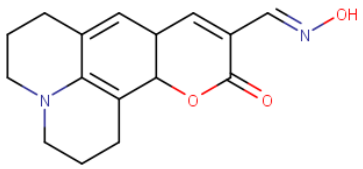

Figure 193. Chemical structure of **M7**.

4.3.1 Bulk tests

Bulk tests were carried out following the procedure described in Section 2.3.3. For the cation test, the solvent medium used was THF : EtOH : H_2O 1 : 10 : 40, while for the anion test, it was THF : EtOH 1 : 51. As stated in Section 2.1.3.2, the goal with this ligand was mainly to probe its ability as an indirect glyphosate sensor, so a more aqueous

[32] https://www.chem.indiana.edu/wp-content/uploads/2018/03/pka-chart.pdf

environment was chosen to try to be closer to potential real-life measurements. The cation and anion bulk test results are shown in Figure 194 and Figure 195, respectively. Also, the response of **M7** against the addition of acidic and basic solutions was probed and the results can be seen in Figure 196.

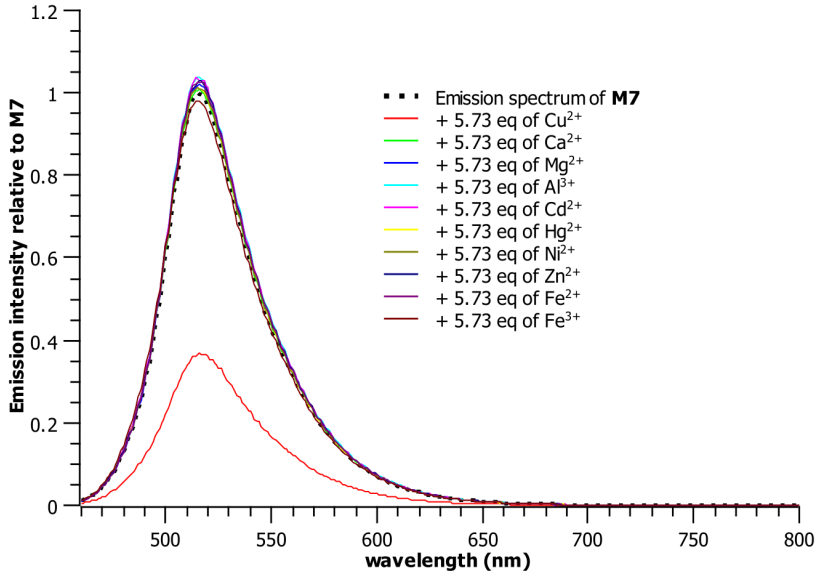

Figure 194. Emission spectrum of **M7** (17.1 μmol/L in THF : EtOH : H_2O 1 : 10 : 40) in presence of an excess (5.73 equivalents) of several metallic cations; λ_{exc} = 448 nm.

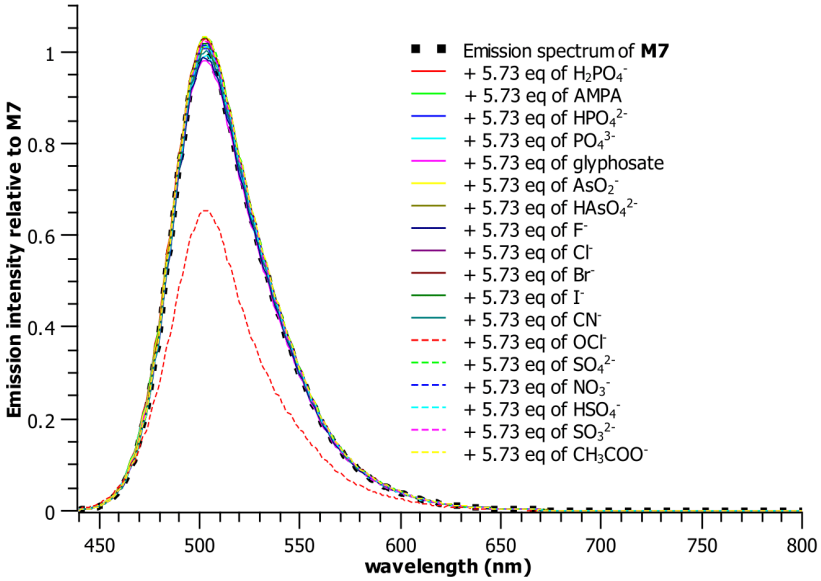

Figure 195. Emission spectrum of **M7** (17.1 μmol/L in THF : EtOH 1 : 51) in presence of an excess (5.73 equivalents) of several anions; λ_{exc} = 448 nm.

The results shown in the cation and anion bulk tests indicate that the emission of **M7** is only impacted by the addition of Cu^{2+} and OCl^-, exactly as predicted in the design of the molecule (Section 2.1.3.2). In both cases, there is a quenching of the emission intensity of around 60 % and 35 %, respectively. Particularly, the selectivity of this ligand towards copper(II) could allow for an excellent indirect glyphosate chemosensor because no other metal cation commonly present in solution seems to impact its fluorescence properties.

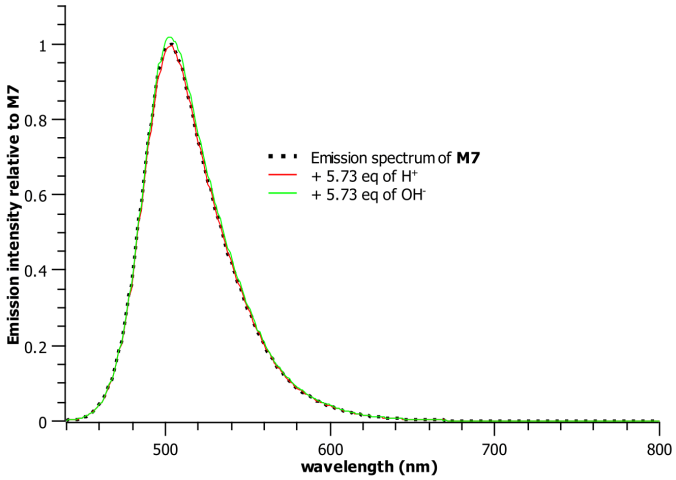

Figure 196. Emission spectra of **M6** when adding acidic or basic solutions. [**M7**] = 17.1 μmol/L in THF : EtOH 1 : 51 medium; λ_{exc} = 431 nm.

As for the tests in acidic and basic ethanol, it can be seen in Figure 196 that these media do not generate any change in the emission spectrum of **M7**. This means that a potential protonation of the nitrogen atom of the julolidine entity (pK_aH = 5 – 6 [305]) or the nitrogen atom of the oxime group (pK_aH = 4.5 – 5 [252]), or deprotonation of the hydroxy group of the oxime (pK_a = 10 – 11 [288]) do not interfere with the internal charge transfer mechanism of the ligand (which was explained in Section 3.3) at least in the conditions used.

4.3.2 Indirect glyphosate sensing

As **M6** was found sensitive and selective towards Cu^{2+} as far as emission is concerned, exploratory trials to verify the indirect detection of glyphosate and its main decomposition metabolite, AMPA, were carried out. They are shown in Figure 197, where it can be seen that after being initially quenched by adding Cu^{2+}, the emission intensity of the ligand is restored by 100 % and 95 % upon equimolar addition of the pesticide and its metabolite, respectively. These observations tend to support the initial hypothesis that the

complexation of Cu^{2+} by **M6** was weak enough that the cation could be easily displaced when adding the analytes.

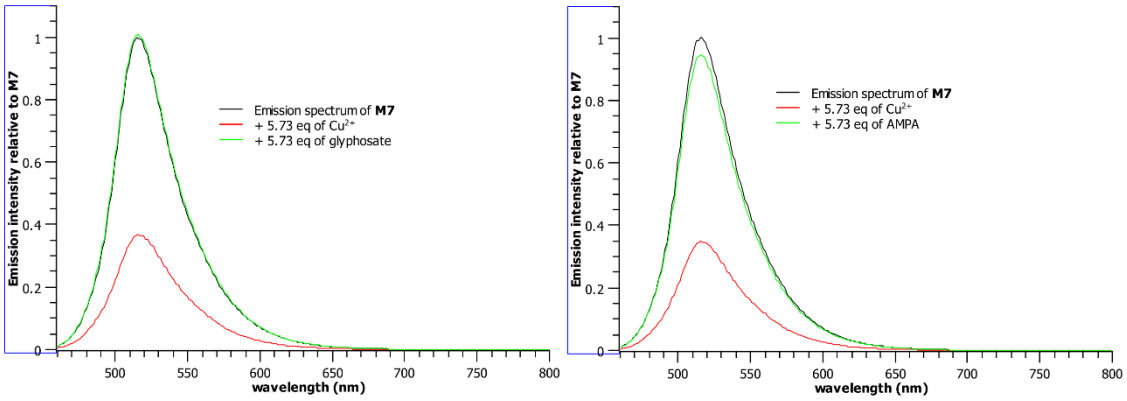

Figure 197. Exploratory trials for the indirect detection of (left) glyphosate and (right) AMPA. [**M7**] = 17.1 μmol/L in THF : EtOH : H_2O 1 : 10 : 40 medium; λ_{exc} = 448 nm.

Unfortunately, the interactions **M7**-Cu^{2+} and **M7**-OCl^-, and the indirect detection of glyphosate could not be further explored due to lack of time. However, the basis is set for supplementary research using this ligand.

4.3.2.1 Conclusion

In conclusion, **M7** is a julolidine-coupled coumarin-oxime compound that exhibits sensitivity towards Cu^{2+} and OCl^-, both by partial quenching the emission. In particular, the selectivity that this ligand exhibits towards copper(II) make it an ideal candidate for indirect sensing of glyphosate and AMPA as it has been proved that addition of these species into the **M7**-Cu^{2+} solution regenerates the emission of the free molecule.

4.4 Porphyrin derivatives: M8-Pd, M8-Pt, M9-Pd and M9-Pt

The last molecules synthesized within the scope of the present thesis work were the two porphyrins **M8** and **M9**, and their palladium(II) and platinum(II) complexes (a scheme depicting their general chemical structures is shown in Figure 198) which, as described in Section 2.1.4.2, were anticipated to probe molecular oxygen. Measuring the concentration of dissolved oxygen is a very important water quality parameter because a myriad of biological processes depends of this value being in a well-defined range. Moreover, its assessment is important for quality control processes in industrial activities such as medicine or bioprocess control.

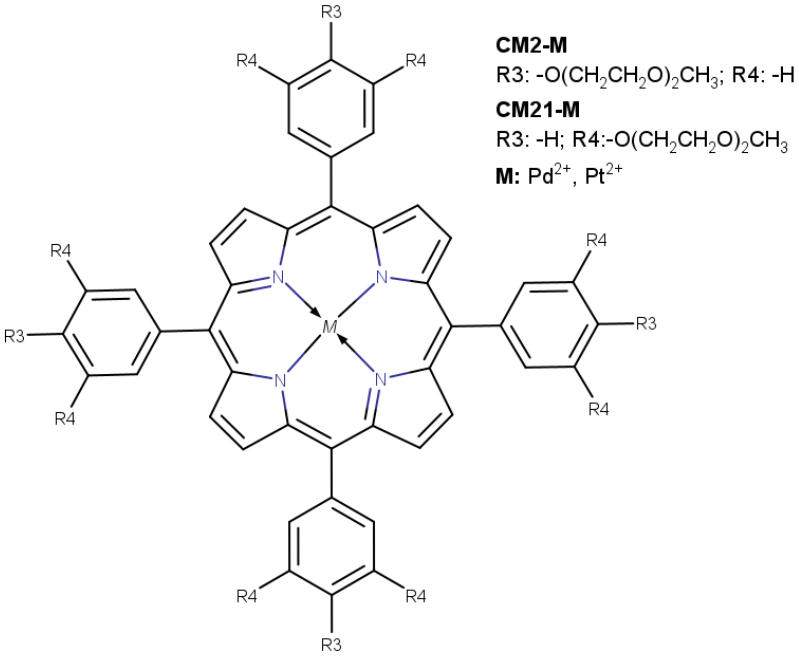

Figure 198. Chemical structure of the two porphyrin derivatives and their complexes.

4.4.1 Oxygen sensing and mechanism

Before being tested, the molecules were dried overnight under vacuum at 60 °C to eliminate possible interferences of gaseous species that could interact with the metallic centers. Then, samples were prepared according to the procedure described in Section 2.3.1 in $CHCl_3$ with a final complex concentration set at 3.7 μmol/L. In the first place, each sample was gently bubbled with argon for 10 minutes and the emission spectrum was recorded. The solutions were subsequently bubbled with oxygen for another 10 minutes to saturate the solution with O_2 and, once again, the emission spectrum was recorded. This cycle was repeated in order to verify the reusability of the complexes as O_2 chemosensors. It should be noted that due to the setup used, it was not possible to accurately control the flux of oxygen or argon used to bubble into the solutions of the complexes. However, it is thought that 10 minutes of exposure to these gases was enough to saturate the samples. Also, in these first exploratory trials, $CHCl_3$ was used as solvent because the porphyrins are highly soluble into it. The results of the O_2 sensitivity tests are reported on Figure 199 to Figure 202.

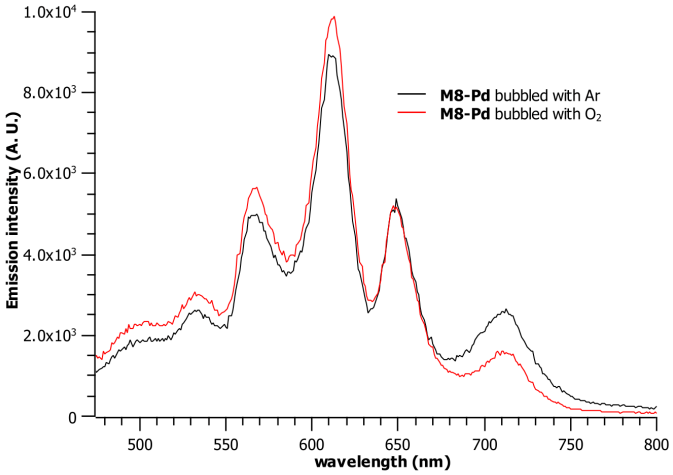

Figure 199. O_2 sensitivity test of **M8-Pd**. The slits used were 5 nm / 5 nm.

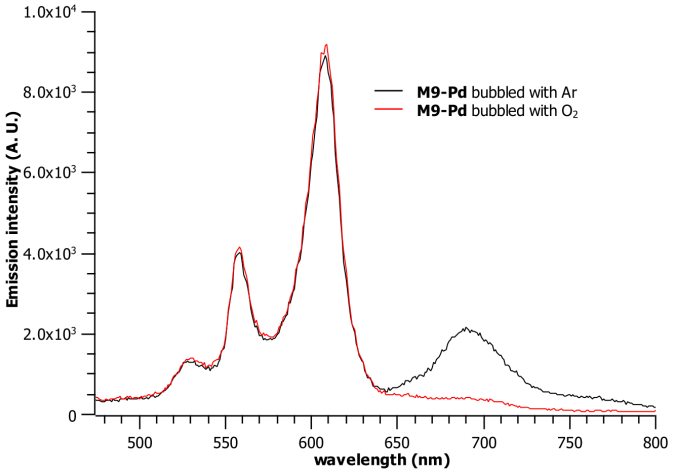

Figure 200. O_2 sensitivity test of **M9-Pd**. The slits used were 5 nm / 5 nm.

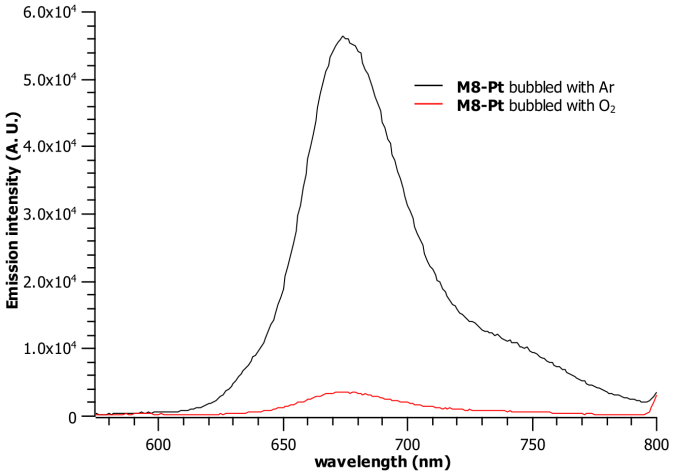

Figure 201. O_2 sensitivity test of **M8-Pt**. The slits used were 5 nm / 5 nm.

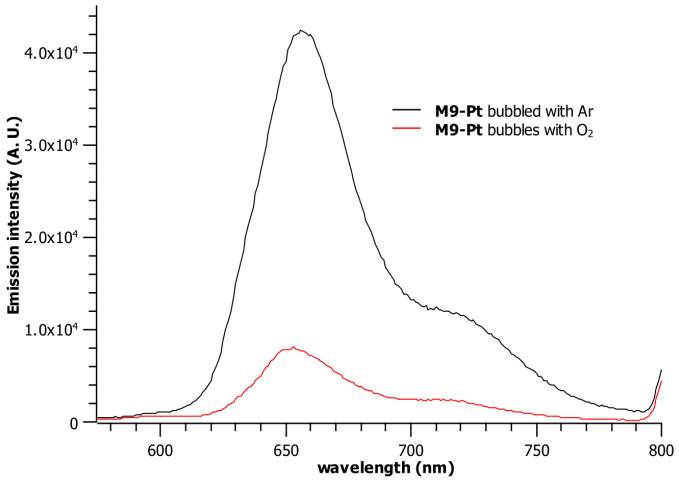

Figure 202. O_2 sensitivity test of **M9-Pt**. The slits used were 5 nm / 5 nm.

It can be appreciated in these results that molecular oxygen effectively quenches the phosphorescence emission of both platinum(II) complexes by 94 % (**M8-Pt**) and 78 % (**M9-Pt**). In the case of the palladium(II) complexes, it is interesting to note that the emission of **M8-Pd** is basically not affected by oxygen, but on the other hand, the band assigned to the phosphorescence emission of **M9-Pd** is quenched by 79 %.

As mentioned in Section 1.2.2.6, a spatial overlap of the wavefunctions of their molecular orbitals is needed for oxygen to quench the triplet state of the porphyrin metallocomplexes. When absorbing energy, the exciton is transferred from the excited triplet state of the luminophore to the excited state of O_2 in a process faster than the phosphorescence decay of the O_2-free complex. Hence, this radiative process is quenched because the energy is no longer being released from the complex, but from O_2 [47] [49] [52]. The Perrin-Jablonski diagram for this quenching mechanism is shown in Figure 203.

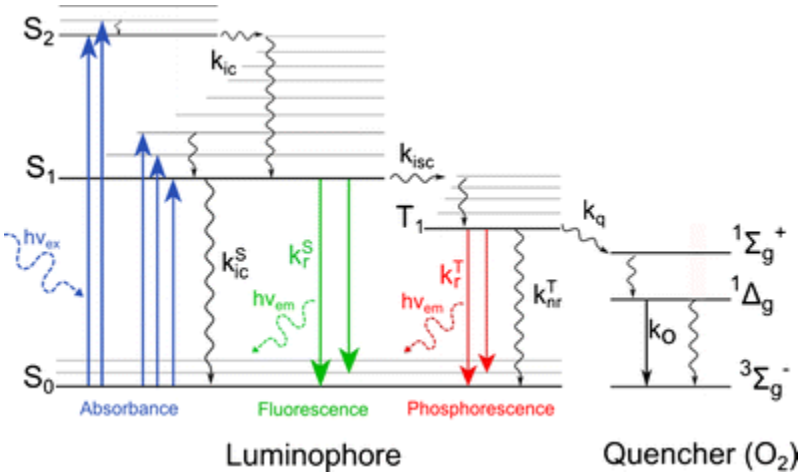

Figure 203. Perrin-Jablonski diagram for the possible de-excitation pathway of the porphyrin metallocomplexes in presence of O_2. The image is taken from [49].

Also, it has been described by density functional calculations that O_2 and a model Pt^{2+}-porphyrin interact by the donation of electrons from the occupied $5d_{Z^2}$ orbital of the metal ion to the 3*p* antibonding orbitals of oxygen, as shown in Figure 204 [94]. Owing to the similarities of the general chemical behavior between the platinum(II) and palladium(II) ions in porphyrin complexes [272], it could be expected that the interaction of the latter with O_2 follows a similar route: the donation of electrons from the occupied $4d_{Z^2}$ orbital to the 3*p* antibonding orbitals of the bound gas molecule.

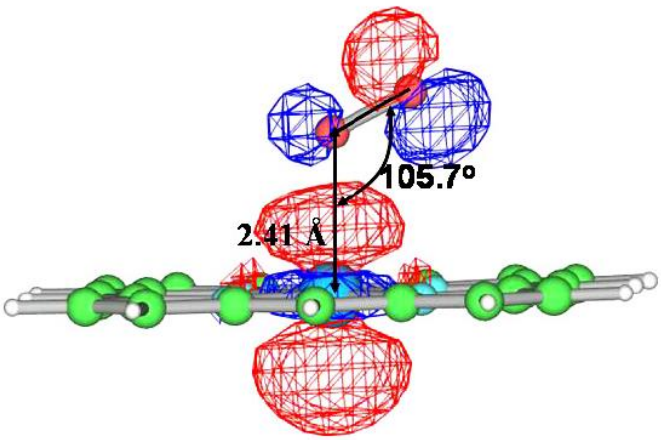

Figure 204. Geometry and molecular orbital interaction of a O_2 – Pt^{2+}-porphyrin species by density functional calculations. The image was taken from [94].

Considering this mechanism, it can be postulated that the spatial overlap between molecular orbitals of O_2 and the **M8-Pd** complex is not effective in order to promote the

transfer of the exciton and as consequence, no substantial phosphorescence quenching occurs. On the contrary, the highest phosphorescence quenching is found for the **M8-Pt** complex.

As for the reusability of the complexes as O_2 chemosensors, it can be seen from Figure 205 to Figure 207 that **M8-Pd**, **M8-Pt** and **M9-Pt** recover the phosphorescence emission when the $CHCl_3$ solutions are bubbled with argon gas in at least three cycles, making them interesting candidates for recyclable dissolved oxygen sensors. Though the emission intensity is not exactly the same as when the test started, this can be attributed to not using controlled fluxes of gas and due to possible small changes in the concentration of the ligand owing to solvent evaporation during bubbling.

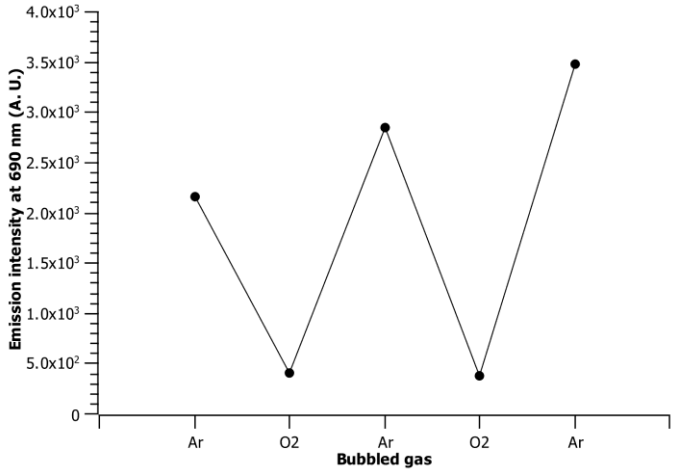

Figure 205. Reusability of the **M9-Pd** chemosensor for O_2 detection (3.7 μmol/L in $CHCl_3$). The slits used were 5 nm / 5 nm.

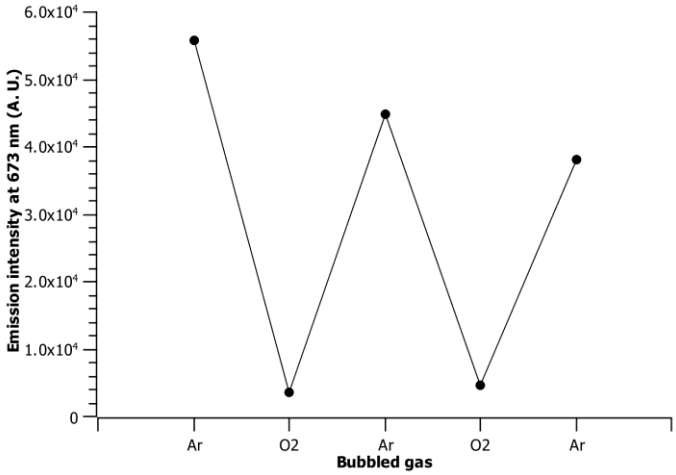

Figure 206. Reusability of the **M8-Pt** chemosensor for O_2 detection (3.7 μmol/L in $CHCl_3$). The slits used were 5 nm / 5 nm.

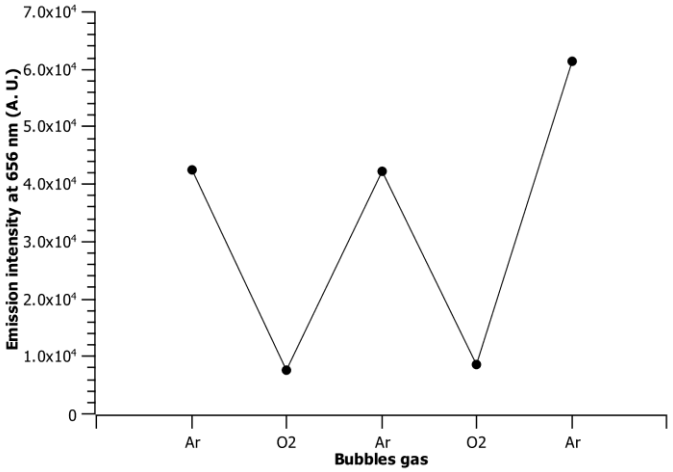

Figure 207. Reusability of the **M9-Pt** chemosensor for O_2 detection (3.7 μmol/L in $CHCl_3$). The slits used were 5 nm / 5 nm.

As mentioned in Section 2.1.4.2, the main objective with the porphyrin metallocomplexes was to probe their ability in the detection of dissolved O_2 in water and hence their design with ether chains that could improve their hydrophilicity. With this in mind, the **M9-Pt** complex was chosen to verify if the sensitivity to O_2 found in chloroform could also be achieved in an aqueous environment.

The aqueous solution of the porphyrin was prepared by pouring 2.5 mL of degassed H_2O into 1.7 mg of **M9-Pt** and vigorously stirring for 5 minutes. Although a major part of the porphyrin was not dissolved, it was figured that the amount was enough to carry out the measurement as the emission spectrum could be recorded. Then, the procedure of the test is of similar nature than those made previously: the solution of porphyrin was bubbled with O_2 and argon in subsequent 10-minute cycles followed by the measurement of the emission intensity. The results of this essay can be seen in Figure 208.

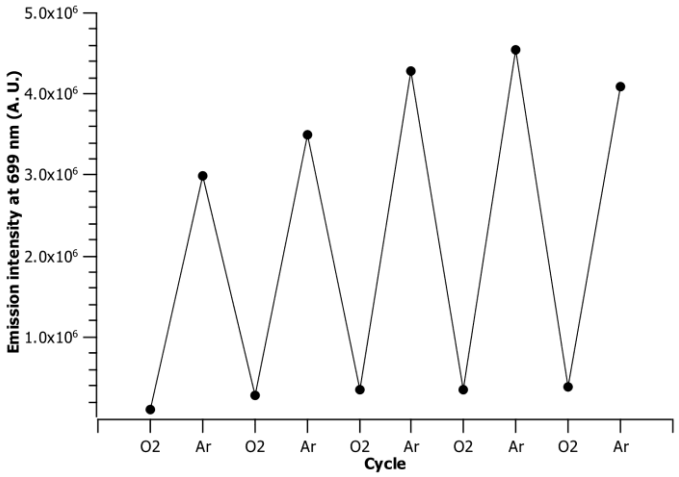

Figure 208. Sensitivity and reusability test of the **M9-Pt** chemosensor for the detection of O_2 in 100 % aqueous medium. The emission intensity values were taken at λ_{em} = 669 nm. λ_{exc} = 401 nm. The slits used were 6 nm / 6 nm.

As can be seen in the graphic, the complex **M9-Pt** is able to detect O_2 even in a 100 % aqueous environment for at least 5 cycles of oxygen-argon gassing. As mentioned before, the differences in the maximum value of emission intensity are due to the fact that the setup used does not allow to precisely control de flux of bubbled gases. In fact, it was experimentally proved that only 2 minutes of bubbling with O_2 were enough to completely quench the phosphorescence of the complex, but at least 25 minutes of bubbling with argon were needed to restore the emission to its maximum value. This makes sense as the oxygen is covalently, albeit weakly, bound to the metal center, while the argon is not.

4.4.2 Conclusion

M8-Pt, **M9-Pd** and **M9-Pt** are metalloporphyrin derivatives that are able to detect molecular oxygen in a pure $CHCl_3$ medium. Moreover, **M9-Pt** is capable to achieve this same detection in a pure aqueous medium as it is soluble in water. This complex has been shown to be reusable for at least 5 cycles of Ar-O_2 gassing.

5 Conclusions and perspectives

5.1 Overall conclusion

Within the scope of the present thesis work, 11 new compounds that show interesting luminescence aptitudes were synthesized: three pyrene derivatives, three benzazole derivatives, one coumarin derivative and four porphyrin-complex derivatives. For each of these compounds, their photophysical properties in terms of understanding their absorption and emission spectra were thoroughly analyzed and discussed, and their capabilities for being used as chemosensors for the detection of analytes present in aqueous medium was also investigated.

A compendium of all the sensing results against cations and anions, as well as the effect of acidic or basic solutions on the emission spectrum of the **M1** – **M7** molecules is shown in Figure 209, Figure 210 and Figure 211, respectively. In these figures, a two-dimensional plot was elaborated. In the x-axis, the relative change in emission intensity is shown according to the formula $\Delta_r I = \frac{I_f - I_i}{I_i}$, where I_i is the initial emission intensity of the free molecule and I_f is the value when an analyte has been added. In the y-axis, the absolute wavelength variation of the maximum emission intensity is shown according to the formula $\Delta\lambda = \lambda_f - \lambda_i$, where λ_i is the wavelength of the emission maxima of the free molecule and λ_i is the wavelength of the emission maxima when an analyte has been added. This information has been compiled using the data from the bulk tests presented for each molecule in Chapter 4.

These figures show, in essence, the most remarkable responses, either by changes of the emission (quenching or enhancement) or by shifting/appearance of a new band. For example, in Figure 209 it can be seen that the molecule **M6** provides the best response against zinc(II) due to the appearance of a new band that is ~70 nm blue shifted in comparison with that one of the free molecule. The best results are highlighted in each figure.

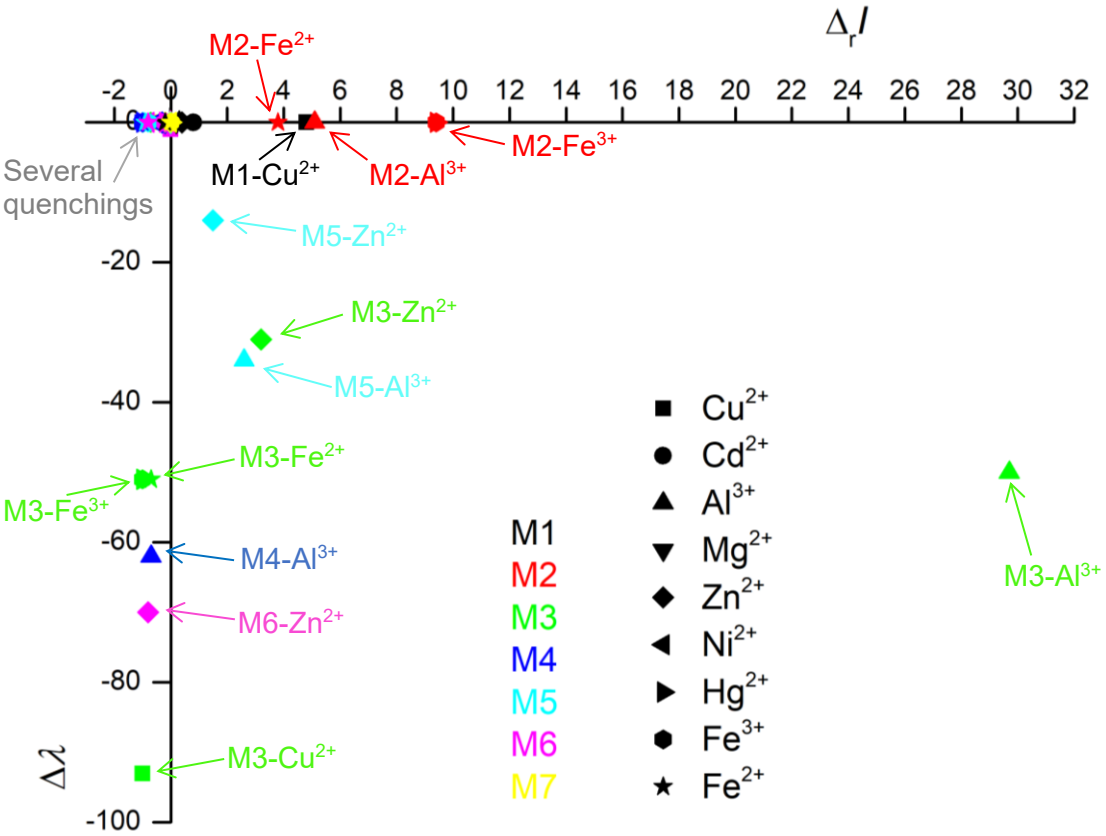

Figure 209. Summary of the sensing results of all the molecules against metallic cations.

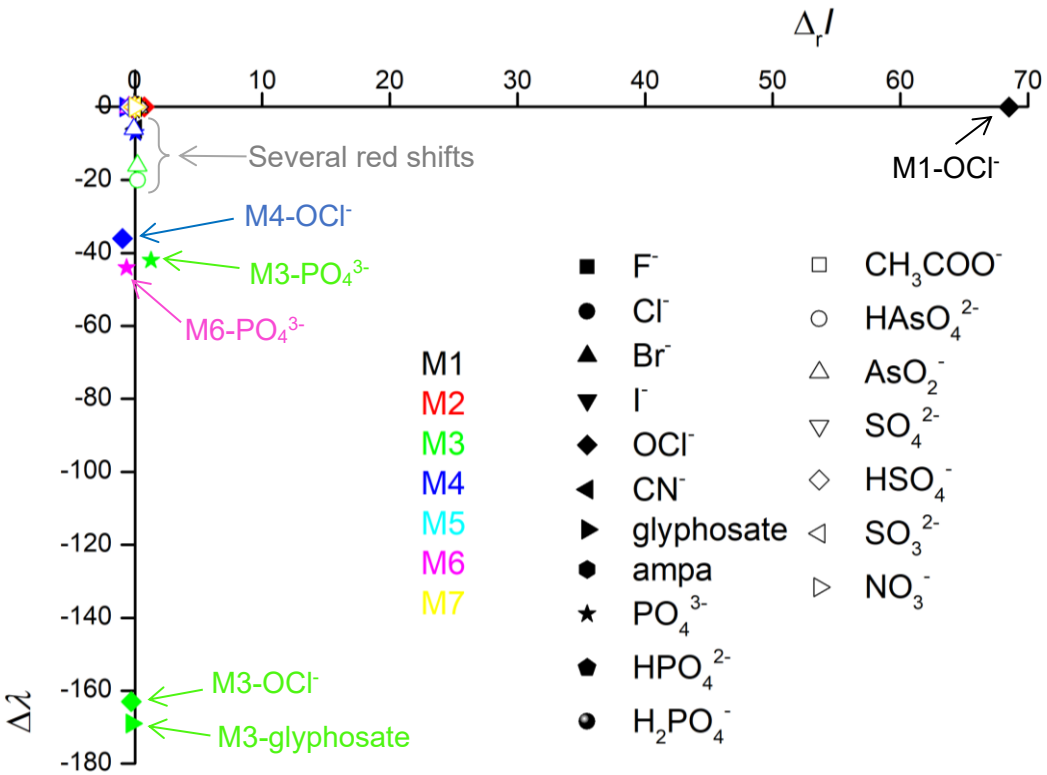

Figure 210. Summary of the sensing results of all the molecules against anionic species.

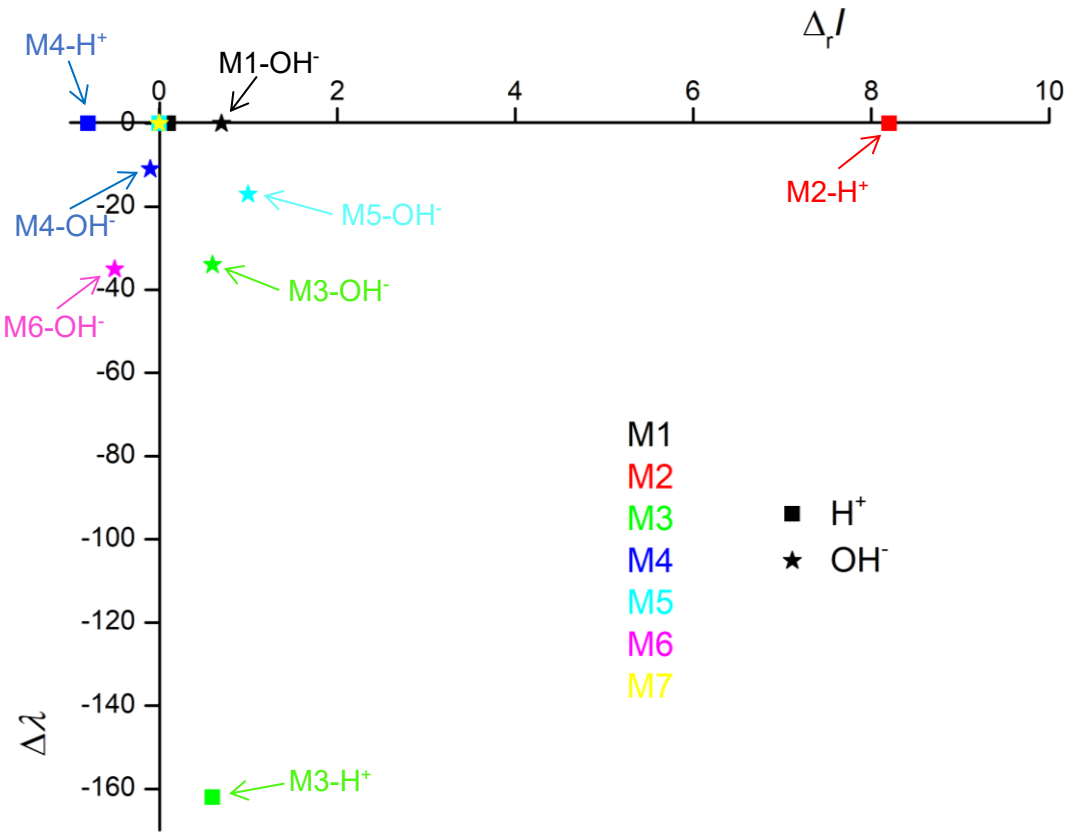

Figure 211. Summary of the responses of all the molecules in acidified or basified medium.

The most important results obtained from the 11 new compounds are presented with more detail in Table 3, where the solvent system and the proposed sensing mechanisms are also mentioned. In summary, **M1** is a thiourea-pyrene chemosensor that is able to detect Cu^{2+} and OCl^-. **M2** is a pyrene derivative bearing a Schiff-base with an *OH* group in *ortho* position that was found to be able to detect Al^{3+}, Fe^{2+} and Fe^{3+}. The last pyrene derivative, **M3**, possesses alternating acidic and basic groups that allow for a direct and fast, albeit non-quantitative, detection of the widespread and toxic pesticide glyphosate. Then, **M4**, **M5** and **M6** are all 2-(2-hydroxyphenyl)benzazole derivatives that allow for a ratiometric detection of Al^{3+} and/or Zn^{2+}, the former one being able to also detect the hypochlorite anion by a mechanism that does not involve an immediate chemical reaction. This reactivity has not been reported in the literature until now. For these six molecules, the limits of detection towards their target analytes (presented in Table 4) are low enough to consider the compounds for potential use in real-life water quality control systems or, for the particular case of zinc(II), in measuring its deficiency in human cells.

For its part, the coumarin derivative, **M7**, allows for an indirect detection of glyphosate thanks to an easy decomplexation of the copper cation. Finally, three out of the four

porphyrin complexes, namely **M8-Pt**, **M9-Pd** and **M9-Pt**, have shown excellent sensing aptitudes to detecting dissolved O_2, the latter one even being able to achieve this sensitivity in 100 % aqueous medium.

Table 3. Summary of the sensing results obtained with the 11 molecules presented in this thesis manuscript

Molecule	Chemical family	Solvent system	Sensing aptitudes	Sensing mechanism
M1	Pyrene derivative	100 % THF	Cu^{2+}	Inhibition of the pyrene-thiourea free rotation
			OCl^-	Oxidation to a urea
M2	Pyrene derivative	100 % THF	Al^{3+}, Fe^{2+}, Fe^{3+}	Inhibition of the -C=N free isomerization
M3	Pyrene derivative	THF : EtOH 0.5 : 99.5	Glyphosate, several cations	Not investigated due to instability of solution
M4[33]	Benzimidazole derivative	THF : H_2O 0.5 : 99.5	Al^{3+}	Inhibition of ESIPT
			OCl^-	Inhibition of ESIPT and slow deoximation to an aldehyde
M5[31]	Benzoxazole derivative	EtOH : H_2O 1 : 4	Al^{3+}	Inhibition of ESIPT
			Zn^{2+}	CHEF
M6[31]	Benz(oxa,thia)zole derivative	THF : EtOH : H_2O 0.4 : 49.8 : 49.8	Zn^{2+}	Inhibition of ESIPT
M7	Coumarin derivative	THF : EtOH : H_2O 1 : 10 : 40	Cu^{2+}	Not investigated
			Indirect glyphosate detection	Decomplexation of Cu^{2+}
		THF : EtOH 1 : 51	OCl^-	Not investigated
M8-Pt	Platinum-porphyrin derivative	100 % $CHCl_3$	O_2	Oxygen-promoted deactivation of triplet state

[33] The sensitivity of the three benzazole compounds to Fe^{2+}, Fe^{3+} and Cu^{2+} is not being considered.

M8-Pd	Palladium-porphyrin derivative	100 % $CHCl_3$	-	-
M9-Pt	Platinum-porphyrin derivative	100 % H_2O	O_2	Oxygen-promoted deactivation of triplet state
M9-Pd	Palladium-porphyrin derivative	100 % $CHCl_3$	O_2	Oxygen-promoted deactivation of triplet state

Table 4. Summary of the calculated limits of detection of our molecules towards their target analytes

Molecule	Analyte	Limit of detection
M1	Cu^{2+}	9.71 μmol/L
	OCl^-	1.01 μmol/L
M2	Al^{3+}	0.06 μmol/L
	Fe^{2+}	0.03 μmol/L
	Fe^{3+}	0.04 μmol/L
M4	Al^{3+}	0.14 μmol/L
	OCl^-	1.08 μmol/L
M5	Al^{3+}	0.30 μmol/L
	Zn^{2+}	3.43 μmol/L
M6	Zn^{2+}	0.29 μmol/L

5.2 Future perspectives

To better confirm the results presented in this manuscript, future research could be oriented to the obtention of single crystals suitable for X-ray crystallography and utilizing a global analysis for obtaining the association constant values of the molecules with their target analytes. Moreover, lifetime measurements such as time-correlated single photon counting could be used to further characterize both the free molecules and the species they form when interacting with their analytes. This technique could be especially useful for characterizing the interaction of the porphyrin derivatives with molecular oxygen, as it involves the quenching of the long-lived triplet state of the complex.

Then, particularly for the case of **M3**, the base for the development of a direct glyphosate chemosensor, which has not been reported in the literature until now, and involves the alternation of acidic and basic groups, has been set and could be worth of further investigation. Taking the results obtained with this molecule as a starting point, two axes of research are proposed. The first involves the design of derivatives that do not contain an *OH* group in *ortho* position to a Schiff base, but maintain the alternance of acidic and basic groups. This proposal is thought to keep the selectivity towards glyphosate while losing the ability to detect metallic cations, increasing the selectivity of the molecule. The second proposal relies on the election of a proper solvent system, which should

preferentially contain water, in which the molecule, either **M3** or a new one, is stable and the sensitivity towards the pesticide can be achieved.

In the case of **M7**, the lack of time did not allow for a complete study of the sensing mechanism of this molecule towards OCl^- and Cu^{2+}, nor to the decomplexation reaction that glyphosate generates to the **M7**-Cu^{2+} species. Hence, future work could be dedicated to complete the missing tests, most importantly, the calibration curves and the interference essays, as well as the characterization of the possible reaction product of the molecule with hypochlorite.

Lastly, as has been mentioned before, other members of our research group are currently exploring the functionalization of these molecules onto carbonaceous materials in order to elaborate resistive sensors. It can then be envisioned that devices containing our molecules could be fabricated for being used in real-life assessment of analytes in water. In particular, efforts are being made on the development of porphyrin-functionalized single-walled carbon nanotubes in order to detect dissolved molecular oxygen in pure water medium.

6 Cited bibliography

[1] X. Wang, X. Lu and J. Chen, "Development of biosensor technologies for analysis of environmental contaminants," *Trends in Environmental Analytical Chemistry,* vol. 2, pp. 25 - 32, 2014.

[2] O. M. L. Alharbi, A. A. Basheer, R. A. Khattab and I. Ali, "health and environmental effects of persistent organic pollutants," *Journal of Molecular Liquids,* vol. 263, pp. 442 - 453, 2018.

[3] M. Jin, H. Yuan, B. Liu, J. Peng, L. Xu and D. Yang, "Review of the distribution and detection methods of heavy metals in environment," *Analytical Methods,* vol. 12, pp. 5747 - 5766, 2020.

[4] P. B. Tchounwou, C. G. Yedjou, A. K. Patlolla and D. J. Sutton, "Heavy metal toxicity and the environment," in *Molecular, Clinical and Envinronmental Toxicology*, Basel, Springer, 2012, pp. 133 - 164.

[5] X. Wu, S. J. Cobbina, G. Mao, H. Xu, Z. Zhang and L. Yang, "A review of toxicity and mechanisms of individual and mixtures of heavy metals in the environment," *Environmental Science and Pollution Research,* vol. 23, pp. 8244 - 8259, 2016.

[6] F. Zheng, F. Dong, L. Zhou, Y. Chen, J. Yu, X. Luo, X. Zhang, Z. Lv, X. Xia and J. Xue, "Research progress on heterogenous reactions of pollutant gases on the surface of atmospheric mineral particulate matter in China," *Atmosphere,* vol. 13, no. 8, p. 1283, 2022.

[7] R. A. Wuana and F. E. Okieimen, "Heavy metals in contaminated soils: a review of sources, chemistry, risks and best available strategies for remediation," *International Scholarly Research Network,* vol. 2011, 2011.

[8] M. Lamine Sall, A. K. Diagne Diaw, D. Gningue-Sall, S. E. Aaron and J.-J. Aaron, "Toxic heavy metals: impact on the environment and human health, and treatment with conducting organic polymers, a review," *Environmental Science and Pollution Research,* vol. 27, pp. 29927 - 29942, 2020.

[9] S. Sharma, A. K. Nagpal and I. Kaur, "Appraisal of heavy metal contents in groundwater and associated health hazards posed to human population of Ropar wetland, Punjab, India and its environs," *Chemosphere,* vol. 227, pp. 179 - 190, 2019.

[10] L. Joseph, B.-M. Jun, J. R. V. Flora, C. M. Park and Y. Yoon, "Removal of heavy metals from watr sources in the eveloping world using low-cost materials: A review," *Chemosphere,* vol. 229, pp. 142 - 159, 2019.

[11] Kiran, R. Bharti and R. Sharma, "Effect of heavy metals: An overview," *Materials Today: Proceedings,* vol. 51, p. 880 885, 2021.

[12] U. Okereafor, M. Makhata, L. Mekuto, N. Uche-Okereafor, T. Sebola and V. Mavumengwana, "Toxic metal implications on agricultural soils, plants, animals, aquatic life and human health," *Environmental Research and Public Health,* vol. 17, no. 7, p. 2204, 2020.

[13] A. U. Rehman, S. Nazir, R. Irshad, K. Tahir, K. U. Rehman, R. U. Islam and Z. Wahab, "Toxicity of heavy metals in plants and animals and their uptake by magnetic iron oxide nanoparticles," *Journal of Molecular Liquids,* vol. 321, p. 114455, 2021.

[14] R. Verma, K. Vijayalakshmy and V. Chaudhiry, "Detrimental impacts of heavy metals on animal reproduction: A review," *Journal of Entomology and Zoology Studies,* vol. 6, no. 6, pp. 27-30, 2018.

[15] Q. Sun, Y. Li, L. Shi, R. Hussain, K. Mehmood, Z. Tang and H. Zhang, "Heavy metals induced mithocondrial dysfunction in animals: Molecular mechanism of toxicity," *Toxicology,* vol. 469, p. 153136, 2022.

[16] National Institute of Environmental Health Sciences, "National Institute of Environmental Health Sciences," United States government, [Online]. Available: https://www.niehs.nih.gov/health/topics/agents/pesticides/index.cfm. [Accessed 13 May 2020].

[17] World Health Organization, "World Health Organization," United Nations, [Online]. Available: https://www.who.int/topics/pesticides/en/. [Accessed 13 May 2020].

[18] Y. Liu, X. Pan and J. Li, "A 1961 - 2010 record of fertilizer use, pesticide application and cereal yields: a review," *Agronomy for Sustainable Development,* vol. 35, pp. 83 - 93, 2015.

[19] D. Gunnell, M. Eddleston, M. R. Phillips and F. Konradsen, "The global distribution of fatal pesticide self-poisoning: Systematic review," *BMC Public Health,* vol. 7, no. 357, 2007.

[20] United States Environmental Protection Agency, "Recognition and management of pesticide poisonings," United States Environmental Protection Agency, Washington, 2013.

[21] A. Moretto, "Pesticide residues: organophosphates and carbamates," *Encyclopedia of Food Safety,* vol. 3, pp. 19 - 22, 2014.

[22] D. A. Jett, "Central Cholinergic Neurobiology," in *Handbook of Developmental Neurotoxicology*, 1998, pp. 257 - 274.

[23] P. Kaushik and G. Kaushik, "An assessment of structure and toxicity correlation in organochlorine pesticides," *Journal of Hazardous Materials,* vol. 143, no. 1 - 2, pp. 102 - 111, 2007.

[24] R. Kanissery, B. Gairhe, D. Kadyampakeni, O. Batuman and F. Alferez, "Glyphosate: Its environmental persistence and impact in crop health and nutrition," *Plants,* vol. 8, no. 11, p. 499, 2019.

[25] I. Heap and S. O. Duke, "Overview of glyphosate-resistant weeds worldwide," *Pest Management Science,* vol. 74, no. 5, pp. 1040 - 1049, 2018.

[26] S. M. Bradberry, A. T. Proudfoot and J. A. Vale, "Glyphosate Poisoning," *Toxycological Reviews,* vol. 23, pp. 159 - 167, 2004.

[27] J. P. Kaur Gill, N. Sethi, A. Mohan, S. Datta and M. Girdhar, "Glyphosate toxicity for animals," *Environmental Chemistry Letters,* vol. 16, pp. 401 - 426, 2018.

[28] Occidental Chemical Corp., Sodium Hypochlorite Handbook, Dallas, 2000.

[29] R. J. Slaughter, M. Watts, J. A. Vale, J. R. Grieve and L. J. Schep, "The clinical toxicology of sodium hypochlorite," *Clinical Toxicology,* vol. 57, no. 5, 2019.

[30] Z. Mohammadi, "Sodium hypochlorite in endodontics: an update review," *International Dental Journal,* vol. 58, no. 6, pp. 329 - 341, 2008.

[31] C. C. Winterbourn, M. B. Hampton, J. H. Livesey and A. J. Kettle, "Modeling the reactions of superoxide and myeloperoxidase in the neutrophil phagosome: implications for microbial killing," *Journal of Biological Chemistry,* vol. 281, no. 52, pp. 39860 - 39869, 2006.

[32] P. Chen, Z. Zheng, Y. Zhu, Y. Dong, F. Wang and G. Liang, "Bioluminescent turn-on probe for sensing hypochlorite in vitro and in tumors," *Analytical Chemistry,* vol. 89, no. 11, pp. 5693 - 5696, 2017.

[33] M. Cho, V.-N. Nhuyen and J. Yoon, "Simultaneous detection of hypochlorite and singlet oxygen by a thiocoumarin-based ratiometric fluorescent probe," *ACS Measurement Science Au,* vol. 2, no. 3, pp. 219 - 223, 2022.

[34] Y.-H. Yan, H.-L. Ma, J.-Y. Miao, B.-X. Zhao and Z.-M. Lin, "A ratiometric fluorescent probe based on a novel recognition mechanism for monitoring endogenous hypochlorite in living cells," *Analytica Chimca Acta,* vol. 1064, pp. 87 - 93, 2019.

[35] N. Noguchi, A. Nakada, Y. Itoh, A. Watanabe and E. Niki, "Formation of active oxygen species and lipid peroxidation induced by hipochlorite," *Archives of Biochemistry and Biophysics,* vol. 397, no. 2, pp. 440 - 447, 2002.

[36] N. Parveen, S. Chowdhury and S. Goel, "Environmental impacts of the widespread use of chlorine-based didinfectants during the COVID-19 pandemic," *Environmental Science and Pollution Research,* vol. 29, pp. 85742 - 86760, 2022.

[37] S. T. Petsch, "The Global Oxygen Cycle," in *Treatise on Geochemistry*, Amherst, Elsevier Science, 2003, pp. 515 - 555.

[38] J.-P. Jenny, P. Francus, A. Normandeau, F. Lapointe, M.-E. Perga, A. Ojala, A. Schimmelmann and B. Zolitschka, "Global spread of hypoxia in freshwater ecosystems during the last three centuries is caused by local human pressure," *Global Change Biology,* vol. 22, no. 4, pp. 1481 - 1489, 2016.

[39] C. Rönnberg and E. Bonsdorff, "Baltic Sea eutrohication: area-specific ecological consequences," *Hydrobiologia,* vol. 514, pp. 227 - 241, 2004.

[40] J. Pierre, "Chemistry of dioxygen and its activated species," in *Analysis of free radicals in biological systems*, Birkäuser Bassel, 1995.

[41] X. Huang and J. T. Groves, "Oxygen activation and radical transformations in heme proteins and metalloporphyrins," *Chemical Reviews,* vol. 118, pp. 2491 - 2553, 2018.

[42] R. Y. N. Ho, J. F. Liebeman and J. S. Valentine, "Overview of energetics and reactivity of oxygen," in *Active oxygen in chemistry*, Chapman & Hall, 1995.

[43] B. Valeur and I. Leray, "Design principles of fluorescent molecular sensors for cation recognition," *Coordination Chemsitry Reviews,* vol. 205, pp. 3 - 40, 2000.

[44] Y. Wang, L. Shen, Z. Gong, J. Pan, X. Zheng and J. Xue, "Analytical methods to analyze pesticides and herbicides," *Water Environmetal Research,* vol. 91, no. 10, pp. 1009 - 1024, 2019.

[45] M. LeDoux, "Analytical methods applied to the determination of pesticide residues in foods of animal origin. A review of the past two decades," *Journal of Chromatography A,* vol. 1218, no. 8, pp. 1021 - 1036, 2011.

[46] P. A. Souza Tette, L. Rocha Guidi, M. B. de Abreu Glória and C. Fernandes, "Pesticides in honey: A review on chromatographic analytical methods," *Talanta,* vol. 149, pp. 124 - 141, 2016.

[47] R. Paolesse, S. Nardis, D. Monti, M. Stefanelli and C. Di Natale, "Porphyrinoids for chemical sensor application," *Chemical Reviews,* vol. 117, pp. 2517 - 2583, 2017.

[48] A. Hulanicki, S. Glab and F. Ingman, "Chemical sensors definition classification," *International Union of Pure and Applied Chemistry,* vol. 63, no. 9, pp. 1247 - 1250, 1991.

[49] M. Quaranta, S. M. Borisov and I. Klimant, "Indicators for optical oxygen sensors," *Bionanalytical Reviews,* vol. 4, pp. 115 - 157, 2012.

[50] L. Basabe-Desmonts, D. N. Reinhoudt and M. Crego-Calama, "Design of fluorescent materials for chemical sensing," *Chemical Society Reviews,* vol. 36, pp. 993 - 1017, 2007.

[51] O. S. Wolfbeis, "Luminiscent sensing and imaging of oxygen: Fierce competition to the Clark electrode," *Bioessays,* vol. 37, pp. 921 - 928, 2015.

[52] M. Schäferling, "The art of fluorescence imaging with chemical sensors," *Angewandte Chemie International Edition,* vol. 51, pp. 3532 - 3554, 2012.

[53] A. Gupta and N. Kumar, "A review of mechanisms for fluorescent "turn-on" probes to detect Al(III) ions," *RSC Advances,* vol. 6, pp. 106413 - 106434, 2016.

[54] L. Min, X. Yu, M. Li, N. Liao, A. Bi, Y. Jiang, S. Liu, Z. Gong and W. Zeng, "Fuorescent probes for the detection of magnesium ion (Mg(II)): from design to application," *RSC Advances,* vol. 8, p. 12573, 2018.

[55] A. C. Sedgwick, L. Wu, H.-H. Han, S. D. Bull, X.-P. He, T. D. James, J. L. Sessler, B. Z. Tang, H. Tian and J. Yoon, "Exited-state intramolecular proton-transfer (ESIPT) based fluorescence sensors and imaging agents," *Chemical Society Reviews,* vol. 47, p. 8842, 2018.

[56] N. Boens, V. Leen and W. Dehaen, "Fluorescent indicators based on BODIPY," *Chemical Society Reviews,* vol. 41, pp. 1130 - 1172, 2012.

[57] H. S. Jung, P. Verwilst, W. Y. Kim and J. S. Kim, "Fluorescent and colorimetric sensors for the detection of humidity or water content," *Chemical Society Reviews,* vol. 45, pp. 1242 - 1256, 2016.

[58] J. Wu, W. Liu, J. Ge, H. Zhang and P. Wang, "New sensing mechanisms for design of fluorescent chemosensors emerging in recent years," *Chemical Society Reviews,* vol. 40, pp. 3483 - 3495, 2011.

[59] Y. Hong, J. W. Y. Lam and B. Z. Tang, "Aggregation-induced emission: phenomenon, mechanism and applications," *Chemical Communications,* pp. 4332 - 4353, 2009.

[60] A. Depauw, "Synthèse et étude photophysique de sondes fluorescentes pour la detection de cations alcalins en milieux aqueux," Cachan, 2014.

[61] M. Formica, V. Fusi, L. Giorgi and M. Micheloni, "New fluorescent chemosensors for metal ions in solution," *Coordination Chemistry Reviews,* vol. 256, no. 1 - 2, pp. 170 - 192, 2012.

[62] N. Kwon, Y. Hu and J. Yoon, "Fluorescent chemosensors for various analytes including reactive oxygen species, bithiol, metal ions and toxic gases," *ACS Omega,* vol. 3, pp. 13731 - 13751, 2018.

[63] D. Wu, A. C. Sedgwick, T. Gunnlaugsson, E. U. Akkaya, J. Yoon et T. D. James, «Fluorescent chemosensors: the past, present and future,» *Chemical Society Reviews,* vol. 46, p. 7105, 2017.

[64] P. Ashokkumar, V. T. Ramakrishnan and P. Ramamurthy, "Photoinduced Electron Transfer (PET) based Zn(II) fluorescent probe: transformation of turn-on sensors into ratiometric ones with dual emission in acetonitrile," *The Journal of Physical Chemistry A,* vol. 115, pp. 14292 - 14299, 2011.

[65] R. D. Hancock and A. E.-. Martell, "The chelate, cryptate and macrocyclic effects," *Comments on Inorganic Chemistry: A Journal of Critical Discussion of the Current Literature,* vol. 6, no. 5 - 6, pp. 237 - 284, 1988.

[66] Q. Zhang, R. Ma, Z. Li and Z. Liu, "A multi-response crown-ether based colorimetric/fluorescent chemosensor for higly selective detection of Al3+, Cu2+ and Mg2+," *Spectrochimica Acta Part A: Molecular and Biomolecular Spectroscopy,* vol. 228, p. 117857, 2020.

[67] K. Huang, Y. Liu, P. Zhao, L. Liang, Q. Wang and D. Qin, "A pyridyl functionalized rhodamine chemodosimeter for selective fluorescent detection of mercury ions and cell imaging," *Spectrochimica Acta Part A: Molecular and Biomolecular Spectroscopy,* vol. 282, p. 121688, 2022.

[68] S. A. Nsibande and P. B. C. Forbes, "Fluorescence detection of pesticides using quantum dot materials - A review," *Analytica Chimica Acta,* vol. 954, no. 16, pp. 9 - 22, 2016.

[69] D. Su, H. Li, X. Yan, Y. Lin and G. Lu, "Biosensors based on fluorescence carbon nanomaterials for detection of pesticides," *Trends in Analytical Chemistry,* vol. 134, p. 116126, 2021.

[70] R. Umapathi, B. Park, S. Sonwal, G. M. Rani, Y. Cho and Y. S. Huh, "Advances in optical-sensing strategies for on-site detection of pesticides in agricultural foods," *Trends in Food Science & Technology,* vol. 119, pp. 69 - 89, 2022.

[71] M. Bhattu, M. Verma and D. Kathuria, "Recent advances in the detection of organophosphate pesticides: a review," *Analytical Methods,* vol. 13, pp. 4390 - 4428, 2021.

[72] M. Rigobello-Masini, E. A. Oliveira Pereira, G. Abate and J. C. Masini, "Solid-phase extraction of glyphosate in the analysis of environmental, plant and food samples," *Chromatographia,* vol. 82, pp. 1121 - 1138, 2019.

[73] M. M. Peixoto, G. F. Bauerfeldt, M. H. Herbst, M. S. Pereira and C. O. da Silva, "Study of the stepwise deprotonation reactions of glyphosate and the corresponding pKa values in aqueous solution," *The Journal of Physical Chemistry A,* vol. 119, no. 21, pp. 5241 - 5249, 2015.

[74] M. Gui, J. Jiang, X. Wang, Y. Yan, S. Li, X. Xiao, T. Liu, T. Liu and Y. Feng, "Copper-ion-mediated glyphosate detection with N-heterocycle based polyacetylene as sensing platform," *Sensors and Actuators B: Chemical,* vol. 243, pp. 696 - 703, 2017.

[75] J. Guan, J. Yang, Y. Zhang, X. Zhang, H. Deng, J. Xu, J. Wang and M.-S. Yuan, "Employing a fluorescent and colorimetric pocolyl-functionalized rhodamine for the detection of glyphosate pesticide," *Talanta,* vol. 224, p. 121834, 2021.

[76] O. Ordeig, R. Mas, J. Gonzalo, F. J. del Campo, F. J. Muñoz and C. de Haro, "Continous detection of hypochlorous acid/hypochlorite for water quality monitoring and control," *Electroanalysis,* vol. 17, no. 18, pp. 1641 - 1648, 2005.

[77] D. Canistro, S. Melega, D. Ranieri, A. Sapone, B. Gustavino, M. Monfrinotti, M. Rizzoni and M. Paolini, "Modulation of cytochrome P450 and induction of DNA damage in Cyprinus carpio exposed in situ to surface water treated with chlorine or alternatice disinfectants in different seasons," *Mutation Research / Fundamentals and Molecular Mechanisms of Mutagenesis,* vol. 729, no. 1 - 2, pp. 81 - 89, 2012.

[78] C. Zwiener, S. D. Richardson, D. M. De Marini, T. Grummt, T. Glauner and F. H. Frimmel, "Drowning in disinfection byproducts? Assessing swimming pool water," *Environmental Science & Technology,* vol. 41, no. 2, pp. 363 - 372, 2007.

[79] Z.-G. Song, Q. Yuan, P. Lv and K. Chen, "Research progress of small molecule fluorescent probes for detecting hypochlorite," *Sensors,* vol. 21, no. 19, p. 6326, 2021.

[80] N. Kwon, Y. Chen, X. Chen, H. K. Myung and J. Yoon, "Recent progess on small molecule-based fluorescent imaging probes for hypochlorous acid (HOCl)/hypochlorite (OCl-)," *Dyes and Pigments,* vol. 200, p. 110132, 2022.

[81] C. Ma, G. Zhong, Y. Zhao, Y. Fu, P. Zhang and B. Shen, "Recent development of synthetic probes for detection of ypochlorous acid/hypochlorite," *Spectrochimic Acta Part A: Molecular and Biomolecular Spectroscopy,* vol. 240, p. 1185545, 2020.

[82] M. P. Algi, "A fluorescent hypochlorite probe built on 1,10-phenantroline scaffold and its ion recognition features," *Journal of Fluorescence,* vol. 26, no. 2, pp. 487 - 496, 2016.

[83] H. So, H. Lee, G. D. Lee, M. Kim, M. H. Lim and K.-T. Kim, "A thiourea-based fluorescent chemosensor for bioimaging hypochlorite," *Journal of Industrial and Engineering Chemistry,* vol. 89, pp. 436 - 441, 2020.

[84] J. Li, A. Gong, G. Shi and C. Chai, "A novel ratiometric flurescent probe for the selective determination of HClO based on the ESIPT mechanism and its application in real samples," *RSC Advances,* vol. 9, p. 30943, 2019.

[85] X. Zhang, F. Zhang, B. Yang and B. Liu, "A simple strategy for constructing PET fluorescent probe and its application in hypochlorite detection," *Spectrochimica Acta Part A: Molecular and Biomolecular Spectroscopy,* vol. 258, p. 119827, 2021.

[86] P. Li, Y. Sun, X. Zhang, X. Wu, R. Li, D. Cao, R. Guan, Z. Liu and L. Ma, "Photophysical properties of a coumarin amide derivative and its sensing for hypochlorite," *Journal of Photochemistry & Photobiology, A: Chemistry,* vol. 411, p. 113196, 2021.

[87] X. Xu and Y. Qian, "A novel pyridyl triphenylamine-BODIPY aldoxime: Naked-eye visible and fluorometric chemodosimeter for hypochlorite," *Spectrochimica Acta Part A: Molecular and Biomolecular Spectroscopy,* vol. 183, pp. 356 - 361, 2017.

[88] A. K. Verma and T. N. Singh, "Prediction of water quality from simple field parameters," *Environmental Earth Sciences,* vol. 69, pp. 821 - 829, 2013.

[89] P. Lehner, C. Staudinger, S. M. Borisov, J. Regensburger and I. Klimant, "Intrinsic artefacts in optical oxygen sensors - How reliable are our measurements?," *Chemistry: A European Journal,* vol. 21, pp. 3978 - 3986, 2015.

[90] H.-Y. Li, S.-N. Zhao, S.-Q. Zang and J. Li, "Functional metal-organic frameworks as effective sensors of gases and volatile compounds," *Chemical Society Reviews,* vol. 49, pp. 6364 - 6401, 2020.

[91] Y. Zhao, H. Zhang, Q. Jin, D. Jia and T. Liu, "Ratiometric optical fiber dissolved oxygen sensor based on fluorescence quenching principle," *Sensors,* vol. 22, no. 13, p. 4811, 2022.

[92] T. Burger, M. Velásquez Hernández, C. Carbonell, J. Rattenverger, H. Wiltsche, P. Falcaro, C. Slugovc and S. M. Borisov, "Luminescent porphyrinic metal-organic frameworks for oxygen sensing: correlation of nanostructure and sensitivity," *ACS Applied Nanomaterials,* vol. 6, pp. 248 - 260, 2023.

[93] K. Norvaiša, M. Kielmann and M. O. Senge, "Porphyrins as colorimetric and photometric biosensors in modern bioanalytical systems," *ChemBioChem,* vol. 21, no. 13, pp. 1793 - 1807, 2020.

[94] E. Sy and H. Kasai, "Characterization of platinum porphyrins and its interaction with oxygen by density functional theory," *e-Journal of Surface Science and Technology,* vol. 3, pp. 473 - 475, 2005.

[95] X. Wang, "Conjugated polymers for the elaboration of ohmic sensors for water monitoring," Paris, 2018.

[96] X. Wang, Q. Lin, S. Ramachandran, G. Pemboung, R. B. Pansu, I. Leray, B. Lebental and G. Zucchi, "Optical chemosensors for metal ions in aqueous medium with polyfluorene derivatives: sensitivity, selectivity and regeneration," *Sensors and Actuators B: Chemical,* vol. 286, pp. 521 - 532, 2019.

[97] N. P. E. Barry and B. Therrien, "Chapter 13 - Pyrene: The Guest of Honor," in *Organic Nanoreactors. From Molecular to Supramolecular Organic Compounds*, Academic Press, 2016, pp. 421 - 461.

[98] S. Fery-Forgues and C. Vanucci-Bacqué, "Recent trends in the design, synthesis, spectroscopic behavior and applications of benzazole-based molecules with solid-state luminescence enhancement properties," in *Aggregation-Induced Emission. Topics in Currently Chemistry Collections*, Springer, 2022, pp. 129 - 169.

[99] L. Meng, C. Fu and Q. Lu, "Advanced technology for functionalization of carbon nanotubes," *Progress in Natural Science,* vol. 19, no. 7, pp. 801 - 810, 2009.

[100] P. Petrov, F. Stassin, C. Pagnoulle and R. Jérôme, "Non-covalent funcitonalization of multi-walled carbon nanotubes by pyrene containing polymers," *Chemical Communications,* pp. 2904 - 2905, 2003.

[101] V. Georgakilas, K. Kordatos, M. Prato, D. M. Guldi, M. Holzinger and A. Hirsch, "Organic Functionalization of Carbon Nanotubes," *Journal of the American Chemical Society,* vol. 124, no. 5, pp. 760 - 761 , 2002.

[102] Y. Liu, Y.-L. Yan, J. Lei, F. Wu and H. Ju, "Functional multiwalled carbon nanotube composite with iron picket-fence porphyrin and its electrocatalytic behavior," *Electrochemistry Communications,* vol. 9, pp. 2564 - 2570, 2007.

[103] E. Maligaspe, A. S. Sandanayaka, T. Hasobe, O. Ito and F. D'Souza, "Sensitive efficiency of photoinduced electron transfer to band gaps of semiconductive single-walled carbon nanotubes with supramolecularly attached zinc porphyrin bearing pyrene glues," *Jornal of the American Chemical Society,* vol. 132, pp. 8158 - 8164, 2010.

[104] Z. Kowser, U. Rayhan, T. Akther, C. Redshaw and T. Yamato, "A brief review on novel pyrene based fluorometric and colorimetric chemosensors for the detection of Cu(II)," *Material Chemistry Frontiers,* vol. 5, p. 2173, 2021.

[105] X.-Q. Wang, Q.-H. Ling, W. Wang and L. Xu, "Pyrene-based metallocycles and metallocages: more than fluorophores," *Materials Chemistry Frontiers,* vol. 4, p. 3190, 2020.

[106] S. Claucherty and H. Sakaue, "An optical-chemical sensor using pyrene-sulfonic acid for unsteady surface pressure measurements," *Sensors and Actuators A: Physical,* vol. 317, p. 112359, 2021.

[107] K. Ayyavoo and P. Velusamy, "Pyrene based materials as fluorescenr probes in chemical and biological fields," *New Journal of Chemistry,* vol. 45, p. 10997, 2021.

[108] S. Karuppannan and J.-C. Chambron, "Supramolecular chemical sensors based on pyrene monomer-excimer dual luminescence," *Chemistry. An Asian Journal,* vol. 4, pp. 964 - 984, 2011.

[109] H. Huang, Z. Xin, L. Yuan, B.-Y. Wang and Q.-Y. Cao, "New ferrocene-pyrene dyads bearing amide/thiourea hybrid donors for anion recognition," *Inorganica Chimica Acta,* vol. 483, pp. 425 - 430, 2018.

[110] T. Gunnlaugsson, A. P. Davis, G. M. Hussey, J. Tierney and M. Glynn, "Desing, synthesis and photophysical studies of simple fluorescent anion PET sensors using charge neutral thiourea receptors," *Organic Biomolecular Chemistry,* vol. 2, pp. 1856 - 1863, 2004.

[111] X. Shang, Z. Yang, J. Fu, P. Zhao and X. Xu, "The synthesis and anion recognition property of symmetrical chemosensors involving thiourea groups: theory and experiments," *Sensors,* vol. 15, pp. 28166 - 28176, 2015.

[112] M. Lee, D. Choe, S. Park, H. Kim, S. Jeong, K.-T. Kim and C. Kim, "A novel thiosemicarbazole-based fluorescent chemosensor for hypochlorite in near-perfect aqueous solution and zebrafish," *Chemosensors,* vol. 9, p. 65, 2021.

[113] Q. Lin, Y. Huang, X. Fan, X. Zheng, X. Chen, X. Zhan and H. Zheng, "A ratiometric fluorescent probe for hypochlorous acid determination: excitation and the dual-emission wavelengths at NIR region," *Talanta,* vol. 170, pp. 496 - 501, 2017.

[114] T. C. Pham, V.-N. Nguyen, Y. Choi, D. Kim, O.-S. Jung, D. J. Lee, H. J. Kim, M. W. Lee, J. Yoon, H. M. Kim and S. Lee, "Hypochlorite-activated fluorescence emission and actibacterial activities of imidazole derivatives for biological applications," *Frontiers in Chemistry,* vol. 9, p. 713078, 2021.

[115] P. Zhang, H. Wang, D. Zhang, X. Zeng, R. Zeng, L. Xiao, H. Tao, Y. Long, P. Yi and J. Chen, "Two-photon fluorescent probe for lysosome-targetable hypochlorous acid detection in living cells," *Sensors and Actuators B: Chemical,* vol. 255, pp. 2223 - 2231, 2018.

[116] X. Zhang, Y. Zhang and Z. Zhu, "A fluorescein semicarbazide-based fluorescent probe for highly selective and rapid detection of hypochlorite in aqueous solution," *Analytical Methods,* vol. 4, p. 4334, 2012.

[117] W. Lin, C. Wu, Z. Liu, C. Lin and Y. Yen, "A new selective colorimetric and fluorescent sensor for Hg(II) and Cu(II) based on a thiourea featuring a pyrene moiety," *Talanta,* vol. 81, pp. 1209 - 1215, 2010.

[118] D. Maity and T. Govindaraju, "Highly selective visible and near-IR sensing of Cu(II) based on thiourea-salicylaldehyde coordination in aqueous media," *Chemistry, A European Journal,* vol. 17, pp. 1410 - 1414, 2011.

[119] P. Qin, C. Niu, G. Zeng, J. Zhu and L. Yue, "Determination of trace levels of Cu(II) or Hg(II) in water samples by a thiourea-based fluorescent probe," *Analytical Sciences,* vol. 24, pp. 1205 - 1208, 2008.

[120] H. So, H. Cho, H. Lee, M. C. Tran, K.-T. Kim and C. Kim, "Detection of zinc(II) and hypochlorite by a thiourea-based chemosensor via two emission channels and its applucation in vivo," *Microchemical Journal,* vol. 155, p. 104788, 2020.

[121] M. Vonlanthen, C. M. Connelly, A. Deiters, A. Linden and N. S. Finney, "Thiourea-based fluorescent chemosensor for aqueous media ion detection and cellular imaging," *The Journal of Organic Chemistry,* vol. 79, pp. 6054 - 6060, 2014.

[122] M. R. Maddani and K. R. Prabhu, "A concise synthesis of substituted thiourea derivatives in aqueous medium," *Journal of Organic Chemistry,* vol. 75, no. 7, pp. 2327 - 2332, 2010.

[123] C.-M. Chau, T.-J. Chuan and K.-M. Liu, "A higly efficient one-pot method for the synthesis of thioureas and 2-imino-4-thiazolidinones under microwave condiutions," *RSC Advances,* vol. 4, p. 1276, 2014.

[124] T. B. Nguyen, L. Ermolenko and A. Al-Mourabit, "Three-component reaction between isocyanides, aliphatic amines and elemental sulfur: preparation of thioureas under mild conditions with complete atom economy," *Synthesis,* vol. 46, no. 23, pp. 3172 - 3179, 2014.

[125] D. Maity and T. Govindaraju, "Naphtaldehyde-Urea/Thiourea conjugates as turn-on fluorescent probes for Al(III) based on restricted C=N isomerization," *European Journal of Inorganic Chemistey,* vol. 36, pp. 5479 - 5485, 2011.

[126] Y.-G. Zhang, Z.-H. Shi, L.-Z. Yang, X.-L. Tang, Y.-Q. An, Z.-H. Ju and W.-S. Liu, "A facile fluorecent probe based on coumarin derived Schiff base for Al(III) in aqueous media," *Inorganic Chemistry Communications,* vol. 39, pp. 86 - 89, 2014.

[127] J.-S. Wu, W.-M. Liu, X.-Q. Zhuang, F. Wang, P.-F. Wang, S.-L. Tao, X.-H. Zhang, S.-K. Wu and S.-T. Lee, "Fluorescence turn on of coumarin derivatives by metal cations: A new signaling mechanism based on C=N isomerization," *Organic Letters,* vol. 9, no. 1, pp. 33 - 36, 2007.

[128] P. Roy, "Recent advances in the development of fluorescent chemosensors for Al(III)," *Dalton Transactions,* vol. 50, p. 7156, 2021.

[129] P. Kaur, J. Singh, R. Singh, V. Kaur and D. Talwar, "Extending photophysical behaviour of Shiff base tripod for the speciation of iron and fabrication of INHIBIT type molecular logic gate for recognition of Zn(II) and Cd(II) cations," *Polyhedron,* vol. 125, pp. 230 - 237, 2017.

[130] N. H. Kim, J. Lee, S. Park, J. Jung and D. Kim, "A Schiff base fluorescence enhancement probe for Fe(III) and its sensing applications in cancer cells," *Sensors,* vol. 19, p. 2500, 2019.

[131] G. R. You, G. J. Park, S. A. Lee, K. Y. Ryu and C. Kim, "Chelate-type Schiff base acting as a colorimetric sensor for iron in aqueous solution," *Sensors and Actuators B: Chemical,* vol. 215, pp. 188 - 195, 2015.

[132] Y. W. Choi, G. J. Park, Y. J. Na, H. Y. Jo, S. A. Lee, G. R. You and C. Kim, "A single Schiff base molecule for recognizing multiple ions: A fluorescence sensor for Zn(II) and Al(III) and colorimetric sensor for Fe(II) and Fe(III)," *Sensors and Actuators B: Chemical,* vol. 194, pp. 343 - 352, 2014.

[133] K. B. Kim, H. Kim, E. J. Song, S. Kim, I. Noh and C. Kim, "A cap-type Schiff base acting as a fluorescence sensor for zinc(II) and a colorimetric sensor for iron(II), copper (II), and zinc (II) in aqueous media," *Dalton transactions,* vol. 42, p. 16569, 2013.

[134] W. H. Hsieh, C.-F. Wan, D.-J. Liao and A.-T. Wu, "A turn-on Schiff base fluorescent sensor for zinc ion," *Tetrahedron Letters,* vol. 53, pp. 5848 - 5851, 2012.

[135] Y. Zhou, J. Y. Jung, H. R. Jeon, Y. Kim, S.-J. Kim and J. Yoon, "A novel supermolecular tetrameric vandate-selective colorimetric and "off-on" sensor with pyrene ligand," *Organic Letters,* vol. 13, no. 10, pp. 2742 - 2745, 2011.

[136] W. Pan, X. Yang, Y. Wang, L. Wu, N. Liang and L. Zhao, "AIE-ESIPT based colorimetric and "OFF-ON" fluorescence Schiff base sensor for visual and fluorescent determination of Cu(II) in an aqueous media," *Journal of Photochemistry & Photobiology, A: Chemistry,* vol. 420, p. 113506, 2021.

[137] R. W. Layer, «The chemistry of imines,» *Chemical Reviews,* vol. 63, nº 5, pp. 489 - 510, 1963.

[138] W. Al Zoubi, A. A. A. Al-Hamdani, S. D. Ahmed, H. M. Basheer, R. S. A. Al-Luhaibi, A. Dib and Y. G. Ko, "Synthesis, characterization, and antioxidant activities of imine compounds," *Journal of Physical Organic Chemistry,* vol. 32, no. 3, p. e3916, 2019.

[139] S. Morales, F. G. Guijarro, J. L. García Ruano and M. B. Cid, "A general aminocatalytic method for the synthesis of aldimines," *Journal of the American Chemical Society,* vol. 136, no. 3, pp. 1082 - 1089, 2014.

[140] B. E. Love, T. S. Boston, B. T. Nguyen and J. R. Rorer, "A comparison of imine forming methodologies," *Organic preparation and procedures International: The New Journal for Organic Synthesis,* vol. 31, no. 4, pp. 399 - 405, 1999.

[141] E. A. Katayev, Y. A. Ustynyuk and J. L. Sessler, "Receptors for tetrahedral oxyanions," *Coordination Chemistey Reviews,* vol. 250, pp. 3004 - 3037, 2006.

[142] C. Spangler, M. Schaeferling and O. S. Wolfbeis, "Fluorescent probes for microdetermination of inorganic phosphates and biophosphates," *Microchimica Acta,* vol. 161, pp. 1 - 39, 2008.

[143] W. Li, X. Gong, X. Fan, S. Yin, D. Su, X. Zhang and L. Yuan, "Recent advances in molecular fluorescent probes for organic phosphate biomolecules recognition," *Chinese Chemical Letters,* vol. 30, pp. 1775 - 1790, 2019.

[144] J. L. Sessler, J. M. Davis, V. Král, T. Kimbrough and V. Lynch, "Water soluble sapphyrins: potential fluorescent phosphate anion sensors," *Organic Biomolecular Chemistry,* pp. 4113 - 4123, 2003.

[145] J. Pouessel, S. Abada, N. Le Bris, M. Elhabiri, L. J. Charbonnière and R. Tripier, "A new bis-tetraamine ligand with a chromophoric 4-(9-anthracenyl)-2,6-

dimethylpyridyl linker for glyphosate and ATP sensing," *Dalton Transactions,* vol. 42, p. 4859, 2013.

[146] D. Ma, Q. Cai and H. Zhang, "Mild method for Ullmann Coupling reaction of amines and aryl halides," *Organic Letters,* vol. 5, no. 14, pp. 2453 - 2455, 2003.

[147] N. Miyaura and A. Suzuki, "Palladium-catalyzed cross-coupling reactions of organoboron compounds," *Chemical Reviews,* vol. 95, no. 7, pp. 2457 - 2483, 1995.

[148] J. K. Stille, "The palladium-catalyzed cross-coupling reactions of organotin reagents with organic electrophiles [New synthetic methods]," *Angewandte Chemie International Edition,* vol. 25, no. 6, pp. 508 - 524, 1986.

[149] K. Sonogashira, "Development of Pd-Cu catalyzed cross-couplingof terminal acetylenes with sp2 carbon halides," *Journal of Organometallic Chemistry,* vol. 653 , no. 1 - 2, pp. 46 - 49, 2002.

[150] M. D'Alterio, È. Casals-Cruañas, N. V. Tzouras, G. Talarico, S. P. Nolan and A. Poater, "Mechanistic aspects of the palladium-catalyzed Suzuki-Miyaura cross-coupling reaction," *Chemistry. A European Journal,* vol. 27, no. 54, pp. 13481 - 13493, 2021.

[151] D. Blakemore, "Suzuki-Miyaura Coupling," in *Synthetic Methods in Drug Discovery*, Royal Society of Chemistry, 2016, p. 455.

[152] A. J. J. Lennox and G. C. Lloyd-Jones, "The slow-release strategy in Suzuki Miyaura coupling," *Israel Journal of Chemistry,* vol. 50, no. 5 - 6, pp. 664 - 674, 2010.

[153] X. Gao, J. Liu, X. Zuo, X. Feng and Y. Gao, "Recent advances in synthesis of benzothiazole compounds related to green chemistry," *Molecules,* vol. 25, p. 1675, 2020.

[154] Q. Fang, Y. Li, Y. Wang, F. Yao, S. Wang, Y. Qian, G. Yang and W. Huang, "Feasible organic films using noninterfering emitters for sensitive and spacial high-temperature sensing," *Journal of Materials Chemistry C,* vol. 6, pp. 8115 - 8121, 2018.

[155] J. A. Maertens, "History of the development of azole derivatives," *Clinical Microbiology and Infection,* vol. 10, no. 1, pp. 1 - 10, 2004.

[156] Z. Benzekri, H. Serrar, S. Sibous, S. Boukhris, A. Ouasri, A. Rhandour and A. Souizi, "Hybrid crystal NH3(CH2)4NH3SiF6 as an efficient catalyst for the synthesis of benzoxazoles, benzimidazoles and benzothiazoles under solvent-

free conditions," *Green Chemistry Letters and Reviews,* vol. 9, no. 4, pp. 223 - 228, 2016.

[157] Y. Yang, Y. Ding, W. Shi, F. Ma and Y. Li, "The effects of amino group meta- and para-substitution on ESIPT mechanism of amino 2-(2'-hydroxyphenyl) benzazole derivatives," *Journal of Luminescence,* vol. 218, p. 116836, 2020.

[158] Y. Zhang, C. Shang, Y. Cao, M. Ma and C. Sun, "Insights into the photophysical properties of 2-(2'-hydroxyphenyl) benzazoles derivatives: Application of ESIPT mechanism on UV absorbers," *Spectrochimica Acta Part A: Molecular and Biomolecular Spectroscopy,* vol. 280, p. 121559, 2020.

[159] N. Alarcos, M. Gutierrez, M. Liras, F. Sánchez and A. Douhal, "An abormally slow proton transfer reaction in a simple HBO derivative due to ultra fast intramolecular-charge transfer events," *Physical Chemistry Chemistry Physics,* vol. 17, pp. 16257 - 16269, 2015.

[160] V. S. Padalkar and S. Seki, "Excited-state intramolecular proton-transfer (ESIPT)-inspired solid state emitters," *Chemical Society Reviews,* vol. 45, pp. 169 - 202, 2016.

[161] V. S. Padalkar, A. Tathe, V. D. Gupta, V. S. Patil, K. Phatangare and N. Sekar, "Synthesis and photo-physical characteristics of ESIPT inspired 2-substituted benzimidazole, benzoxazole and benzothiazole fluorescent derivatives," *Journal of Fluorescence,* vol. 22, pp. 311 - 322, 2012.

[162] M. H. Lee, J. S. Kim and J. L. Sessler, "Small molecule-based ratiometric fluorescence probes for cations, anions and biomolecules," *Chemical Society Reviews,* vol. 44, pp. 4185 - 4191, 2015.

[163] A. Douhal, F. Amat-Guerri, M. P. Lillo and A. U. Acuña, "Proton transfer spectroscopy of 2-(2'-hydroxyphenyl)imidazole and 2-(2'-hydroxyphenyl)benzimidazole dyes," *Journal of Photochemistry and Photobiology A: Chemistry,* vol. 78, no. 2, pp. 127 - 138, 1994.

[164] G. R. Suman, S. G. Bubbly and S. B. Gudennavar, "Benzimidazole and benzothiazole fluorophores with large Stokes shift and intense sky-blue emission in aggregation as Al(III) and Ob(II) sensors," *Journal of Luminescense,* vol. 215, p. 116688, 2019.

[165] E. Horak, P. Kassal and I. Murkovic Steinberg, "Benzimidazole as a structural unit in fluorescent chemical sensors: the hidden properties of a multifunctional heterocyclic scaffold," *Supramolecular Chemistry,* 2017.

[166] N. Perin, M. Hranjec, G. Pavlović and G. Karminski-Zamola, "Novel aminated benzimidazo[1,2-α]quinolines as potential fluorescent probes for DNA detection: Microwave-assisted synthesis, spectroscopic characterization and crystal-structure determination," *Dyes and Pigments,* vol. 91, pp. 79 - 88, 2011.

[167] A. Bhattacharyya, S. Kumar Mandal and N. Guchhait, "Imine-amine tautomerism vs. Keto-enol tautomerisation: Acceptor basicity dominates over acceptor electronegativity in ESIPT process through six-member intramolecular H-bonded network," *Journal of Physical Chemistry A,* vol. 123, no. 47, pp. 10246 - 10253, 2019.

[168] B. Guo, H. Nie, W. Yang, Y. Tian, J. Jing and X. Zhang, "A highly sensitive and rapidly responding fluorescent probe with a large Stokes shift for imaging intracellular hypochlorite," *Sensors and Actuators B: Chemical,* vol. 236, pp. 459 - 465, 2016.

[169] S. I. Reja, V. Bhalla, A. Sharma, G. Kaur and M. Kumar, "A highly sensitive fluorescent probe for hypochlorite and its endogenous imaging in living cells," *Chemical Communications,* vol. 50, p. 11911, 2014.

[170] W. Lin, L. Long, B. Chen and W. Tan, "A ratiometric fluorescent probe for hypochlorite based on a deoximation reaction," *Journal of European Chemistry,* vol. 15, pp. 2305 - 2309, 2009.

[171] C. Wu, X. Lin and Q. Wang, "Determination of hypochlorite via fluorescence change from blue to green based on 4-(1 H-imidazo [4,5-f] [1,10]-phenantrolin-2-yl) benzaldehyde oxime," *Journal of Fluorescence,* vol. 31, pp. 1125 - 1132, 2021.

[172] M. A. Tzani, C. Gabriel and I. N. Lykakis, "Selective synthesis of benzimidazoles from o-phenylendiamine and aldehydes promoted by supported nanoparticles," *Nanomaterials,* vol. 10, no. 12, p. 2405, 2020.

[173] J. C. Duff and E. J. Bills, "Reactions between hexamethylenetetramine and phenolic compounds. Part I. A new method for the preparation of 3- and 5-aldehydosalicylic acids," *Journal of the Chemical Society,* pp. 1987 - 1988, 1932.

[174] H. Zhao, C. P. Vandenbossche, S. G. Koenig, S. P. Singh and R. P. Bakale, "An efficient synthesis of enamides from ketones," *Organic Letters,* vol. 10, no. 3, pp. 505 - 507, 2008.

[175] Y.-q. Jiang, S.-h. Jia, X.-y. Li, Y.-m. Sun, W. Li, W.-w. Zhang and G.-q. Xu, "An efficient NaHSO3- promoted protocol for chemoselective synthesis of 2-substituted benzimidazoles in water," *Chemical Papers,* vol. 72, pp. 1265 - 1276, 2018.

[176] M. M. Henary and C. J. Fahrni, "Excited State Intramolecular Proton Transfer and metal ion complexation of 2-(2'-hydroxyphenyl)benzazoles in aqueous solution," *Journal of Physical Chemistry,* vol. 106, pp. 5210 - 5220, 2002.

[177] Y. Shang, S. Zheng, M. Tsakama, M. Wang and W. Chen, "A water-soluble, small molecular fluorescence probe based on 2-(2'-hydroxyphenyl) benzoxazole for Zn(II) in plants," *Tetrahedron Letters,* vol. 59, no. 45, pp. 4003 - 4007, 2018.

[178] L. He, B. Dong, Y. Liu and W. Lin, "Fluorescent chemosensors manupulated by dual/triple interplaying sensing mechanisms," *Chemical Society Reviews,* vol. 45, pp. 6449 - 6461, 2016.

[179] X.-l. Yue, Z.-q. Wang, C.-r. Li and Z.-y. Yang, "Naphtalene-derived Al3+ selective fluorescent chemosensor based on PET and ESIPT in aqueous solution," *Tetrahedron Letters,* vol. 58, no. 48, pp. 4532 - 4537, 2017.

[180] A. Jana, B. Das, S. K. Mandal, S. Mabhai, A. R. Khuda-Bukhsh and S. Dey, "Deciphering the CHEF-PET-ESIPT liason mechanism in a Zn2+ chemosensor and its application in cell imaging study," *New Journal of Chemistry,* vol. 2016, pp. 5976 - 5984, 2016.

[181] R. V. Kumar, "Synthetic strategies towards benzoxazole ring systems," *Asian Journal of Chemistry,* vol. 16, pp. 1241 - 1260, 2004.

[182] A. V. Panfilov, Y. D. Markovich, I. P. Ipashev, A. A. Zhirov, A. F. Eleev, V. K. Kurochin, A. T. Kirsanov and G. V. Nazarov, "Sodium borohydride in reductive amination reactions," *Pharmaceutical Chemistry Journal,* vol. 34, no. 2, pp. 76 - 78, 2000.

[183] J. Chang, K. Zhao and S. Pan, "Synthesis of 2-arylbenzoxazoles via DDQ promoted oxidative cyclization of phenolic Schiff bases - a solution-phase strategy for library synthesis," *Tetrahedron Letters,* vol. 43, pp. 951 - 954, 2002.

[184] S. Das, H. K. Indurthi, P. Asati, P. Saha and D. K. Sharma, "Benzothiazole based fluorescent probes for the detection of biomolecules, physiological conditions, and ions responsible for deseases," *Dyes and Pigments,* vol. 199, p. 110074, 202.

[185] M. Duran and M. Ç. Canbaz, "pKa determination of newly synthesized N-(benzothiazole-2-yl)-2-(4,5-dimethyl-1-(phenylamino)-1H-imidazol-2-ylthio)acetamide derivatives," *Industrial & Engineering Chemistry Research,* vol. 52, no. 25, pp. 8355 - 8360, 2013.

[186] N.-N. Li, C.-F. Bi, C.-G. Xu, C.-B. Fan, W.-S. Gao, Z.-A. Zong, S.-S. Zuo, C.-F. Niu and Y.-H. Fan, "A bifunctional probe based on napthalene derivative for absorbance-ratiometric detection of Ag+ and fluorescence "turn-on!" sensing of

Zn2+ and its practical application in water samples, walnut and living cells," *Journal of Photochemistry & Photobiology A: Chemistry,* vol. 390, p. 112299, 2020.

[187] H. López-Ruiz, H. Briseño-Ortega, S. Rojas-Lima, R. Santillan and N. Farfán, "Phenylboronic acid catalyzed-cyanide promoted, one pot synthesis of 2-(2-hydroxyphenyl)benzoxazole derivatives," *Tetrahedron Letters,* vol. 52, pp. 4308 - 4312, 2011.

[188] H. Reyes, H. I. Beltran and E. Rivera-Becerril, "One pot synthesis of 2-phenylbenzoxazoles by potassium cyanide assisted reaction of o-aminophenols and benzaldehydes," *Tetrahedron Letters,* vol. 52, no. 2, pp. 308 - 310, 2011.

[189] X.-y. Sun, T. Liu, J. Sun and X.-j. Wang, "Synthesis and applciation of coumarin fluorescence probes," *RSC Advances,* vol. 10, p. 10826, 2020.

[190] I. Cazin, E. Rossegger, G. Guedes de la Cruz, T. Griesser and S. Schlögl, "Recent advances in functional polymers containing coumarin chromophores," *Polymers,* vol. 13, no. 1, p. 56, 2021.

[191] Y. Jung, J. Jung, Y. Huh and D. Kim, "Benzo[g]coumarin-based fluorescent probes for bioimaging applications," *Journal of Analytical Methods in Chemistry,* vol. 2018, 2018.

[192] J. Breidenbach, U. Bartz and M. Gütschow, "Coumarin as a structural component of substrates and probes for serine and cysteine proteases," *Biochimica et Biophysica Acta (BBA) - Proteins and Proteomics,* vol. 1868, no. 9, p. 140445, 2020.

[193] S. R. Trenor, A. R. Shultz, B. J. Love and T. E. Long, "Coumarins in polymers: from light harvesting to photo-cross-linkable tissue scaffolds," *Chemical Reviews,* vol. 104, pp. 3059 - 3077, 2004.

[194] D. Cao, Z. Liu, P. Verwilst, S. Koo, P. Jangili, J. Seung Kim and W. Lin, "Coumarin-based small-molecule fluorescent chemosensors," *Chemical Reviews,* vol. 119, no. 18, pp. 10403 - 10519, 2019.

[195] O. García-Beltrán, B. K. Cassels, N. Mena, M. T. Nuñez, O. Yañez and J. Caballero, "A coumarinylaldoxime as a specific sensor for Cu2+ and its biological application," *Tetrahedron Letters,* vol. 55, pp. 873 -876, 2014.

[196] M. Lončarić, D. Gašo-Sokač, S. Jokić and M. Molnar, "Recent advances in synthesos of coumarin derivatives from different starting materials," *Biomolecules,* vol. 10, no. 1, p. 151, 2020.

[197] A. Vilsmeier and A. Haack, "Über die Einwirkung von Halogenphosphor auf Alky-formanilide. Eine neue Methode zur Darstellung sekundärer und tertiärer p-Alkylamino-benzaldehyde," *Berichte der deutschen chemischen Gesellschaft (A and B Series),* vol. 60, no. 1, pp. 119 - 122, 1927.

[198] H. S. Jung, K. C. Ko, J. H. Lee, S. H. Kim, S. Bhuniya, Y. J. Lee, Y. Kim, S. J. Kim and J. S. Kim, "Rationally designed fluorescence turn-ON sensors: a new design strategy based on orbital control," *Inorganic Chemistry,* vol. 49, pp. 8552 - 8557, 2010.

[199] M. d. G. Vicente and K. M. Smith, "Synthesis anf functionalizations of porphyrin macrocycles," *Current Organic Synthesis,* vol. 11, no. 1, pp. 3 - 28, 2014.

[200] M. Biesaga, K. Pyrzynska and M. Trojanowicz, "Porphyrins in analytical chemistry. A review," *Talanta,* vol. 51, pp. 209 - 224, 2000.

[201] S. A. Krasnikov, N. N. Sergeeva, M. M. Brzhezinskaya, A. B. Preobrajenski, Y. N. Sergeeva, N. A. Vinogradov, R. Pütner, A. A. Cafolla, M. O. Senge and A. S. Vinogradov, "An X-ray absorption and photoemission study of the electronic structure of Ni porphyrins and Ni N-confused porphyrin," *Journal of Physics: Condensed Matter,* vol. 20, pp. 1 - 6, 2008.

[202] A. R. Ramuglia, V. Budhija, K. H. Ly, M. Marquardt, M. Schwalbe and I. M. Weidinger, "An iron porphyrin complex with pendantpyridine substituents facilitates electrocatalytic CO2 reduction via second coordination sphere effects," *ChemCatChem. The European Society Journal for Catalysis ,* vol. 13, no. 18, pp. 3934 - 3944, 2021.

[203] Y. Amao and I. Okura, "Optical oxygen sensor devices using metalloporphyrins," *Journal of Porphyrins and Phthalocyanines,* vol. 13, pp. 1111 - 1122, 2009.

[204] M. V. Volosnykh, S. M. Borisov, M. A. Konovalov, A. A. Sinelshchikova, Y. G. Gorbunova, A. Y. Tsivadze, M. Meyer and A. Bessmertnykh-Lemeune, "Platinum(II) and palladium(II) compelxes with electron-deficient meso-diethoxyphorylporphyrins: synthesis, structure and tuning of photphysical properties by varying peripheral substituents," *Dalton Transactions,* vol. 48, pp. 8882 - 8898, 2019.

[205] Y. Wang, F. Qin, H. Zhang, M. Kou and Z. Zhang, "A high-performance optical trace oxygen sensor based on the room-temperature phosphorescence from a palladium(II) octaethylporphyrin," *Measurement,* vol. 206, p. 112275, 2023.

[206] W. Wu, W. Wu, S. Ji, H. Guo, X. Wang and J. Zhao, "The synthesis of 5,10,15,20-tetraarylporphyrins and their platinum(II) complexes as luminescent oxygen sensing materials," *Dyes and pigments,* vol. 89, pp. 199 - 211, 2011.

[207] C.-S. Chu, T.-W. Sung and Y.-L. Lo, "Enhanced optical oxygen sensing property based on Pt(II) complex and metal-coated silica nanoparticles embedded in sol-gel matrix," *Sensors and Actuators B: Chemical,* vol. 185, pp. 287 - 292, 2013.

[208] C. Huo, H. Zhang, H. Zhang, H. Zhang, B. Yang, P. Zhang and Y. Wang, "Synthesis and assembly with mesoporous silica MCM-48 of platinum(II) porphyrin complexes bearing carbazyl groups: Spectroscopic and oxygen sensing properties," *Inorganic Chemistry,* vol. 45, pp. 4735 - 4742, 1006.

[209] E. Roussakis, Z. Li, N. H. Nowell, A. J. Nichols and C. L. Evans, "Bright, "clickable" porphyrins for the visualization of oxygenation under ambient light," *Angewandte Chemie International Edition,* vol. 54, no. 49, pp. 14728 - 14731, 2015.

[210] Y. Mao, Z. Mei, J. Wen, G. Li, Y. Tian, B. Zhou and Y. Tian, "Honeycomb structured porous films from a platinum porphyrin-grafted poly(styrene-co-4-vinylpyridene) copolimer as an optical sensor," *Sensors and Actuators B: Chemical,* vol. 257, pp. 944 - 953, 2018.

[211] Y. Zhao, T. Ye, H. Chen, D. Huang, T. Zhou, C. He and X. Chen, "A dissolved oxygen sensor based on composite fluorinated xerogel doped with platinum porphyrin dye," *Luminiscence,* vol. 26, pp. 29 - 34, 2011.

[212] Y. Tian, B. R. Shumway and D. R. Meldrum, "A new crosslinkable oxygen sensor covalently bonded into Poly(2-hydroxyethyl methacrylate)-CO-Polyacrylamide thin film for dissolved oxygen sensing," *Chemistry of Materials,* vol. 22, no. 6, pp. 2069 - 2078, 2010.

[213] K. Zhang, H. Zhang, Y. Wang, Y. Tian, J. Zhao and Y. Li, "High sensitivity and accuracy dissolved oxygen (DO) detection by using PtOEP/poly(MMA-co-TFEMA) sensing film," *Spectrochimica Acta Part A: Molecular and Biomolecular Spectroscopy,* vol. 170, pp. 242 - 246, 2017.

[214] A. S. Holmes-Smith, A. Hamill, M. Campbell and M. Uttamlal, "Electropolymerised platinum porphyrin polymers for dissolved oxygen sensing," *Analyst,* vol. 124, pp. 1463 - 1466, 1999.

[215] M. O. Senge, "Stirring the porphyrin alphabet soup - functionalization reactions for porphyrins," *Chemical Communications,* vol. 47, pp. 1943 - 1960, 2011.

[216] A. D. Adler, F. R. Longo, J. D. Finarelli, J. Goldmacher, J. Assour and L. Korsakoff, "A simplified synthesis for meso-tetraphenylporphyrin," *Journal of Organic Chemistry,* vol. 32, no. 2, p. 476, 1967.

[217] J. S. Lindsey, I. C. Schreiman, H. C. Hsu, P. C. Kearney and A. M. Marguerettaz, "Rothemund and Adler-Longo reactions revisited: synthesis of tetraphenyl porphyrins under equilibrium conditions," *Journal of Organic Chemistry,* vol. 52, pp. 827 - 836, 1987.

[218] R. Frlan and D. Kikelj, "Recent progress in diaryl ether synthesis," *Synthesis,* vol. 14, pp. 2271 - 2285, 2006.

[219] G. Mann, C. Incarvito, A. L. Rheingold and J. F. Hartwig, "Palladium-catalyzed C-O coupling involving unactivated aryl halides. Sterically induced reductive elimination to form the C-O bond in diaryl ethers," *Journal of the American Chemical Society,* vol. 121, pp. 3224 - 3225, 1999.

[220] K. E. Torraca, S.-I. Kuwabe and S. L. Buchwald, "A high yield, general method for the catalytic formation of oxygen heterocycles," *Journal of the American Chemical Society,* vol. 122, pp. 12907 - 12908, 2000.

[221] E. Sperotto, G. P. M. van Klink, G. van Koten and J. G. de Vries, "The mechanism of the modified Ullmann reaction," *Dalton Transactions,* vol. 39, pp. 10338 - 10351, 2010.

[222] Z. Chen, Y. Jiang, L. Zhang, Y. Guo and D. Ma, "Oxalic diamides and tert-butoxide: two types of ligands enabling practical acces to alkyl aryl ethers via Cu-catalyzed coupling reaction," *Journal of the American Chemical Society,* vol. 141, pp. 3541 - 3549, 2019.

[223] J. Niu, P. Guo, J. Kang, Z. Li, J. Xu and S. Hu, "Copper(I)-catalyzed aryl bromides to form intermolecular and intramolecular carbon-oxygen bonds," *Journal of Organic Chemistry,* vol. 74, pp. 5075 - 5078, 2009.

[224] Y. Guo, X.-M. Fan, M. Nie, H.-W. Liu, D.-H. Liao, X.-D. Pan and Y.-F. Ji, "Practical ligand-free copper catalyzed short-chain alkoxylation of unactivated aryl bromides," *European Journal of Organic Chemistry,* pp. 4744 - 4755, 2015.

[225] J. Huang, Y. Chen, J. Chan, M. L. Ronk, R. D. Laarsen and M. M. Faul, "An efficient copper-catalyzed etherification of aryl halides," *Synlett,* vol. 10, pp. 1419 - 1422, 2011.

[226] H. Zhang, D. Ma and W. Cao, "N,N-dimethylglycine-promoted Ullmann-type coupling reactions of aryl iodides with aliphatic alcohols," *Synlett,* vol. 2, pp. 243 - 246, 2007.

[227] J. D'Angelo and M. B. Smith, "Chapter 8 - Common Fundamental Reactions in Organic Chemistry," in *Hybrid Retrosynthesis. Organic Synthesis using Reaxys and Scifinder*, Elsevier, 2015, pp. 77 - 149.

[228] G. Zhang, S. Yang, X. Zhang, Q. Lin, D. K. Das, J. Liu and X. Fang, "Dynamic kinetic resolution enabled by intramolecular benzoin reaction: synthetic applications and mechanistic insight," *Journal of the American Chemical Society,* vol. 138, no. 25, pp. 7932 - 7938, 2016.

[229] A. D. Adler, F. R. Longo, F. Kampas and J. Kim, "On the preparation of metalloporphyrins," *Journal of Inorganic and Nuclear Chemistry,* vol. 32, no. 7, pp. 2443 - 2445, 1970.

[230] R. C. Kwong, S. Sibley, T. Dubovoy, M. Baldo, S. R. Forrest and M. E. Thompson, "Efficient, saturated red organic light emitting devices based on phosphorescence platinum(II) prophyrins," *Chemistry of Materials,* vol. 11, pp. 3709 - 3713, 1999.

[231] C. O. Paul-Roth, S. Drouet, A. Merhi, J. A. G. Williams, L. F. Gildea, C. Pearson and M. C. Petty, "Synthesis of platinum complexes of fluorenyl-substituted porphyrins used as phosphorescent dyes for solution-processed organic light-emitting devices," *Tetrahedron,* vol. 69, pp. 9625 - 9632, 2013.

[232] K. Rurack, "Fluorescence Quantum Yields: Methods of Determination and Standards," in *Standardization and Quality Assurance in Fluorescence Measurements*, Heidelberg, Springer, 2008, pp. 101 - 145.

[233] International Union of Pure and Applied Chemistry, «Nomenclature, symbols, units and their usage in spectrochemical analysis - II. data interpretation and analytical chemistry division,» *Spectrochimica Acta Part B: Atomic Spectroscopy,* vol. 33, nº 6, pp. 241 - 245, 1978.

[234] D. Brynn Hibbert and P. Thodarson, "The death of the Job Plot, transparency, open science and online tools, uncertainty estimation methods and other developments in supramolecular chemistry data analysis," *Chemical Communications,* vol. 52, p. 12792, 2016.

[235] F. Ulatowski, K. Dąbrowa, T. Bałakier and J. Jurczak, "Recognizing the limited applicability of Job Plots in studying host-guest interactions in supramolecular chemistry," *Journal of Organic Chemistry,* vol. 81, no. 5, pp. 1746 - 1756, 2016.

[236] P. Thordarson, "Determining association constants from titration experiments in supramolecular chemistry," *Chemical Society Reviews,* vol. 40, pp. 1305 - 1323, 2011.

[237] R. S. Becker, I. S. Singh and E. Jackson, "Comprehensive spectroscopic investigation of polynuclear aromatic hydrocarbons. I. Absorption spectra and state assignments for the tetracyclic hydrocarbons and their alkylsubstituted derivatives," *The Journal of Chemical Physics,* vol. 38, p. 2144, 1963.

[238] P.-F. Hsu and Y. Chen, "Synthesis of a pyrene-derived Schiff base and its selective fluorescent enhancement by zinc and aluminum ions," *International Journal of Organic Chemistry,* vol. 8, pp. 207 - 228, 2018.

[239] H.-T. Tsai, Y. R. Bhorge, A. J. Pape, S. N. Janaki and Y.-P. Yen, "A selective colorimetric and fluorescent chemodosimeter for Fe(III) ion based on hydrolisis of Schiff base," *Journal of the Chinese Chemical Society,* vol. 62, pp. 316 - 320, 2015.

[240] B. R. Jali and J. B. Baruah, "Recent progress in Schiff bases in detection of fluoride ions," *Dyes and Pigments,* vol. 195, p. 109575, 2021.

[241] L. Zang, D. Wei, S. Wang and S. Jiang, "A phenolic Schiff base for highly selective sensing of fluoride and cyanide via different channels," *Tetrahedron,* vol. 68, no. 2, pp. 636 - 641, 2012.

[242] A. Ramnathan, K. Sivakumar and K. Subramanian, "Simmetrically substituted thiourea derivatives," *Acta Crystallographica Section C,* vol. 51, pp. 2446 - 2450, 1995.

[243] H. Itagaki, "Fluorescence Spectroscopy," in *Experimental Methods in Polymer Science*, Academic Press, 2000, pp. 155 - 260.

[244] S. Paul, A. R. Choudhury and N. Dey, "Dual-mode multiple ion sensing via analyte-specific modulation of keto-enol tautomerization of an ESIPT active pyrene derivative: experimental findings and computational rationalization," *ACS Omega,* vol. 8, pp. 6349 - 6360, 2023.

[245] O. K. Abou-Zied, "Spectroscopy of hydroxyphenyl benzazoles in solution and human serum albumin: detecting flexibility, specificity and high affinity to the warfarin drug binding site," *RSC Advances,* vol. 3, p. 8747, 2013.

[246] P. Majumdar and J. Zhao, "2-(2-hydroxyphenyl)-benzothiazole (HBT)-rhodamine dyad: Acid-switchable absorption and fluorescence excited-state intramolecular proton transfer (ESIPT)," *The Journal of Physical Chemistry: B,* vol. 119, no. 6, pp. 2384 - 2394, 2015.

[247] Y.-P. Tong, S.-L. Zheng and X.-M. Chen, "Structures, photoluminescence and Theorettcal studies of two Zn(II) complexes with substituted 2-(2-

hydroxyphenyl)benzimidazoles," *European Journal of Inorganic Chemistry,* pp. 3734 - 3741, 2005.

[248] H. Auweter, H. Haberkorn, W. Heckmann, D. Horn, E. Lüddecke, J. Rieger and H. Weiss, "Supramolecular structure of precipitated nanosize β-carotene particles," *Angewandte Chemie International Edition,* vol. 38, no. 15, pp. 2188 - 2191, 1999.

[249] A. Bhattacharyya, S. C. Makhal and N. Guchhait, "Simple chloro substituted HBT derivative portraying coupling of AIE and ESIPT phenomenon: ratiometric detection of S(2-) and CN(-) in 100% aqueous medium," *Journal of Photochemistry and Photibiology A: Chemistry,* vol. 388, p. 112177, 2020.

[250] A. Helal, N. Thi Thu Thao, S. W. Lee and H.-S. Kim, "Thiazole-based chemosensror II: synthesis and fluorescence sensing of fluoride ions based on inhibition of ESIPT," *Journal of Inclusion Phenomena and Macrocyclic Chemistry,* vol. 66, pp. 87 - 94, 2010.

[251] Q. Huang, Q. Guo, J. Lan and J. You, "Tuning the dual emission of keto/enol forms of excited-state intramolecular proton transfer (ESIPT) emitters via intramolecular charge transfer (ICT)," *Dyes and Pigments,* vol. 193, p. 109497, 2021.

[252] N. Mehio, M. A. Lashely, J. W. Nugent, L. Tucker, B. Correia, C.-L. Do-thanh, S. Dai, R. D. Hancock and V. S. Bryantsev, "Acidity of the amidoxime functional group in aqueous solution: A combined experimental and computational study," *Journal of Physical Chemistry B,* vol. 119, no. 8, pp. 3567 - 3576, 2015.

[253] V. S. Ríos, M. C. Ríos Rodríguez, M. Mosquera and F. Rodríguez-Prieto, "Excited-state intramolecular proton transfer in 2-(3'-hydroxy-2'-pyridyl)benzoxazole. Evidence of coupled proton and charge transfer in the excited state of some o-hydroxyarylbenzazoles," *Journal of Physical Chemistry A,* vol. 111, no. 10, pp. 1814 - 1826, 2007.

[254] J. R. Lakowicz, Principles of Fluorescence Spectroscopy, New York: Springer, 2007.

[255] T. Schwarze, J. Riemer, S. Eidner and H.-J. Holdt, "A higly K+ selective two-photon fluorescent probe," *Chemistry. A European Journal,* vol. 21, no. 32, pp. 11306 - 11310, 2015.

[256] T. López Arbeloa, F. López Arbeloa, M. J. Tapia and I. López Arbeloa, "Hydrogen-bonding effect on the photophysical propertiesof 7-aminocoumarin derivatives," *Journal of Physical Chemistry,* vol. 97, pp. 4704 - 4707, 1993.

[257] S. Sharma J. and N. Sekar, "Deep-red/NIR emitting coumarin derivatives - Synthesis, photophysical properties, and biological applications," *Dyes and Pigments,* vol. 202, no. 2022, p. 110306, 2022.

[258] C. Hu, J. Li and L. Yan, "A fluorescent probe for hypochlorite with colorimetric and fluorometric characteristics and imaging in living cells," *Analytical Biochemistry,* vol. 566, pp. 32 - 36, 2019.

[259] A. B. Ormond and H. S. Freeman, "Effects of substituents on the photophysical properties of simmetrical porphyrins," *Dyes and Pigments,* vol. 96, no. 2, pp. 440 - 448, 2013.

[260] E.-J. Sun, Z.-Y. Sun, M. Yuan, D. Wang and T.-S. Shi, "The synthesis and properties of meso-tetra(4-alkylamidophenyl)porphyrin liquid crystals and their Zn complexes," *Dyes and Pigments,* vol. 81, pp. 124 - 130, 2009.

[261] M. Uttamlal and A. S. Holmes-Smith, "The excitation wavelength dependent fluorescence of porphyrins," *Chemical Physics Letters,* vol. 454, pp. 223 - 228, 2008.

[262] M. Gouterman, "Spectra of porphyrins," *Journal of Molecular Spectroscopy,* vol. 6, pp. 138 - 163, 1961.

[263] G. Calogero, A. Bartolotta, G. Di Marco, A. Di Carlo and F. Bonaccorso, "Vegetable-based dye-sensitized solar cells," *Chemical Society Reviews,* vol. 44, pp. 3244 - 3294, 2015.

[264] T. Hashimoto, Y.-K. Choe, H. Nakano and K. Hirao, "Theoretical study of the Q and B bands of free-base, magnesium and zinc porphyrins, and their derivatives," *Journal of Physical Chemistry,* vol. 103, pp. 1894 - 1904, 1999.

[265] D. B. Papkovsky and T. C. O'Riordan, "Emerging applications of phosphorescence metalloporphyrins," *Journal of Fluorescence,* vol. 15, no. 4, pp. 569 - 584, 2005.

[266] S. M. A. Pinto, Â. C. B. Neves, M. J. F. Calvete, A. R. Abreu, M. T. S. Rosado, T. Costa, H. Burrows and M. M. Pereira, "Metalloporphyrin triads: Synthesis and photochemical characterization," *Journal of Photochemistry and Photobiology A: Chemistry,* vol. 242, pp. 59 - 66, 2012.

[267] J. E. Rogers, K. A. Nguyen, D. C. Hufnagle, D. G. McLean, W. Su, K. M. Gossett, A. R. Burke, S. A. Vinogradov, R. Pachter and P. A. Fleitz, "Observation and interpretation of annulater porphyrins: studies on the photophysical properties of meso-tetraphenylmetalloporphyrins," *Journal of Physical Chemistry A,* vol. 107, no. 51, pp. 11331 - 11339, 2003.

[268] H. L. Kee, J. Bhaumik, J. R. Diers, P. Mroz, M. R. Hamblin, D. F. Bocian, J. S. Lindsey and D. Holten, "Photophysical characterization of imidazolium-substituted Pd(II), In(II), and Zn(II) porphyrins as photosensitizers for photodynamic therapy," *Journal of Photochemistry and Photobiology A: Chemistry,* vol. 200, no. 3 - 5, pp. 346 - 355, 2008.

[269] J. Schneider, K. Q. Vuong, J. A. Calladine, X.-Z. Sun, A. C. Whitwood, M. W. George and R. N. Perutz, "Photochemistry and photophysics of a Pd(II) metalloporphyrin: Re(I) tricarbonyl bypiridine molecular diad and its activity toward the photoreduction of CO2 to CO," *Inorganic Chemistry,* vol. 50, pp. 11877 - 11889, 2011.

[270] M. A. Filatov, F. Etzold, D. Gehrig, F. Laquai, D. Busko, K. Landfester and S. Baluschev, "Interplay between singlet and triplet excited states in a conformationally locked donor-acceptor dyad," *Dalton Transactions,* vol. 44, pp. 19207 - 19217, 2015.

[271] P. Kubát and J. Mosinger, "Photophysical properties of metal complexes of meso-tetrakis(4-sulphonatophenyl)poprhyrin," *Journal of Photochemistry and Photobiology A: Chemistry,* vol. 96, pp. 93 - 97, 1996.

[272] D. Eastwood and M. Gouterman, "Poprhyrins. Luminescence of Co, Ni, Pd, Pt complexes," *Journal of Molecular Spectroscopy,* vol. 35, pp. 359 - 375, 1970.

[273] W. C. Li and H. F. Tse, "Health risk and significance of mercury in the environment," *Environmental Science and Pollution Research,* vol. 22, pp. 192 - 201, 2015.

[274] C. A. Flemming and J. T. Trevors, "Copper toxicity and chemistry in the environment: A review," *Water, Air and Soil Pollution,* vol. 44, pp. 143 - 158, 1989.

[275] H. Wajeeha Ejaz, W. Wang and M. Lang, "Copper toxicity link to pathogenesis of Alzheimer's disease and therapeutics approaches," *International Journal of Molecular Sciences,* vol. 21, no. 20, p. 7660, 2020.

[276] N. Kaur, G. Kaur, U. A. Fegade, A. Singh, S. K. Sahoo, A. S. Kuwar and N. Singh, "Anion sensing with chemosensors having multiple -NH recognition units," *TrAC Trends in Analytical Chemistry,* vol. 95, pp. 86 - 109, 2017.

[277] W. C. Schiessl, N. K. Summa, C. F. Weber, S. Gubo, C. Dücker-Benfer, R. Puchta, N. J. R. van Eikema Hommes and R. van Eldik, "Experimental and theoretical approaches to the protonation of thiourea: a convenient nucleophile in coordination chemistry revisited," *Journal of Inorganic and General Chemistry,* vol. 631, pp. 2812 - 2819, 2005.

[278] G. Jakab, C. Tancon, Z. Zhang, K. M. Lippert and P. R. Schreiner, "(Thio)urea organocatalyst equilibrium acidities in DMSO," *Organic Letters,* vol. 14, no. 7, pp. 1724 - 1727, 2012.

[279] X. Chen, W. Zeng, X. Yang, X. Lu, J. Qu and R. Liu, "Thiourea based conjugated polymer fluorescent chemosensor for Cu(II) and its use for detection of hydrogen peroxide and glucose," *Chinese Journal of Polymer Science,* vol. 34, no. 3, pp. 324 - 331, 2016.

[280] D. Udhayakumari, S. Velmathi, P. Venkatesan and S. Wu, "Anthracene coupled thiourea as colorimetric sensor for F-/Cu(II) and fluorescent sensor for Hg(II)/picric acid," *Journal of Luminiscence,* vol. 161, pp. 411 - 416, 2015.

[281] S. Krzewska, L. Pajdowski and H. Podsiadły, "Studies on the reaction of copper (II) with thiourea-II: The modification of bjerrum's method. The determination of equilibrium in simultaneous redox and complexation reactions," *Journal of Inorganic and Nuclear Chemistry,* vol. 42, no. 1, pp. 87 - 88, 1980.

[282] I. Das and M. Halder, "Counterpointing scenarios on the fate of different prototropic forms of norfloxacin housed in the pocked of lysozyme: The nonelectrostatic interactions in the protein are in the controlling role on the prototropic equlibria of the guest," *ACS Omega,* vol. 2, pp. 5504 - 5517, 2017.

[283] G. L. Klein, "Aluminm toxicity to bone: A multisystem effect?," *Osteoporosis and Sarcopenia,* vol. 5, no. 1, pp. 2 - 5, 2019.

[284] R. H. Alasfar and R. J. Isaifan, "Aluminum environmental pollution: the silent killer," *Environmental Health and Pollution Research,* vol. 28, pp. 44587 - 44597, 2021.

[285] J. Yang, A. Acharjya, M.-Y. Ye, J. Rabeah, S. Li, Z. Kochovski, S. Youk, J. Roeser, J. Grüneberg, C. Penschke, M. Schwarze, T. Wang, Y. Lu, R. van de Krol, M. Oschatz, R. Schomäcker, P. Saalfrank and A. Thomas, "Protonated imine-linked covalent organic frameworks for photocatalytic hydrogen evolution," *Photocatalysis,* vol. 60, no. 19797 - 19803, p. Angewandte Chemie International Edition, 2011.

[286] Y. Tao, S. Liu, Y. Zhang, Z. Chi and J. Xu, "A pH-responsive polymer based on dynamic imine bonds as a drug delivery material with pseudo target release behavior," *Polymer Chemistry,* vol. 9, pp. 878 - 884, 2018.

[287] M. D. Liptak, K. C. Gross, P. G. Seybol, S. Feldgus and G. C. Shields, "Absolute pKa determinations for substituted phenols," *Journal of the American Chemical Society,* vol. 124, no. 22, pp. 6421 - 6427, 2002.

[288] M. Mosquera, J. C. Penedo, M. C. Ríos Rodríguez and F. Rodríguez-Prieto, "Photoinduced inter- and intramolecular proton transfer in aqueous and ethanolic solutions of 2-(2'-hydroxyphenyl)benzimidazole: evidence of tautomeric and conformational equilibria in the ground state," *Journal of Physical Chemistry,* vol. 100, pp. 5398 - 5407, 1996.

[289] H.-O. Bertrand, M.-O. Christen and J.-L. Burgot, "New tautomerism suggested by pKa determinations," *Analyst,* vol. 120, pp. 2639 - 2642, 1995.

[290] L. Antonov, S. Kawauchi and K. Shirata, "Acid dissociation constants for the benzimidazole unit in the polybenzimidazole chain: configuration effects," *Molecules,* vol. 27, p. 1064, 2022.

[291] S. Bhowal and A. Ghosh, "Highly selective fluorescence turn-on-off sensing of OH-, Al3+ and Fe3+ ions by tuning ESIPT in metal organic frameworks and mitochondria targeted bio-imaging," *RSC Advances,* vol. 11, p. 27787, 2021.

[292] S. Sinha, B. Chowdhury and P. Ghosh, "A highly sensitive ESIPT-based ratiometric fluorescence sensor for the detection of Al(III)," *Inorganic Chemistry,* vol. 55, no. 18, pp. 9212 - 9220, 2016.

[293] N. C. Lim and C. Brückner, "DPA-substituted coumarins as chemosensors for zinc(II): modulation of the chemosensor characteristics by variation of the position of the chelate coumarin," *Chemical Communications,* pp. 1094 - 1095, 2004.

[294] M. M. Henary, Y. Wu and C. J. Fahrni, "Zinc(II)-selective ratiometric fluorescent sensor based on inhibition of excited-state intramolecular proton transfer," *Chemistry - A European Journal,* vol. 10, pp. 3015 - 3025, 2004.

[295] F. A. Chipem, S. Kumar Behera and G. Krishnamoorthy, "Ratiometric fluorescence sensing ability of 2-(2'-hydroxyphenyl)benzimidazole and its nitrogen substituted analogues towards metal ions," *Sensors and Actuators B: Chemical,* vol. 191, pp. 727 - 733, 2014.

[296] D. Udhayakumari, S. Saravanamoorthy, M. Ashok and S. Velmathi, "Simple imine linked colorimetric and fluorescent receptor for sensing Zn(II) ions in aqueous medium based on inhibitionof ESIPT mechanism," *Tetrahedron Letters,* vol. 52, pp. 4631 - 4635, 2011.

[297] H. Kuzhandaivel, S. Banu Basha, I. D. Charles, N. Raju, U. Singaravelu and K. S. Nallathambi, "Performance of 2-hydroxy-1-naphthaldehyde-2-amino thiazole as a highly selective turn-on fluorescent chemosensor for Al(III) ions. Detection and biological applications," *Journal of Fluorescence,* vol. 31, pp. 1041 - 1053, 2021.

[298] N. Roohani, R. Hurrell, R. Kelishadi and R. Schulin, "Zinc and its importance for human health: An integrated review," *Journal of Research in Medical Sciences,* vol. 18, no. 2, pp. 144 - 157, 2013.

[299] Z. Yuan, Q. Tang, K. Sreenath, J. T. Simmons, A. H. Younes, D.-e. Jiang and L. Zhu, "Absorption and emission sensitivity of 2-(2'hydroxyphenyl)benzoxazole to solvents and impurities," *Photochemistry and Photobiology,* vol. 91, no. 3, pp. 586 - 598, 2015.

[300] A. Islam, N. Zaidi, H. Ahmad and S. Yadav, "Synthesis, characterization, and systematic studies of a novel aluminum selective chelating resin," *Environmental Monitoring Assesment,* vol. 186, pp. 5843 - 5853, 2014.

[301] H. R. Hoveyda, S. J. Rettig and C. Orvig, "Coordination chemistry of 2-(2'-hydroxyphenyl)-2-benzoxazolewith gallium(III) and aluminum(III): two uncommon group 13 metal environments stabilized by a biologically relevant binding group," *Inorganic Chemistry,* vol. 32, pp. 4909 - 4913, 1993.

[302] M. Das, M. Brahma and G. Krishnamoorthy, "Host-guest interaction aided Zn carry and delivery by ESIPT active 2-(2'-hydrpoxyphenyl)benzoxazole," *Spectrochimica Acta Part A: Molecular and Biomolecular Spectroscopy,* vol. 281, p. 121474, 2022.

[303] R. G. Pearson, "Hard and soft acids and bases," *Journal of the American Chemical Society,* vol. 85, no. 22, pp. 3533 - 3539, 1963.

[304] M. Misono, E. Ochiai, Y. Saito and Y. Yoneda, "A new dual parameter scale for the strength of Lewis acids and bases with the evaluation of their softness," *Journal of Inorganic and Nuclear Chemistry,* vol. 29, no. 11, pp. 2685 - 2691, 1967.

[305] H. Lee, S. Lee and M. S. Han, "Turn-On fluorescent pH probes for monitoring alkaline pH using bis[2-(2'hydroxyphenyl)benzazole] derivatives," *Sensors,* vol. 23, p. 2044, 2023.

[306] A. Nano, "Towards optical memories: switchable optical systems for electron and energy transfer processes," Strasbourg, 2015.

[307] K. M. Herrmann and L. M. Weaver, "The Shikimate pathway," *Annual Review of Plant Physiology and Plant Molecular Biology,* vol. 50, pp. 473 - 503, 1999.

VI. List of publications

1. C. Murga, A. Bhattacharya, S. Wang, B. Amouroux, N. Casaretto, S. Bourcier, I. Leray, G. Zucchi, “Selective ion sensing in aqueous media with ESIPT active fluorescent probes – A particular case for hypochlorite detection,” *Dyes and Pigments*, vol. 218, pp. 111524, 2023. https://doi.org/10.1016/j.dyepig.2023.111524

VII. List of oral presentations and posters

1. Murga, Christian and Zucchi, Gaël (2022, December 5 - 8). Oral presentation: *A novel 2-(2-hydroxyphenyl)-benzimidazole-based ESIPT molecule for the selective detection of Al^{3+} and OCl^- by fluorescence in near perfect aqueous medium*. Science et Technologue des Systèmes pi-Conjugués. St. Malo, Bretagne, France.

2. Murga, Christian and Zucchi, Gaël (2022, October 10 - 13). Poster: *Luminescent molecules as sensing materials: design, synthesis and sensing performance of a new benzimidazole derivative*. 9ème Congrès du LPICM. Moliets et Maa, Nouvelle-Aquitaine, France.

3. Murga, Christian and Zucchi, Gaël (2021, October 19). Poster: *Luminescent molecules as sensing materials*. 2021 LPICM PhD Day. Palaiseau, Île-de-France, France.

4. Murga, Christian and Zucchi, Gaël (2021, September 27). Poster: *Luminescent molecules as sensing materials*. 1ère journée Eugène Demarçay. Palaiseau, Île-de-France, France.

ECOLE DOCTORALE

Titre : Molécules conjuguées pour l'élaboration de capteurs optiques pour la surveillance de l'eau

Mots clés : synthèse, photophysique, molécules conjuguées, capteurs optiques

Résumé : Le rejet inconsidéré de produits chimiques dans l'air, le sol et l'eau constitue une menace importante pour l'environnement, devenant un problème de santé publique majeur. À cet égard, la détermination de la qualité de l'eau du robinet reçue par le grand public est un problème urgent auquel il faut s'attaquer.
Pour ce faire, deux axes peuvent être délimités : la mesure de la présence de familles chimiques ayant des effets toxiques sur l'homme, telles que les métaux lourds et les pesticides, et la mesure d'espèces dont la présence est généralement indicative d'un environnement sain, comme l'anion hypochlorite et l'oxygène moléculaire dissous.
Bien qu'il existe déjà plusieurs méthodes différentes pour détecter et surveiller ces produits chimiques, telles que la GC-MS ou la HPLC, elles nécessitent des instruments lourds et coûteux, ainsi que du personnel hautement qualifié pour les utiliser.
Par conséquent, dans le but de développer des techniques simples et rapides, l'objectif de ce projet est de concevoir et de synthétiser de nouvelles molécules conjuguées ayant des propriétés optiques adéquates. Ces molécules sont conçues de telle manière que leur luminescence est modifiée lorsqu'elles interagissent avec un analyte conduisant à la détection de ce dernier, voire la détermination précise de sa concentration.
Dans le cadre de ce travail de thèse, 11 nouveaux composés dotés de capacités de détection ont été développés à partir des familles chimiques pyrène, benzazole, coumarine et porphyrine. Les études de détection effectuées par spectroscopie de luminescence ont montré qu'ils peuvent détecter efficacement les ions Al^{3+}, Fe^{2+}, Fe^{3+}, Cu^{2+}, Zn^{2+}, OCl^-, glyphosate et O_2 dissous dans des environnements aqueux.

Title : Conjugated molecules for the elaboration of optical sensors for water monitoring

Keywords : synthesis, photophysics, conjugated molecules, optical sensors

Abstract : The indiscriminate release of chemicals into the air, soil and water possesses a significant threat to the environment and has developed into a significant public health concern. In this regard, the effective and efficient measure of the quality of tap water that is received by the general public is an urgent problem that needs to be tackled.
To achieve this, two axes can be delimited: measuring the presence of chemical families that that have toxic effects on humans such as heavy metals and pesticides; and measuring species which presence is generally indicative of a healthy environment such as the hypochlorite anion and dissolved molecular oxygen.
Although several different methodologies already exist to detect and monitor these chemicals, such as GC-MS or HPLC, they require heavy and expensive instrumentation, and highly skilled personnel to operate them.
Hence, as there is an increasing need of being able to detect analytes present in the environment using simple and fast techniques, the goal of this project is to design and synthesize novel conjugated small molecules with adequate optical properties. These molecules are such that, upon interacting with a target analyte, can change their fluorescence or phosphorescence in a way that qualification and/or quantification of such species can be made.
Within the scope of this thesis work, 11 new compounds with sensing capabilities have been developed using the pyrene, benzazole, coumarin and porphyrin chemical families. Sensing studies with these compounds show that they can effectively detect Al^{3+}, Fe^{2+}, Fe^{3+}, Cu^{2+}, Zn^{2+}, OCl^-, glyphosate and O_2 in aqueous environments.